An Integrated Boltzmann+Hydrodynamics Approach to Heavy Ion Collisions

Dissertation
zur Erlangung des Doktorgrades
der Naturwissenschaften

vorgelegt beim Fachbereich Physik
der Johann Wolfgang Goethe-Universität
in Frankfurt am Main

von
Hannah Petersen
aus Frankfurt am Main

Frankfurt am Main 2009
(D30)

vom Fachbereich Physik (13) der Johann Wolfgang Goethe-Universität als Dissertation angenommen.

Dekan: Prof. Dr. D. H. Rischke

Gutachter: JProf. Dr. M. Bleicher, Prof. Dr. H. Stöcker

Datum der Disputation: 22. April 2009

1 Zusammenfassung

Diese Arbeit basiert auf folgenden Publikationen:

- "(3+1)-Dimensional Hydrodynamic Expansion with a Critical Point from Realistic Initial Conditions" [Ste08a],
- "How sensitive are di-leptons from rho mesons to the high baryon density region?" [Vog08b],
- "How can we explore the onset of deconfinement by experiment?" [Aic07],
- "UrQMD-2.3 - Changes and Comparisons" [Pet08a],
- "A Fully Integrated Transport Approach to Heavy Ion Reactions with an Intermediate Hydrodynamic Stage" [Pet08b],
- "Effects of a phase transition on HBT correlations in an integrated Boltzmann + Hydrodynamics approach" [Li08b],
- "Charged particle (pseudo-)rapidity distributions in proton+anti-proton, proton+proton and Pb+Pb/Au+Au collisions from SPS to LHC energies from UrQMD" [Mit08],
- "Ideal hydrodynamics and elliptic flow at SPS energies: Importance of the initial conditions" [Pet09a],
- "Elliptic flow in an integrated (3+1)d microscopic+macroscopic approach with fluctuating initial conditions" [Pet08c],
- "$\langle m_T \rangle$ excitation function: Freeze-out and equation of state dependence" [Pet09b],
- "Centrality and system size dependence of (multi-strange) hyperons at 40 and 158A GeV: A comparison between a binary collision and a Boltzmann+hydrodynamics hybrid model" [Pet09c],
- "Strangeness fluctuations and MEMO production at FAIR"[Ste08b].

1.1 Einführung

Wenige Mikrosekunden nach dem Urknall hat im frühen Universum ein Phasenübergang vom Quark-Gluon-Plasma (QGP) zu einem Hadrongas stattgefunden. Im QGP sind die Quarks und Gluonen nicht mehr in einzelne Hadronen eingeschlossen, das heißt, sie können sich frei über einen größeren Raumbereich bewegen. Aus Gitterrechnungen der Quantenchromodynamik (QCD) erwartet man, dass die kritische Temperatur für den Phasenübergang von hadronischer Materie zum Quark-Gluon-Plasma bei ca. $T_c \approx$ 170 MeV (ca. 10 Mrd. °C) liegen sollte. Dieser Übergang ist insofern von besonderem Interesse, da hierbei alle uns umgebende Materie im Universum erzeugt wurde.

Heutige Experimente an Schwerionenbeschleunigern ermöglichen es seit kurzem diesen Zustand des Universums wie er vor 13 Mrd. Jahren herrschte auf der Erde zu erzeugen ("Urknall im Labor") und erlauben es uns daher zu studieren, wie dieser Phasenübergang stark wechselwirkender QCD-Materie genau abgelaufen ist. Die experimentelle Erforschung dieser Phänomene findet zur Zeit an den größten Teilchenbeschleunigern am CERN (Centre Europeen de la Recherche Nucleaire) in Genf, am RHIC (Relativistic Heavy Ion Collider) in Brookhaven bei New York und an der GSI-Helmholtzzentrum für Schwerionenforschung in Darmstadt statt. Hier werden Blei- bzw. Goldionen auf ultrarelativistische Energien beschleunigt und aufeinander geschossen. Je nach Beschleunigungsenergie kann man dann verschiedene Aspekte der Zustandsgleichung von stark wechselwirkender Materie studieren. Insbesondere in ultra-relativistischen Schwerionenkollisionen kann man in der Tat Bedingungen ähnlich zu denen im frühen Universum erzeugen.

Bei diesen Kollisionen werden tausende neue Teilchen erzeugt, deren Orts- und Impulsverteilung dann gemessen werden können. Um nun aus den gemessenen Daten etwas über den anfänglich erzeugten Zustand lernen zu können, ist die Entwicklung von theoretischen Modellen unverzichtbar. Die theoretische Beschreibung von Schwerionenkollisionen erfordert hohen mathematischen und numerischen Aufwand. Die typischen Zeitskalen für einen solchen Prozess sind Femtometer, d.h. etwa 10^{-23} Sekunden. Das bedeutet, es handelt sich um einen sehr schnellen explosionsartigen Prozess.

In dieser Arbeit werden zunächst die Ansätze vorgestellt, die heutzutage am meisten verwendet werden. Mittels Gitter-QCD-Rechnungen lassen sich die thermodynamischen Eigenschaften stark wechselwirkender Materie und Eigenschaften gebundener Zustände vorhersagen. Allerdings ist diese Vorhersagekraft beschränkt durch die endliche Größe des Gitters und der Zellen und entsprechende Extrapolationen und es sind keinerlei dynamische Rechnungen möglich. Statistische Modelle erlauben es mittels großkanonischer Verteilungsfunktionen aus den Teilchenzahlen im Endzustand auf die Temperatur und die Dichte am Ausfrierzeitpunkt zurück zu schließen. Eine dynamische Beschreibung des kollektiven Verhaltens des erzeugten Systems ist durch hydrodynamische Modelle, die auf der Annahme des lokalen thermischen Gleichgewichts beruhen, gegeben. Hier sind in letzter Zeit vor allem die Entwicklung von viskosen Hydrodynamik-Rechnungen und Entwicklungen auf dem Gebiet der sogenannten Hybridmodelle hervorzuheben. Diese

Hybridmodelle beruhen auf der Kombination eines Transport-Modells mit einer hydrodynamischen Rechnung. Ein weiterer sowohl für die Beschreibung der partonischen als auch der hadronischen Phase sehr erfolgreicher Ansatz sind mikroskopische Modelle. Auf Grund des explosiven Nicht-Gleichgewicht-Charakters der Kollision kann nur durch mikroskopische Ansätze der ganze Kollisionsprozess von der Initialisierung der Kerne bis zum Endzustand konsistent dynamisch beschrieben werden. Diese Beschreibungen beruhen meist auf der relativistischen Boltzmanngleichung.

1.2 Das UrQMD-Modell

Eine Lösung für die Dynamik der heißen, dichten QCD-Materie durch explizite numerische Integration der Bewegungsgleichungen stellt die Ultra-relativistische Quantenmolekulardynamik (UrQMD) dar, die in unserer Arbeitsgruppe entwickelt worden ist. Die essentiellen Bestandteile dieses Transportmodells sind die berücksichtigten Teilchenarten und die Berechnung der Reaktions-Wirkungsquerschnitte. Dieses Modell erlaubt es, die gesamte Raum-Zeit-Dynamik der Hadronen und Color-Strings zu bestimmen. Im Detail werden hierzu ca. 10.000 gekoppelte Integro-Differentialgleichungen gelöst, d.h. die Hadronen werden auf relativistischen Trajektorien propagiert und wechselwirken über $2 \leftrightarrow 2$, $2 \rightarrow n$ und $1 \rightarrow n$ Reaktionen.

Als Grundlage für die weiteren Entwicklungen im Rahmen dieser Arbeit war es nötig, das bestehende UrQMD-Modell eingehend zu testen und Vergleiche zwischen den neuesten Resultaten und den gemessenen Daten anzustellen. Das aktuelle Modell beschreibt die grundlegenden Observablen wie Teilchenmultiplizitäten und -spektren gut, allerdings wird beispielsweise zu wenig elliptischer Fluss bei hohen Energien und zu wenig Seltsamkeit erzeugt. Außerdem ist es nicht möglich den Phasenübergang im Rahmen des reinen Transportmodells konsistent zu beschreiben. Nach einer entsprechenden Erweiterung war es möglich, Vorhersagen für die Teilchenproduktion am Large Hadron Collider (LHC) zu machen, der deutlich höhere Strahlenergien liefern wird, als es bisher möglich war.

Um den Phasenübergang nun durch Implementation einer anderen Dynamik für die QGP-Phase in das bestehende UrQMD-Modell zu simulieren, ist es in jedem Fall notwendig zu wissen, wann das System eine kritsche Teilchen- oder Energiedichte erreicht hat. Diese Größen sind in einer Nicht-Gleichgewichts-Transportrechnung wie es UrQMD darstellt aber nicht intrinsisch bekannt, sondern müssen berechnet werden. Hierbei muss vor allem die relativistische Natur der Schwerionenkollisionen berücksichtigt werden. Das ist bei der Wahl des Koordinatensystems für die Dichteberechnung entscheidend, da die Längenkontraktion zu dramatischen Erhöhungen der Dichte führen kann. Deswegen wird die Berechnung der Baryonendichte innerhalb des Transportmodells untersucht und ein neues stabiles Verfahren implementiert. Für den zeitlichen Verlauf der Baryonen- bzw. Quarkdichten können so vernünftige Ergebnisse für Schwerionenkollisionen bei allen Energien berechnet werden.

Als eine Vorstufe zu der Entwicklung des integrierten Hybridmodells werden Studien von Phasendiagrammtrajektorien mittels eines hydrodynamischen Modells mit Anfangsbedingungen, die durch UrQMD generiert wurden, durchgeführt. Daraus kann man schließen, dass es stark von der verwendeten Zustandsgleichung abhängt, bei welchen Strahlenergien ein signifikanter Teil des Systems den kritischen Punkt erreicht.

1.3 Das Hybridmodell

Eine andere Möglichkeit die QGP-Phase zu modellieren ist die Anwendung der Methoden der relativistischen Hydrodynamik. Schon seit vielen Jahren werden hydrodynamische Modelle für die Beschreibung von Schwerionenkollisionen verwendet. Dieser makroskopische Ansatz, innerhalb dessen die erzeugte heiße und dichte Zone als expandierende Flüssigkeit angesehen wird, ist gerade aktuell sehr erfolgreich in der Beschreibung kollektiver Eigenschaften des Systems. Die Presse-Meldungen, dass am Relativistic Heavy Ion Collider (RHIC) in den USA das QGP als “perfect liquid” gefunden wurde, beziehen sich genau auf diesen Erfolg.

In der relativistischen Hydrodynamik wird die in Schwerionenkollisionen erzeugte extrem dichte und heiße Materie als eine Art Flüssigkeitstropfen beschrieben. Hierbei werden keine einzelnen Teilchenbahnen mehr berechnet, sondern das System wird durch seine thermodynamischen Eigenschaften charakterisiert. Das heißt, das System wird in viele kleine Zellen unterteilt, denen jeweils eine Temperatur, eine Energiedichte, eine mittlere Geschwindigkeit, eine Baryonendichte und ein Druck zugeordnet werden. Diese Zellen werden dann nach den nötigen Erhaltungssätzen (Energie, Netto-Baryonenzahl) propagiert. Als zusätzliche Spezifizierung des Systems geht in diesen makroskopischen Ansatz die Zustandsgleichung der Materie ein. Die Zustandsgleichung beschreibt den Zusammenhang zwischen Druck, Energiedichte und Baryonendichte. Durch eine Änderung der Zustandsgleichung kann auch der Phasenübergang zum Quark-Gluon-Plasma simuliert werden.

Bei der Entwicklung eines integrierten mikro- +makroskopischen Modells müssen nun insbesondere die zwei Schnittstellen zwischen den verschiedenen Beschreibungen (Transport und Hydrodynamik) im einzelnen durchdacht und implementiert werden. Um realistische Anfangsbedingungen für die hydrodynamische Rechnung zu generieren, läuft die Transportrechnung bis zu dem Zeitpunkt, an dem die zwei kollidierenden Kerne vollständig durcheinander durchgelaufen sind. Dies entspricht dem frühestmöglichen Zeitpunkt, an dem ein lokales Gleichgewicht erwartet werden kann wie es für die hydrodynamische Beschreibung nötig ist. Die einzelnen Teilchen werden dann durch die Darstellung als gaußförmige Wellenpakete in zugehörige Dichteverteilungen übersetzt. Die durch das Transportmodell generierten Anfangsbedingungen sind nicht symmetrisch und nicht-trivial. Die Baryonen- und Energiedichteverteilungen fluktuieren von Ereignis zu Ereignis. Auch die anf nglichen Geschwindigkeitsverteilungen sind nicht-trivial.

Während der hydrodynamischen Phase stehen drei verschiedene Zustandsgleichungen

zur Verfügung. Darunter ist eine rein hadronische Zustandsgleichung mit denselben Freiheitsgraden wie sie im UrQMD enthalten sind. Damit besteht die Möglichkeit innerhalb der gleichen Anfangs- und Ausfrierbedingungen die Unterschiede in der Dynamik zu untersuchen. Des weiteren gibt es eine chirale Zustandsgleichung und eine Zustandsgleichung, die einen Phasenübergang erster Ordnung zum QGP beruhend auf dem MIT-Bag-Modell beschreibt.

Die zweite Schnittstelle ist der sogenannte Ausfrierzeitpunkt, an dem die Materie wieder dünner wird und die freie Weglänge so groß wird, dass man keine Hydrodynamik mehr anwenden kann. Wenn alle Zellen des Gitters, das für die hydrodynamische Rechnung verwendet wird, unter einer bestimmten Energiedichte liegen, werden durch thermische Verteilungsfunktionen entsprechend des Cooper-Frye-Formalismus die Dichten wieder in einzelne Teilchen umgesetzt. Die weiteren Zerfälle und Kollisionen werden dann wieder in dem Transportmodell berechnet. Hierbei ist es wichtig die Quantenzahlen zu erhalten.

Es hat sich herausgestellt, dass das vollständig gleichzeitige Ausfrieren des kompletten Systems bei höheren Energien zu einer unphysikalischen longitudinalen Temperaturverteilung führt. Deshalb gibt es nun auch die Möglichkeit transversale Scheiben nacheinander auszufrieren, was insbesondere für die Rapiditätsspektren (Verteilungen in der Geschwindigkeit entlang der Strahlachse) zu besseren Ergebnissen führt und effektiv einem gleichzeitigen Ausfrierpunkt in der Eigenzeit der jeweiligen Zellen entspricht.

1.4 Ergebnisse für verschiedene Observablen

Zunächst wurden Rechnungen mit einer hadronischen Zustandsgleichung ohne Phasenübergang gemacht, um die Unterschiede in den Observablen, die allein durch die verschiedene Dynamik zustande kommen, zu erkennen. Als erstes wurden die Multiplizitäten, und Transversalimpuls- und Rapiditätsspektren berechnet. Dies sind die grundlegenden Observablen, an denen man testen kann, ob die Reaktionsdynamik und -kinematik mit dem Experiment übereinstimmt. Die longitudinalen Impulsverteilungen sind nicht sensitiv auf die Dynamik der Hochdichtephase während die Transversalimpulsspektren für verschiedene Teilchensorten und Einschussenergien deutliche Abhängigkeiten auf die Expansion zeigen. Außerdem wurden die Abhängigkeiten dieser Observablen auf die Wahl der zwei Schnittstellen getestet. Es treten keine großen Abhängigkeiten auf und das bestätigt die Wahl unserer Bedingungen. Zeitentwicklungen verschiedener Observablen wurden ebenfalls berechnet und beide Modelle verglichen. Dabei wurde festgestellt, dass diese auch an den Schnittstellen weitgehend glatt sind und keine großen Sprünge auftreten. Auch dies sichert die physikalischen Grundlagen unseres Modells.

Untersuchungen komplexerer Beobachtungsgrößen weisen darauf hin, dass durchaus Unterschiede zwischen der integrierten hydrodynamischen Beschreibung und der reinen Transportrechnung auftreten. Beispielsweise ist die Produktion seltsamer Teilchen (Teilchen, die mindestens ein s-Quark oder ein $\bar{s}$-Quark enthalten) erhöht, weil es sehr schwierig ist, diese in Resonanzen oder durch Stringanregung im reinen UrQMD-Modell zu er-

zeugen. Die Thermalisierung in der Hydrodynamik führt zu höheren Anzahlen seltsamer Teilchen, die sogar für die Zentralitätsabhängigkeit in guter Übereinstimmung mit den experimentellen Daten sind.

Insbesondere durch die aus dem Nichtgleichgewichts-Modell erzeugten nicht-trivialen Anfangsbedingungen, kann die Anregungsfunktion des elliptischen Flusses mit unserem Modell besser beschrieben werden als bisher. Die Anfangsbedingungen sind nicht symmetrisch und auch die Geschwindigkeitsverteilungen am Anfang sind keine simplen Parametrisierungen, sondern reflektieren die Teilchenproduktion in den anfänglichen Stößen. Außerdem ist die Expansion bei hohen Energien stärker und durch die höheren Druckgradienten im Anfangszustand werden höhere Werte für den elliptischen Fluss erzielt.

Die Anregungsfunktion der mittleren transversalen Masse ist sowohl auf den genauen Ausfrierprozess als auch auf Änderungen der Zustandsgleichung sensitiv. Für den qualitativ besten Verlauf muss man entweder Nichtgleichgewichtseffekte oder einen starken Phasenübergang erster Ordnung einbeziehen. Die Messung der Teilchenkorrelationen mit Hilfe der HBT-Technik bestätigt dieses Ergebnis, wobei hier der genaue Ausfrierprozess keine so große Rolle spielt, solange die Wechselwirkungen in der späten Phase berücksichtigt werden.

Contents

List of Figures

2 Introduction

Strongly interacting matter is very important for our understanding of the universe since all the matter that we are made of consists mainly of quarks and gluons. They are the elementary particles that are - according to today's knowledge - the basic constituents of protons, neutrons and all other hadron species. The fundamental theory that describes the strong interaction is Quantum Chromodynamics (QCD). The running coupling in QCD leads to features as "asymptotic freedom" and confinement. If one tries to pull color charges apart the interaction gets so strong that it is more likely to produce a new quark-antiquark-pair than to seperate the quarks from each other. This picture has led to the so called string model that describes how hadrons are formed. On the contrary, if one heats or compresses hadronic matter more and more a phase transition to a new state of matter is expected. The reverse transition from a quark gluon plasma (QGP) to a hadron gas has also occured in the early universe, some microseconds after the Big Bang.

Fig. 2.1 shows a schematic picture of the phase diagram of strongly interacting matter. The usual nuclear matter that all the nuclei consist of is located at zero temperature around nuclear matter ground state density. The early universe has probably developed along the temperature axis at very low densities cooling down and expanding to its present dimensions. Going to high densities at low temperatures one reaches again exotic matter that might be found in neutron stars as e.g. color superconducting matter. In between there is at lower temperatures and high baryon densities a first order phase transition from the hadron gas to the QGP phase followed by a critical endpoint with a second order phase transition and a cross-over transition at high temperatures and low densities. Theoretically the detailed structure of the phase diagram is not yet fully established.

In high energetic heavy ion collisions the phase diagram of strongly interacting matter is explored experimentally. By colliding nowadays mostly gold or led ions highly compressed and heated nuclear matter is formed under controlled conditions in the laboratory. This explosive process happens on very short timescales of 10^{-23} seconds $\approx$ 1 fm/c seconds. In the course of the collision the beam energy is converted into particle production and thousands of particles have to be measured in the detectors.

One of the main purposes of the research in heavy ion collisions at high beam energies is to explore the existence of the QGP as well as its properties [Hai96, Bas99a, QM08]. The equation of state (EoS) of nuclear matter is one of the key points to gain further understanding since the EoS directly provides the relationship between the pressure and the energy at a given net-baryon density. Phase transitions (PT), e.g., from the

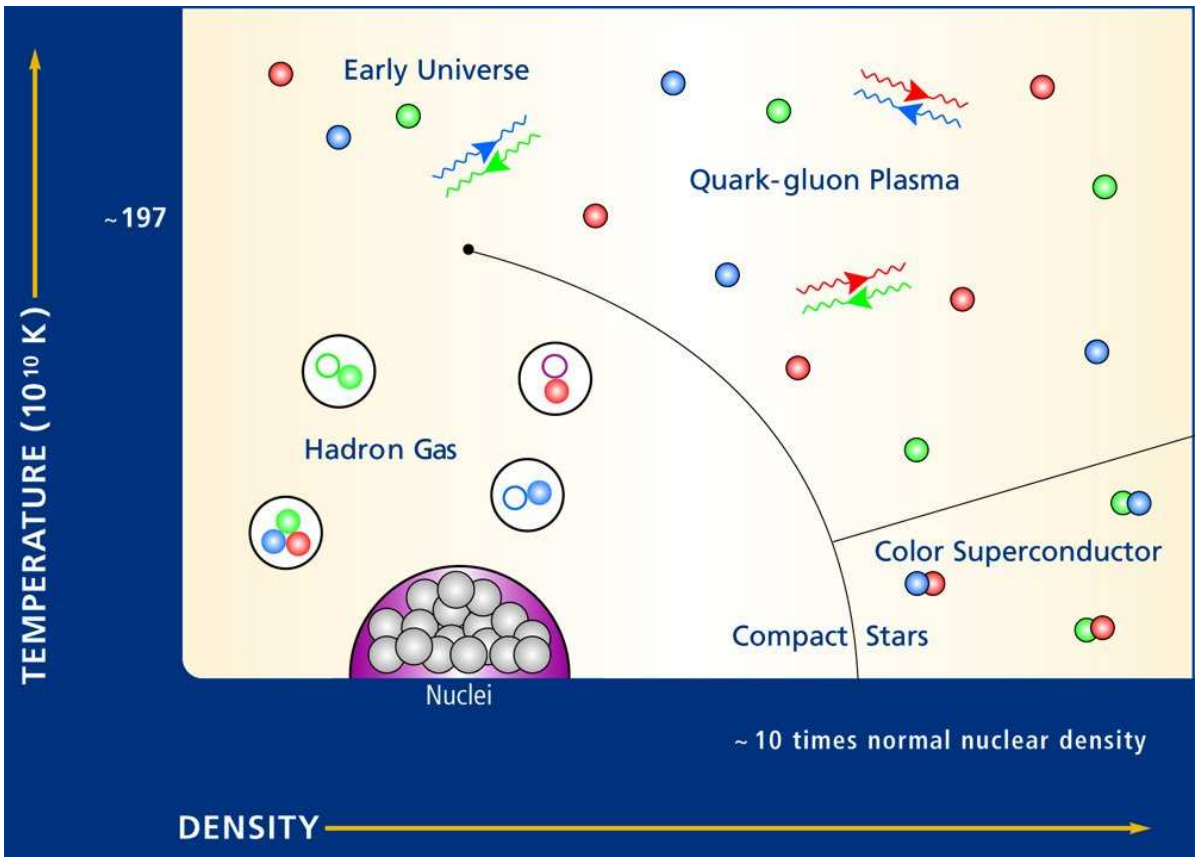

Figure 2.1: Schematic picture of the phase diagram of strongly interacting matter in the temperature-density-plane (taken from [ICE06]).

hadron resonance gas phase (HG) to the color-deconfined QGP (see e.g., [Ris95a, Spi98a, Blu07]), constitute themselves in changes of the underlying EoS.

There are three most important locations of accelerators for heavy ion collisions either running or in preparation to run in the near future. There is the SIS (=SchwerIonen Synchrotron) at GSI (Helmholtzzentrum für Schwerionenforschung) near Darmstadt at the lowest energies (below $E_{\mathrm{lab}} \sim 2A$ GeV) [Sen93, Ani05, Aga07]. In the future the Facility for Antiproton and Ion Research (FAIR) will be build with the SIS-100 and SIS-300 which will run up to $E_{\mathrm{lab}} \sim 30A$ GeV. This new accelerator is supposed to test the high-μ_B-region in the phase diagram and reach very high luminosities [FAIR].

The Alternating Gradient Synchrotron (AGS) at Brookhaven National Laboratory (BNL) on Long Island near New York has taken data in the energy regime of $E_{\mathrm{lab}} \sim 2-11A$ GeV [Pin99, Ahl00b, Ell03]. This machine serves now as the pre-accelerator for the Relativistic Heavy Ion Collider (RHIC) which runs at the highest energies available at the moment ($\sqrt{s_{NN}} = 56 - 200$ GeV). At these energies, it is claimed that a new phase of matter is created which behaves like a strongly coupled nearly perfect liquid. These statements are mostly based on the observation of jet quenching, high p_t hadron suppression due

to medium interactions, and the high elliptic flow values that are compatible with some hydrodynamics predictions [Ads05, Bac05, Ars05, Adc05]. In the near future there will be a low energy program at RHIC to explore the region in the phase diagram of higher densities and lower temperatures. This energy scan program will be very useful to cross check the results from SPS and to have a more detailed look at interesting observables.

The third accelerator where most of the data discussed in this thesis has been taken is the Super Proton Synchrotron (SPS) at Centre Europeen de la Recherche Nucleaire (CERN) near Genf in Switzerland. The SPS has taken data in the intermediate energy regime of $E_{\mathrm{lab}} \sim 20 - 160A$ GeV [Ada03, Alt05c, Arn06]. The intermediate SPS energy regime still raises a lot of interest because evidence for the deconfinement phase transition is expected at those energies and the possibility of a critical endpoint and a first-order phase transition is not yet excluded. Several beam-energy dependent observables such as the particle ratios [Afa02a, Alt08a], the flow [Kol01a, Ble02a, Pet06a], the HBT parameters [Ris96b, Ada03, Li08a] show a non-monotonic behaviour around $E_{\mathrm{lab}} = 30 - 40A$ GeV and the interpretation remains still unclear. At the same place a new machine, the Large Hadron Collider (LHC) will be build and put into operation next year. The LHC will provide p+p collisions with $\sqrt{s_{NN}}$ up to 14 TeV and heavy ion collisions with at maximum $\sqrt{s_{NN}} = 5.5$ TeV [Car04, Ale06].

The study of a many-body-problem such as a heavy ion collision in QCD is not possible from first principles. Therefore, one needs effective theories and models to simulate the dynamics of heavy ion reactions in order to learn something about the hot and dense stage of the evolution from the final state particle distributions. This thesis is focussed on the task to develop an approach that can be applied to simulate heavy ion collisions in a broad range of beam energies. The idea is to have the possibility to explore effects of changes in the equation of state on observables in a consistent manner.

The most promising observables are the following ones:

- The particle multiplicities and spectra might tell us something about the degree of thermalization of the matter and the differences between chemical freeze-out where the particle abundancies are fixed and kinetic freeze-out where all interactions cease.
- The mean transverse momentum excitation function has been proposed as a signal for the observation of the phase transition many years ago [VaH82] and has been further explored in the following years [Gor03, Gaz04]. It might be sensitive to the transverse expansion, but also to the freeze-out process and the degrees of freedom of the matter.
- The transverse collective flow [Stö86, Oll92, Vol08] is very sensitive to the pressure gradients in the early stage of the collisions. Especially, the elliptic flow which measures the momentum space anisotropy of the final particle distributions which is caused by a coordinate space anisotropy in non-central collisions is as a self-quenching effect very sensitive to the early stage dynamics.
- Particle correlations measured with the Hanbury-Brown-Twiss (HBT) technique

reflect the lifetime and the size of the fireball [Lis05, Lis08].

In this work a new Boltzmann + hydrodynamics hybrid approach is proposed for the description of heavy ion collisions in the broad energy range from $E_{\mathrm{lab}} = 2 - 160A$ GeV. In Chapter 3 the present status of different possibilities to model heavy ion reactions and effective theories for strongly interacting matter is reviewed. Then, the Ultra-relativistic Quantum Molecular Dynamics (UrQMD) approach is introduced (Chapter 4) because it serves as the basis of the hybrid approach. Some features and recent results of this hadronic microscopic transport approach are shown and predictions for the particle multiplicties at LHC energies are presented. The topic of Chapter 5 is the calculation of thermodynamic quantities in such a transport model. First, we will concentrate on the baryon density and in the second part discuss first results for phase diagram trajectories in a hydrodynamic model using initial conditions that are generated by UrQMD.

Chapter 6 introduces the main achievement in this thesis, the integrated 3+1 dimensional Boltzmann + hydrodynamics hybrid approach that incorporates an ideal hydrodynamic evolution in the UrQMD approach. All ingredients, like the initial conditions, the hydrodynamic evolution and the equation of state and the freee-out will be explained in detail. Parameter tests, time evolutions and the final state interactions are investigated in Chapter 7. The following Chapters concentrate on results from this hybrid approach. In Chapter 8 the multiplicities and spectra for protons, pions and kaons are compared in a purely hadronic scenario to explore the effect of the change in the dynamics from transport to ideal fluid dynamics. In Chapter 9 the centrality and system size dependence of strangeness production is explored. The elliptic flow excitation function (Chapter 10) is very sensitive to the change of the dynamics. The higher pressure gradients due to the lower mean free path in the hybrid model calculation lead to higher flow values. The mean transverse mass excitation function as another classical phase transition observable is explored in detail in Chapter 11. Chapter 12 shows a systematic investigation of the HBT correlations of pions in the SPS energy regime. The results are rather insensitive to the freeze-out prescription that is applied but clearly dependent on the equation of state. Chapter 13 summarizes the main results of this work.

3 Theoretical Approaches to Heavy Ion Collisions

One of the main motivations to study high energy heavy ion collisions is the creation of a new deconfined phase of strongly interacting matter, the so called Quark-Gluon Plasma (QGP) [Hai96, Bas99a]. Since it is not possible to directly detect free quarks and gluons it is essential to model the evolution of the reaction as realistically as possible. Many different theoretical approaches are employed to learn something about the hot and dense stage of the reaction from the final state observables. In this Chapter the most prominent approaches are presented and some examples for recent results are given.

3.1 Lattice QCD

One attempt to solve Quanten Chromodynamics (QCD) from first principles is to discretize the action and put it on a lattice[Aok06a, Kar07a, Kar07b]. In this way, static properties like particle masses as bound states of the theory or thermodynamic properties can be determined. Dynamical calculations are not possible at the moment in this framework. There are different techniques to reach the physical limits; there are calculations for different approximations like quenched QCD which means that only gluonic degrees of freedom are considered or 2-3 flavour QCD or most realistically 2+1 flavour QCD where two light flavours and one heavier flavour is taken into account. At low baryo-chemical potentials lattice QCD (lQCD) is very successful in predicting the structure of the phase diagram. Still the predictions for the critical temperature where the phase transition from a hadron gas to the QGP is expected vary between 150-190 MeV depending on the specific formalism and the kind of extrapolations that are used.

Fig. 3.1 shows a compilation of results for the critical temperature at zero baryo-chemical potential. Circles indicate that the determination of the transition temperature is based on observables sensitive to chiral symmetry restoration, i.e. the chiral condensate and susceptibilities deduced from it. Squares indicate that observables sensitive to deconfinement have been used to determine the transition temperature, e.g. the Polyakov loop, its susceptibility and/or light and strange quark number susceptibilities. The diamond indicates that both sets of observables have been analyzed. Depending on the continuum extrapolation and the approximations that are used the results differ between $T_c = 150 - 190$ MeV.

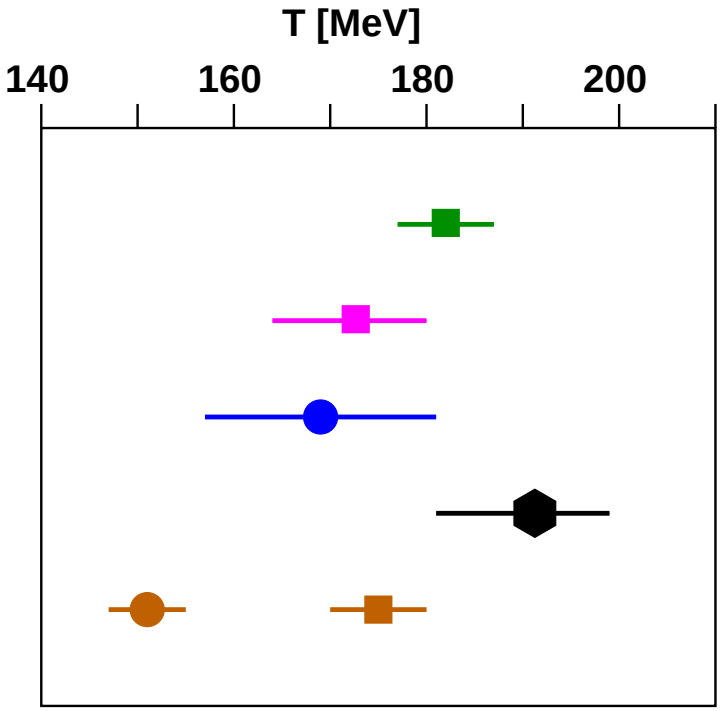

Figure 3.1: Transition temperatures determined in several recent studies of QCD thermodynamics. From top to bottom the first two data points show results obtained in simulations of 2-flavor QCD using clover improved Wilson fermions on lattices with temporal extent $N_\tau = 8$, 10 and 12 [Bor06, Bor07] and $N_\tau = 4$ and 6 [Mae07], respectively. The remaining data points have been obtained in simulations of QCD with 2 light quark masses and a physical strange quark mass. They are based on calculations with staggered fermions using the asqtad action on $N_\tau = 4$, 6 and 8 lattices [Ber05], the p4fat3 action on $N_\tau = 4$, 6 [Che06] and 1-link, stout smeared action on $N_\tau = 4$, 6, 8 and 10 lattices [Aok06b]. With the exception of results presented in [Mae07] all calculations aimed at an extrapolation to the continuum limit ($N_\tau \to \infty$) for physical values of the quark masses. All results have been rescaled to a common physical scale using $r_0 = 0.469$ fm [Gra05]. The figure is taken from [Kar07b].

Especially going to higher baryochemical potentials is not a trivial task. There are recent calculations in which the so far popular picture of the phase diagram as it is depicted in Fig. 2.1 is questioned [For07]. With an ansatz that relies on a series expansion in imaginary chemical potential where one can link the sign of the coefficients to the the curvature of the critical surface in the quark mass plane at finite chemical potentials. These studies indicate that the scenario that there is no critical point and only a crossover phase transition from low to high chemical potentials is very likely.

With phenomenological approaches, e.g. a quasi-particle approach [Lev98, Blu05], it is possible to match lattice QCD data and to extract information for an equation of state. This equation of state can then be used in hydrodynamic approaches as an input. Lattice

QCD calculations are useful to fix independently the input for dynamical calculations and to get deeper insights into the basic thermodynamic properties of QCD.

3.2 Thermodynamic Models

One interesting property of the created hot and dense hadronic matter is the establishment of thermally equilibrated matter. To test this assumption it is possible to fit final particle yields with a statistical model. The idea is that parts of the two nuclei are stopped and after the fireball expansion the particles that fly into the detector are produced according to thermal distributions. Another interpretation is that the hadronization process itself is statistical and particle production happens according to thermal weights. There are many different realizations of this ansatz like [BrM95, BrM96, Cle99, Bec02, Tor05, Kis06]. Most of them use the assumption of the grand-canonical ensemble, but there exist also calculations in other ensembles [Hau08, Bec04a, Bec04b, Liu04]. Especially for strange particles canonical suppression might play an important role [Ham00, Kra07].

Let us assume that the elementary process leads to statistical/thermal particle production. I.e. we can apply thermodynamics to calculate the particle spectra and yields. The starting point is the phase space density:

$$\frac{dN}{d^3p d^3x} = \frac{g}{(2\pi)^3} \frac{1}{\exp((E-\mu)/T) + \alpha} \tag{3.1}$$

Here, E is the energy ($E^2 = p^2 + m^2$), g is the degeneracy factor, μ denotes the chemical potential and T is the temperature. The constant α can be $+1$ for Fermions, 0 for Boltzmann (classical) particles or -1 for Bosons. For Boltzmann (classical) particles spectra can be calculated analytically. This is also the limit for a very hot and dilute Fermi/Bose gas. Quantum effects play a role only at very low temperatures and energies. Therefore we put $\alpha = 0$ in the following. After a change of variables and some integrations one obtains the analytic formula

$$N = \frac{gVT^3 e^{\mu/T}}{2\pi^2} \frac{m^2}{T^2} K_2\left(\frac{m}{T}\right) . \tag{3.2}$$

With $m \gg T$ this simplifies to

$$N = \frac{gVe^{\mu/T}}{2\pi^2} T^{3/2} m^{3/2} \sqrt{\frac{\pi}{2}}\, e^{-m/T} \tag{3.3}$$

Particle ratios allow to extract μ and T if V is the same for all particles.

After rewritint the differential yield in appropriate variables the transverse mass distribution at midrapidity is obtained by setting $y \approx 0$ and $\cosh y = 1$.

$$\frac{1}{m_\perp} \frac{d^2N}{dm_\perp\, dy}\bigg|_{y\approx 0} = \frac{gVe^{\mu/T}}{(2\pi)^2} m_\perp\, e^{-m_\perp/T} \tag{3.4}$$

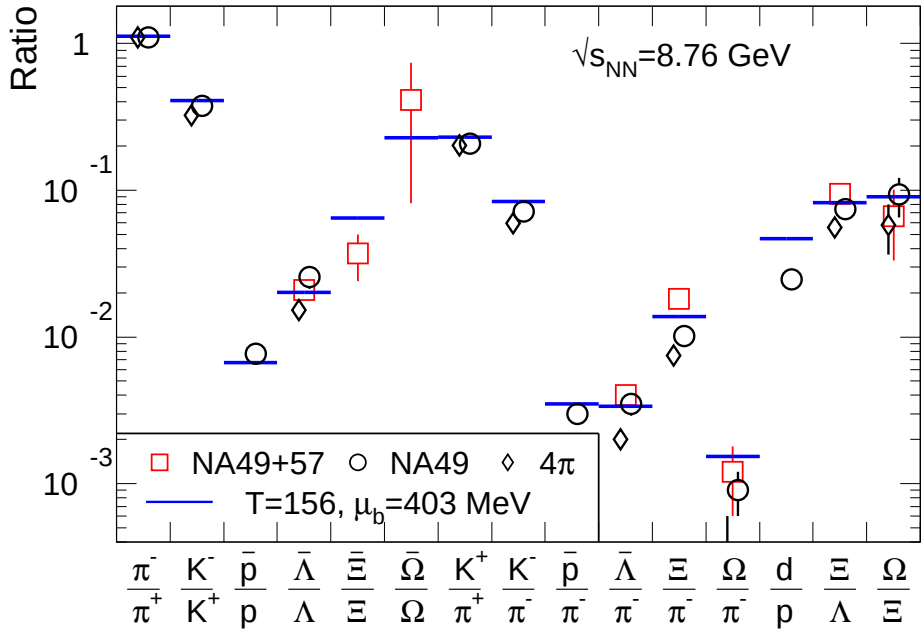

Figure 3.2: Hadron yield ratios with best fit at the SPS beam energy of 40 AGeV using the NA49 and NA57 mid-rapidity data (the ratios K^-/π^-, d/p, Ξ/π^- and Ω/π^- are not included in the fits). The NA49 4π data are plotted for comparison (diamonds). For the ratios Ω/π^- and Ω/Ξ, the Ω yield includes both Ω and $\bar{\Omega}$ (The figure is taken from [Ani06].

The spectrum has an exponential form. This allows to extract T simply from the $m_\perp$ spectrum.

As an example, Fig. 3.2 shows the thermal fit of hadron ratios at $E_{\rm lab} = 40A$ GeV. The extracted temperature and the chemical potential are 156 MeV and 403 MeV respectively. These values correspond to the chemical freeze-out where the abundancies of the different species are fixed.

Also e+e- data can be fit with thermal distributions, so the conclusions about the establicshment of equilibrium remain unclear [Bec08]. Another question is if it is possible to apply the fits to data at midrapidity or only to 4π yields. For resonances thermal fits do not work because of the difference between chemical and kinetic freeze-out. Overall, statistical fits to final state particle distributions give some first insights into the properties of the newly produced strongly interacting matter, but do not even try to govern the dynamical evolution. In general, medium modifications of the particle properties like the mass and the width are not taken into account in this simplified ansatz.

3.3 Hydrodynamics

3.3.1 Ideal Hydrodynamics

Hydrodynamics has been proposed many years ago as a tool for the description of the hot and dense stage of heavy ion reactions where the matter might behave like a locally thermalized ideal fluid [Sch74, Stö80, Ris95b, Ris95a, Agu01, Hir02, Kol03, Ham05, Non07]. In this approach it is possible to model phase transitions explicitly because one of the major inputs to a hydrodynamic calculation is the equation of state (EoS). The hydrodynamic description has gained importance over the last few years because the high elliptic flow values that have been observed at RHIC seem compatible with some ideal hydrodynamic predictions [Kol01a, Kol01b, Huv01]. As an example Fig. 3.3 shows the differential elliptic flow results for different particle species. In the low p_T region ($p_T < 2$ GeV) the ideal hydrodynamic calculations (lines) describe the experimental data (symbols) well. The bulk matter of the created system shows clearly collective behaviour which is in accordance with idela fluid dynamics, especially for central collisions of gold nuclei at RHIC energies in the midrapidity region.

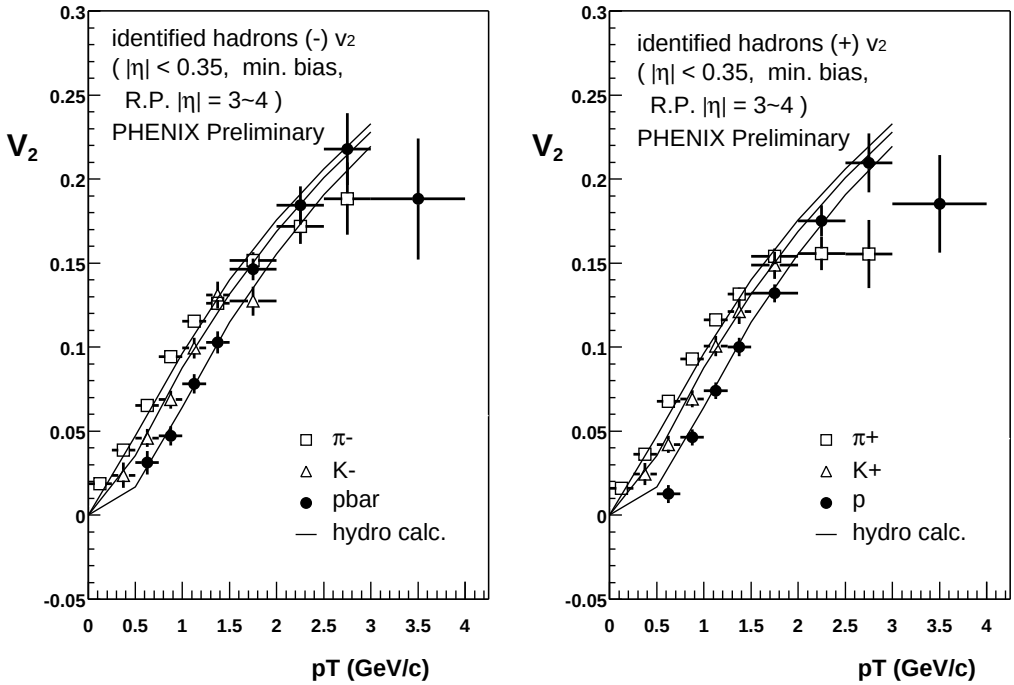

Figure 3.3: Preliminary results for $v_2(p_t)$ of identified pions, kaons and protons with negative (left) and positive (right) charge, measured by the PHENIX Collaboration [Esu03] at $\sqrt{s_{\mathrm{NN}}} = 200A$ GeV in minimum bias Au+Au collisions and compared with hydrodynamic calculations. The figure is taken from [Kol03].

The initial conditions and freeze-out prescription are the boundary conditions for a hydrodynamic calculation and therefore a crucial input. Thus, the hydrodynamic results depend strongly on the initial and final state prescription that is applied in the specific calculation. Usually, the initial conditions are parametrized according to a Glauber model or the Color Glass Condensate ansatz and the freeze-out is calculated according to the Cooper-Frye formula. The particles decouple on a e.g. isothermal hypersurface and then fly on straight lines to the detector.

For the hydrodynamical evolution local equilibrium is assumed and zero viscosity which corresponds to zero mean free path. The differential equations that govern the dynamics are the conservation of the energy-momentum-tensor and posssible currents as e.g. the net baryon density current [Lan53, Cla86]:

$$\partial_\mu T^{\mu\nu} = 0 \quad \text{and} \quad \partial_\mu N^\mu = 0, \tag{3.5}$$

where $T^{\mu\nu}$ is the energy-momentum tensor and N^μ is the baryon current. For an ideal fluid the energy-momentum tensor and the net baryon number current take the simple form

$$T^{\mu\nu} = (\epsilon_{\text{lrf}} + P)\, u^\mu\, u^\nu - P\, g^{\mu\nu} \quad \text{and} \quad N^\mu = \rho_{\text{lrf}}\, u^\mu \tag{3.6}$$

where ϵ_{lrf}, P and ρ_{lrf} are the local rest frame energy density, pressure and net baryon density, respectively. $u^\mu = \gamma(1, \vec{v})$ is the four velocity of the cell and $g^{\mu\nu} = diag(+,-,-,-)$ is the metric tensor. The local rest frame is defined as the frame where $T^{\mu\nu}$ has diagonal form, (i.e. all off-diagonal elements vanish). The four-velocity of the cells is calculated via the transformation into the local rest frame.

The energy density and the net baryon number density are propagated in timesteps on a spatial grid. The coordinate space is divided into small cells in which the distribution functions correspond to equilibrium distributions (Fermi or Bose distribution). In the Eulerian formulation the grid is fixed in space-time and the matter flows through the cells while in the Lagrangian formulation the amount of matter in one cell is fixed and they deform accordingly. In this macroscopic approach the propagated quantities are net baryon number and energy densities which can be translated into information about the temperature and chemical potential via the specific equation of state (EoS). Since the evolution is driven by pressure gradients and the pressure is determined via the EoS, the EoS is the essential ingredient for the hydrodynamical evolution.

Different kinds of hydrodynamic models include 1+1 dimensional Landau type models [Lan53] or 2+1 transverse dimensions with assumed boost invariance and Bjorken expansion in the longitudinal direction [Bjo83] or full 3+1 dimensional models. Besides the one fluid prescription also multi-fluid approaches have proven to be successful, e.g three seperate fluids, one projectile, one target and one fireball fluid including source terms between the fluids [Bra00b, Iva06].

Hydrodynamics is still a macroscopic approach, but it is useful to describe the collective

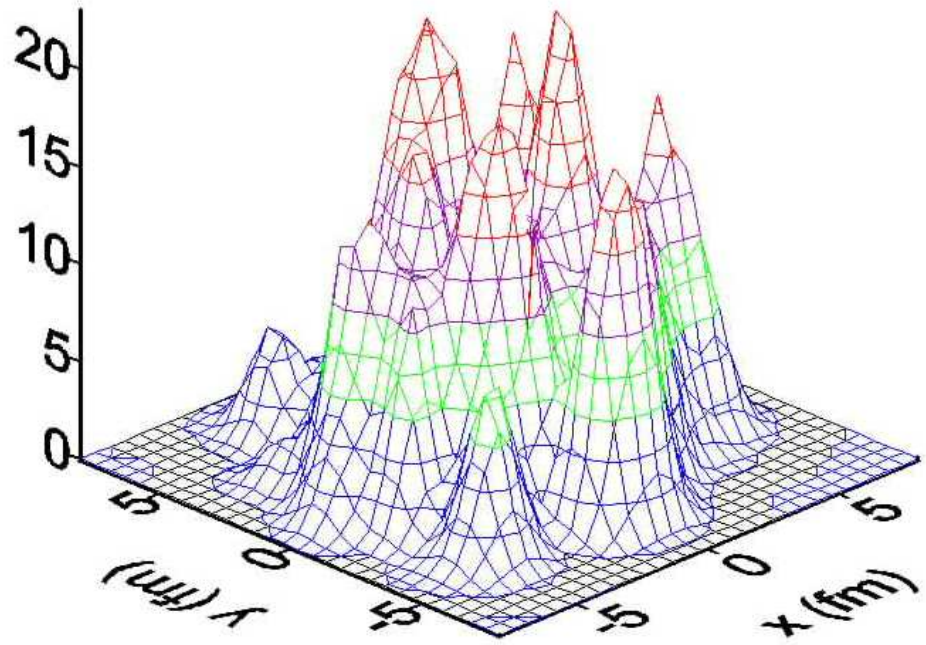

Figure 3.4: Example of initial energy density in the $\eta = 0$ plane. The figure has been taken from [Anr06a].

dynamics of the system and one can take it as an advantage that the equation of state is an explicit input. On the other hand, the description is strongly dependent on the boundary condition, e.g. the initial conditions and the freeze-out criterion, that have to be constraint by observables. In this kind of approach one still gets no information on the microscopic level, but there is at least some dynamics involved.

3.3.2 Hybrid Approaches

To get a more consistent picture of the whole dynamics of heavy ion reactions various so called microscopic plus macroscopic (micro+macro) hybrid approaches have been launched during the last decade. Most noteworthy in this respect are the pioneering studies related to a coupling between UrQMD (Ultra-relativistic Quantum Molecular Dynamics) and hydrodynamics (a detailed systematic investigation of this coupling procedure can be found in the following references [Dum99, Bas99c, Bas00, Sof01, Sof02, Non06, Non07, Ste08a, Pet08b]). Especially, the most recent developments of a fully integrated transport approach including hydrodynamic stage for the hot and dense stage of the evolution are subject of this thesis and will be explained in detail in later Chapters.

Other approaches in the same spirit are, e.g., the NEXSpheRIO approach that uses initial conditions calculated in a non-equilibrium model (NEXUS) followed by an ideal hydrodynamic evolution [Pai97, Agu02, Soc04, Gra05, Anr06a, Anr06b, Agu07] or a hybrid

approach by Toneev et al. which uses QGSM initial conditions followed by a three-dimensional hydrodynamic evolution [Sko06]. In this way event-by-event fluctuations are taken into account and the calculation mimics more realistically the experimental case. As an example, Fig. 3.4 shows the initial energy density distribution in the transverse plane that is used by NEXspheRIO. For the freeze-out NEXspheRIO employs a continuous emission scenario or a standard Cooper-Frye calculation. Other groups, e.g., Teaney et al. [Tea01b], Hirano et al. [Hir06, Hir08], Bass/Nonaka [Non07], are using smooth Glauber or Color Glass Condensate initial conditions followed by a full two- or three-dimensional hydrodynamic evolution and calculate the freeze-out by a subsequent hadronic cascade. The separation of chemical and kinetic freeze-out and final state interactions like resonance decays and rescatterings are taken into account. There are two major conclusions from these previous studies: The treatment of the initial state fluctuations and the final decoupling is of major importance for a sound interpretation of the experimental data.

Unfortunately, all presently existing micro+macro approaches rely on a complete separation of the three main ingredients (initial conditions, hydrodynamic evolution, transport calculation). Thus, it is impossible to compare the evolution of the system between hydrodynamics and transport simulation directly and from the same initial conditions. This may provide essential new insights into the role of viscosity and local equilibration. In addition, the usual separation of the program code does not allow for a dynamical coupling between hydrodynamics and transport calculation, which would be desirable to consistently solve the freeze-out puzzle [And99, Mag99, Bug99, Bug03]. The main part of this thesis covers a new hybrid approach that we have developed which tries to resolve some of these problems.

3.3.3 Viscous Hydrodynamics

After the great success of ideal hydrodynamics to describe the differential elliptic flow data at RHIC, the next straight forward step is to allow for small deviations from the equilibrium assumption. These deviations can be characterized by transport coefficients, bulk and shear viscosity and heat conductivity. The most important one for heavy ion collisions seems to be the shear viscosity that measures the transfer of momentum transverse to the fluid velocity and is therefore related to the mean free path in the system. There are different attempts to calculate this coefficient for quantum chromodynamics in e.g. pQCD [Huo07, Xu08a, Xu08b], chiral perturbation theory [Chn07]. The most famous result for the ratio between the shear viscosity and the entropy is the result that has been calculated using the AdS/CFT correspondence, where a universal lower bound for conformal field theories as $\eta/s = 1/4\pi$ [Pol01] has been found.

To quantify more precisely how far away the system is from local thermal equilibrium it is necessary to develop viscous hydrodynamics codes. First results including shear viscosity in 2+1 dimensions based on the Israel-Stewart equations that govern second order viscous dynamics have been published recently [Hei06, Rom07, Son08, Luz08]. As an example,

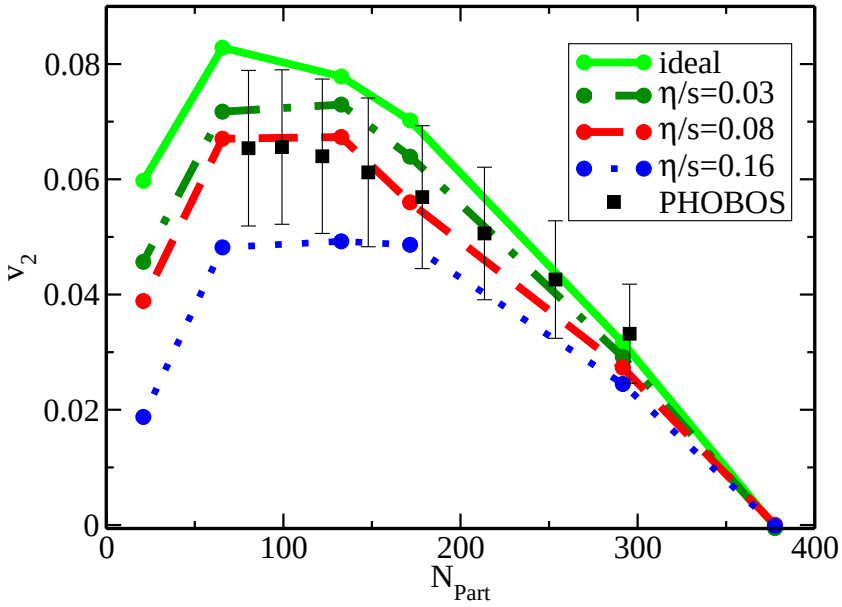

Figure 3.5: PHOBOS [Alv07a] data on p_T integrated v_2 for charged particles in Au+Au collisions at $\sqrt{s} = 200$ GeV, compared to the hydrodynamic model for various viscosity ratios η/s. Error bars for PHOBOS data show 90% confidence level systematic errors. The figure has been taken from [Rom07].

Fig. 3.5 shows the centrality dependence of integrated elliptic flow applying different values for the shear viscosity. There are many attempts to approaches to quantify the deviation from local equilibrium of the matter created in heavy ion collisions also employing transport approaches [Mol05, Koi07, Dum07, El08]. The inclusion of bulk viscosity might be necessary when the system approaches the phase boundary between QGP and hadron gas [Pae06, Tor08a, Den08, Tor08b].

3.4 Transport Approaches

Approaches that aim at the description of heavy ion reactions consistently from the initial state to the final state are transport approaches based on relativistic transport theory [Bay61, DeG80]. This microscopic description has been applied quite successfully to the partonic as well as to the hadronic stage of the collision. At lower energies, there are hadronic transport approaches based on quantum molecular dynamics (QMD), like e.g. [Aic86, Hat89, Cas90, Aic91, Stö92, Kho92] partly including medium effects or potential interactions. Going to higher energies a full relativistic treatment is crucial and the excitation of resonances and strings govern most of the dynamics without introducing explicit quark and gluon degrees of freedom as in e.g. UrQMD [Bas98b, Ble99c], which

will be explained in more detail in the next Chapter or other hadron-string transport approaches like FRITIOF [Ano83], VENUS [Wer93], HSD [Cas00], RQMD [Sor89], QGSM [Ame90]. Other approaches treat only partonic degrees of freedom [Gei92, Mol05, Xu05] or a combination of a hadronic and a partonic stage[Lin05, Cas08].

Unfortunately, most transport approaches are restricted to $2 \rightarrow n$ scattering processes. Thus, if the particle density increases it becomes questionable if a restriction to two-particle interaction is still justified. While first attempts to include multi-particle interactions have been proposed [Xu05, Bar01, Lar07, Blb07, Blb08], this extension of transport theory is still in its infancy. To explain hadronization and the phase transition between the hadronic and the partonic phase on a microscopic level is also one of the main open issues that still has to be resolved. It is therefore difficult to find an appropriate prescription of the phase transition in such a microscopic approach. First, however promising attempts to solve the microscopic hadronization problem can be found in the literature [Ano77, Els95, Bir99, Tra99, Hof00, Lin05]. In transport theory no assumptions about the equilibration of the matter are employed and one can get insights about the microscopic processes that happen during the evolution. The hadronic transport approach that this work is based on is the Ultra-relativistic Quantum Molecular Dynamics approach which will be described in more detail in the next Chapter.

4 The Ultra-relativistic Quantum Molecular Dynamics Model

In this Chapter the Ultra-relativistic Quantum Molecular Dynamics (UrQMD) approach will be described in more detail. It is a hadronic transport approach which has been very successfully applied to heavy ion reactions in the whole energy range from $E_{\rm lab} = 100A$ MeV to $\sqrt{s_{\rm NN}} = 200$ GeV. The main advantage of a transport approach is that no assumptions about the equilibration of the matter are necessary and one generates the full space-time dynamics for all the particles. We review here some general basics about the Boltzmann equation and the specific effective solution as it is implemented in UrQMD. Then, we concentrate on recent developments and discuss results for multiplicities and mean transverse momentum excitation functions in p-p and A-A collisions in the context of the available data. In the last part of this Chapter predictions for the charged particle multiplicities at LHC energies are presented.

4.1 The Boltzmann Equation

The modelling of the dynamical evolution of heavy ion reactions is essential to gain further insights about the properties of the newly produced hot and dense QCD matter. Transport theory aims at the description of all stages of the collision on the basis of an effective solution of the relativistic Boltzmann equation [DeG80]

$$p^\mu \cdot \partial_\mu f_i(x^\nu, p^\nu) = \mathcal{C}_i \quad . \tag{4.1}$$

This equation describes the time evolution of the distribution functions for particle species i and includes the full collision term on the right hand side. The interaction with external potentials leads to an additional term on the left hand side. The influence of potentials gets small at higher energies compared to the energy that is transferred by collisions. Therefore, they are dropped in Eqn. 4.1 and are not further discussed here. Usually, the collision kernel is truncated on the level of binary collisions and $2 \rightarrow n$ processes to keep the calculation numerically tractable. This microscopic approach has the advantage that it is applicable to non-equilibrium situations and the full phase space information is available at all stages of the heavy ion reaction. The restriction to binary collisions assumes large mean free paths of the particles. Between interactions the particle trajectories are given by straight line trajectories and particles are assumed

to be in asymptotic states between the collisions (no "memory effect").

In principle, there are different possibilities how to implement a transport approach. Either a test-particle method can be used (as used in e.g. HSD) or real particles are propagated event by event. Both techniques have advantages and disadvantages and we discuss here the molecular dynamics method as it is applied in UrQMD.

4.2 Basic processes in UrQMD

The Ultra-relativistic Quantum Molecular Dynamics model (UrQMD) [Ble99c, Bas98b, Pet08a] is a microscopic many body approach and can be applied to study hadron-hadron, hadron-nucleus and heavy ion reactions from $E_{\rm lab} = 100A$ MeV to $\sqrt{s_{NN}} = 200$ GeV. This non-equilibrium transport approach constitutes an effective solution of the relativistic Boltzmann equation (see Eqn. 4.1). The underlying degrees of freedom are hadrons and strings that are excited in high energetic binary collisions.

The projectile and target nuclei are initialised according to a Woods-Saxon profile in coordinate space and Fermi momenta are assigned randomly for each nucleon in the rest frame of the corresponding nucleus. The hadrons are propagated on straight lines until the collision criterium is fulfilled. If the covariant relative distance $d_{\rm trans}$ between two particles gets smaller than a critical distance that is given by the corresponding total cross section a collision takes place,

$$d_{\rm trans} \leq d_0 = \sqrt{\frac{\sigma_{\rm tot}}{\pi}}, \quad \sigma_{\rm tot} = \sigma(\sqrt{s}, \text{type})\,. \tag{4.2}$$

Each collision process is calculated in the rest frame of the binary collision. The reference frame that is used for the time ordering of the collisions and later on also for the switchings to and from the hydrodynamic phase is the equal speed-system of the nucleus-nucleus collision (for symmetric systems the equal speed system is identical to the center of mass system).

In UrQMD 55 baryon and 32 meson species, ground state particles and all resonances with masses up to 2.25 GeV, are implemented with their specific properties and interaction cross sections. In addition, full particle-antiparticle symmetry is applied. Isospin symmetry is assumed and only flavour-SU(3) states are taken into account. The elementary cross sections are calculated by detailed balance or the additive quark model or are fitted and parametrized according to the available experimental data. For resonance excitations and decays the Breit-Wigner formalism, utilizing their vacuum properties is employed.

Towards higher energies, the treatment of sub-hadronic degrees of freedom is of major importance. In the present model, these degrees of freedom enter via the introduction of a formation time for hadrons produced in the fragmentation of strings [Ano86, Nil87, Sjo94]. String excitation and fragmentation is treated according to the Lund model. For

hard collisions with large momentum transfer ($Q > 1.5$ GeV) PYTHIA is used for the calculation. A phase transition to a quark-gluon state is not incorporated explicitly into the model dynamics. Let us shortly review the major physics questions and topics in which UrQMD has been used in the past:

- The thermal properties of the UrQMD model have been investigated. It was shown that a detailed analysis of the model in equilibrium yields an effective equation of state of Hagedorn type [Bel98, Brv99]. Further studies involve the exploration of the systems evolution in the QCD phase diagram and the equilibation time scales of QCD matter. This includes also studies on the active degrees of freedom and the relation between pressure and energy density (equation of state) [Bas98a, Brv98, Bel98, Web98, Brv99, Brv99, Brv01, Brv00, Foc06].

- The UrQMD transport model has been successfully used to predict and interprete experimental data at various energies and for a multitude of observables and reaction systems, e.g. hadron yields, transverse and longitudinal spectra [Bas99d, Ble00a, Brt04],

- strangeness production, multi-strange baryons and antiprotons [Ble99a, Sof99a, Ble00d, Ble00e, Brt04],

- hadron resonance production e.g. K^*,ρ,Λ^*,Δ [Ble02c, Ble03, Ble04, Vog06a, Vog06b, Vog08a],

- radial, directed and elliptic flow [Ble99b, Sof99b, Ble02a, Ble05, Zhu05, Zhu06a, Zhu06b, Zhu:2006c, Lu06, Pet06a, Pet06b, Pet06c, Pet07, Vog07],

- event-by-event fluctuations [Ble98a, Ble98b, Ble00b, Ble00c, Koh02, Jeo06, Has06, Kon06, Has07, Lun07],

- particle correlations and HBT [Mon99, Li06c, Li07a, Li07b, Li08a, Li08c],

- real photon and dilepton production [Ern98, Dum98, Won01, Scu06, Vog08b],

- Drell-Yan, charm, D-mesons and J/Ψ production and dynamics [Spi98b, Spi98c, Spi99a, Spi98d, Spi99b, Spi99c, Rei03, Zhu07] and

- studies at low beam energies to explore potential effects and isospin asymmetries [Li05a, Li05b, Li06a, Li06b].

Furthermore, the UrQMD model has been used within various hybrid model studies ranging from air shower simulations [Dre03, Dre04] to hybrid models for relativistic heavy ion reactions. Most noteworthy are the pioneering studies related to a coupling between UrQMD and hydrodynamics, see e.g. [Dum99, Bas99b, Bas99c, Bas00, Sof01, Sof02, Ble02b, Zee04, Non06, Non07, Ste08a].

4.3 Recent Development

4.3.1 Inclusion of Pythia

To employ the UrQMD transport approach at higher energies (above $\sqrt{s}_{\mathrm{NN}} \cong 10$ GeV) it is important to treat the initial hard collisions carefully. Therefore, we have implemented the latest version (6.409) of Pythia [Sjo06] to perform those hard collisions instead of the normal UrQMD string excitation and fragmentation routine. Note that Pythia 6.4 is technically not anymore the latest version since there is a new C++ implementation (current version 8.1). However, Pythia 6.4 is the latest stable and full-featured Fortran implementation, which is still considered to be the benchmark for the physics processes.

The minimal center of mass energy in the individual two particle reactions for a Pythia call is $\sqrt{s}_{\mathrm{min}} = 10$ GeV (applicability limit of Pythia). Hard collisions are defined as collisions with momentum transfer $Q > 1.5$ GeV. The transition between the low energy string routine and Pythia is smooth and given by the probability distribution for hard scatterings determined from Pythia. The standard low energy string routine is called to perform the string excitation and fragmentation calculation for soft collisions only.

Leading particles produced by Pythia strings are treated in analogy to the leading particles created in the standard UrQMD string fragmentation procedure. Leading particles are the particles that contain the quarks or diquarks of the original hadrons. Those leading particles are allowed to interact with a fraction of one third, two third (for diquarks) or a half (for mesons) of their normal cross section during their formation time of $\sim$ 1fm/c, while all the other newly produced particles do not interact until they are fully formed. To account for coherence effects the cross sections for leading particles from Pythia are additionally suppressed by a factor 0.4.

4.3.2 Treatment of High Mass Resonances

In the previous version UrQMD-1.3p1 the resonances with masses up to 2.2 GeV are included with all their vacuum properties and decay dynamics. For processes at higher energies string excitation and fragmentation dominates the interaction in UrQMD-1.3p1. Since the angular distributions of the particles produced by strings are forward-backward peaked the resulting mean transverse momenta were found to be too low compared to experimental data. To reproduce the experimentally measured high $\langle p_T \rangle$ values a modified treatment of high mass resonances similar to RQMD is introduced. This modified treatment of meson-baryon interactions in the intermediate energy regime is described in the following.

A continuous spectrum of high mass resonance states is included in the energy regime between $\sqrt{s}_{coll} = 1.67$ GeV and $\sqrt{s}_{coll} = 3$ GeV for meson-baryon reactions. These particle excitations are treated as pseudo-resonances instead of strings. Below $\sqrt{s}_{coll} =$ 1.67 GeV normal resonance excitation takes place. Above $\sqrt{s}_{coll} = 3$ GeV the standard

UrQMD string fragmentation is called. The properties for the unknown resonances are extrapolated from the in mass closest known resonance of same type.

To fix the strangeness production in the decay process of these new resonance states which was reduced because of the new production of high mass resonances instead of strings, the branching ratios of high lying resonances are changed to the corresponding branching ratios obtained from string decays of the same mass. Further adjustments are made to keep the particle properties in line with the Particle Data Book 2006. All branching ratios and other resonance properties are within the limits of the Particle Data Book 2006.

4.3.3 Other Important Changes

The following list contains the most important smaller changes that have been implemented:

- New Regge-parametrisations for total and elastic cross-sections at high energies are implemented for all the elementary reactions for which they are available.
- The mass distribution of the nucleon resonances N^* has been fixed via inclusion of the Δ resonances.
- Adjustment of the Ξ and Ω production rates in p-p-collisions to newly available data via a change of the double strange diquark suppression factor.
- The single strange diquark suppression factor is set to 0.5 to reproduce the measured $\bar{\Lambda}$ production in p-p collisions.
- A new subroutine which provides a faster initialization that is needed for cosmic air shower simulations is introduced.
- Changes that need to be made to run UrQMD at LHC energies have been studied. The necessary adjustments are described in detail in the User Guide, but are not implemented in the default version UrQMD-2.3.

4.4 UrQMD-2.3 Results for p+p and A+A Collisions

In this Section the results of the new version UrQMD-2.3 are compared to the calculations using UrQMD-1.3p1 in the context of the available experimental data. We have concentrated on bulk observables like multiplicities and mean transverse momenta to demonstrate the major differences. Here we refrain from explaining all the details of the shown figures, but concentrate on the effects of the changes that are described above. The full/dotted lines refer always to the UrQMD-2.3 (shown as full lines) and UrQMD-1.3p1 (shown as dotted lines) results, while experimental data are depicted as symbols.

First, the excitation functions of the total multiplicities and the mean transverse momentum for elementary p-p collisions are shown. Only inelastic p-p collisions are taken into account, so there is particle production usually from one hard interaction. Comparing the calculations to experimental data for p-p collisions is very useful to fix the parameters that are introduced in the strang fragmentation formalism as e.g the strangeness suppression factors that are necessary according to the Schwinger picture. A good agreement to the data from elementary collisions is necessary for all further studies of heavy ion ractions.

In Fig. 4.1 an enhanced production of pions, kaons and antiprotons due the implementation of Pythia is visible for energies above $\sqrt{s}_{\mathrm{NN}} \gtrsim 50$ GeV. In general, the particle production increases with increasing beam energy for all particle species. Only the proton yield stays constant because the protons already exist in the beginning. In most cases only one of the initial protons gets excited and the other proton just scatters off. The $\bar{\Lambda}$ yield is reduced in UrQMD-2.3 and has been adjusted by the single strange diquark suppression factor. The Ω yield is increased in UrQMD-2.3 and was adjusted by a change of the double strange diquark suppression factor. Preliminary NA49 data for Ξ and Ω production in p-p was used to adjust the multiplicities.

Fig. 4.2 shows the $\langle p_T \rangle$ of produced particles in p-p collisions. The mean transverse momentum measures the transverse energy that is transferred to the particles because of the collision. There is a steep raise as a function of energy leading to a almost constant value specific for the particle species. For baryons the mean transverse momentum is around 600 MeV while for mesons it is slightly lower ($300 - 450$ MeV) due to the lower mass of pions and kaons. The inclusion of pQCD hard scatterings in UrQMD-2.3 leads to a slight increase of the $\langle p_T \rangle$ at higher energies compared to UrQMD-1.3p1. Especially the mean transverse momentum of kaons is now in better agreement with the experimental data at RHIC energies.

In the following the explanation of the changes on the results for heavy ion collisions (Au+Au/Pb+Pb) are given. All the calculations have been performed for central collisions ($b < 3.4$ fm).

Fig. 4.3 shows the excitation function of 4π multiplicities for different particle species. Again the particle production increases as it is expected with e=increasing beam energy except for the protons that are already existent in the initial state. The overall agreement between the UrQMD-2.3 calculation and the experimental data is very good for pions, kaons and lambdas. The yields of the (multi-)strange baryons has changed because of the new treatment of high mass resonances and the adjustments of the strangeness suppression factors. The multiplicities of multistrange hyperons is still underestimated by the transport approach due to a lack of thermalization of strangeness. The threshold energy to produce Ξ's and Ω's is quite high in resonance exciations and string fragmentations. The same effect is also visible for the yields at midrapidity that are shown in Fig. 4.4. In this case, also expermintal data points for protons and antiprotons are available and the UrQMD calculations are in reasonable agreement over the whole energy regime. The decrease that can be observed in the Λ yield at midrapidity is due to the fact that

the Λ production follows the net proton distribution.

In Figs. 4.5 and 4.6 the excitation functions of the mean transverse momentum and mean transverse mass for different particle species are shown. The new calculations with UrQMD-2.3 generally result in an increase in transverse momentum, resulting in a better description of the experimental data. This increase is due to the modified treatment of the high mass resonances that decay isotropically. The mean transverse momentum is a measure of the energy deposition during the heavy ion reaction. It reflects how much momentum is transferred from the longitudinal to the transverse direction. Furthermore, it is sensitive to the radial expansion dynamics and the pressure gradients that develop in the course of the evolution. A more detailed discussion of the mean transverse mass excitation function can be found in Chapter 11.

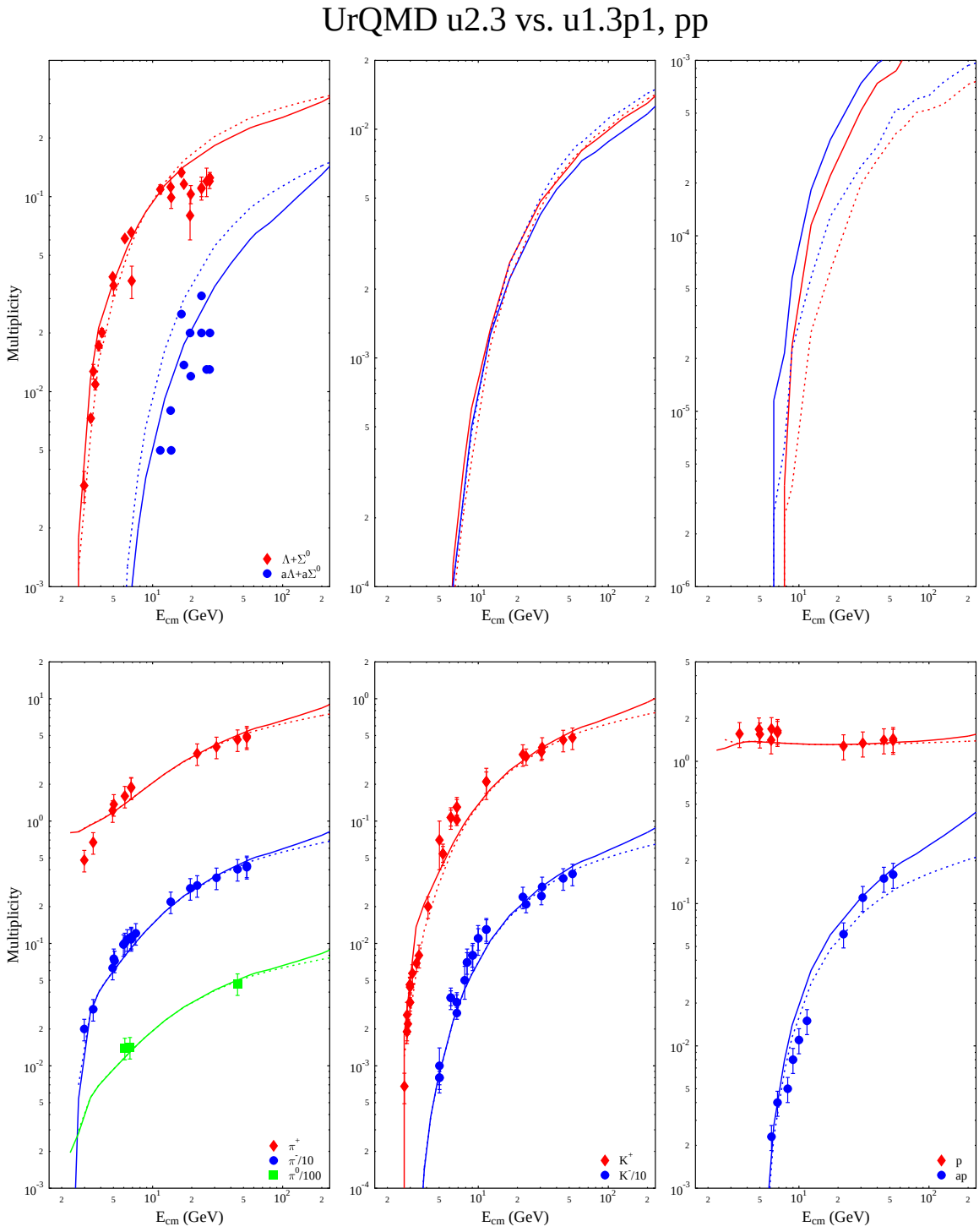

Figure 4.1: Excitation function of particle multiplicities (4π) in inelastic p-p collisions from $E_{\mathrm{lab}} = 2$ AGeV to $\sqrt{s_{NN}} = 200$ GeV. UrQMD-2.3 calculations are depicted with full lines, while UrQMD-1.3p1 calculations are depicted with dotted lines. The corresponding data from different experiments [Anu73, Ros75]are depicted with symbols.

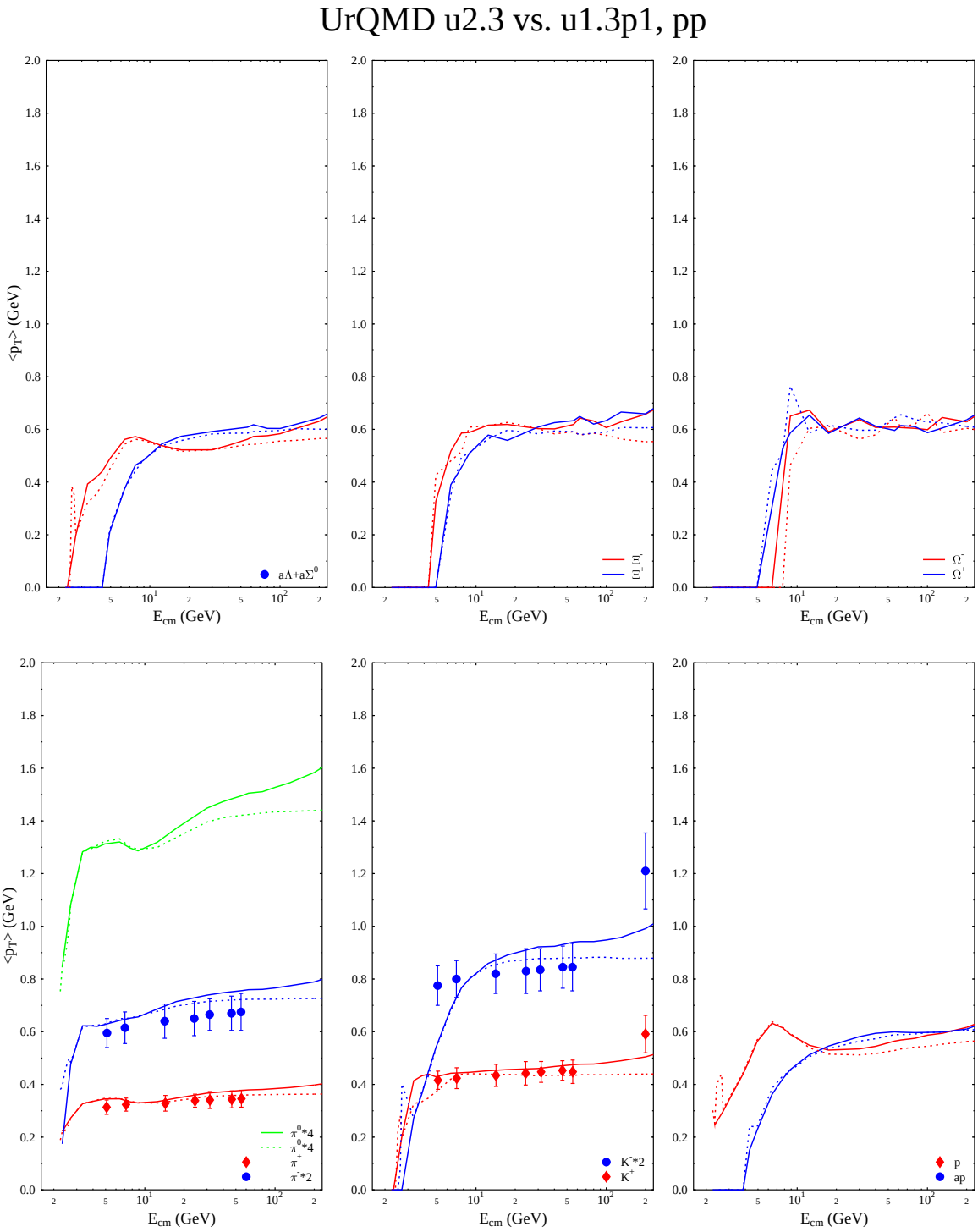

Figure 4.2: Excitation function of $\langle p_T \rangle$ values for different particle species at midrapidity ($|y| < 0.5$) in inelastic p-p collisions from $E_{\mathrm{lab}} = 2$ AGeV to $\sqrt{s_{NN}} = 200$ GeV. UrQMD-2.3 calculations are depicted with full lines, while UrQMD-1.3p1 calculations are depicted with dotted lines. The corresponding data from different experiments [Ros75] are depicted with symbols.

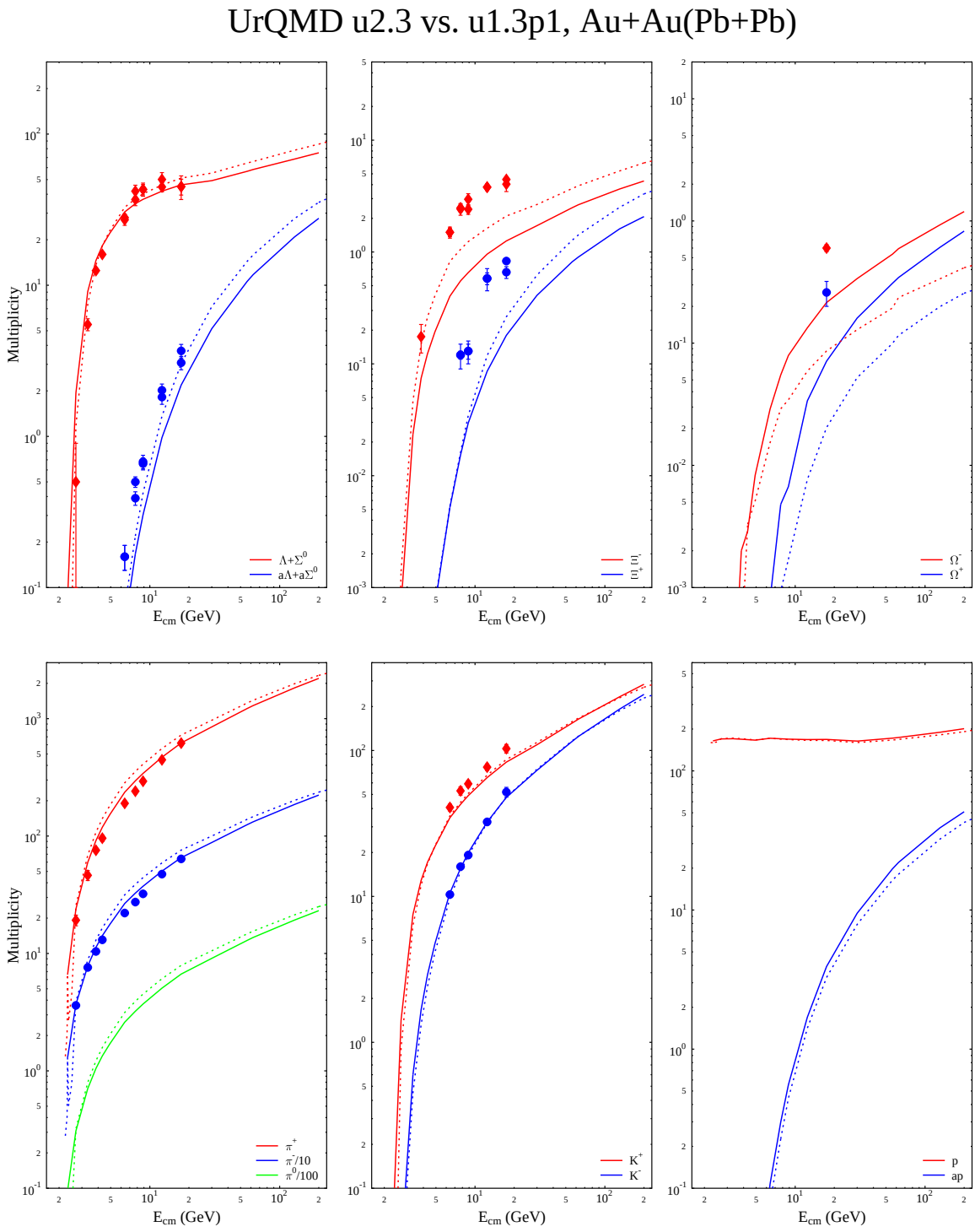

Figure 4.3: Excitation function of particle multiplicities (4π) in Au+Au/Pb+Pb collisions from $E_{\rm lab} = 2$ AGeV to $\sqrt{s_{NN}} = 200$ GeV. UrQMD-2.3 calculations are depicted with full lines, while UrQMD-1.3p1 calculations are depicted with dotted lines. The corresponding data from different experiments [Kla03, Pin02, Chu03, Alt08a, Afa02a, Anc04a, Ric05, Mit06, Alt08c, Blm05, Afa02b, Alt05a] are depicted with symbols.

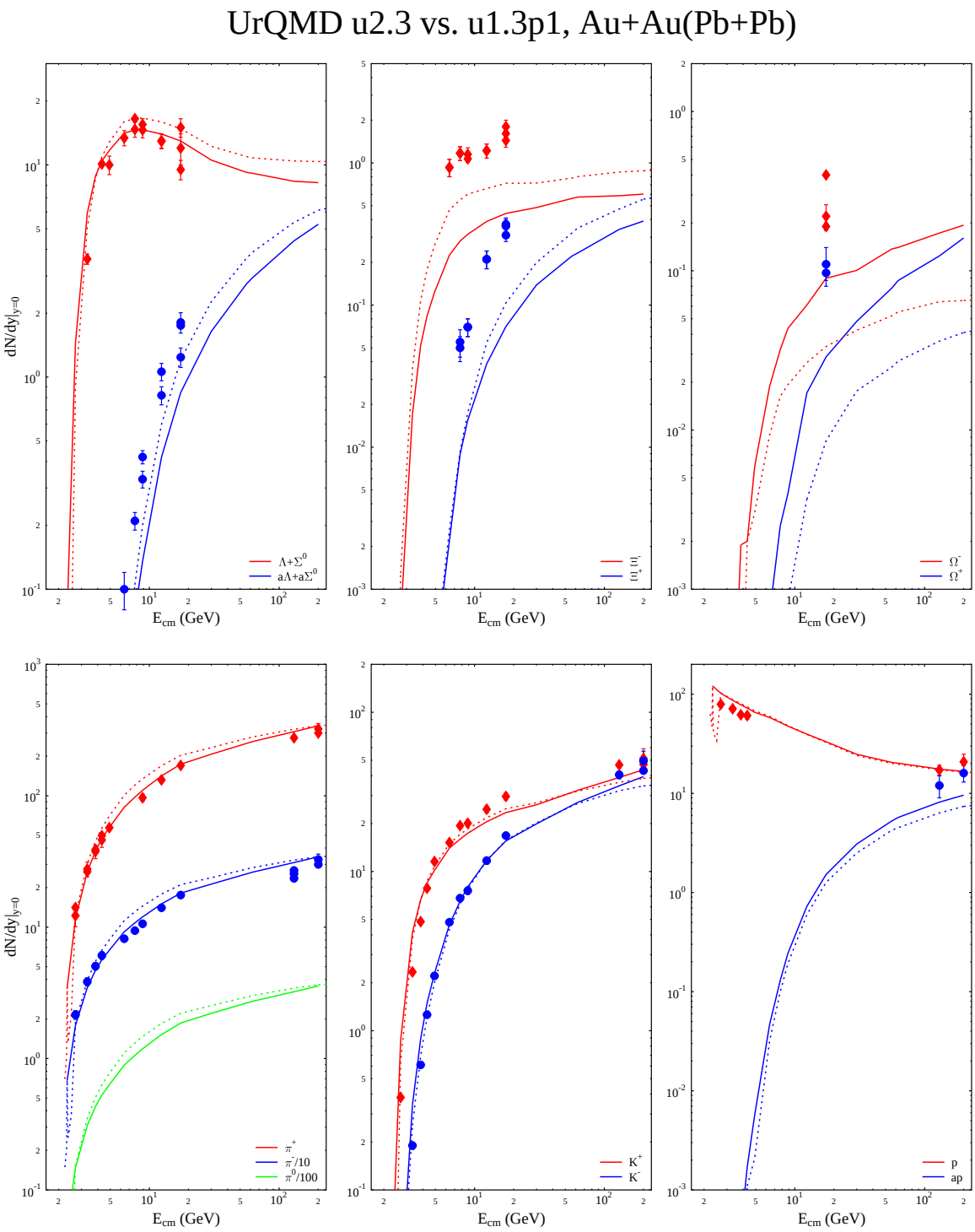

Figure 4.4: Excitation function of particle yields at midrapidity ($|y| < 0.5$) in Au+Au/Pb+Pb collisions from $E_{\text{lab}} = 2$ AGeV to $\sqrt{s_{NN}} = 200$ GeV. UrQMD-2.3 calculations are depicted with full lines, while UrQMD-1.3p1 calculations are depicted with dotted lines. The corresponding data from different experiments [Ahl00a, Kla03, Afa02a, Adc04, Lee04, Ahl00b, Ant99, Oue03, Ahm96, Mit06, Alt08c, Alt05a, Mis02, Ads04] are depicted with symbols.

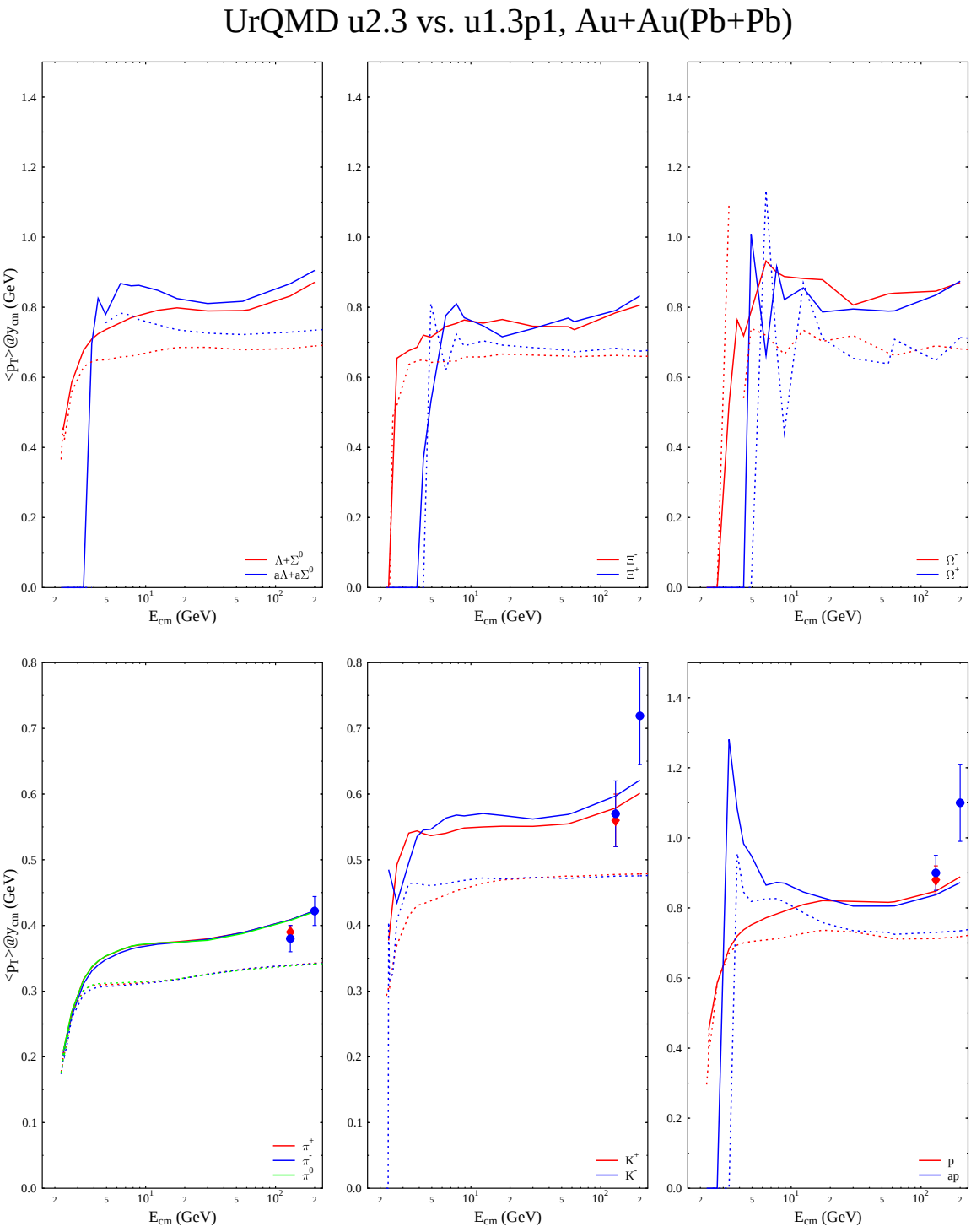

Figure 4.5: Excitation function of $\langle p_T \rangle$ values for different particle species at midrapidity ($|y| < 0.5$) in Au+Au/Pb+Pb collisions from $E_{\mathrm{lab}} = 2$ AGeV to $\sqrt{s_{NN}} = 200$ GeV. UrQMD-2.3 calculations are depicted with full lines, while UrQMD-1.3p1 calculations are depicted with dotted lines. The corresponding data from different experiments [Adc04, Ads04] are depicted with symbols.

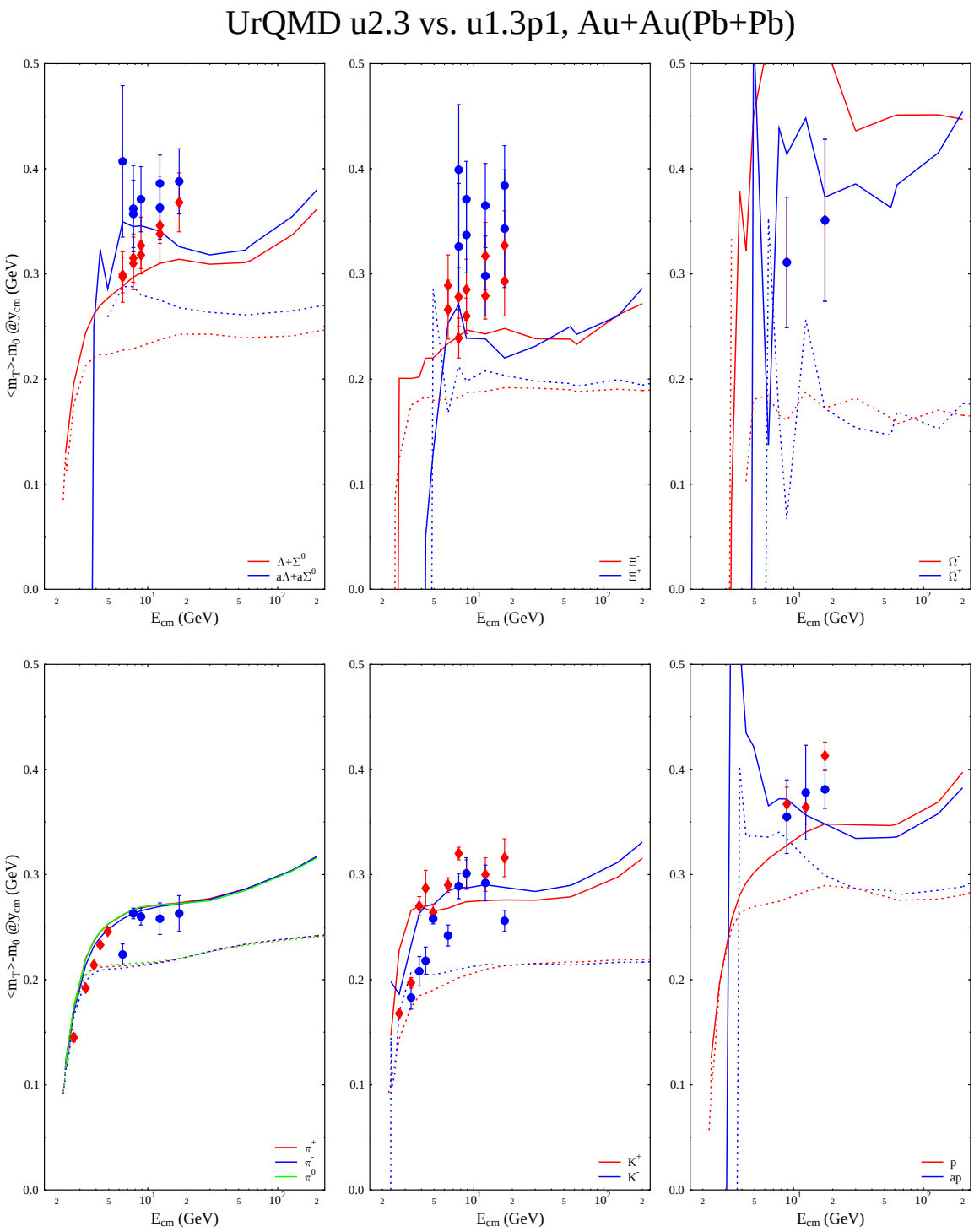

Figure 4.6: Excitation function of $\langle m_T \rangle - m_0$ values for different particle species at midrapidity ($|y| < 0.5$) in Au+Au/Pb+Pb collisions from $E_{\mathrm{lab}} = 2$ AGeV to $\sqrt{s_{NN}} = 200$ GeV. UrQMD-2.3 calculations are depicted with full lines, while UrQMD-1.3p1 calculations are depicted with dotted lines. The corresponding data from different experiments [Ahl00a, Ahl00b, Afa02a, Anc04b, Ric05, Alt08a, Mit06, Alt08c, Afa03, Ver99, Anc04a, Afa02b, Alt05a] are depicted with symbols.

Apart from the success of transport simulations to describe spectra and yields certain problems remain:

- Elliptic flow values above SPS energies are too small [Ble02a, Pet06a],
- HBT radii hint to a very small R_o/R_s ratio [Kni06, Li08a],
- Strangeness, especially multi-strange baryons are not produced in sufficient amounts [Sof99a].

These observables that are sensitive to the early stage of the collision (pressure) or to the approach of thermal and chemical equilibrium during the collision history hint to the fact that a purely hadronic transport model may not be sufficient to describe the dynamics of the hot and dense stage of heavy ion reactions at higher energies [Ble02a, Mol04, Hei02, Pet06a, Li08a]. Therefore, these observations exemplify the need to embed a full three-dimensional relativistic fluid dynamics description for these stages of the reaction as it has been done in this work and is described in Chapter 6.

4.5 LHC Predictions

In this Section predictions for the charged particle multiplicities in p-p and Pb+Pb collisions at the Large hadron collider (LHC) are presented based on [Mit08].

High energy nucleon-nucleon and nucleus-nucleus collisions are an excellent tool to study nuclear matter under extreme conditions of temperature and density. First day observable is the abundance of charged particles in elementary (anti-)proton-proton collisions and in heavy-ion collisions. This allows for a first exploration of parton densities in the early stage and provides stringent limits for nearly all available theoretical models. It directly reflects how much of the initial beam energy can be converted to new particles and it is therefore directly linked to the stopping mechanism of the initial protons and nucleons. Thus, the particle multiplicity contains information about the entropy of the system and the gluon density in the first stage of the collision. In nucleus-nucleus collisions more particles are produced compared to nucleon-nucleon collisions. By scaling the produced particle multiplicity in Pb+Pb/Au+Au collisions by N_{part} (the number of participating nucleons) it can be tested whether nucleus-nucleus collisions are just a sum of nucleon-nucleon collisions or if a more collective type of physics is taking place. The RMS-width of the charged particle pseudorapidity distribution gives information about the longitudinal expansion of the system. Starting from a model benchmark in comparison to data from SPS, RHIC and Tevatron, we proceed to a prediction for the charged particle density expected at LHC energies. In the present calculation the microscopic transport model Ultra-relativistic Quantum Molecular Dynamics (UrQMD) in version 2.3 has been used that has been described in detail in the previous Sections.

Let us start by setting the stage for further investigations by comparing UrQMD calculations with measurements performed in p+$\bar{\mathrm{p}}$ and Pb+Pb/Au+Au collisions from 17.3 GeV at the CERN-SPS to 1.8 TeV at Fermilab. This systematic comparison sets the

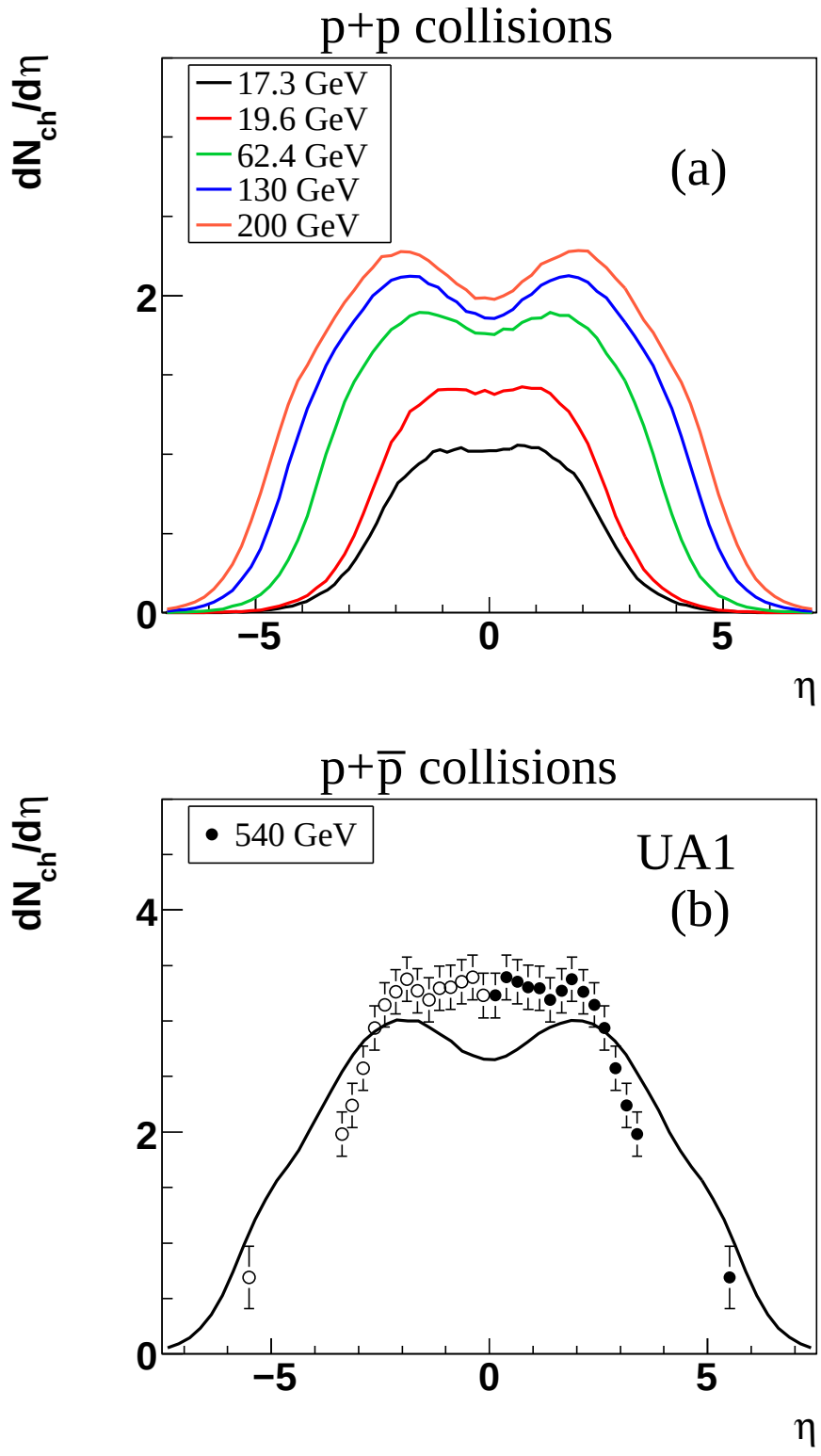

Figure 4.7: Pseudorapidity distribution of charged particles in inelastic minimum bias p+p collisions from top SPS energies to the highest RHIC energies predicted by UrQMD (a). The pseudorapidity distribution of charged particles in inelastic minimum bias p+$\bar{\text{p}}$ collisions measured by the UA1 collaboration [Aro83] (b). The closed symbols indicate measured points, whereas the open points are reflected with respect to mid-pseudorapidity. The solid line represents calculations from UrQMD, in inelastic minimum bias p+$\bar{\text{p}}$.

foundation for the following predictions for p+p and Pb+Pb collisions at LHC energies.

Fig. 4.7 (a) shows the $dN_{ch}/d\eta$ distribution (η being the pseudorapidity) for charged particles in inelastic [1] minimum bias p+p collisions from top SPS to top RHIC energies predicted from UrQMD. Fig. 4.7 (b) presents measurements performed by the UA1 collaboration [Aro83] for inelastic minimum bias p+$\bar{\text{p}}$ collisions at 540 GeV. The closed points show the measured region in η, whereas the open points are the reflected points at $\eta = 0$. With increasing energy the leading hadron effect becomes more visible and from the gap between the humps the strength of the stopping effect is visible. The system is becoming more transparent at higher energies which is reflected in the change of the pseudorapidity distribution from a Gaussian to a double Gaussian shape [Bjo83, Lan53]. The same structure is also visible for the charged particle pseudorapidity distribution in inelastic minimum bias p+$\bar{\text{p}}$ collisions at $\sqrt{s}$ = 53, 200, 546 and 900 GeV measured by the UA5 collaboration [Aln87] (see Fig. 4.8 (a)) and the P238 [Har97] and CDF [Abe90] collaboration in inelastic minimum bias p+$\bar{\text{p}}$ collisions at 630 GeV and 1.8 TeV collision energy (see Fig. 4.8 (b)). A difference is observed between the experiments P238 and CDF at 630 GeV collision energy. At first glance it seems that a discrepancy between the measurements of UA1 and UA5 at 540 GeV and 546 GeV exists. However, in [Aro83] the authors assure the reader that both experiments agree within the error, therefore we refrain from discussing possible reasons for the apparent discrepancies.

The solid lines in Figs. 4.7 and 4.8 represent calculations from UrQMD in inelastic minimum bias p+$\bar{\text{p}}$ collisions. Unfortunately, no measurements of charged particle pseudorapidity distributions were performed for inelastic minimum bias p+p collisions at SPS (17.3 GeV) and RHIC energies to complete the overall picture (note however, that pion distributions at SPS and RHIC are well described by the present model [Pet08a]). Comparing UrQMD to the measurements from the UA1 (see Fig. 4.7 (b)) and UA5 (see Fig. 4.8 (a)) the model describes the UA1 data on a level of $\approx 20\%$ and the UA5 data within 5% accuracy. Moving to higher energies UrQMD describes the measured peseudorapidity distribution performed by P238 (see Fig. 4.8 (b)) at 630 GeV quite well. Comparing UrQMD to the measurements from CDF at 630 GeV it agrees on a level of $\approx 25\%$. Also here, the reader should notice the difference in the measurements between P238 and CDF at 630 GeV. For the measurements at 1.8 TeV the deviation is on the level of less than 10 %.

Moving on to nucleus-nucleus reactions, Fig. 4.9 shows the dN_{π^-}/dy and $dN_{ch}/d\eta$ distribution in Pb+Pb and Au+Au collisions for different experiments and energies from SPS to RHIC energies. Fig. 4.9 (a) presents the dN/dy distribution of negatively charged pions measured by the NA49 collaboration [Afa02a, Alt08a] from 6.3 to 17.3 GeV (7% most central collisions for 6.3 - 12.3 GeV, 5% most central collisions for 17.3 GeV) center-of-mass energy. It is visible that UrQMD overpredicts the measurements at mid-rapidity by $\approx 5\%$ except for the ones at 17.3 GeV collision energy. Going to the higher RHIC energies (Fig. 4.9 (b)) we compare to the measurements from the PHOBOS collaboration [Alv07b, Bac06, Bac03]. It is visible that the multiplicity increases with collision energy

[1] In UrQMD an inelastic collision is defined when at least one particle is created.

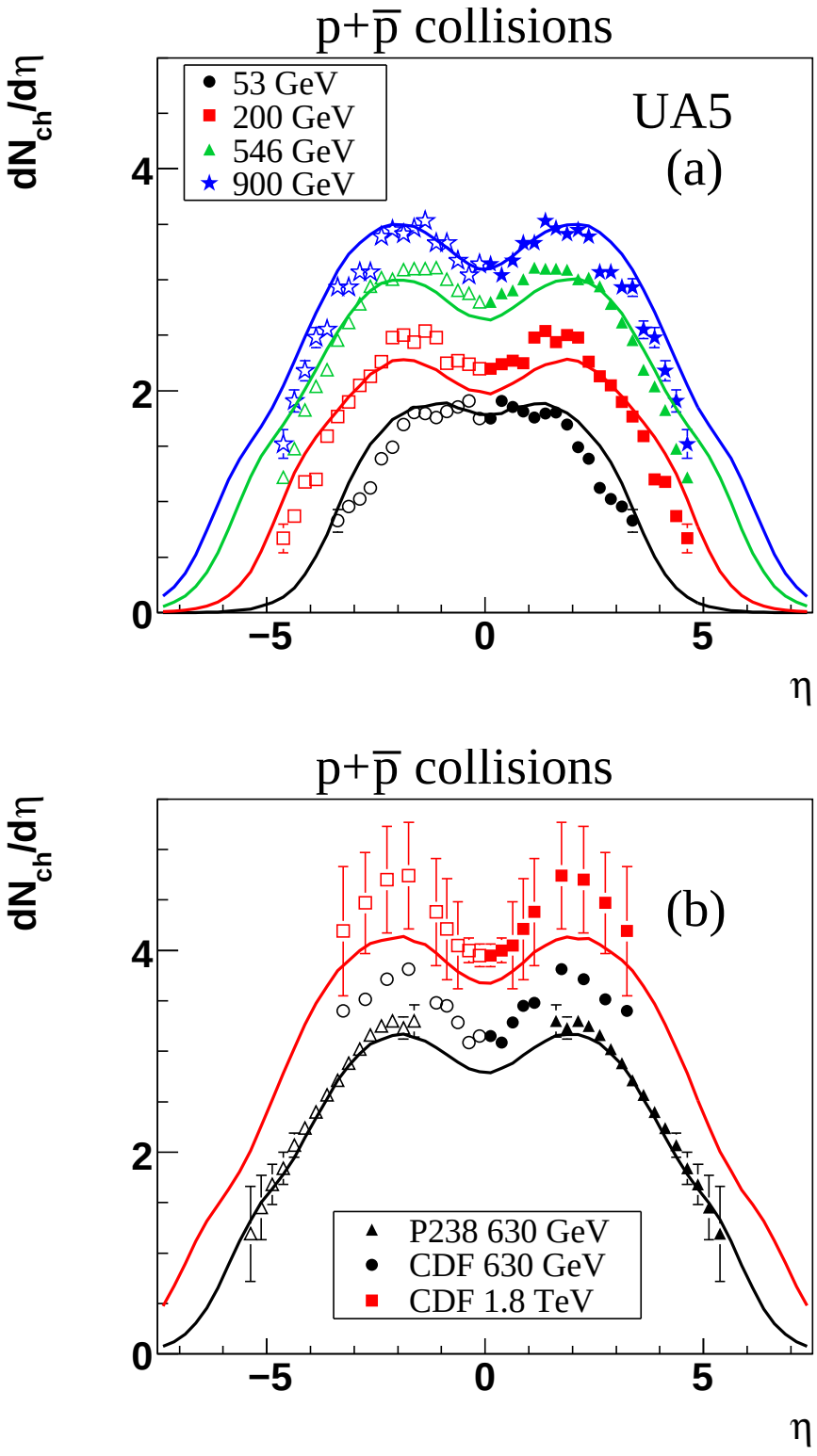

Figure 4.8: Pseudorapidity distribution of charged particles in inelastic minimum bias p+$\bar{\text{p}}$ collisions for different energies measured by the UA5 [Aln87] (a), CDF [Abe90] and P238 [Har97] (b). The closed symbols indicate measured points, whereas the open points are reflected with respect to mid-pseudorapidity. The solid line represent calculations from UrQMD, in inelastic minimum bias p+$\bar{\text{p}}$.

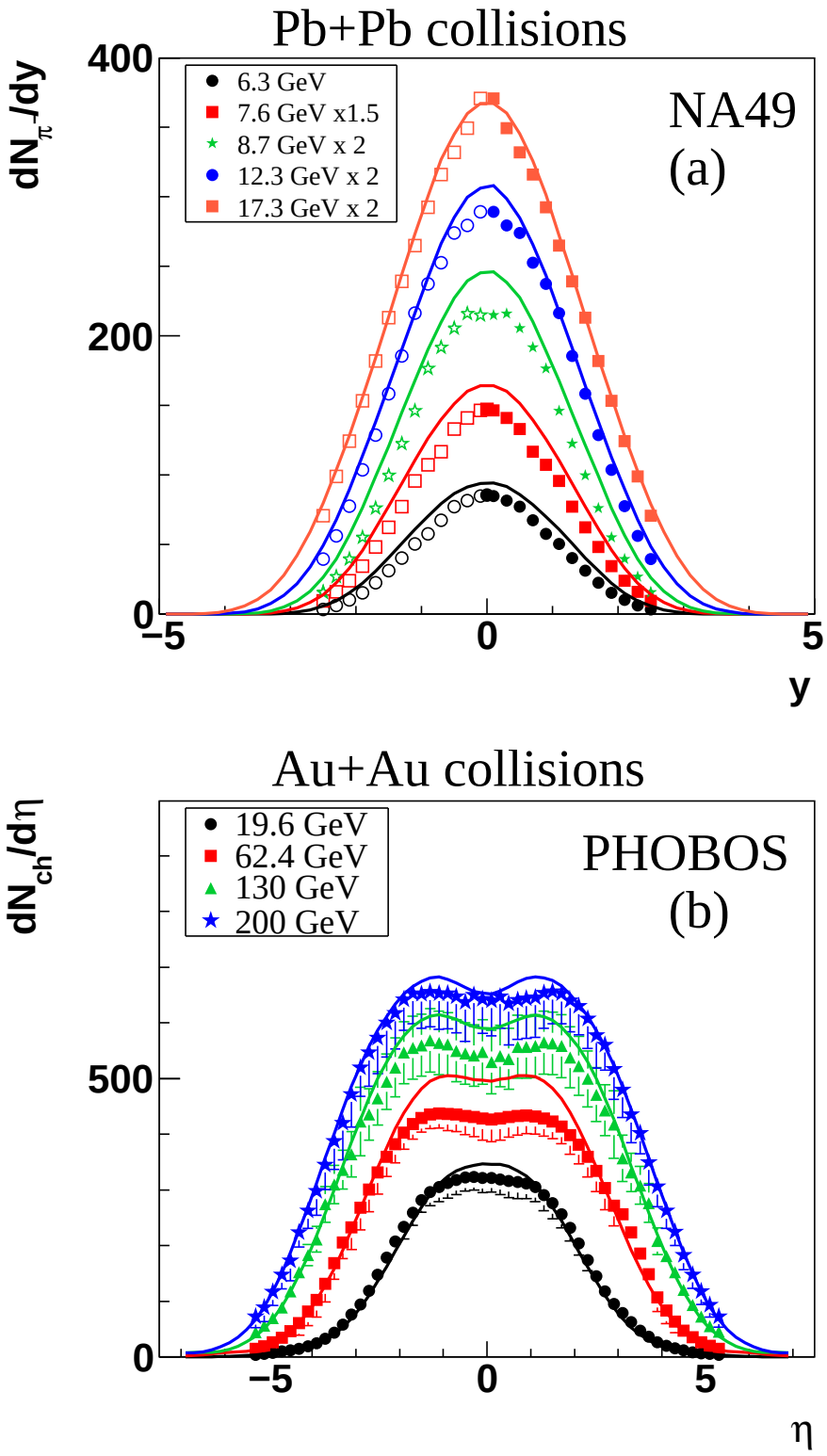

Figure 4.9: Rapidity distribution of π^- in Pb+Pb collisions at SPS energies from 6.3 to 17.3 GeV (7% most central collisions for 6.3 - 12.3 GeV, 5% most central collisions for 17.3 GeV) measured by the NA49 collaboration [Afa02a, Alt08a] (a). The pseudorapidity distribution of charged particles in Au+Au collisions (6% most central collisions, $b \leq$ 3.55 fm for the data from 19.6 - 130 GeV and $b \leq 3.65$ fm for the 200 GeV dataset) at RHIC energies from 19.6 to 200 GeV performed by the PHOBOS collaboration [Abr02, Alv07b, Bac06, Bac03] (b). The solid line represent calculations from UrQMD ($b \leq 3.9$ fm for 7% most central Pb+Pb collisions from 6.3 - 12.3 GeV, $b \leq 3.4$ fm for 5% most central Pb+Pb collisions at 17.3 GeV, $b \leq 3.6$ fm for 6% most central Au+Au collisions from 19.6 - 130 GeV and $b \leq 3.7$ fm for 6% most central Au+Au collisions at 200 GeV).

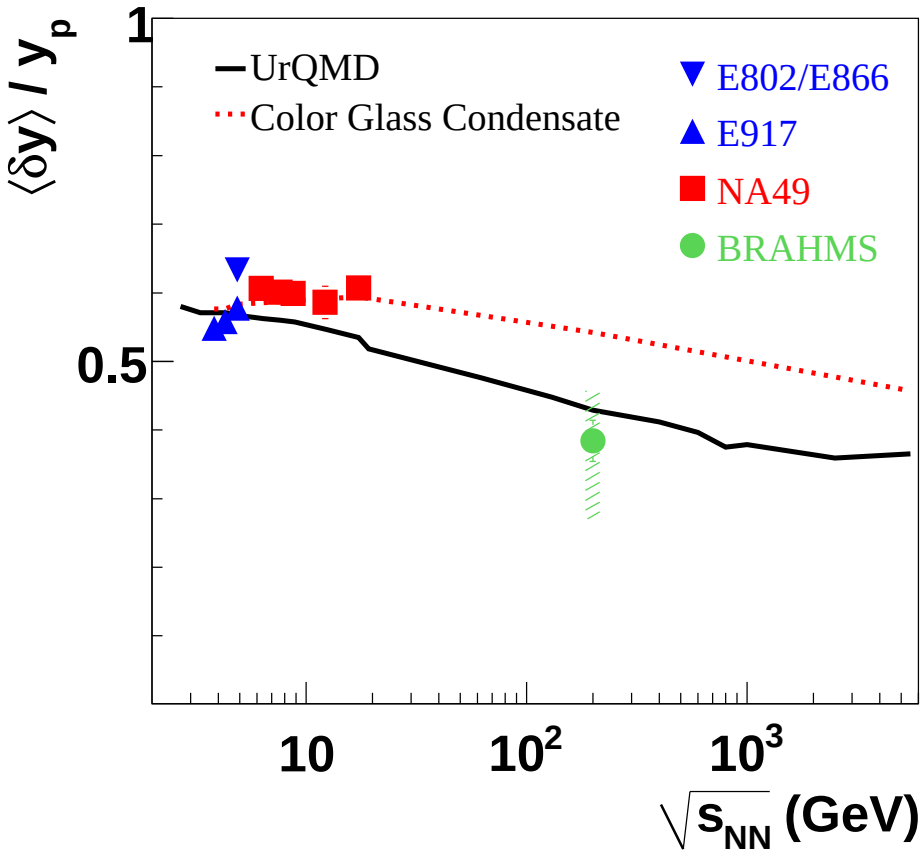

Figure 4.10: Relative rapidity shift $\langle \delta y \rangle / y_p$ as a function of the center-of-mass energy in relativistic heavy ion collisions from AGS to RHIC energies [Vid95, Bac01, App99, Bea04, Blm07]. The black line represents the prediction made by UrQMD from low AGS to LHC energies. The dotted line represents calculations from a color glass condensate model [Meh08].

from 19.6 to 200 GeV (6% most central collisions). Furthermore the shape of the spectra is also changing as already seen for p+p collisions due to the fact that the the colliding nuclei become increasingly transparent [Bjo83, Lan53]. This is reflected in the UrQMD prediction where the shape of the spectra is also changing with energy. UrQMD slightly (20%) overpredicts the measurements around mid-pseudorapidity at 62.4 GeV and 130 GeV.

A crucial point for particle production in A+A reactions is how much of the initial longitudinal motion is transformed to particles and transverse expansion. This is best characterized by an investigation of the energy (rapidity) loss of the initial nucleons. New measurements at SPS energies (20A - 80A GeV) [Blm07] combined with previously published results from AGS to RHIC energies [Vid95, Bac01, App99, Bea04] are available to test the predictions performed by the UrQMD model. Fig. 4.10 depicts the

energy evolution of the relative rapidity loss of the incoming nucleons in Au+Au/Pb+Pb reactions up to LHC energies. The net-baryon distribution ($\mathrm{d}N_{B-\bar{B}}/\mathrm{d}y$) is made by using the calculated rapidity spectra for p, $\bar{p}$, n, $\bar{n}$, Λ, $\Sigma^{\pm}$, Σ^{0}, Ξ^{-}, Ξ^{0} and Ω^{-} and their anti-particles respectively. From the net-baryon distribution an average rapidity shift $\langle \delta y \rangle$ can be calculated as follows:

$$\langle \delta y \rangle = y_p - \frac{2}{\langle N_{\mathrm{part}} \rangle} \int_0^{\infty} y \frac{dN_{B-\bar{B}}}{dy} dy, \tag{4.3}$$

where y_p is the projectile rapidity and $\langle N_{\mathrm{part}} \rangle$ the number of participating nucleons. It is clearly visible in the data that $\langle \delta y \rangle / y_p$ decreases from ≈ 0.6 at AGS energies to 0.4 at top RHIC energies which indicates that the relative baryon stopping is slightly weaker at RHIC energies as compared to lower AGS and SPS energies. The same trend is also observed in UrQMD [2] (black line in Fig. 4.10) where the absolute stopping follows the trend going from AGS to LHC energies. Another approach is also shown in Fig. 4.10 from a color glass condensate model [Meh08] (dotted line). In this model the authors are using the rapidity distribution of net protons ($p - \bar{p}$) in central heavy-ion collisions as a testing ground for saturation physics and that the valance quark parton distribution is well known at large x, which corresponds to the forward and backward rapidity region.

From these studies of the energy deposition (stopping) and particle production, we conclude that UrQMD has a valid basis for further extrapolations in energy and allows us to make predictions for LHC energies.

The predictions for the charged particle pseudorapidity distributions at LHC energies are shown in Fig 4.11 (a) for inelastic minimum bias p+p collisions at 5.5, 10 and 14 TeV and for the 5% most central ($\langle N_{\mathrm{part}} \rangle = 383$) Pb+Pb collisions at 5.5 TeV (b) (solid line).

There are two complementary production mechanisms at LHC energies: hard parton-parton scattering and soft processes. Particles produced in hard scatterings are usually created in primary collisions and are centered in a narrow region around mid-pseudorapidity (seen in dotted line in Fig. 4.11 (b)), whereas soft produced particles are distributed over the full pseudorapidity range (see dashed line in Fig. 4.11 (b)). At LHC energies both mechanisms play an important role so that the pseudorapidiy distribution of charged particles shown in Fig 4.11 (b) (solid line) is the sum of both processes.

Fig. 4.12 (a) shows the measured number of charged particles at mid-pseudorapidity ($\frac{dN_{\mathrm{ch}}}{d\eta}|_{\eta/y=0}$) as a function of $\sqrt{s_{NN}}$ for p+$\bar{\mathrm{p}}$ (circles) [Aro83, Aln87, Abe90] and Pb+Pb/ Au+Au (squares) [Afa02a, Alt08a, Abr02, Alv07b, Bac03, Bac06, Bea01] collisions [3]. It is clearly visible that in A+A collisions N_{ch} scales linearly with the center-of-mass energy.

[2] The difference to previous UrQMD versions are due to implementation of PYTHIA for p+p collisions and the resulting change in the string fragmentation function.

[3] Note that the number of charged particles for NA49 is calculated by adding the midrapidity yields of π^{-}, π^{+}, K^{-} and K^{+}.

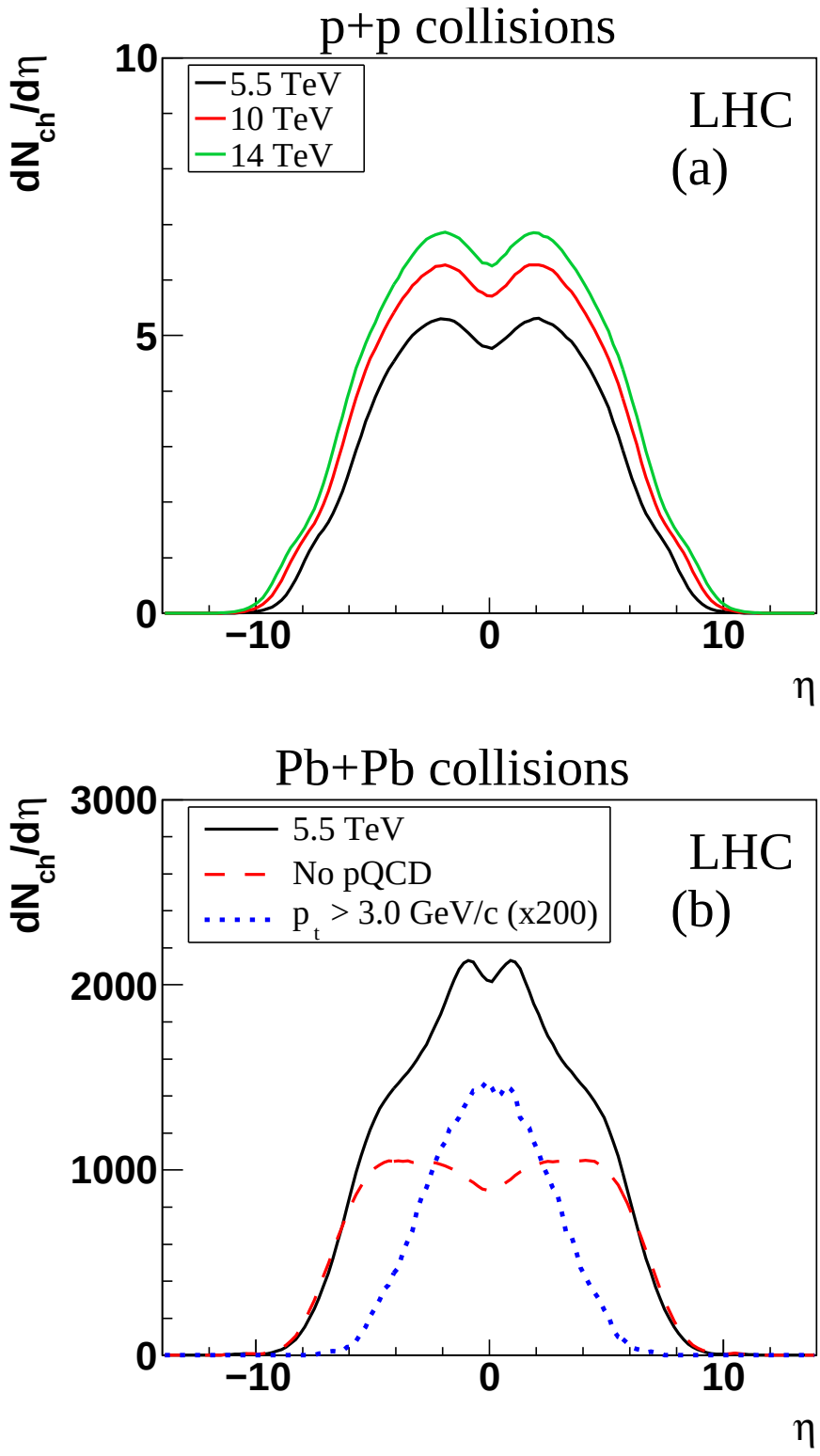

Figure 4.11: Prediction of the charged multiplicity pseudorapidity distribution for inelastic minimum bias p+p collision from $\sqrt{s_{\mathrm{NN}}} = 5.5$ to 14 TeV (a) and Pb+Pb collisions (5% most central collisions, $b \leq 3.35$ fm) at 5.5 TeV (b) collision energy from UrQMD, with PYTHIA (solid line), without pQCD contributions (PYTHIA) (dashed line) and for hard produced particles (dotted line) ($b \leq 3.4$ fm for 5% most central Pb+Pb collisions at 5.5 TeV).

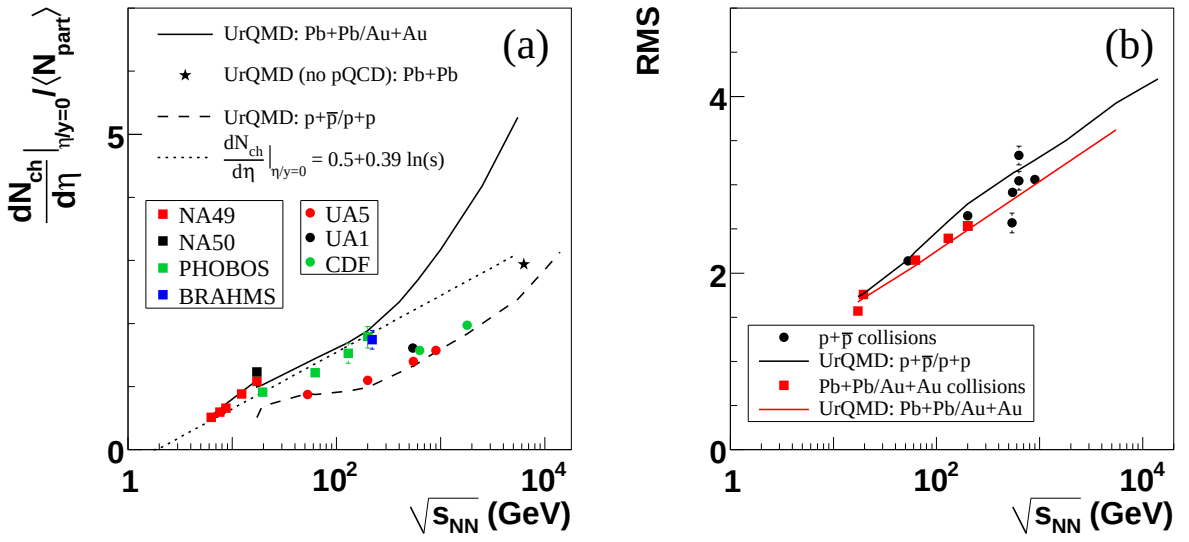

Figure 4.12: The energy dependence of the number of charged particles ($\frac{dN_{\mathrm{ch}}}{d\eta}$) at mid-pseudorapidity for p+$\bar{\mathrm{p}}$ (circles) and Pb+Pb/ Au+Au (squares) collisions divided by N_{part} (a). RMS width of the pseudorapidity rapidity distributions as a function of the center-of-mass energy (b). The black solid line represents calculations from UrQMD for p+$\bar{\mathrm{p}}$/p+p and the red solid line for Pb+Pb/Au+Au collisions respectively.

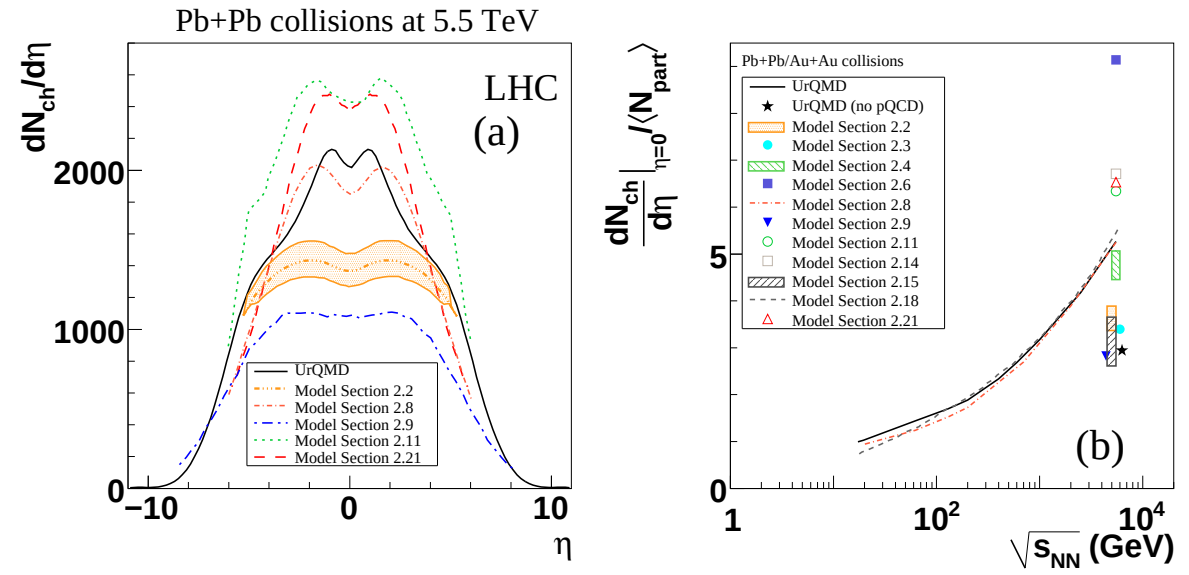

Figure 4.13: Comparison of the predicted pseudorapidity distribution of charged particles (a) and the charged particle multiplicity at mid-pseudorapidity (b) from UrQMD and predictions from various other models [Arm08].

The difference in scaling with N_{part} between p+$\bar{\mathrm{p}}$/p+p and Pb+Pb/Au+Au collisions increases with increasing center-of-mass energy. A simple approach to extrapolate the number of charged particles in Pb+Pb collisions was suggested in [Arm08] by using a fit function ($\frac{dN_{\mathrm{ch}}}{d\eta}|_{\eta/y=0} = 0.5{+}0.39{\cdot}\ln(\mathrm{s})$). It is visible that the fit function and UrQMD agree until top RHIC energies. At higher energies UrQMD predicts a higher multiplicity in central Pb+Pb collisions, especially for top LHC energies as compared to the simple extrapolation. The reason for the increasing numbers of the multiplicity is the increase of hard collisions at LHC energies. When not taking hard collisions into account (see Fig. 4.12 (a)) by switching off PYTHIA and just allow UrQMD to have soft particle production, UrQMD would follow the simple linear fit function. If the LHC data fall on the dotted line, hard collisions are either absent at LHC or saturation effects do effectively suppress a large part of the particle production. UrQMD not only describes the multiplicity and trend in p+$\bar{\mathrm{p}}$/p+p collisions (dashed line) but also in Pb+Pb/Au+Au collision (solid line). Furthermore in UrQMD, if going to LHC energies, the difference between p+p and Pb+Pb collisions becomes larger.

The RMS-width [4] is calculated by fitting the measured pseudorapidity distribution of charged particles from UA1, UA5, P238 and CDF experiments for p+$\bar{\mathrm{p}}$ NA50 and PHOBOS for Pb+Pb/AuAu collisions by a double Gaussian [5] (see Fig. 4.12 (b)). An increase of the RMS-width is observed for p+$\bar{\mathrm{p}}$ and Pb+Pb/Au+Au collisions with the center-of-mass energy. The dependence is linear for p+$\bar{\mathrm{p}}$ and Pb+Pb/Au+Au collisions. In the data, no difference between the RMS-width in p+$\bar{\mathrm{p}}$ and Pb+Pb/Au+Au is visible. UrQMD shows a slight difference between the RMS-width for p+$\bar{\mathrm{p}}$ and Pb+Pb/Au+Au collisions.

To have an overall picture how the presented prediction of UrQMD compares to other approaches Fig. 4.13 depicts the compiled results from other model predictions. Fig. 4.13 (a) shows the predicted pseudorapidity distributions of charged particles from various models [Arm08] in comparison to UrQMD. It is visible that all transport models (hadronic/partonic), including UrQMD, can be put together in one group by predicting a similar shape and multiplicity. The second group are saturation models which in general predict a lower multiplicity (also seen in [Arm00]). This is also visible in Fig. 4.13 (b) where the energy dependence of predicted charged particle multiplicity at mid-pseudorapidity is shown. At first glance it seems that the data would follow more the trend of a straight line but the major part of the models including UrQMD do not favour this trend (also seen in [Sar06]).

[4] RMS = $\sqrt{(\eta_0^2 + \sigma^2)}$

[5] Where double Gaussian means that we parametrized the pseudorapidity distribution by the sum of two Gauss distributions placed symmetrically with respect to mid-pseudorapidity and defined as follows: $\mathrm{dN/d}\eta = \mathrm{N}\ (e^{-\frac{\eta-\eta_0}{2\sigma^2}} + e^{-\frac{\eta+\eta_0}{2\sigma^2}})$, where η_0 is the mean and σ^2 the variance of the distribution.

5 Thermodynamic Quantities in a Transport Approach

To learn more about the time dependence of the thermodynamic properties of the matter created in a heavy ion collision it is useful to extract quantities like energy and particle densities or temperatures and baryo-chemical potentials from a microscopic transport approach. The most recent studies about equilibration times, EoS and phase diagram trajectoreis in microscopic approaches can be found in [Brv08]. In this work we concentrate on the calculation of the net baryon (or particle) density.

5.1 Baryon Density

The follwing procedure to calculate the net baryon density has been introduced in [Vog08b] to explore from which densities dileptons from ρ decays are emitted.

The local baryon density at a space point i is the zeroth component of the baryon four-current $j^\mu = (\rho_B, \vec{j})$. The local rest frame (RF) baryon density at this space point is defined in the frame where the three-current vanishes, $j^\mu_{RF} = (\rho_{B,RF}, \vec{j}_{RF})$, with $\vec{j}_{RF} = 0$. This definition is known as the Eckart frame. Other definitions are possible, e.g. in the Landau frame, the energy-momentum tensor is at rest while a baryon three-current might still be present. We believe however, that the Eckart frame definition captures the relevant physics at the energy regime under investigation.

In the context of the UrQMD model quantities are (per default) calculated in the computational frame (CF) which is (for symmetric systems) the center-of-mass frame of the whole heavy ion collision. In the computational frame one is only able to evaluate $j^\mu_{CF} = (\rho_{B,CF}, \vec{j}_{CF})$ where $\rho_{B,CF} = N/V$ is the baryon density (N denoting baryon number in the volume, V being the small local volume around the position i) and $\vec{j}_{CF} = \rho_{B,CF}\vec{\beta}$. In the limit of an infinitely small volume, the density $\rho_{B,CF}$ is a sum of Gaussians at position i:

$$\begin{aligned} \rho_{CF}(\vec{r_i}) &= \sum_{j=1}^{N} \left(\frac{1}{\sqrt{2\pi}\sigma}\right)^3 \gamma_z \, \mathrm{e}^{\left(-\frac{(x-x_0)^2+(y-y_0)^2+(z-z_0)^2\gamma_z^2}{2\sigma^2}\right)} \\ &= \sum_{j=1}^{N} P_j \end{aligned} \tag{5.1}$$

i.e., a three-dimensional in z-direction contracted and normalised Gaussian with $\gamma_z = 1/\sqrt{1-\beta_z^2}$ being the Lorentz factor for the particle under consideration. More information about the Lorentz contraction of three-dimensional Gaussian distributions can be

found in Appendix A. The normalisation is different for individual particles due to the different γ factors. The nominal width of the Gaussian is in this case $\sigma = 1.5$ fm. The particle that defines position i has to be included in the sum because one is interested in the baryon density in the local rest frame of the cell and not in the density around a particle in its rest frame.

The velocity of the cell is computed with the same Gaussians as used for the density calculation as weighting functions. Therefore, the velocity of the cell in the computational frame is:

$$\vec{\beta}_{CF} = \frac{\sum_{j=1}^{N} \left(\frac{\vec{p_j}}{E_j}\right) \cdot P_j}{\sum_{j=1}^{N} P_j}$$

The last step is to perform a general Lorentz boost of the four-vector j^{μ}_{CF} into the local rest frame of the cell. I.e. a Lorentz transformation with the velocity of the cell $\vec{\beta_{CF}}$. The transformation matrix is the following:

$$\begin{pmatrix} \gamma & -\beta_x\gamma & -\beta_y\gamma & -\beta_z\gamma \\ -\beta_x\gamma & 1+(\gamma-1)\frac{\beta_x^2}{\beta^2} & (\gamma-1)\frac{\beta_x\beta_y}{\beta^2} & (\gamma-1)\frac{\beta_x\beta_z}{\beta^2} \\ -\beta_y\gamma & (\gamma-1)\frac{\beta_y\beta_x}{\beta^2} & 1+(\gamma-1)\frac{\beta_y^2}{\beta^2} & (\gamma-1)\frac{\beta_y\beta_z}{\beta^2} \\ -\beta_z\gamma & (\gamma-1)\frac{\beta_z\beta_x}{\beta^2} & (\gamma-1)\frac{\beta_z\beta_y}{\beta^2} & 1+(\gamma-1)\frac{\beta_z^2}{\beta^2} \end{pmatrix}$$

with $\beta^2 = \beta_x^2 + \beta_y^2 + \beta_z^2$ and $\gamma = 1/\sqrt{1-\beta^2}$. The zero-component of the transformed j^{μ} four-vector is the local rest frame baryon density we are interested in.

In the default setup of UrQMD the net baryon density is calculated after a collision or a decay has occured when the outgoing state is checkes for Pauli blocking. The collision has been performed and the arrays are already newly filled and sorted at this point of the program. One calculates the density always at a position where something (collision, decay,...) has happened. This procedure triggers on higher densities than one would get for an arbitrary grid point. The particle information is given in the computational frame which has the advantage that everything is at the same time.

There is still one problem left: Usually this kind of density is defined as the density of an equilibrated system, but in our calculation we take all particles into account. If one wants only particles which are in a given rapidity bin near the cell one has to invent a complicated self-consistent iteration because one does not know the cell velocity in advance. An alternative idea that did not work out to calculate the particle densities in the local rest frame of the individual particleis presented in Appendix B.

5.1.1 Baryon vs. Quark Density

At low energies and for any hydrodynamical purposes it is necessary to calculate the net baryon density (ρ_B). The baryon density can be normalized to the nuclear ground state density $\rho_0 = 0.16 \frac{1}{\mathrm{fm}^3}$. The way of calculating the density does not depend on the type

of density we want to calculate. We only have to take into account the right particle types with the right weighting. For the baryon density baryons have to be added and antibaryons subtracted. For the velocity calculation the antibaryons have to be counted as baryons with negative velocity, i.e. with a minus sign.

At higher energies the produced matter becomes meson dominated in the interesting regime near midrapidity. Therefore, it is useful to have also the choice to calculate the quark density ($\rho_{q+\bar{q}}$). For this purpose one has to count anti/-baryons three times and mesons two times. This has to be respected also in the velocity calculation. The picture to have in mind is that a (anti-)baryon consists of three particles while a meson consists of two particles which have to be counted at the same location and with the same velocity by chance. For concrete calculations one just has to put a factor 3 or 2 in front of the gaussian for the density sum as well as for the weighting function for the velocity calculation. In this manner, we are now able to calculate any kind of number density, e.g. also a particle density where each hadron is counted as 1.

5.1.2 Time Evolution of the Baryon/Quark Density

To document the four-current-method the time evolution of the quark/baryon density at different energies from $E_{\mathrm{lab}} = 2A$ GeV to $\sqrt{s}_{\mathrm{NN}} = 200A$ GeV is shown. All calculations are performed for the most central collisions ($b = 0$ fm). There is also the test case included where the two nuclei just fly through each other without any interactions. For these studies the density is either averaged over the positions of all hadrons or calculated in the centre of the coordinate system which corresponds to the centre-of-mass frame of the heavy ion collision for symmetric systems.

The time evolution of the net baryon density is an interesting quantity to get a feeling for the duration of the reaction. Please note that for visibility reasons the timescale on the x axis is shortened going from AGS to SPS to RHIC energies. While the reaction lasts more than 10 fm at low energies, the high density stage is over after ~ 2 fm at RHIC energies. The maximum of the particle density is shifted to earlier times going to higher energies. Increasing the energy leads to the expected higher net baryon and quark densities. At lower energies both quantities show the same qualitative shape just scaled by a factor of three while at high energies it is clearly visible that the central region is net baryon free.

The calculation without collision term shows the densities that are reached without any intercations or production of particles, just by the passage of the two Lorentz contracted nuclei. One can read of the time that the two nuclei need to pass each other from these plots. The net baryon density saturates at a value a bit lower than the nuclear ground state density because the hadrons feel the nuclei that they are surounded with. The small deviation from ρ_0 can be explained by edge effects since all particles are weighted equally. The matter seems to sit longer in the centre of the system than the passage time because of the tails of the gaussian distributions.

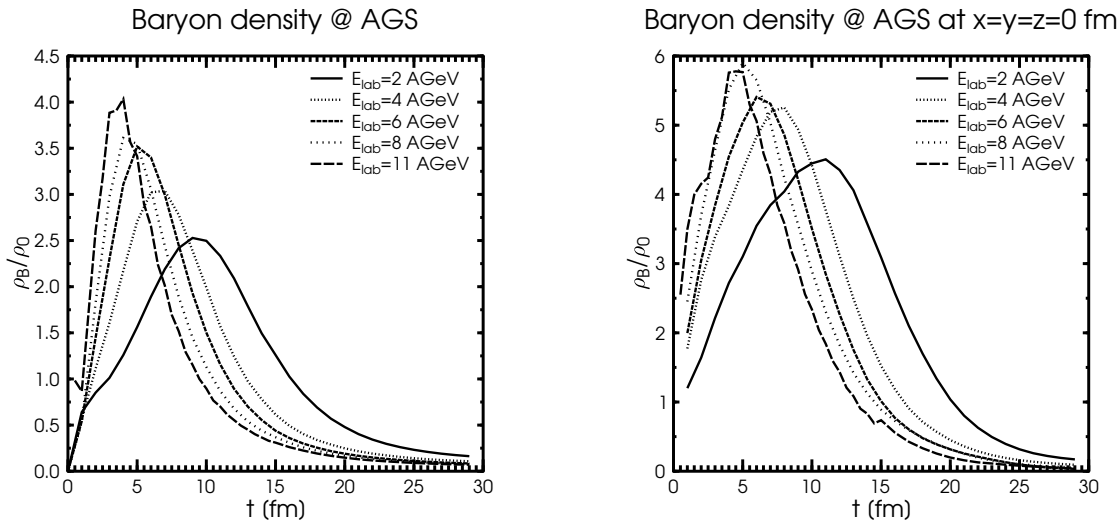

Figure 5.1: Time evolution of the net baryon density averaged over positions of all particles (left) and in the centre at the position $x = y = z = 0$ fm (right) at AGS beam energies. The results are calculated using UrQMD v2.3 at impact parameter $b = 0$ fm.

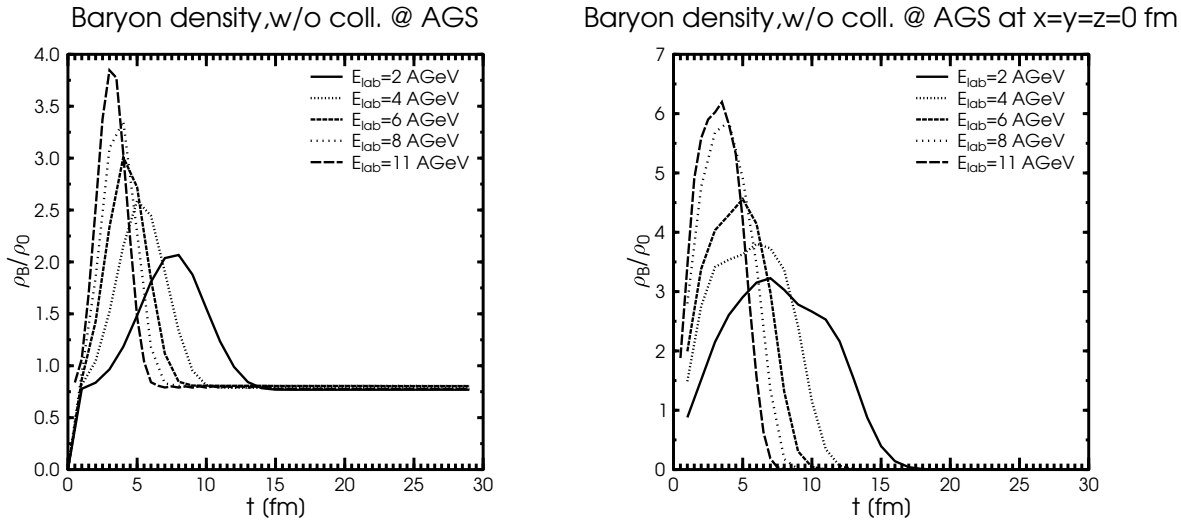

Figure 5.2: Time evolution of the net baryon density averaged over positions of all particles (left) and in the centre at the position $x = y = z = 0$ fm (right) at AGS beam energies. The results are calculated using UrQMD v2.3 without collision term at impact parameter $b = 0$ fm.

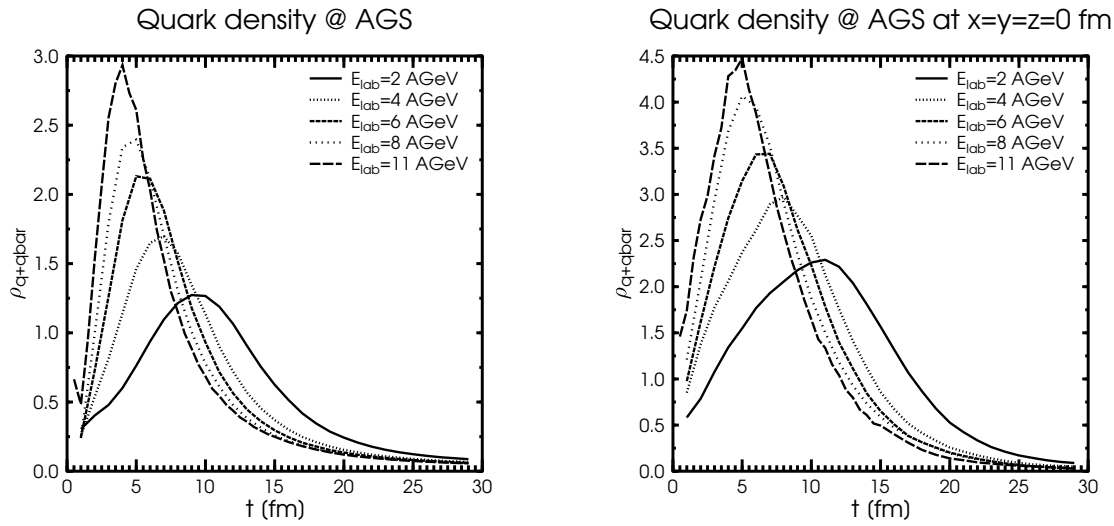

Figure 5.3: Time evolution of the quark density averaged over positions of all particles (left) and in the centre at the position $x = y = z = 0$ fm (right) at AGS beam energies. The results are calculated using UrQMD v2.3 at impact parameter $b = 0$ fm.

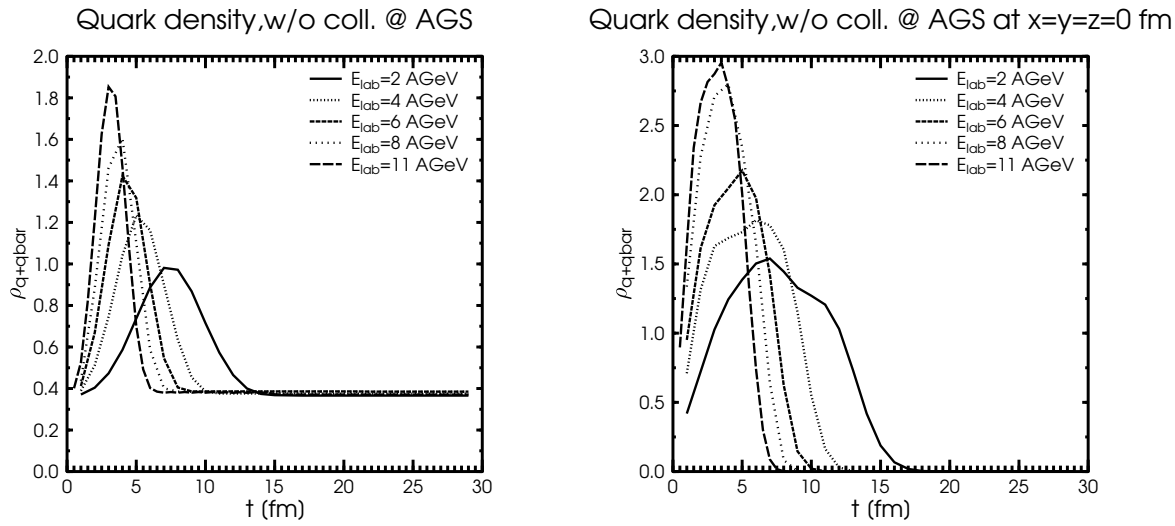

Figure 5.4: Time evolution of the quark density averaged over positions of all particles (left) and in the centre at the position $x = y = z = 0$ fm (right) at AGS beam energies. The results are calculated using UrQMD v2.3 without collision term at impact parameter $b = 0$ fm.

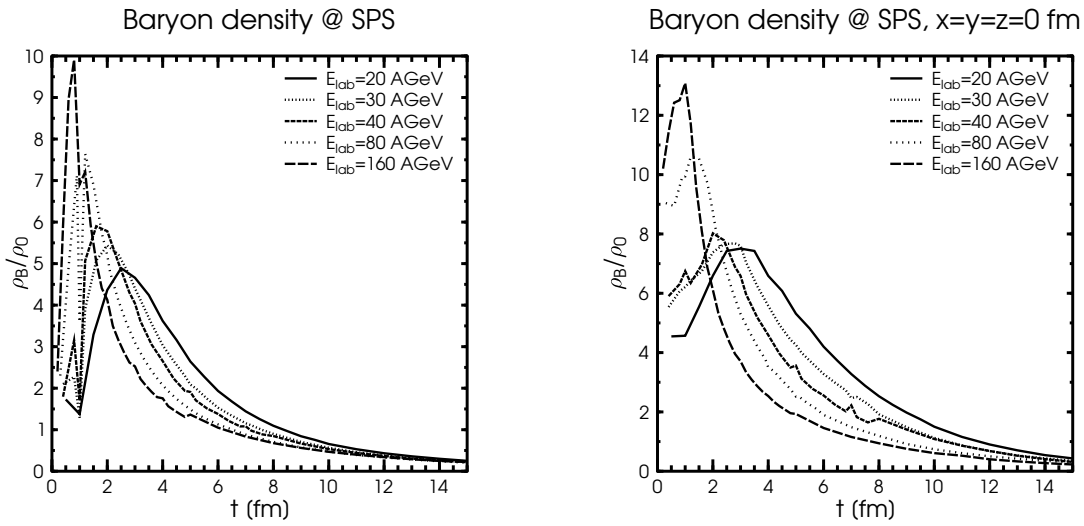

Figure 5.5: Time evolution of the net baryon density averaged over positions of all particles (left) and in the centre at the position $x = y = z = 0$ fm (right) at SPS beam energies. The results are calculated using UrQMD v2.3 at impact parameter $b = 0$ fm.

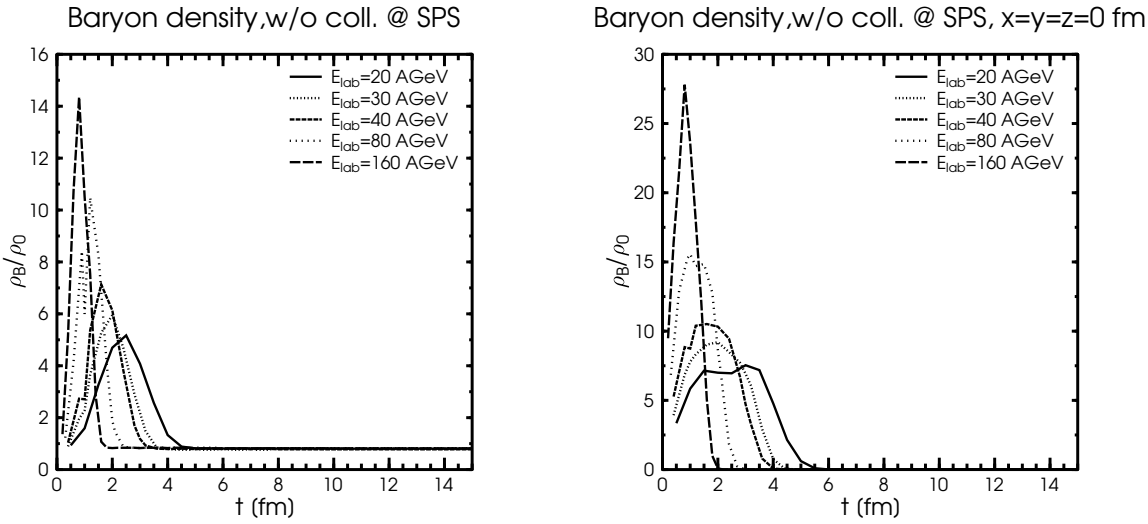

Figure 5.6: Time evolution of the net baryon density averaged over positions of all particles (left) and in the centre at the position $x = y = z = 0$ fm (right) at SPS beam energies. The results are calculated using UrQMD v2.3 without collision term at impact parameter $b = 0$ fm.

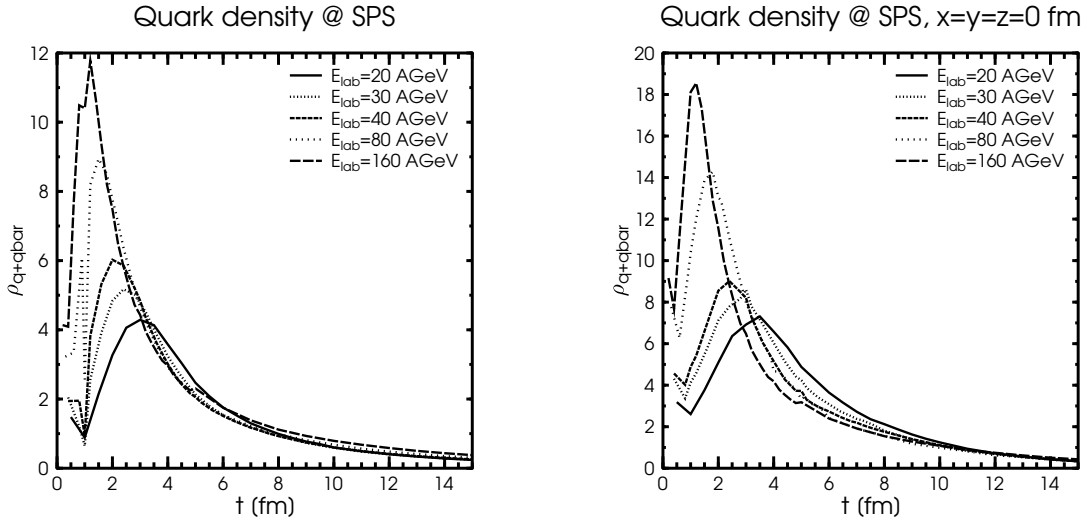

Figure 5.7: Time evolution of the quark density averaged over positions of all particles (left) and in the centre at the position $x = y = z = 0$ fm (right) at SPS beam energies. The results are calculated using UrQMD v2.3 at impact parameter $b = 0$ fm.

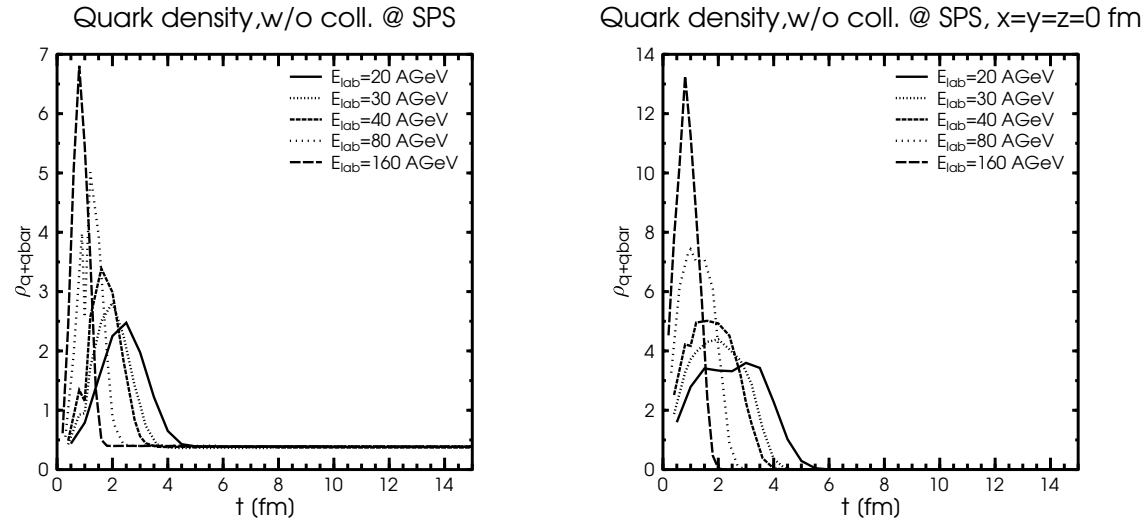

Figure 5.8: Time evolution of the quark density averaged over positions of all particles (left) and in the centre at the position $x = y = z = 0$ fm (right) at SPS beam energies. The results are calculated using UrQMD v2.3 without collision term at impact parameter $b = 0$ fm.

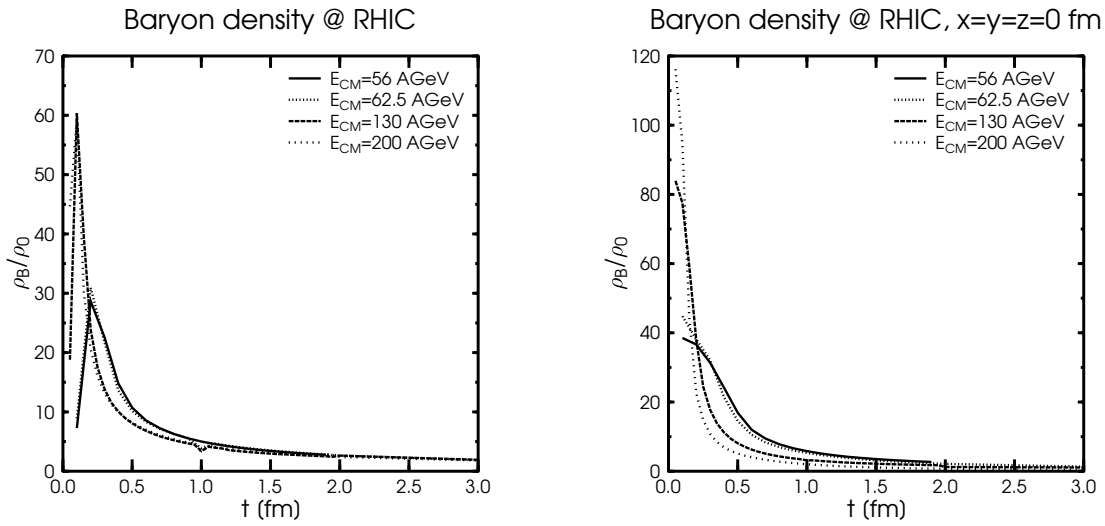

Figure 5.9: Time evolution of the net baryon density averaged over positions of all particles (left) and in the centre at the position $x = y = z = 0$ fm (right) at RHIC beam energies. The results are calculated using UrQMD v2.3 at impact parameter $b = 0$ fm.

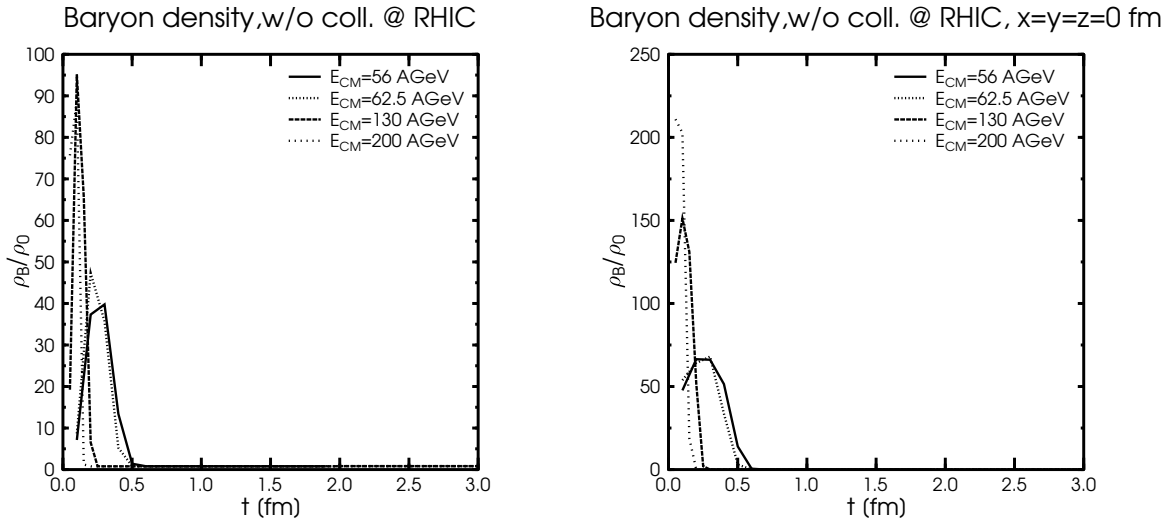

Figure 5.10: Time evolution of the net baryon density averaged over positions of all particles (left) and in the centre at the position $x = y = z = 0$ fm (right) at RHIC beam energies. The results are calculated using UrQMD v2.3 without collision term at impact parameter $b = 0$ fm.

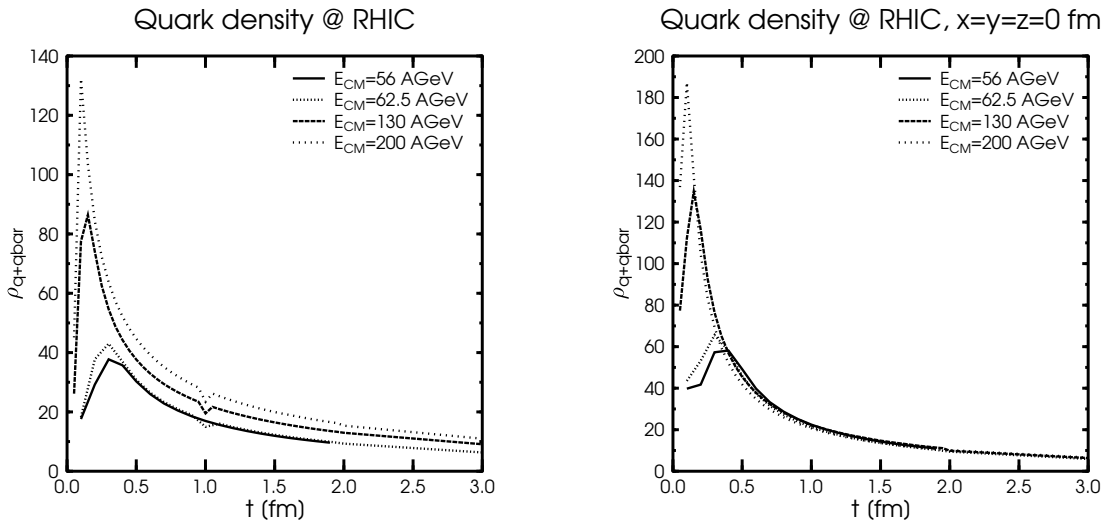

Figure 5.11: Time evolution of the quark density averaged over positions of all particles (left) and in the centre at the position $x = y = z = 0$ fm (right) at RHIC beam energies. The results are calculated using UrQMD v2.3 at impact parameter $b = 0$ fm.

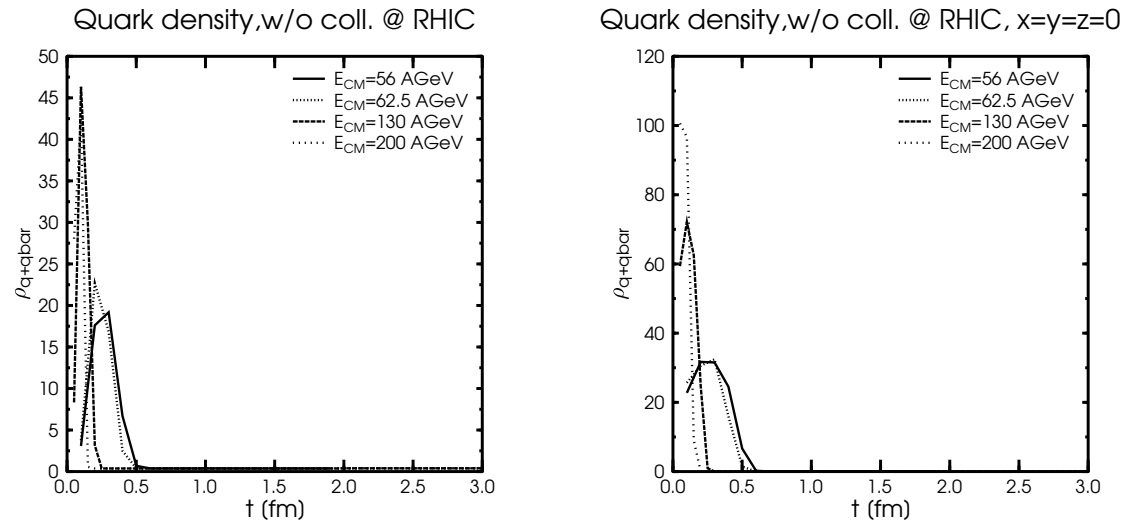

Figure 5.12: Time evolution of the quark density averaged over positions of all particles (left) and in the centre at the position $x = y = z = 0$ fm (right) at RHIC beam energies. The results are calculated using UrQMD v2.3 without collision term at impact parameter $b = 0$ fm.

5.2 Phase Diagram Trajectories

In this Section some explorative studies using UrQMD initial conditions for a hydrodynamic evolution are presented based on [Ste08a, Ste08d]. For a hydrodynamical modelling of heavy ion reactions one needs to specify initial conditions, i.e. an infinite set of space-time points with their corresponding energy- and baryon density. Since experimental data provides mainly information that is integrated over the systems time evolution, the initial state for hydrodynamical simulations has to be inferred from model assumptions or by educated 'guessing' in comparison to data. The latter approach - usually applied for relativistic hydrodynamical simulations of nuclear collisions - is, however, by no means straight forward and highly non-trivial: the connections between (observed) final state and the inferred initial conditions is blurred by the unknown equation of state, potential viscosity effects, and freeze-out problems. Another issue concerns the assumption of thermal equilibrium, which is probably not true at least for the early stage of a heavy ion collisions at intermediate energies.

There have been attempts to solve these problems by describing such collisions with viscous or multi-fluid-hydrodynamic models [Mih88, Mih89, Kat93, Bra97, Rei98, Ble99a, Bra00b, Bra00a, Dum01, Rus04, Iva06, Ton05, Bai07, Son08], but the practical application of these models is difficult. To avoid (some of) these problems we describe the initial stages of the collision with a non-equilibrium transport model (UrQMD). We then use the so obtained distributions for energy- and baryon-density as initial conditions for a one-fluid but fully (3+1)-dimensional hydrodynamical calculation. For the hydrodynamical evolution an EoS with a first order chiral phase transition and a critical endpoint (CEP) at finite μ_B is applied. For a more detailed description of the equation of state see Section 6.3.1.

Let us now turn to the explanation of the initial conditions that have been used. Two different ways to describe the initial conditions and the expansion will be discussed. In one setup the energy and density distributions obtained from the UrQMD transport simulation are mapped to the thermodynamic quantities, which then serve as initial conditions for the (3+1) dimensional hydrodynamic evolution. For a detailed description of this mapping procedure the reader is referred to Section 6.1. In the second setup initial energy- and baryon-densities as obtained from a simple overlap model are employed and then paths of constant entropy per baryon are followed.

This is done for Pb+Pb/Au+Au collisions at $E_{\mathrm{lab}} = 5 - 200A$ GeV with impact parameter $b = 0$ fm. To relate the distributions of energy and baryon number-density to thermodynamic quantities like pressure, temperature, chemical potential or entropy-density, the equation of state described above is used. As an example, Fig. 5.13 shows the initial temperature distribution obtained for $E_{\mathrm{lab}} = 10A$ GeV.

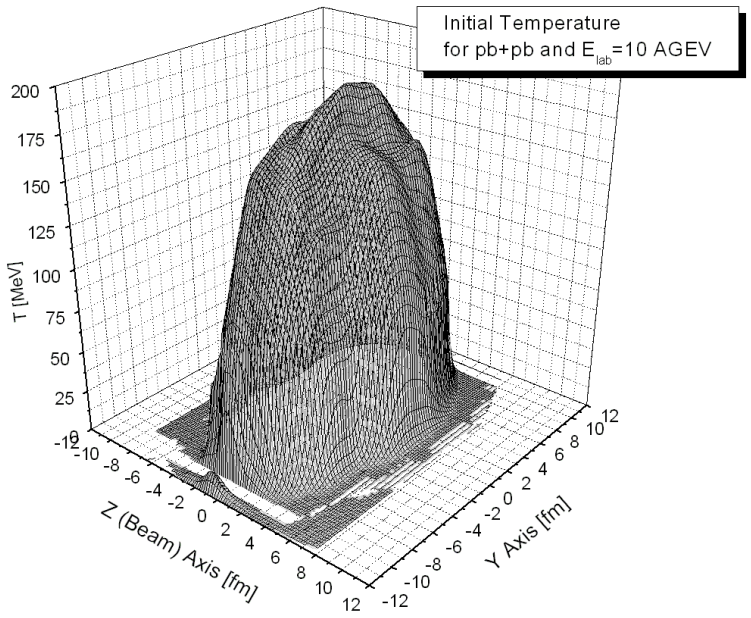

Figure 5.13: The initial temperature distribution in the z-y plane. Where z is the beam-axis and y the out of plane axis.

5.3 Overlap Model Initial Conditions

We contrast the microscopically calculated initial conditions described above with a simplified overlap geometry initial condition. Therefore, we assume that the entire initial beam energy and baryon number equilibrates in a Lorentz-contracted volume determined by the overlap of projectile and target in the center-of-mass frame. This allows to obtain a straightforward estimate for the initial baryon number and energy density:

$$\rho_B^{\text{initial}} = 2\,\gamma_{\text{CMS}}\,\rho_0 \quad , \tag{5.2}$$

$$\epsilon^{\text{initial}} = \sqrt{s}\,\rho_0\,\gamma_{\text{CMS}} \quad . \tag{5.3}$$

It was shown in [Rei98] that in the energy range of interest here, this rather simple approach reproduces the specific entropy production from a three-fluid model quite well.

5.4 Isentropic Expansion Paths

For the subsequent hydrodynamical evolution of the system we apply a fully (3+1)-dimensional one-fluid model. The hydrodynamical equations are solved by means of the SHASTA (SHarp And Smooth Transport Algorithm) as described in [Ris95b]. The EoS with a CEP is provided in tabulated form with a fixed step size in energy and baryon density: $\Delta\epsilon = 0.1$ and $\Delta n = 0.05$ where ϵ and n are given in units of nuclear ground

state densities ($\epsilon_0 \approx 138.5$ MeV and $n_0 \approx 0.15\text{fm}^{-3}$). This hydrodynamical model has been tested vigorously and applied successfully for various initial conditions and physics investigations [Wal92, Scn93, Ris95b, Ris95a, Ris96a, Gyu97, Stö06, Bet08].

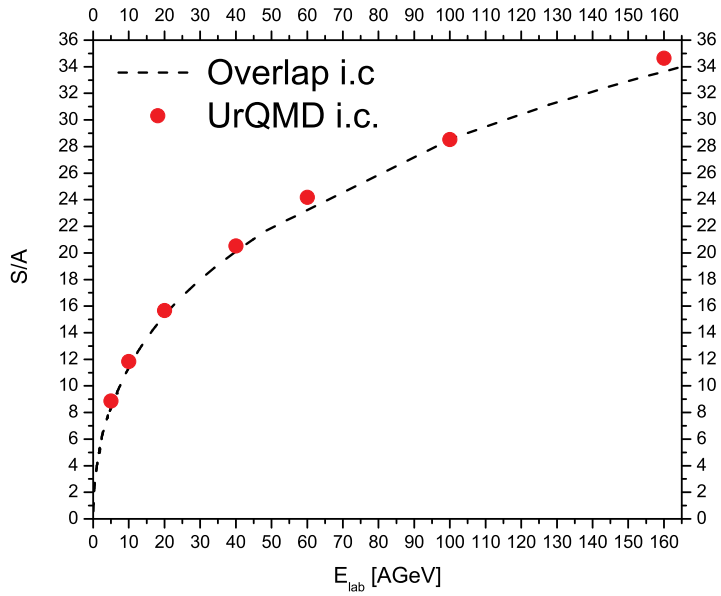

Figure 5.14: Excitation functions of S/A for the geometrical overlap model and UrQMD initial conditions.

Fig. 5.14 depicts the excitation function of the total entropy S per baryon number A for the initial stage of the hydrodynamical evolution for both initial conditions (UrQMD, solid circles; overlap model, dashed line). We have checked that both quantities are separately conserved throughout the whole hydrodynamical evolution, so S/A is a time independent constant[1]. Interestingly, the simple geometric overlap model and the UrQMD initial conditions yield basically the same value of S/A for a given incident energy.

The (isentropic) expansion paths for different beam energies in the ϵ- n plane are shown in Fig. 5.15. Here n is the baryon-number density. Again lines of constant S/A for overlap initial conditions (blue open circles and lines), and the (3+1)-dimensional hydrodynamical evolution with UrQMD initial conditions are compared. The mean values are obtained by weighting the value of a specific quantity in a given cell with the energy density of that cell. E.g., the mean number density is calculated from:

$$< n >= \frac{\sum_{i,j,k} n_{i,j,k} \cdot \epsilon_{i,j,k}}{\sum_{i,j,k} \epsilon_{i,j,k}}, \tag{5.4}$$

[1]It should be noted that entropy conservation is numerically difficult in the present approach if the initial conditions are too 'spiky', thus fixing the minimal value of the Gaussian width for the smearing of the particles.

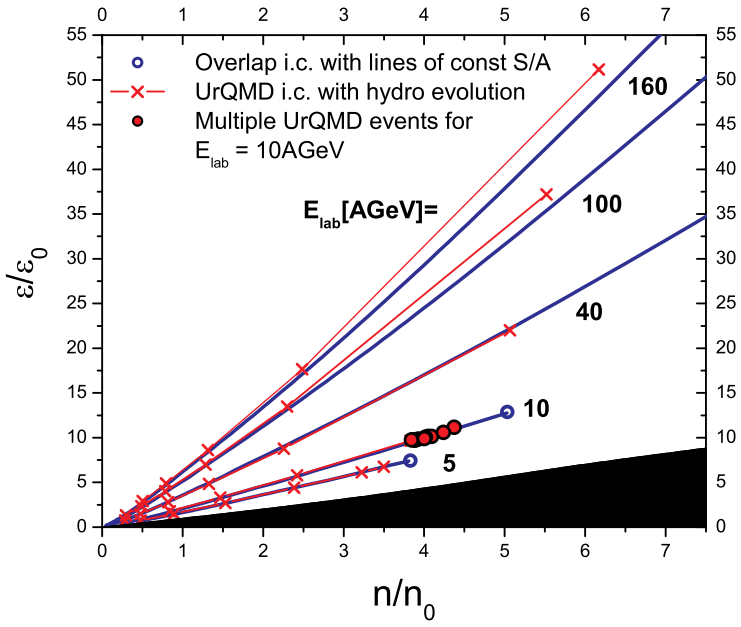

Figure 5.15: Isentropic expansion paths in units of ground state densities ($\epsilon_0 = 138.5$ MeV and $n_0 = 0.15\text{fm}^{-3}$). Red circles correspond to multiple UrQMD events for the same beam energy and impact parameter. The black region indicates the region below $T \leq 0$.

where i, j, k represent the cell indices. The mean values for ϵ, T and μ_q (quark chemical potential) are calculated accordingly. This has been done for equal time intervals of $\Delta t = 2.4$ fm/c. As expected, for a given beam energy, the dynamical paths obtained from the (3+1)-dimensional hydro evolution agree quite well with the lines of constant S/A. The variation in energy and baryon density due to the variation of the initial state in UrQMD even for a fixed impact parameter and fixed beam energy are studied for $E_{\text{lab}} = 10A$ GeV and indicated by the red full circles.

As a next step the hydrodynamic evolution of the system is shown in the $T - \mu_q$ plane in Fig. 5.16. Also indicated is the first order phase transition line and the CEP of the employed chiral EoS. Included are again lines of constant S/A and hydrodynamical evolution paths for the same beam energies (from left to right: $160, 100, 40, 10, 5A$ GeV) as in Fig. 5.15. As one can see, the mean temperatures and chemical potentials of the hydrodynamical evolution are not identical to the respective lines of constant entropy. This is due to the averaging procedure while a single cell does follow the isentropic path. The time evolution of a central cell at the origin in T and μ_q is depicted in comparison (green dashed line with green open circles).

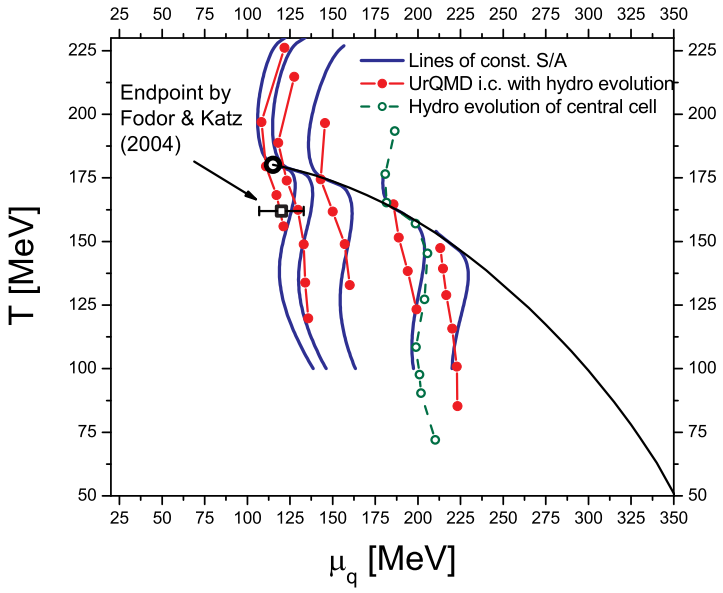

Figure 5.16: Isentropic expansion paths in the $T - \mu_q$ plane for very central Pb+Pb/Au+Au reactions. UrQMD initial conditions with (3+1)-dimensional chiral hydrodynamical evolution (averaged, full red line with circles; central cell, dashed green line with circles), isentropic expansion from the overlap model initial conditions are shown as full line in blue. Beam energies are from left to right: $160, 100, 40, 10, 5A$ GeV. The phase boundary of the model is shown as full black line with the critical end point, the Fodor and Katz critical end point is shown separately with error bars [Fod04].

5.5 The Critical Volume

It is worthwhile to connect the present discussion of the evolution path with UrQMD initial conditions to the results obtained with various models (however without phase transition) that are investigated in [Ars07]. The current findings with the chiral equation state support the main statement given there that it might be possible to reach the phase boundary to the QGP/chiral restoration already at moderate beam energies ($E_{\mathrm{lab}} \sim 5 - 10A$ GeV). A further discussion about the effect of different equations of state will be presented below. It should also be noted that we do not observe a focussing of the hydrodynamical trajectories towards the critical end point in contrast to the findings by [Non05, Asa06]. However, see also the discussion in [Sca01, Sth04].

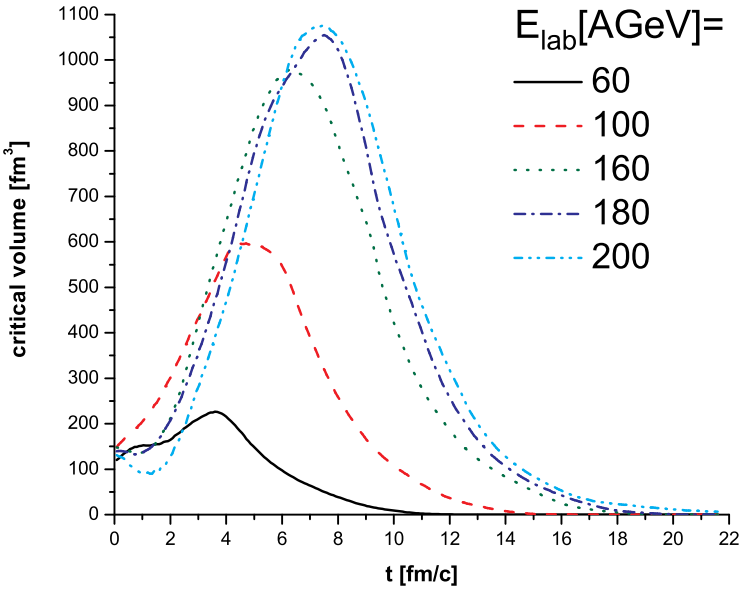

Figure 5.17: Time evolution of the critical volume for different beam energies for the CEP obtained with the chiral EoS.

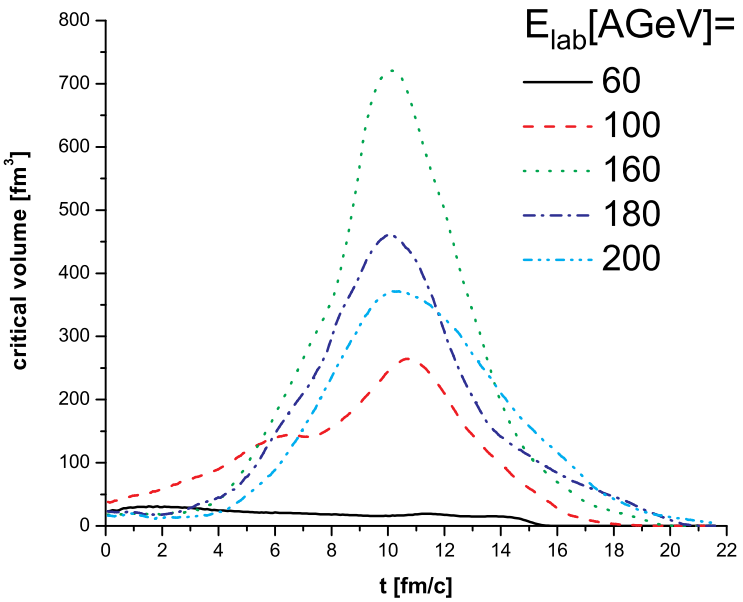

Figure 5.18: Time evolution of the critical volume for different beam energies the CEP obtained by Fodor and Katz [Fod04].

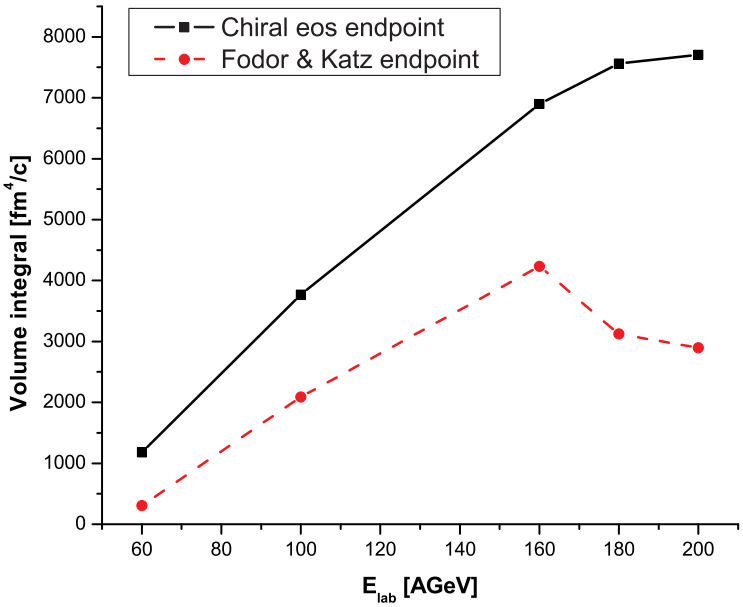

Figure 5.19: Excitation function of the critical space-time volume for the two different CEPs.

Having at hand an EoS with a critical end point it is possible to explore, which fraction of the evolving system stays for how long close to the critical end point. The energy dependence of this exposure tine is also investigated. Therefore, we define a 'critical volume' by adding all cells that have a temperature of $T_{\mathrm{CEP}} \pm 10$ MeV and a chemical potential $\mu_{\mathrm{CEP}} \pm 10$ MeV for each time step. Fig. 5.17 shows the time evolution of this critical volume at various incident energies for the critical end point obtained by the chiral EoS. Despite the surprising fact that the maximal volume is reached for the highest beam energies ($E_{\mathrm{lab}} = 160 - 200A$ GeV) a quite large critical volume of around ~ 200 fm^3 is already predicted at lower energies of $E_{\mathrm{lab}} = 60A$ GeV.

Fig. 5.18 shows the critical volume for the T_{CEP} and μ_{CEP} values obtained by lattice QCD calculations [Fod04], however using the chiral EoS for the dynamics. In contrast to the chiral values in Fig. 5.17 the time for the maximum does not change with the energy in this case. The highest values for the critical volume are still reached at the highest beam energies, but one has to keep in mind that the critical end point for the volume calculation and the critical point in the evolution are different. The influence of different EoS on the critical volume will be discussed below.

To pin down the beam energy to maximise the critical volume for the longest period of time, the total 4-volume is obtained by integration of the critical volume over the time. The space-time volume is shown in Fig. 5.19 as a function of E_{lab}.

Of course the actual size of the critical volume depends on the chosen ΔT and $\Delta\mu$

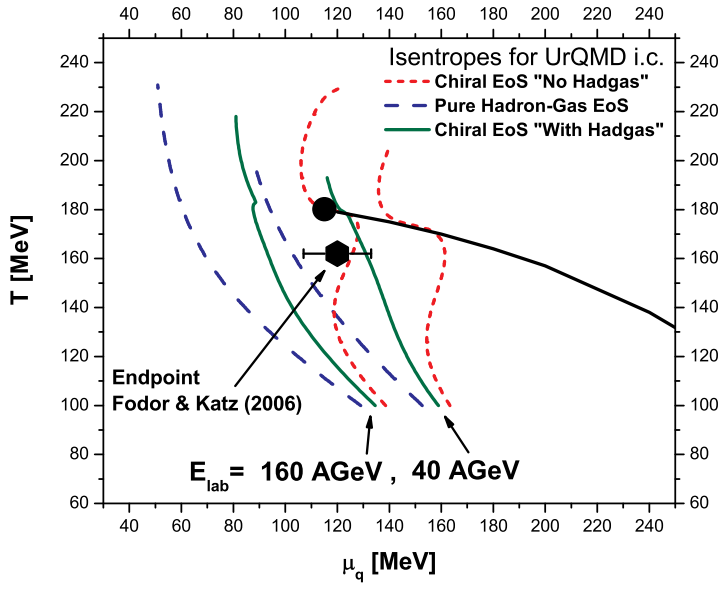

Figure 5.20: Isentropic expansion paths for different beam energies. The dashed lines resemble a pure hadron gas EoS. The short-dashed and straight lines refer to the chiral EoS without and with the completed resonance spectrum.

intervals around T_c and μ_c. Also the choice of the Gaussian width of the particles in the initial condition does have a small influence on the critical volume, since at larger σ the distributions for T and μ_q are wider and more 'smeared out'. However, we have checked that for the CEP obtained with the chiral EoS the excitation function is independent of σ. The integrated critical volume (for the CEP obtained from the chiral model) does steadily increase up to $E_{\rm lab} \approx 200A$ GeV. Having the maximum critical space-time volume in the excitation at such an unexpectedly high beam energy is due to the way the lines of constant entropy behave at the phase boarder (see Fig. 5.16). With the present chiral EoS, the trajectories coming from higher temperatures turn right (towards lower temperatures) at the phase transition line and therefore much higher energies are needed as if they would turn to smaller μ_q (left) and go up the phase line.

As a last step, we modify our chiral EoS by adding all known resonances (except the baryonic decuplett, since it is included by means of a so called 'test'-resonance) with vacuum-masses up to 2 GeV as a free gas. This allows to complete the baryon resonance spectrum without changing the phase structure of the EoS. The position and type of the phase transition in the phase diagram stays unchanged, because the added resonances have no influence on the chiral condensate σ.

In Fig. 5.20 isentropic paths for the two chiral EoS (with and without completed baryon resonance spectrum) are compared to those calculated with a free hadron-gas EoS (all particles have vacuum masses - which is of course not consistent (and only shown for

discussional purposes), since the free hadron-gas EoS does not have any phase transition or CEP). As one can see, a beam energy of $40A$ GeV is more than sufficient for an hadron gas EoS to reach the CEP, while the energy needed with the chiral EoS is $160A$ GeV (without heavy resonances) and $E_{\mathrm{lab}} = 40 - 60A$ GeV when heavy resonances are included.

6 The Hybrid Approach

The main achievement in this work is the development of a new Boltzmann plus hydrodynamics hybrid approach to heavy ion reactions. In this Chapter we describe the specific micro+macro hybrid approach that embeds a hydrodynamic phase in the UrQMD approach mainly based on [Pet08b]. First we explain the initial conditions, then introduce the basics of the hydrodynamic evolution including the different EoS and illustrate how the freeze-out is treated.

Let us start by recalling the main motivations behind this kind of approach to describe the dynamics of a high energy heavy ion reaction. The main idea behind a hybrid approach is to combine the advantages of a transport and a hydrodynamics calculation in the best possible way. Both approaches have been reviewed in Chapters 3 and 4 but let us recall the main aspects that are important for the coupling here.

The microscopic approach has the advantage that it is applicable to non-equilibrium situations and the full phase space information is available at all stages of the heavy ion reaction. The restriction to binary collisions assumes large mean free paths of the particles. This assumption might not be justified in the hot and very dense stage of heavy ion collisions anymore. In this regime the continuum limit in form of relativistic hydrodynamics might fit better to the characteristics of the system. The hydrodynamic evolution is governed by the energy and momentum conservation laws for given initial conditions, i.e. spatial distributions of energy and net baryon number densities. Thus, hydrodynamics is a good tool to describe collective behaviour. Ideal hydrodynamics applies to systems with small mean free path, otherwise viscous effects have to be taken into account [Lan53]. A general advantage of hydrodynamics is the feature to explicitly incorporate phase transitions by changing the EoS.

However, in the late stage of the heavy ion reaction the system gets too dilute to apply ideal fluid dynamics. The hadronic rescatterings and decays of resonances have to be described, e.g., by using a transport description. Overall, there are two crucial points one has to take care of when building up a transport+hydrodynamics hybrid approach. The first is the initial switch from the microscopic to the macroscopic calculation where it has to be ensured that the local equilibrium assumption is fulfilled. The second one is the so called freeze-out where the hydrodynamic fields are mapped to particles that are further propagated in a hadronic cascade. The freeze-out transition must be placed in a region where both descriptions are valid at the same time,e.g., the phase transition region. With this integrated treatment we overcome some of the restrictions of previous microscopic+macroscopic approaches that have been mentioned in Section 3.3.2.

The specific hybrid approach that we have developed is based on the Ultra-relativistic Quantum Molecular Dynamics (UrQMD) transport approach with an intermediate hydrodynamical evolution for the hot and dense stage of the collision. Event-by-event fluctuations are directly taken into account via the non-equilibrium initial conditions generated by the initial collisions and string fragmentations in the microscopic UrQMD model. After a (3+1)-dimensional ideal hydrodynamic evolution, the hydrodynamical fields are mapped to hadrons via the Cooper-Frye equation and the subsequent hadronic cascade calculation within UrQMD proceeds to incorporate the important final state effects for a realistic freeze-out. This implementation allows to compare pure microscopic transport calculations with hydrodynamic calculations using exactly the same initial conditions and freeze-out procedure. The effects of the change in the underlying dynamics - ideal fluid dynamics vs. non-equilibrium transport theory - are explored as a baseline check. The aim is to compare calculations with different EoS within the same framework. It is possible to extract the effect of changes in the EoS, e.g., a phase transition from hadronic matter to the QGP, on observables.

In the following the specific implementation developed here will be discussed in more detail.

6.1 Initial Conditions

The initial conditions for a hydrodynamic evolution are energy and net baryon number density distributions in local thermal equilibrium. Usually, parametrized symmetric distributions according to a Glauber model or a Color Glass Condensate (CGC) calculation are used for this purpose. The height of the densities is taken as a free parameter to fit the final state particle distributions at the specific energy under consideration. Within the NEXspheRIO approach it has been proven that initial fluctuations are very important for different observables. So, we employ a similar approach and calculate the initial conditions microscopically in a transport approach.

The UrQMD model is used to calculate the initial state of a heavy ion collision for the hydrodynamical evolution [Ste08a]. This is necessary to account for the non-equilibrium nature of the very early stage of the collision. Event-by-event fluctuations of the initial state are naturally included by this set-up. The coupling between the UrQMD initial state and the hydrodynamical evolution takes place when the two Lorentz-contracted nuclei have passed through each other. The initial time to begin with the hydrodynamical evolution is calculated via Eqn. 6.1 (and is assumed to be at least 1 fm/c):

$$t_{\text{start}} = \frac{2R}{\gamma v} = \frac{2R}{\sqrt{\gamma^2 - 1}} = 2R\sqrt{\frac{2m_N}{E_{\text{lab}}}}\,, \tag{6.1}$$

where R is the radius of the nucleus, m_N is the nucleon mass and E_{lab} is the kinetic beam energy. The explicit calculation of the given expression of t_{start} is contained in

Appendix C. This assures that (essentially) all initial baryon-baryon scatterings have proceeded and that the energy deposition has taken place. This is the earliest possible transition time where thermalization might be achieved [Brv08]. It is also convenient from the hydrodynamical point of view since at that time the two baryon currents that fly into oppposite directions have separated again.

In general, it is not well-established how and when chemical and kinetic equilibrium might have been reached in the early stage of the collision. One of the problems is, e.g., that the local equilibrium assumption might not apply equally well to all parts of the system at the same time in the computational frame which corresponds to the center of mass system of the two colliding nuclei. As a consequence, the faster particles have had less time in their local rest frame to equilibrate. For the bulk part and the high density region at midrapidity the difference between the two frames is small. These problems are present in all hydrodynamic/macroscopic approaches that rely on an equilibrium assumption and it is not our attempt to resolve these difficulties here. One perspective might be the dynamical coupling between the initial transport calculation and the hydrodynamic evolution including source terms on both sides of the transition surface.

To allow for a consistent and numerically stable mapping of the 'point like' particles from UrQMD to the 3-dimensional spatial-grid with a cell size of $(0.2\,\mathrm{fm})^3$, each hadron is represented by a Gaussian with a finite width. "Pre-formed" hadrons in the process of string fragmentation are also included in the transformation to the hydrodynamic quantities. I.e. each particle is described by a three-dimensional Gaussian distribution of its total energy, momentum (in x-, y-, and z-direction) and baryon number density. The width of these Gaussians is chosen to be $\sigma = 1$ fm. A smaller Gaussian widths leads to numerical instabilities (e.g., entropy production) in the further hydrodynamical evolution, while a broader width would smear out the initial fluctuations to a large extent. To account for the Lorentz-contraction of the nuclei in the longitudinal direction, a Lorentz-gamma-factor is included. The resulting distribution function in the computational frame (cf), e.g., for the energy density, reads:

$$\epsilon_{\mathrm{cf}}(x,y,z) = N e^{-\frac{(x-x_p)^2+(y-y_p)^2+(\gamma_z(z-z_p))^2}{2\sigma^2}} \quad , \tag{6.2}$$

where $N = (1/2\pi)^{3/2}\gamma_z/\sigma^3 E_{\mathrm{cf}}$ provides the proper normalisation, ϵ_{cf} and E_{cf} are the energy density and total energy of the particle in the computational frame, while (x_p, y_p, z_p) is the position vector of the particle. Summing over all single particle distribution functions leads to distributions of energy, momentum and baryon number densities in each cell. This procedure is adapted from the density calculation studies that are presented in Chapter 5.

To allow for calculations at finite impact parameter the spectators - nucleons that have not interacted at all before the start time of the hydrodynamic evolution t_{start} - are propagated separately from the hydrodynamic evolution. The spectators are propagated on straight line trajectories in the usual cascade mode until the end of the hydrodynamic phase has been reached.

Instead of smearing out the initial distributions by describing the point like hadrons as Gaussian distributions, one could also obtain a smooth distribution by averaging over a large sample of UrQMD events. Our procedure of creating a new initial state for each event is motivated by the fact, that the experimental results all relate to observed (averaged) final, and not initial, states. Thus, event-by-event fluctuations of the initial state can be observed, (e.g., in v_2 fluctuations) and have therefore been taken into account properly (for discussion of the importance of these fluctuations see, e.g., [Pai97, Dre07]).

The remaining question is if the system is thermalized enough to assure that the local equilibrium assumption of ideal hydrodynamics is fulfilled. In our case, the hydrodynamic code transforms all the given quantities from the computational frame to the local rest frame of the energy momentum tensor which is also known as the Landau frame. This frame coincides in ideal hydrodynamics with the Eckart frame which is defined as the local rest frame of the baryon number current. The iterative calculation of the cell velocity succeeds if those two frames are close enough to each other. By this transformation the system is forced to local equilibrium.

Please note that the calculation of the initial state is universal for all energies, system sizes and centralities, once the formula for t_{start} has been fixed. The dependence of the final results on this parameter is shown in Section 7.

6.1.1 Initial Energy and Baryon Density

In this Section some exmaples for initial energy and net baryon density distributions are shown.

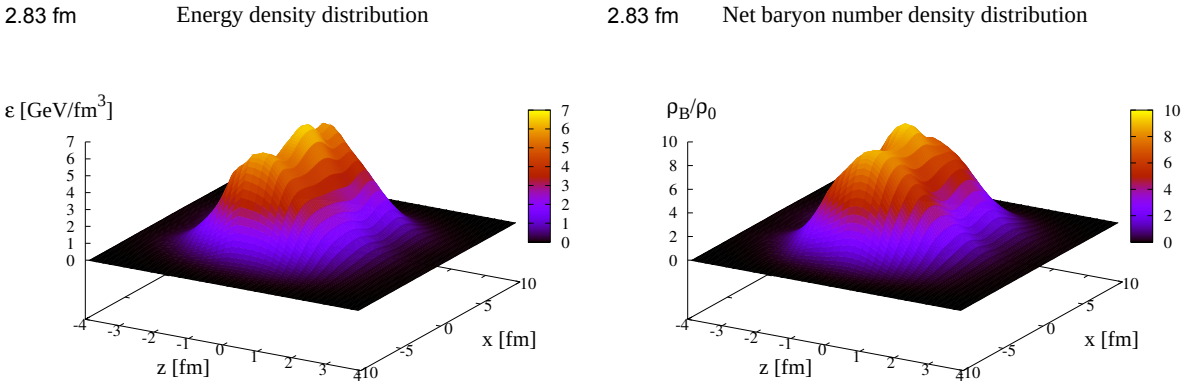

Figure 6.1: Initial energy density/net baryon density (left/right) distribution in the reaction plane ($x-z$ plane) of one central ($b = 0$ fm) Pb+Pb collision at $E_{\text{lab}} = 40A$ GeV. z corresponds to the beam direction and x to the in-plane axis (direction of the impact parameter) of the collision.

As an example, Fig. 6.1 shows the energy and baryon number densities obtained in one

single central ($b = 0$ fm) Pb+Pb collision at $E_{\rm lab} = 40A$ GeV after the initialisation of the hydrodynamic fields. The starting time is in this case $t_{start} = 2.83$ fm and the densities in the figures correspond to the same time. The distribution is displayed in the reaction plane (the $x - z$-plane) to make the differences between the longitudinal and the transverse direction visible. All quantities are given in the local rest frame. The maximum values reach 6 GeV/fm^3 for the energy density and around 8 times the nuclear ground state density for the baryon number density.

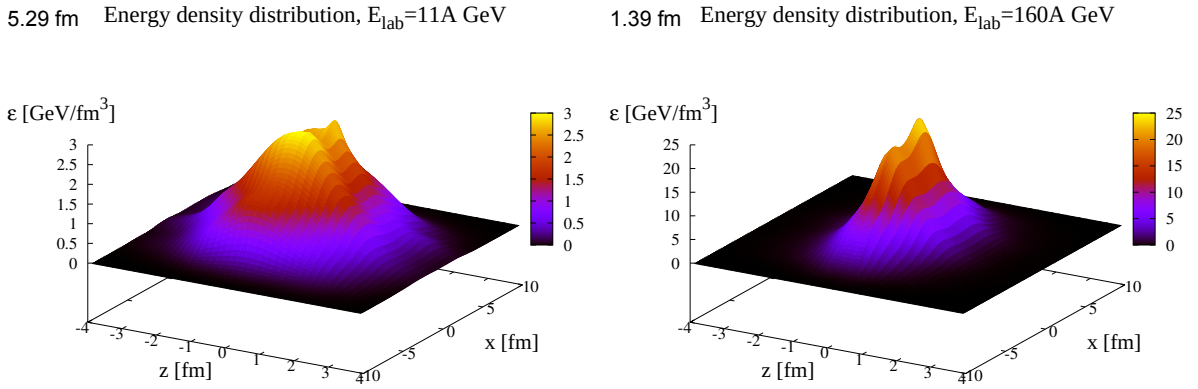

Figure 6.2: Initial energy density distribution for the hydrodynamical stage in the reaction plane ($x - z$ plane) of one central ($b = 0$ fm) Au+Au/Pb+Pb collision at $E_{\rm lab} = 11A$ GeV/$E_{\rm lab} = 160A$ GeV. z corresponds to the beam direction and x to the in-plane axis (direction of the impact parameter) of the collision.

As an example, Fig. 6.2 shows the local rest frame energy density obtained in one single central ($b = 0$ fm) Au+Au/Pb+Pb collision at $E_{\rm lab} = 11$ and $160A$ GeV. The starting time is in this case $t_{\rm start} = 5.29$ fm and $t_{\rm start} = 1.39$ fm respectively and the densities in the figures are given at these times. At the AGS energy the maximum value for the energy density is still rather low around 3 GeV/fm^3 while at the highest SPS energy energy densities of 25 GeV/fm^3 are reached. Furthermore, the effect of the Lorentz contraction of the two nuclei leads to a steeper distribution at higher energies. The distributions are quite smooth which is necessary to provide proper initial conditions for the hydrodynamic evolution. However, one can see some peaks that correspond to local maxima of the distributions ("hot spots") [Gyu97]. The single event distributions are not symmetric, neither in the transverse nor the longitudinal direction.

6.1.2 Initial Velocity Profiles

Let us now turn to the velocity distributions in the initial state. Since the momentum distributions are also mapped from the UrQMD initial particle distributions to the hydrodynamic grid the resulting distribution is non-trivial.

Figs. 6.3 shows the velocity distributions along the x- and the z-axis respectively. The

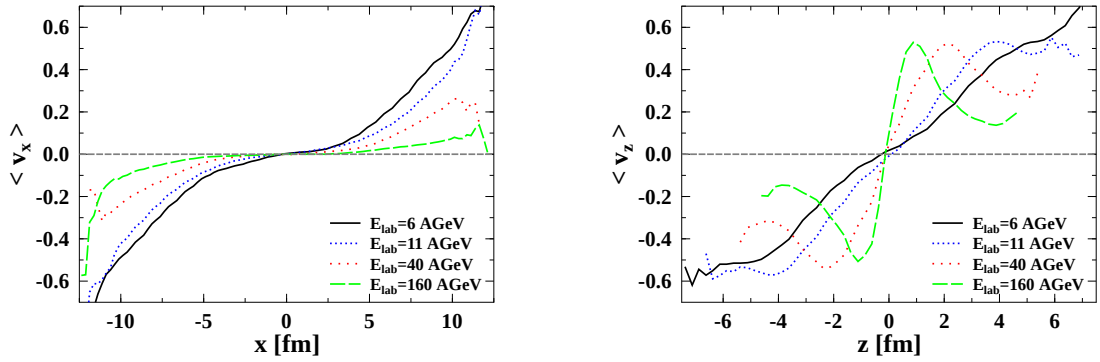

Figure 6.3: Initial velocity in fractions of c in x-direction along the x-axis corresponding to the impact parameter direction (left) and in z-direction along the z-axis corresponding to the beam direction (right) for four different beam energies ($E_{\rm lab} = 6A$ GeV -full black line, $E_{\rm lab} = 11A$ GeV -dotted blue line, $E_{\rm lab} = 40A$ GeV -dotted red line and $E_{\rm lab} = 160A$ GeV -dashed green line). The results are displayed for central ($b = 0$ fm) Au+Au/Pb+Pb collisions.

results have been obtained from the hydrodynamic calculation directly after the transformation to local rest frame quantities which has to be done before the first propagation. For this analysis, the velocities of the cells in the computational frame have been averaged over 100 events for the two different directions. (For real calcluations the distributions are not averaged.) To investigate the structure of the initial conditions for the hydrodynamic evolution the results are displayed for four beam energies ($E_{\rm lab} = 6, 11, 40$ and $160A$ GeV) for central ($b = 0$ fm) Au+Au/Pb+Pb collisions.

Along the impact parameter direction (Fig. 6.3 (left)) the higher stopping power at lower energies is visible. The highest transverse velocities are reached at $E_{\rm lab} = 6A$ GeV while the distribution becomes flat at higher energies. Along the beam direction (Fig. 6.3 (right)) the effect of the Lorentz contraction is nicely observed. Otherwise the distribution resemble almost straight lines as would be expected from a Bjorken picture. The lower values of the velocities at larger longitudinal coordinates (z-axis) correspond to the Gaussian tails of the stopped particles. Those numerical artefacts vanish durig the first few timesteps in the hydrodynamic evolution.

6.2 Hydrodynamic Evolution

The basics of relativistic ideal fluid dynamics have already been discussed in Chapter 3.3. Therfore, we concentrate here on the specific implementation that has been used. Ideal relativistic one fluid dynamics is based on the conservation of energy, momentum and the net baryon number current.

The equations of motion are solved in the following form by employing computational frame quantities $\epsilon_{\rm cf}, p^i$ and $\rho_{\rm cf}$ for the energy, momentum and net baryon number densities.

$$\partial_t \epsilon_{\rm cf} + \nabla \cdot (\epsilon_{\rm cf}\, \vec{v}) = -\nabla \cdot (P\, \vec{v}) \quad (6.3)$$

$$\partial_t \vec{p} + \nabla \cdot (\vec{p}\, \vec{v}) = -\nabla P \quad (6.4)$$

$$\partial_t \rho_{\rm cf} + \nabla \cdot (\rho_{\rm cf}\, \vec{v}) = 0 \quad (6.5)$$

In our case, the full (3+1) dimensional hydrodynamic evolution is performed using the SHASTA algorithm [Ris95b, Ris95a]. The partial differential equations are solved on a three-dimensional spatial Eulerian grid with fixed position and size in the computational frame. The standard size of the grid is 200 cells in each direction while the cell size has been chosen to be $(dx)^3 = (0.2\,\mathrm{fm})^3$ which leads to timesteps of $dt = 0.08$ fm. Depending on the beam energy, the cell sizes may require adjustment to assure a stable solution of the differential equation.

The equation of state is needed as an additional input to calculate the pressure, temperature and chemical potential corresponding to the energy and the baryon number densities. Since the evolution of the system is driven by pressure gradients the EoS has the most important influence on the evolution.

6.3 Equation of State

To solve the hydrodynamical equations, the EoS, the pressure as a function of energy and net-baryon number density, is needed as an input. Since the actual EoS of hot and dense QCD matter is still not precisely known, it may seem disadvantageous to have this additional uncertainty in the model. On the contrary it may prove to be an important trait of the model to be able to study changes on the dynamics of the bulk matter when changing the EoS thus finding observables for a phase transition in hot QCD matter. For recent discussions of different EoS and how to obtain EoS from lattice calculations, the reader is referred to [Blu07, Red08, Bir06]. Serving as an input for the hydrodynamical calculation the EoS strongly influences the dynamics of an expanding system. In the following Sections we describe the three different EoS that have been applied in the hybrid approach.

6.3.1 The Chiral EoS

The present chiral hadronic $SU(3)$ Lagrangian incorporates the complete set of baryons from the lowest flavour-$SU(3)$ octet, as well as the entire multiplets of scalar, pseudoscalar, vector and axial-vector mesons [Pap99]. More details about the Lagrangian and the approximations that have been used can be found in Appendix D. Using the chiral model and adding additional baryonic degrees of freedom as well as adjusting their

scalar and vector coupling, an EoS with a phase structure including a first order phase transition and even a critical endpoint at finite μ_B can be obtained [Zsc07]. This chiral EoS has already been successfully applied to a hydrodynamic calculation (see Chapter 5) [Ste08a]. Here the essentially different equation of state leads to distinguishable different results on the properties of bulk matter. We will refer to this EoS as chiral EoS (CH). Please note that there are no quark and gluon degrees of freedom and no deconfinement transition but only a chiral transition where the hadron masses get changed.

6.3.2 The Hadron Gas EoS

Setting all hadron masses and chemical potentials in the above described chiral model to their vacuum values, and adding all reliably known heavy resonance states - with masses up to 2 GeV [Eid04] - as free particles into Eqn. (D.5), yields a Hadron Gas EoS [Zsc02b]. Hence, the hadronic degrees of freedom included in this EoS are consistent with the active degrees of freedom in the UrQMD model. This enables us to directly compare the dynamics of the hydrodynamic model with the transport simulation. This EoS is a grand canonical description of a free, non interacting gas of hadrons without explicit phase transition. We will refer to it as the Hadron Gas (HG).

6.3.3 The Bag Model

A MIT-Bag model EoS matched to an interacting hadron gas [Ris95a], generating a phase structure with a broad first order phase transition at all μ_B, can also be applied in our model. This EoS, named the Bag Model EoS (BM), follows from coupling a bag model of massless quarks and gluons to a Walecka type of hadron gas including only SU(2) flavours (for details the reader is referred to [Ris95a]). This EoS exhibits a strong first-order phase transition (with large latent heat) for all baryonic chemical potentials μ_B.

6.3.4 Time Evolution of the Pressure

To visualize the differences of these EoS, Fig. 6.4 shows the average pressure of the expanding system, from central Pb+Pb collisions at $E_{\mathrm{lab}} = 20A$ GeV (left plot) and $158A$ GeV (right plot), as a function of time (in the center of mass frame). The vertical line in each plot indicates the starting time of the hydro evolution. The mean value of the pressure has been obtained by weighting the pressure, $P_{i,j,k}$, in every cell by its energy density, $\varepsilon_{i,j,k}$, and integrating over the hydrodynamic grid

$$< P >= \frac{\sum_{i,j,k} P_{i,j,k} \cdot \varepsilon_{i,j,k}}{\sum_{i,j,k} \varepsilon_{i,j,k}}. \tag{6.6}$$

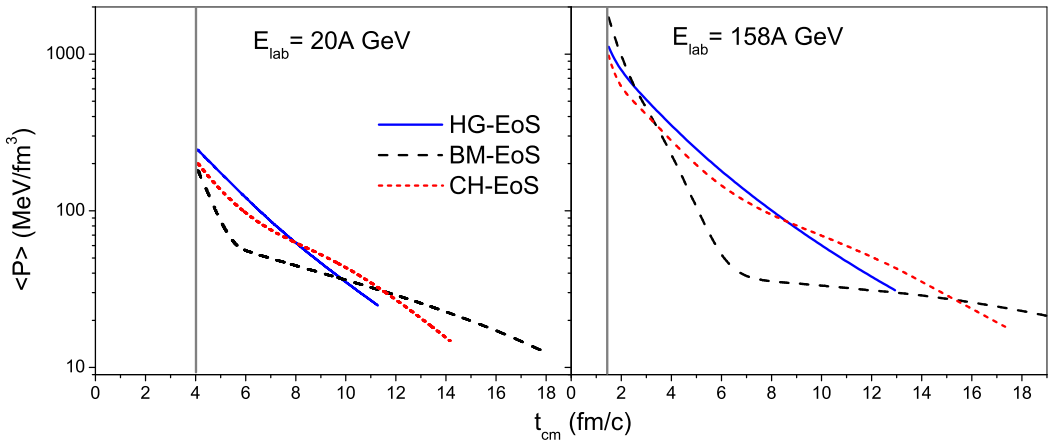

Figure 6.4: Time (in the center of mass frame) evolution of the average pressure for all three EoS and a central Pb+Pb collision at $E_{\rm lab} = 20A$ GeV (left plot) and $E_{\rm lab} = 158A$ GeV (right plot). The vertical line in each plot indicates the starting time of the hydro evolution.

All curves in Fig. 6.4 are plotted until the point in time when the isochronous freeze-out criterion is fulfilled. Compared to the HG the BM-EoS leads to a delayed freeze-out time (i.e. a much longer expansion). While in the first few fm/c of the evolution, the system obeying the BM-EoS expands most violently (due to the high pressure gradient in the QGP phase), once the system enters the mixed phase, its expansion is slowed down considerably. This can be observed as the "kink" in Fig. 6.4. At the higher beam energy, $E_{lab} = 158A$ GeV, this softening of the EoS is even more pronounced. Since the HG-EoS does not contain any phase transition, no softening can be observed, resulting in the shortest expansion time. The chiral CH-EoS lies in between both extreme cases. Although a small kink can be observed, it is not as pronounced as in the BM-EoS.

6.4 Freeze-Out

The decoupling process of the particles from the diluted system is the freeze-out process. There is a difference between chemical and kinetic freeze-out as it has been discussed in Section 3.2. In the context of the hybrid approach we refer to the switching point between the two prescriptions (hydrodynamics and transport) as (hydrodynamic) "freeze-out" which is then followed by the gradual decoupling of the particles as given by the cascade calculation. Two different prescriptions of this switching procedure are described in this Section.

6.4.1 Isochronous Freeze-Out

First of all, one has to define a reasonable criterion where the transition from the hydrodynamics to the transport calculation can be placed. In our case, the hydrodynamic evolution is stopped, if the energy density drops below five times the nuclear ground state energy density (i.e. ~ 730 MeV/fm^3) in all cells. This criterion corresponds to a T-μ_B-configuration where the phase transition is expected (see dotted line in Fig. 6.6), i.e. a region where the hydrodynamic and the transport description are valid at the same time. The hydrodynamic fields are mapped to hadrons according to the Cooper-Frye equation [Coo74]

$$E\frac{dN}{d^3p} = \int_\sigma f(x,p)p^\mu d\sigma_\mu \tag{6.7}$$

where $f(x,p)$ are the boosted Fermi or Bose distributions corresponding to the respective particle species. Since we are dealing with an isochronous freeze-out, the normal vector on the hypersurface is $d\sigma_\mu = (d^3x, \vec{0})$.

Let us note that it is of utmost importance to consider the same degrees of freedom on both sides of the hypersurface because otherwise energy and momentum conservation is violated. In our case, this is assured by the inclusion of the same particle species in the hadronic part of the equation of state for the hydrodynamic calculation as in the transport calculation. In principle, it might also happen that particles are moving back into the hydrodynamic phase, however, the explosive character of heavy ion reactions, i.e. the rapid expansion flow suppresses the back-streaming effect. Therefore, this effect is negligible in our situation [Bug04].

The assumption of an isochronous freeze-out leads to fluctuations of the temperature and baryo-chemical potential distributions and not to single values for some of the thermodynamic quantities on the hypersurface. The quality of this approach and that the two (hydrodynamics and transport) prescriptions are valid through the applied range of switching temperatures is shown in the next Section, where parameter tests and the time evolutions of the particle yields are explored in detail.

Fig. 6.5 shows the distribution of energy in the cells at freeze-out with respect to temperature and baryo-chemical potential at $E_{\rm lab} = 40A$ GeV. We present here the energy distribution and not the number of cells because it is more interesting to know where the energy of the system sits than considering the many almost empty cells that do essentially not contribute to particle production. From Fig. 6.5 one obtains the mean values of the distributions that are in line with results from statistical model fits. The mean values of, e.g., the temperature can be calculated as

$$\langle T \rangle = \frac{\sum_{i,j,k} T(i,j,k)\rho_B(i,j,k)}{\sum_{i,j,k} \rho_B(i,j,k)}, \tag{6.8}$$

where i,j,k are the cell indices and the sum runs over all cells of one event. The net

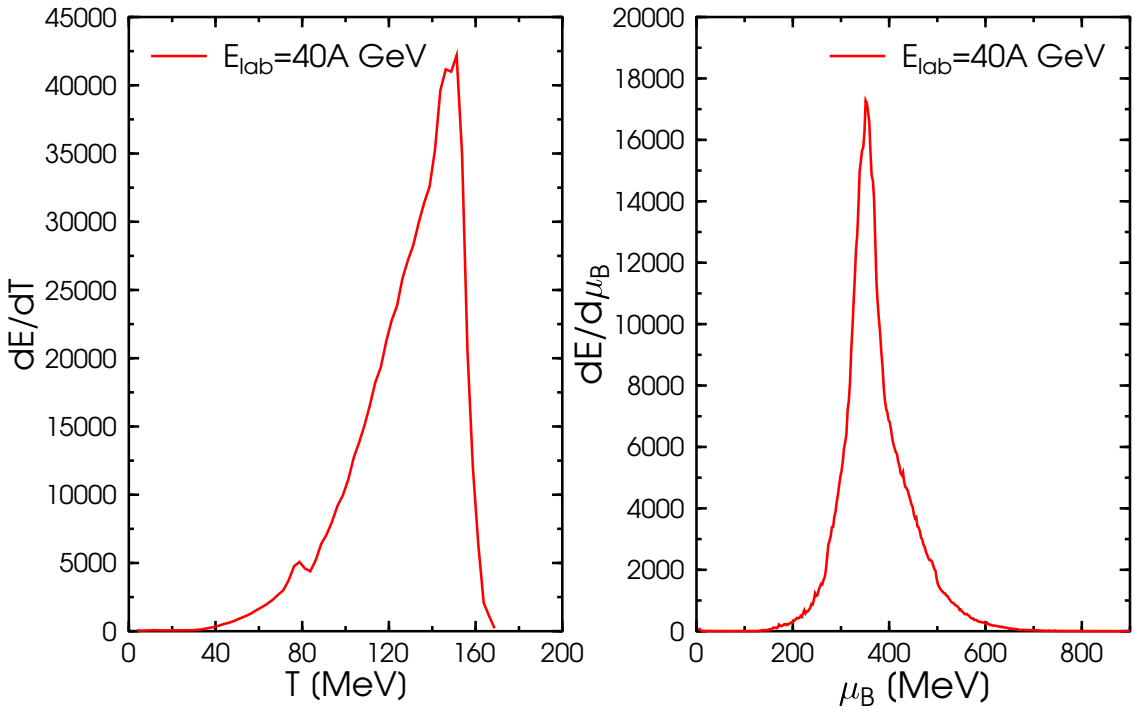

Figure 6.5: Distribution of the energy in the cells at freeze-out at $E_{\rm lab} = 40A$ GeV.

baryon number density ρ_B has been used as a weighting factor.

To illuminate this finding in more detail, Fig. 6.6 shows the mean values of the temperature and baryo-chemical potential distributions at different energies in the $T - \mu_B$-plane for central ($b = 0$ fm) Au+Au/Pb+Pb collisions. Also, the widths of the distributions are depicted as "error" bars. Fig. 6.6 shows that the present freeze-out distributions are similar to the parametrized curve for chemical freeze-out as calculated by Cleymans et al. from statistical model fits to final particle multiplicities. The calculation by Dumitru et al. shows mean values as well as widths of temperature and baryo-chemical potential distributions that have been obtained by statistical model fits to final particle yields employing the assumptions of an inhomogeneous freeze-out hypersurface. This calculation also leads to similar values as our calculation.

The effect that the mean temperature at the transition to the transport prescription saturates or even drops down a little at higher beam energies is related to the rapidity distribution of the temperature in the hydrodynamic cells at freeze-out which is shown in Fig. 6.7 for three different beam energies. At low beam energies the midrapidity region coincides with the hottest region at freeze-out. At higher SPS energies the situation changes. The hottest cells are at high rapidities while the midrapidity region has already cooled down well below the temperature of 170 MeV. This problem might be resolved by a different freeze-out prescription on another hypersurface (e.g.,isotherm, iso-ϵ) and

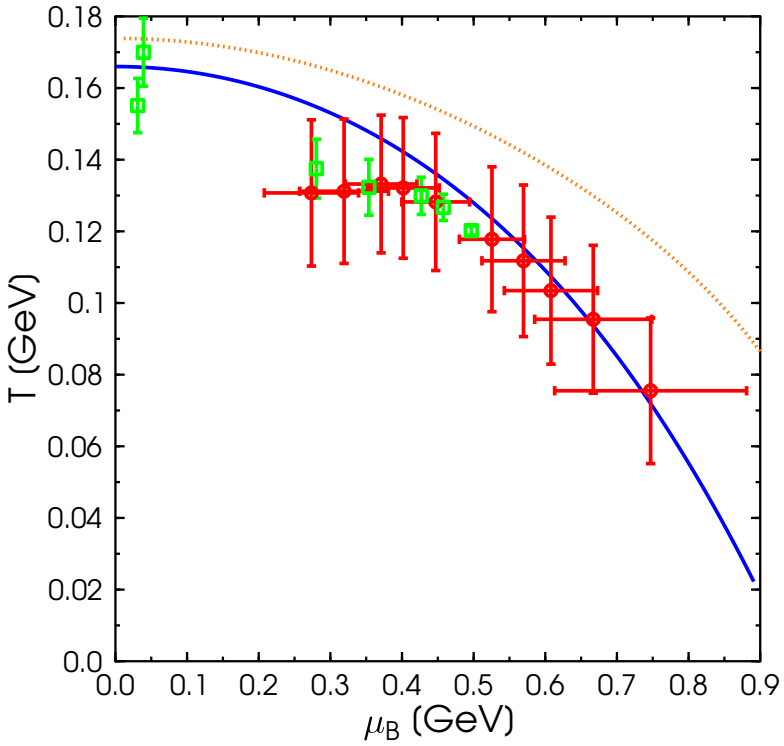

Figure 6.6: Mean values of temperatures and baryo-chemical potentials at freeze-out for different beam energies are depicted as red circles (starting in the lower right corner at $E_{\rm lab} = 2A$ GeV and going through 4,6,8,11,20,30,40 and 80 to $E_{\rm lab} = 160A$ GeV in the upper left). The error bars indicate the width of the distribution. The dotted line depicts the line of constant energy density ($\epsilon = 5 \cdot \epsilon_0$) that corresponds to our freeze-out criterium. For comparison the freeze-out line calculated by Cleymans et al. [Cle98, Cle06] (full line) and results from Dumitru et al. [Dum056](green open squares) are shown.

is subject to the next Section. The best solution will be the dynamical coupling between hydrodynamics and transport which allows also for back-streaming contributions.

In the following the practical implementation will be explained in more detail. The implementation is based on a Monte Carlo sampling of Eqn. 6.7 and follows the general steps:

1. The particle numbers N_i are calculated according to the following formula,

$$N_i = n_i \cdot \gamma \cdot V_{cell} = \int d^3p f_i(x,p) \cdot \gamma \cdot V_{cell} \tag{6.9}$$

where the index i runs over the different particle species like, e.g., π, p, ρ or Δ. γ is the boost factor between the computational frame and the cell. V_{cell} is

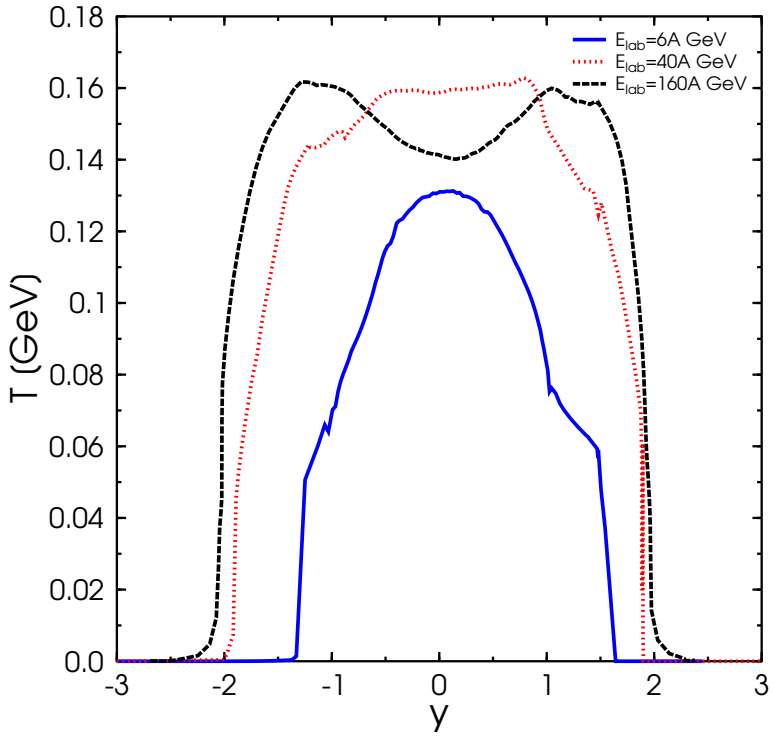

Figure 6.7: Rapidity profile of the freeze-out temperatures in the spatial plane with $x = y = 0$ fm for central Au+Au/Pb+Pb collisions at three different beam energies ($E_{\mathrm{lab}} = 6,\ 40$ and $160A$ GeV).

the volume of the cell in the computational frame and n is the particle number density. All cells with temperatures that are lower than 3 MeV are discarded from the following procedure because of numerical reasons. The local rest frame equilibrium distribution function is denoted by $f_i(x, p)$. To simplify the calculation, a relativistic Boltzmann distribution is used for all particles, except pions. It has been checked, that the Boltzmann approximation is sufficient to describe all particle species it is applied to. For the Boltzmann distribution the momentum integration leads to the following result for the particle number density

$$n_i = \frac{4\pi g m^2 T}{(2\pi)^3} \exp\left(\frac{\mu}{T}\right) K_2\left(\frac{m}{T}\right) \tag{6.10}$$

where g is the degeneracy factor for the respective particle species, m is the mass of the particle to be produced, T the temperature of the cell and K_2 is the modified Bessel function. The detailed calculation that leads to this result can be found in Appendix E. The chemical potential μ includes the baryo-chemical potential and the strangeness chemical potential in the following way

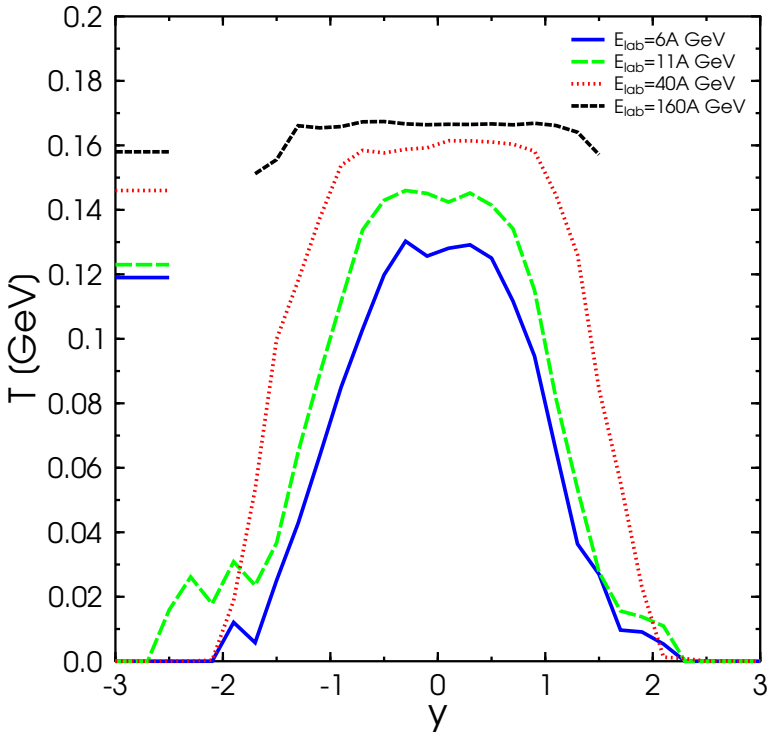

Figure 6.8: Rapidity profile of the freeze-out temperatures in the spatial plane with $x = y = 0$ fm for central Au+Au/Pb+Pb collisions at four different beam energies ($E_{\mathrm{lab}} = 6,\ 11,\ 40$ and $160A$ GeV). The small lines on the temperature axis indicate the corresponding chemical freeze-out temperature as extracted from [Cle06].

$$\mu = B \cdot \mu_B + S \cdot \mu_S \tag{6.11}$$

where S is the quantum number for strangeness and B is the baryon number.

For pions the Bose distribution has to be taken into account because the pion mass is on the order of the temperature of the system. In this case, the momentum integration involves an infinite sum over modified Bessel functions

$$n_\pi = \frac{g_\pi m_\pi^2 T}{(2\pi)^2} \sum_{k=1}^{\infty} \frac{1}{k} K_2\left(\frac{k m_\pi}{T}\right) . \tag{6.12}$$

To calculate the number of particles in the computational frame the particle number density has to be multiplied with the Lorentz-stretched volume of the cell ($V_{\mathrm{cell}} = (0.2)^3 \mathrm{fm}^3$).

2. The average total number of particles in the cell, $\langle N \rangle$, is the sum over all particle numbers $N_i = n_i \gamma V_{\text{cell}}$

$$\langle N \rangle = \sum_i N_i \,. \tag{6.13}$$

3. The total number of particles emitted from a cell, N, is obtained from a Poisson distribution according to $P(N) = \frac{\langle N \rangle^N}{N!} e^{-\langle N \rangle}$.

   In the limit of small mean values, the Poisson distribution becomes $P(1) \approx \langle N \rangle$. Thus it can be decided by one random number between 0 and 1 if a particle is produced in the respective cell. If the random number is smaller than $\langle N \rangle$ one particle is produced and there is no particle production otherwise. The full Poisson distribution is used, if the particle number $\langle N \rangle$ is larger than (0.01). This assures an accuracy better than 1 %.

4. The particle type is chosen according to the probabilities $N_i / \langle N \rangle$.

5. The I_3 component of the isospin is distributed randomly because UrQMD assumes full isospin symmetry. To conserve the overall charge of the system and the initial isospin-asymmetry the probability to generate the isospin component that leads to the right value of the charge that should be obtained in the end is favoured. The other isospin components are exponentially suppressed. The power of the exponential is proportional to the difference of the total charge generated by this produced particle and the required value.

6. The 4-momenta of the particles are generated according to the Cooper-Frye equation (see Eqn. 6.7). For baryons and strange mesons the chemical potentials for baryon number and strangeness are taken into account. To use the rejection method in an efficient way the maximum of the distribution must be calculated (see Appendix F).

7. The particle vector information is transferred back into the UrQMD model. The subsequent hadronic cascade calculation incorporates important final state effects as, e.g., rescatterings of the particles and resonance decays.

The above mentioned steps are pursued on random cells until the initial net baryon number is reached. Strangeness and charge are also conserved in each event separately, energy conservation is fulfilled for the mean values averaged over several events. Aiming at a realistic description of heavy ion reactions we perform the freeze-out for each event separately and do not average over many freeze-outs for one hydrodynamical evolution.

6.4.2 Gradual Freeze-Out

Another freeze-out procedure has been introduced to account for the large time dilatation that occurs for fluid elements at large rapidities. Faster fluid elements need a longer time to cool down to the same temperatures than the cells at midrapidity since the

hydrodynamic calculation is performed in the center-of-mass frame of the collision. At higher energies the isochronous hypersurface increasingly differs from an iso-τ hypersurface (τ is the proper time). To mimic an iso-τ hypersurface we therefore freeze out transverse slices, of thickness $\Delta z = 0.2$fm, whenever all cells of that slice fulfill our freeze-out criterion. For each slice we apply the isochronous procedure described above separately. By doing this we obtain a rapidity independent freeze-out temperature even for the highest beam energies (see Fig. 6.8). The midrapidity transition temperatures are slightly larger than the chemical freeze-out temperatures that have benn parametrized by Cleymans et al. [Cle06] because in our case the chemical freeze-out happens during the following cascade evolution. For lower energies ($E_{lab} \lesssim 80A$ GeV) the two procedures yield very similar results for the temperature distributions. The hydrodynamic fields are then again mapped to particle degrees of freedom via the Cooper-Frye equation on this new hypersurface. In the following we will refer to this procedure as "gradual freeze-out"(GF).

In the following Sections the hybrid approach has been applied using the hadron gas EoS and the isochronous freeze-out procedure.

7 Test Scenarios

7.1 Parameter Tests

In this Section we investigate the dependences of observables on parameters of the implementation. Two important parameters have to be determined. The first one is the starting time t_{start} which defines the initial switch from UrQMD to the hydrodynamic evolution. The second parameter is the freeze-out criterion which is parametrized as an energy density criterion. While varying one parameter we have fixed the other one to the default value ($1 \cdot \ t_{start}$ or $5 \cdot \epsilon_0$).

Fig. 7.1 (left,top) shows calculations of the total, i.e. pion and kaon (4π) multiplicities, for four different starting times at two beam energies. The open symbols depict always the result at the highest AGS energy ($E_{\rm lab} = 11A$ GeV) and the filled symbols are the results at the SPS energy ($E_{\rm lab} = 40A$ GeV). The starting time is varied in factors of the default value that has been calculated via Eqn. 6.1. Displayed are results from halved to doubled initial time. One observes a higher pion production for earlier starting times compared to the pion production in the standard setup (1 $t_{\rm start}$). This may be explained by the fact that the system is forced more strongly to equilibrium and the cascade evolution lasts longer. If the hydrodynamic evolution is started at later times (1.5 or 2 t_{start}) the resulting pion multiplicities are not affected anymore. The kaon yield is essentially not sensitive to the switching time. To summarize, varying the starting time by a factor of 4 results in a change in the pion and kaon production of less than $\pm 10\%$ compared to the pion and kaon production in the default configuration (1 $t_{\rm start}$). In Fig. 7.1 (left,bottom) the mean transverse mass of pions and kaons at midrapidity is shown. The mean transverse mass values are calculated for the same four different starting times at the two exemplary beam energies as before. Here the results do also not change more than $\pm 15\%$ for a large spectrum of starting times. Therefore, our choice of the starting time as the geometrical criterium when the nuclei have passed through each other is sensible and stable. It is the earliest possible time where thermalization may have been achieved and the baryon currents have disconnected.

Fig. 7.1 (right,top) is the equivalent picture to Fig. 7.1 (left,top), however displaying the dependence of the total pion and kaon multiplicities on the freeze-out criterion. The default value for the transition energy density is $5\epsilon_0$ while we have varied it from $(4 - 10)\epsilon_0$. The higher the freeze-out energy density the earlier the hydrodynamic evolution is stopped because the cells reach this critical energy density value earlier. As a consequence the kaon yields raises with an increase of the energy density criterium,

while the pions remain virtually unchanged for all investigated transition criteria.

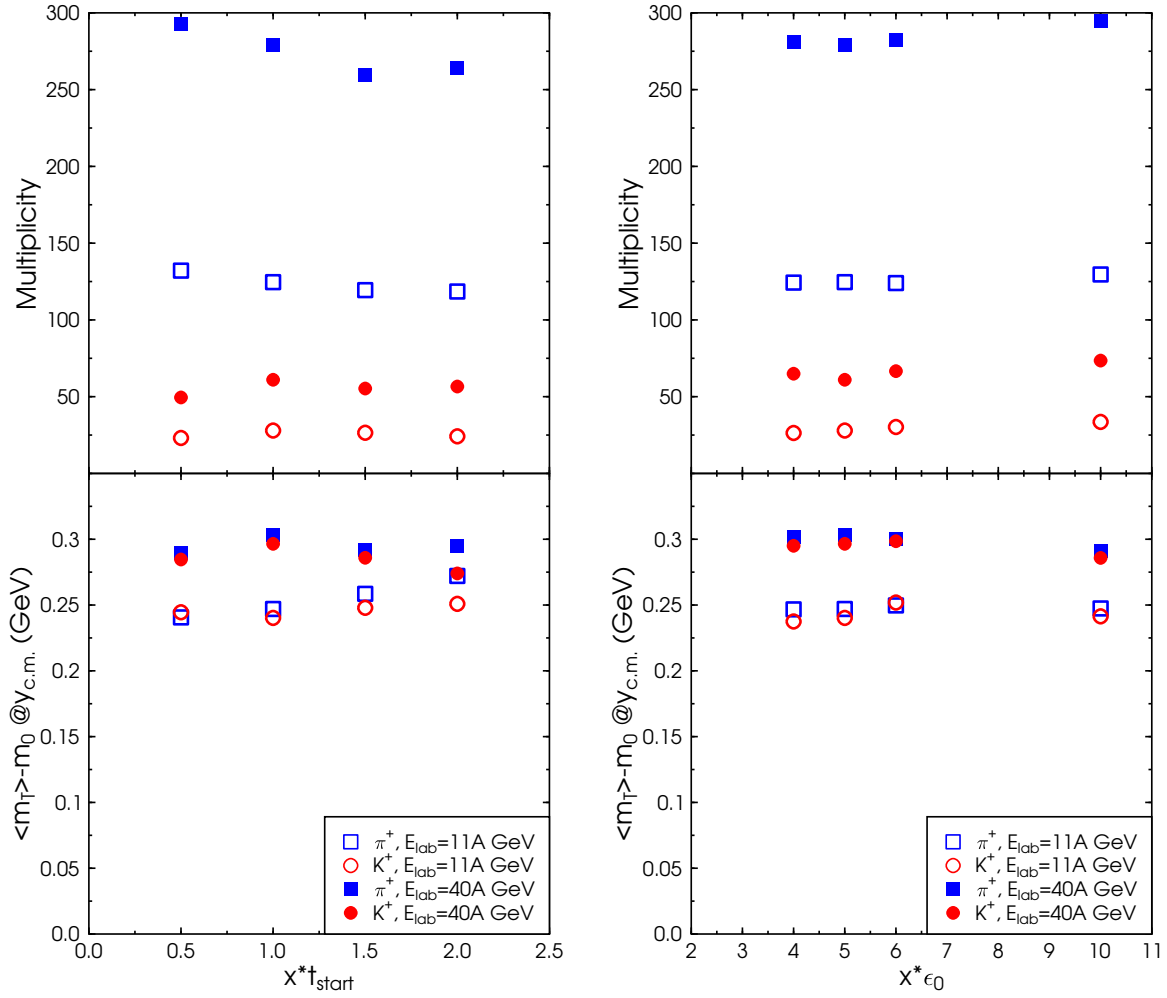

Figure 7.1: Pion and kaon multiplicities (upper panel) and mean transverse mass of pions and kaons at midrapidity ($|y| < 0.5$) (lower panel) for four different starting times/four four different freeze-out criteria (left/right) for central ($b < 3.4$ fm) Au+Au/Pb+Pb collisions. The open symbols depict the result at $E_{\mathrm{lab}} = 11A$ GeV while the filled symbols are the results at $E_{\mathrm{lab}} = 40A$ GeV.

Fig. 7.1 (right,bottom) shows the results for the pions and kaons mean transverse mass for two beam energies and different freeze-out criteria. Again one observes only a very weak dependence on the freeze-out criterion. Furthermore, the mean transverse mass values for the two different meson species are very similar since they acquire the same transverse flow. These findings confirm that our choice for the freeze-out criterium as $5\epsilon_0$ is robust.

7.2 Timescales

In this Section the time scales that are important will be explored. Let us start with a table that summarizes the mean durations of the hydrodynamic and the hadronic phase of the collision for different starting times and freeze-out parameters at $E_{\rm lab} = 40A$ GeV.

$x \cdot t_{start}$	$x \cdot \epsilon_0$	$\langle t_{hydro} \rangle$ [fm]	$\langle t_{hadronic} \rangle$[fm]
1	4	7.68	15.63
1	5	7.72	16.07
1	6	6.84	16.49
1	10	4.60	17.29
0.5	5	7.03	14.59
1.5	5	6.22	17.50
2	5	4.91	17.61

Table 7.1: This table contains the mean durations of the hydrodynamic evolution and the hadronic calculation afterwards for different starting times and freeze-out criteria for central ($b < 3.4$ fm) Pb+Pb collisions at $E_{\rm lab} = 40A$ GeV.

The duration of the hydrodynamic evolution is a well-defined period for each event because of the isochronous freeze-out. The average is therefore an average over 100 events. The hadronic stage starts when the hydrodynamic evolution is stopped and it ends when the particles have undergone their last interaction. An interaction can be an inelastic or an elastic collision or a decay.

The averaged time duration of the stages of the reaction (given in Table 7.1) reflect the expectations. The lower the freeze-out energy density the later the hydrodynamic freeze-out proceeds and therefore the hydrodynamic evolution lasts longer while the hadronic stage is shortened. The later the hydrodynamic evolution starts, the bigger t_{start} is, the shorter the hydrodynamic evolution lasts. The hadronic phase does not show a clear trend. To first approximation the final UrQMD stage lasts for 16.5 ± 2 fm independent of the parameters.

Fig. 7.2 shows the beam energy dependences of the timescales for the chosen values of t_{start} and the freeze-out energy density, from $E_{\rm lab} = 2 - 160A$ GeV. The starting time decreases as a function of beam energy from more than 10 fm at low energies to less than 2 fm at higher SPS energies. The mean duration of the hydrodynamic as well as the hadronic phase of the reaction grow with raising energy.

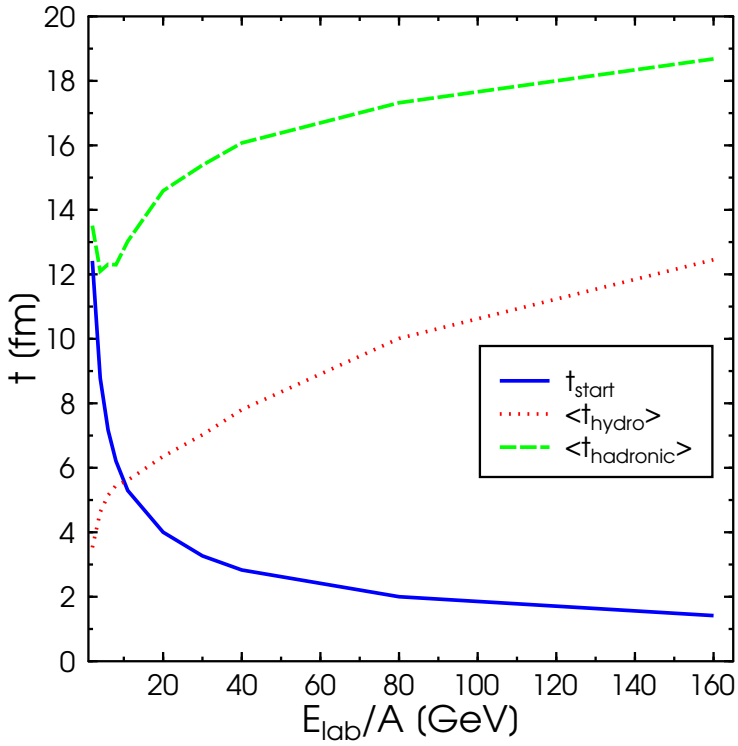

Figure 7.2: Beam energy dependence of the starting time t_{start} (blue full line), the averaged time for the hydrodynamic evolution $\langle t_{hydro} \rangle$ (red dotted line) and the mean duration of the hadronic stage $\langle t_{hadronic} \rangle$ (green dashed line) of central ($b < 3.4$ fm) Au+Au/Pb+Pb collisions.

7.3 Time Evolution

In the following Section we investigate the time evolution of different quantities and compare the results of the hybrid model calculation to the UrQMD calculation without an hydrodynamic stage. Since the net baryon density is directly propagated on the hydrodynamic grid, it serves as a good example to compare to the default UrQMD calculation. In the microscopic approach the local rest frame density is calculated as the zero component of the net baryon number current in the frame where the corresponding local velocity vanishes as it has been explained in Chapter 5 [Vog08b].

Fig. 7.3 shows the time evolution of the net baryon number density at the center of a central Pb+Pb collision at $E_{\text{lab}} = 40A$ GeV. The blue full line depicts the default UrQMD calculation while the red full line depicts the result of the hybrid model calculation. The result has some spikes because here we compare single events. There are two important observations: The absolute values of the net baryon number densities

are very similar in both cases and there are no obvious discontinuities at the switching points to and from the hydrodynamic model calculation. The smoothness of the curve confirms our choice of parameters.

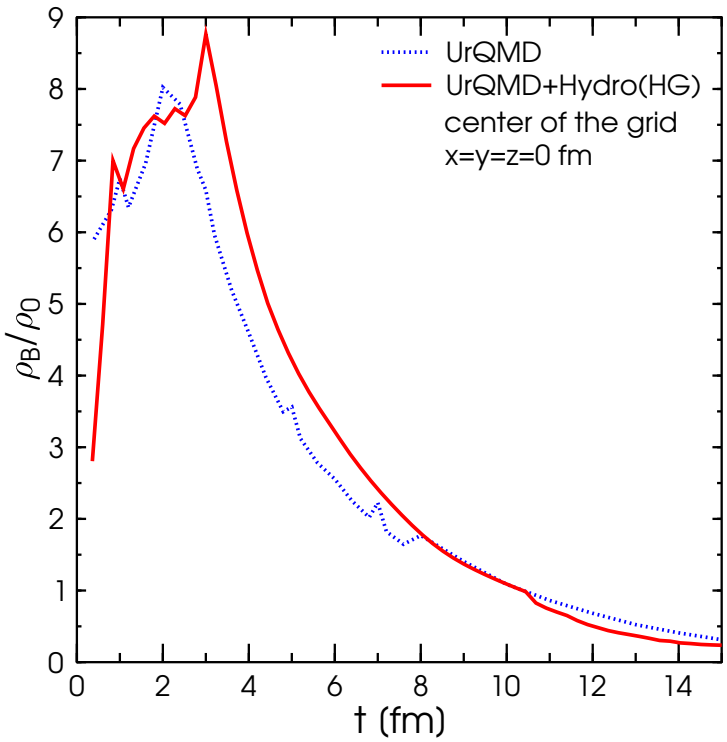

Figure 7.3: Time evolution of the net baryon number density in the local rest frame for central ($b = 0$ fm) Pb+Pb collisions at $E_{\mathrm{lab}} = 40A$ GeV.

In Fig. 7.4 (top and middle) the time evolution of the particle yields in the two different models for the most central Pb+Pb collisions at $E_{\mathrm{lab}} = 40A$ GeV is compared. The multiplicities at different timesteps are extracted from the hydrodynamic evolution by converting the number densities to particle numbers via the freeze-out procedure (see Section 6.4). Fig. 7.4 (top) depicts the total particle multiplicity (red circles and full line) and the midrapidity multiplicity (blue squares and full line). The full lines indicate the default UrQMD calculation, while the symbols show the results of the hybrid model. The multiplicities increase rapidly in the initial 3 fm/c and then decrease a little, followed by a slower constant raise until the final multiplicity is reached. This qualitative behaviour is very similar in both approaches. The decrease of the multiplicity can be associated with the thermalization because absorption and production processes are on the same order. Note again that there are no discontinuities at the switching times in the hybrid calculation.

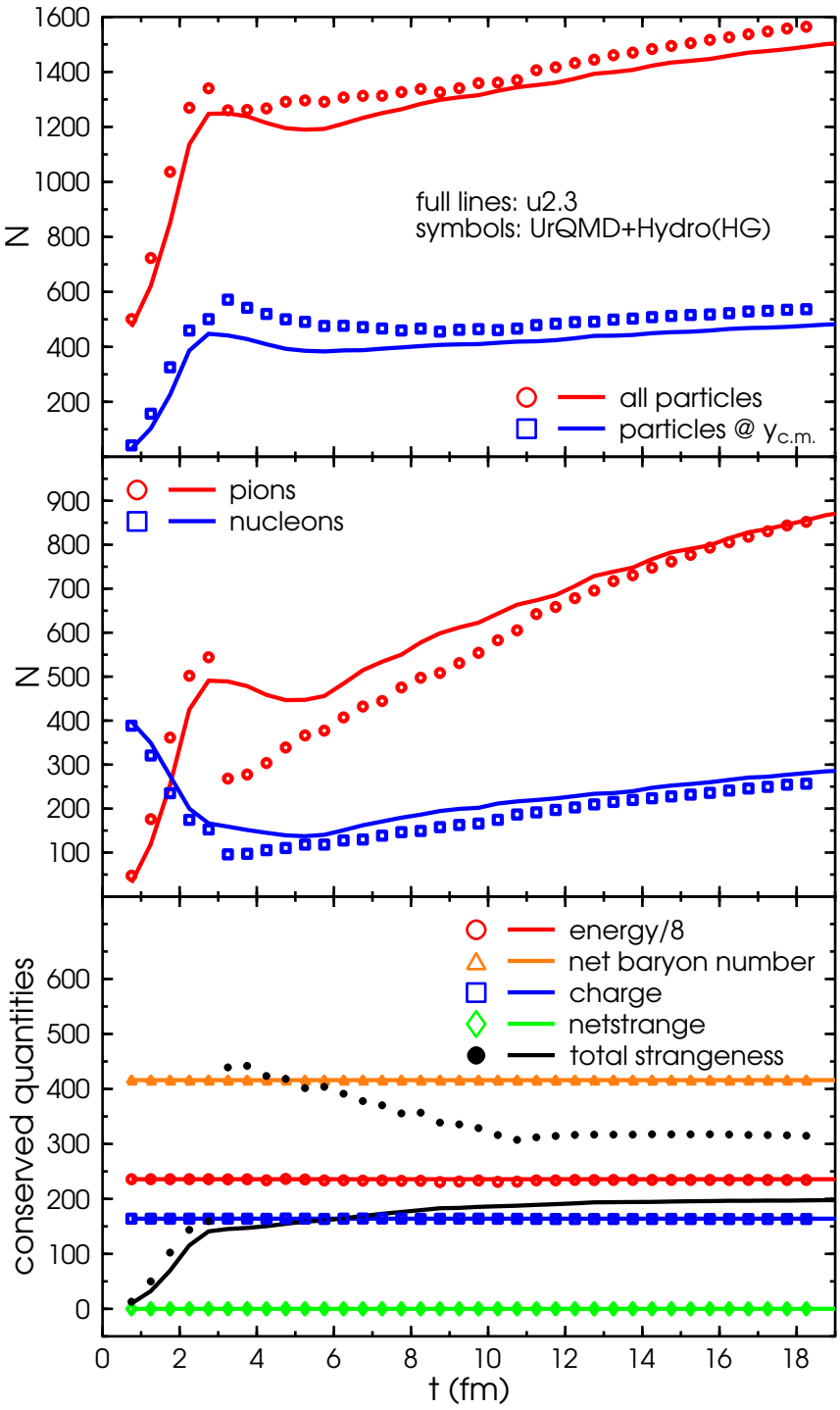

Figure 7.4: Time evolution of the total particle number and the midrapidity ($|y| < 0.5$) yield (upper panel), of the total number of pions and nucleons (middle panel) and of the conserved quantities (lower panel) for central ($b = 0$ fm) Pb+Pb collisions at $E_{\mathrm{lab}} = 40A$ GeV. Results of the hybrid model calculation UrQMD+Hydro (HG) are depicted with symbols while UrQMD-2.3 results are represented by lines. The total energy of the system (red circles and line) has been divided by eight for visibility reasons. The other conserved quantum numbers are net baryon number (orange triangles and line), the overall charge (blue squares and line) and the strangeness (green diamonds and line). The total strangeness (black dots and line) is given by the sum of s- and $\bar{s}$-quarks.

Next, we explore the time evolution for two particle species in more detail. In Fig 7.4 (middle), the pions (red circles and full line) represent the newly produced particles while the nucleons (blue squares and full line) are already there in the beginning as the constituents of the two incoming nuclei. The qualitative behaviour of the temporal evolution of the pion yield is similar to that discussed above for the total multiplicity. The decrease at the starting time of the hydrodynamic evolution $t \sim 3$ fm/c is much stronger than in the model without hydrodynamic phase, because of the instant thermalization at the transition time. The default UrQMD transport calculation results in a similar, but much smoother, shape of the curve. This similarity hints to the fact that the microscopic calculation also equilibrates the hot and dense matter to a rather large degree. The number of nucleons decreases in the beginning due to the production of resonances and string excitations. At the thermalization the minimum is reached and the number of nucleons increases slowly until the final value is reached. In this case, not only the qualitative behaviour is independent of the underlying dynamics but also the absolute values are very close to each other.

To check quantum number and energy conservation the temporal evolution of all the important quantities in both approaches for central Pb+Pb collisions at $E_{\rm lab} = 40A$ GeV is depicted in Fig. 7.4 (bottom). The default UrQMD calculations are indicated by full lines while the hybrid model calculations with integrated hydrodynamic evolution are depicted by symbols. The net baryon number (orange triangles and full line), the charge (blue squares and full line) and the net strangeness (green diamonds and full line) are exactly conserved in both approaches. The total energy (red circles and full line) is only on average over several events conserved in the hybrid model calculation due to the freeze-out prescription. But the fluctuations are on a 5% level. Note however, that the total strangeness in the system ($s + \bar{s}-$ quarks) is very different in both approaches. In the default transport calculation (black line) the total strangeness increases in the early stage of the collision and remains constant. This is contrasted by the hybrid calculation (dots). Due to the local thermal equilibration and the thermal production of strange particles in the hybrid calculation the yield of strange quarks jumps to a higher value at the switching time (t_{start}). The total strangeness then decreases as the system cools down, but the final value remains 50% higher than in the default transport calculation.

7.4 Final State Interactions

The last step is the analysis of the freeze-out process, i.e. how much hadronic interactions happen after the hydrodynamic evolution. For this purpose, we have calculated the number of collisions during the hadronic cascade calculation in dependence of time and $\sqrt{s}$ of the elementary collisions. The corresponding distributions are shown in Figs. 7.5 and 7.6, respectively, for three different beam energies (11, 40 and 160A GeV, from top to bottom).

Fig. 7.5 shows the collision rates for meson-meson, meson-baryon and baryon-baryon

interactions. The grey area indicates the average time span of the hydrodynamic phase. One observes that substantial collision rates are present directly after the transition to UrQMD. The collision rates stay high for 5 fm/c, and after 30-40 fm/c the system is completely frozen out. Only some resonance decays proceed for longer. According to the composition of the system the baryon-baryon and baryon-meson interactions dominate the lower beam energy result, while at the highest SPS energy the meson-meson together with the meson-baryon interactions are the most abundant type of collision indicating the transition from baryon dominated to meson dominated systems. Note that the overlap of the hadronic interaction phase with the hydrodynamic evolution results from the fact that the duration of the different stages fluctuates in the present approach. Shown here is the average duration of the hydrodynamic evolution.

Fig. 7.6 shows the $\sqrt{s}$ distribution of the elementary collision in the freeze-out process. One nicely observes all the resonance peaks in the corresponding channels. This figure suggests that the most abundant meson-baryon collisions are excitations of the Δ resonance (i.e. πN interactions) since there is a sharp peak at the Δ mass ($m_\Delta = 1.232$ GeV). For meson-meson reactions the ρ and the ω peaks are clearly present. This result indicates that there is still resonance regeneration even at this late stage of the system's evolution.

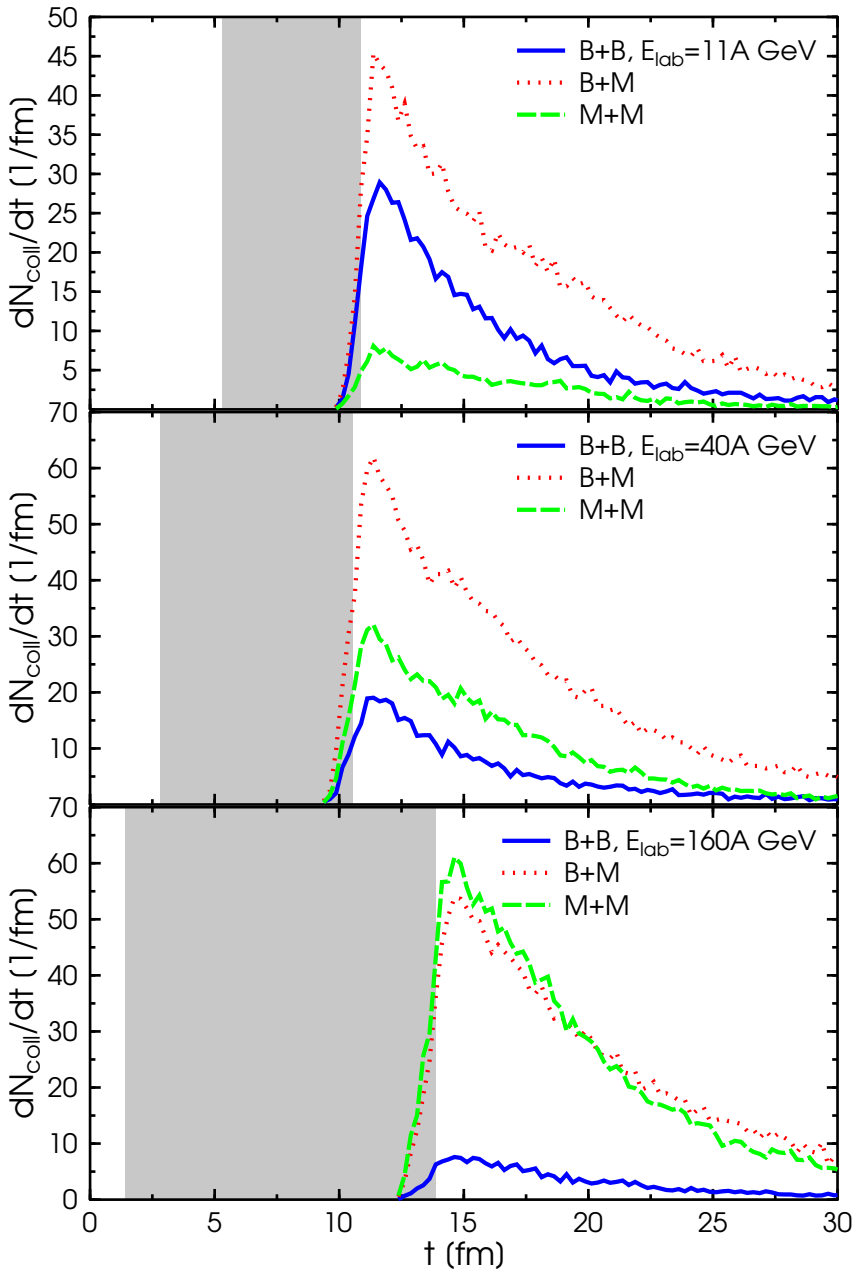

Figure 7.5: Temporal distribution of binary collisions in the hadronic cascade calculation after the hydrodynamic evolution. The upper plot depicts the result at $E_{\rm lab} = 11A$ GeV, the middle plot at $E_{\rm lab} = 40A$ GeV and the lowest plot at the highest SPS energy ($E_{\rm lab} = 160A$ GeV) for central ($b < 3.4$ fm) Au+Au/Pb+Pb collisions. The full line refers to baryon-baryon collisions (B+B), the dotted line to baryon-meson collisions (B+M) and the dashed line to meson-meson collisions (M+M). The grey shaded area depicts the averaged duration of the hydrodynamic evolution.

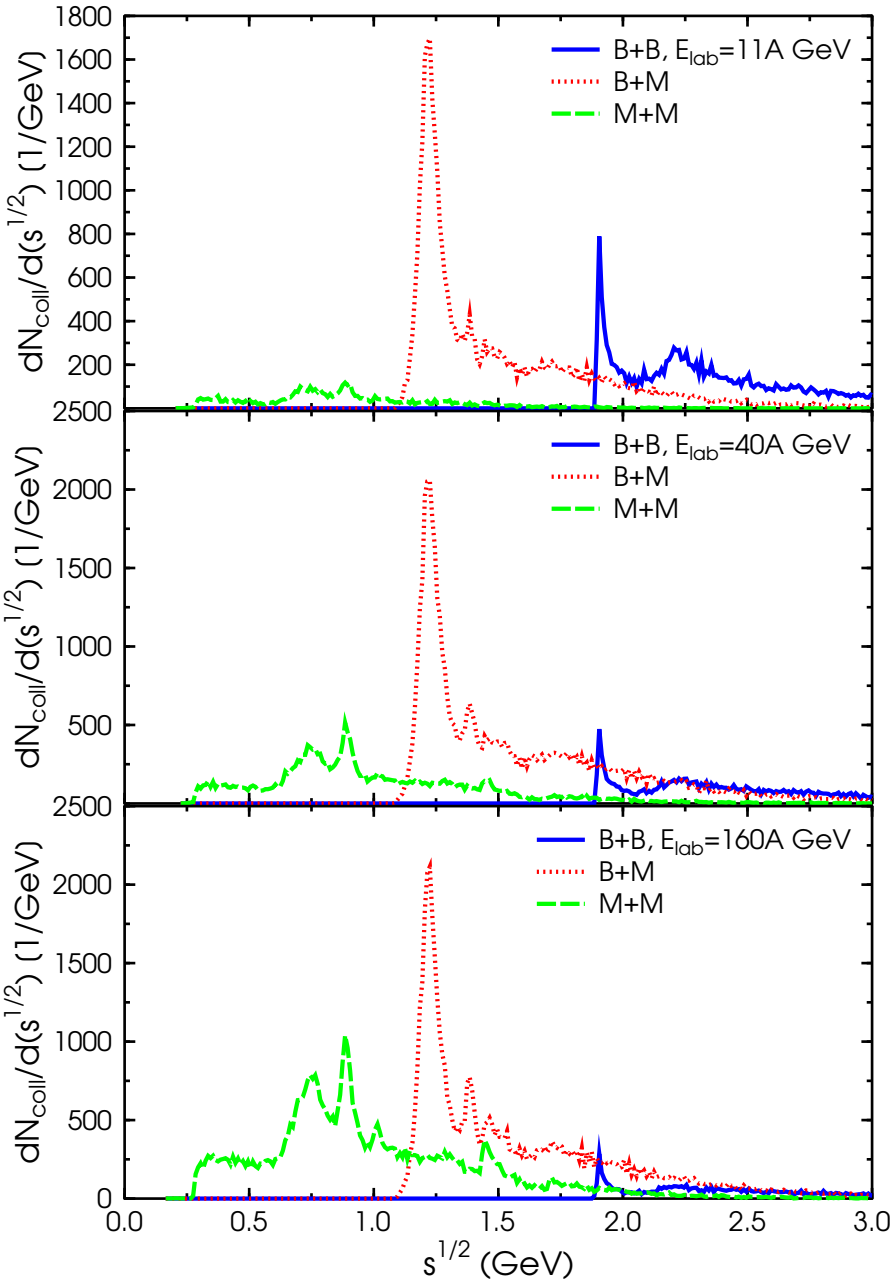

Figure 7.6: Distribution of the $\sqrt{s}$ values for the binary collisions in the hadronic cascade calculation after the hydrodynamic evolution. The upper plot depicts the result at $E_{\mathrm{lab}} = 11A$ GeV, the middle plot at $E_{\mathrm{lab}} = 40A$ GeV and the lowest plot at the highest SPS energy ($E_{\mathrm{lab}} = 160A$ GeV) for central ($b < 3.4$ fm) Au+Au/Pb+Pb collisions. The full line refers to baryon-baryon collisions (B+B), the dotted line to baryon-meson collisions (B+M) and the dashed line to meson-meson collisions (M+M).

8 Multiplicities and Particle Spectra

8.1 Bulk Multiplicities

We start with a comparison of the multiplicities and particle spectra in the two frameworks [Pet08d]. Calculations with the embedded hydrodynamic evolution employing a hadron gas equation of state for the high density stage of the collisions are compared to the reference results of the default transport calculation (UrQMD-2.3). Since both calculations use the same initial conditions and freeze-out prescription it allows to extract, which observables are sensitive to the change in the underlying dynamics, thus allowing to explore the effect of local equilibration, of viscosities and heat conductivity. The hybrid model calculation is in the following always depicted as full lines while the default UrQMD-2.3 calculations are depicted as dotted lines. Note that we do not tune any parameters for different energies or centralities for the hybrid model calculation. The starting time for the hydrodynamic expansion is always calculated using Eqn. 6.1 and the fixed energy density criterium ($5\epsilon_0$) for the freeze-out (as explained in Section 6.4) is always employed.

At present we have calculated results imposing a hadron gas EoS to provide a baseline calculation to disentangle the effects of the different assumptions for the underlying dynamics in a transport vs. hydrodynamic calculation. The purely hadronic calculations can be compared in the broad energy regime from $E_{\rm lab} = 2 - 160A$ GeV where a vast amount of experimental data from BNL-AGS and CERN-SPS exists and which will be explored in more detailed energy scans by the FAIR project near GSI and the critRHIC program. Studies employing different EoS are delayed to future work to concentrate on effects of the underlying dynamics first.

In Fig. 8.1 the excitation functions of the total multiplicities are shown for central Au+Au/Pb+Pb collisions for $E_{\rm lab} = 2 - 160A$ GeV. The present hybrid approach simulations have been restricted to this energy range because for calculations at higher energies some numerical subtleties have to be resolved, e.g. a dynamical grid size for the hydrodynamical evolution. Compared to the default simulation, the pion and proton multiplicities are decreased over the whole energy range in the hybrid model calculation due to the conservation of entropy in the ideal hydrodynamic evolution. The non-equilibrium transport calculation produces entropy and therefore the yields of non-strange particles are higher. The production of strange particles however, is enhanced due to the establishment of full local thermal equilibrium in the hybrid model calculation. Since the abundance of strange particles is relatively small they survive the

interactions in the UrQMD evolution that follows the hydrodynamic freeze-out almost without re-thermalization. The abundancies of strange particles, especially of (multi-) strange hyperons is explored in the next Chapter 9.

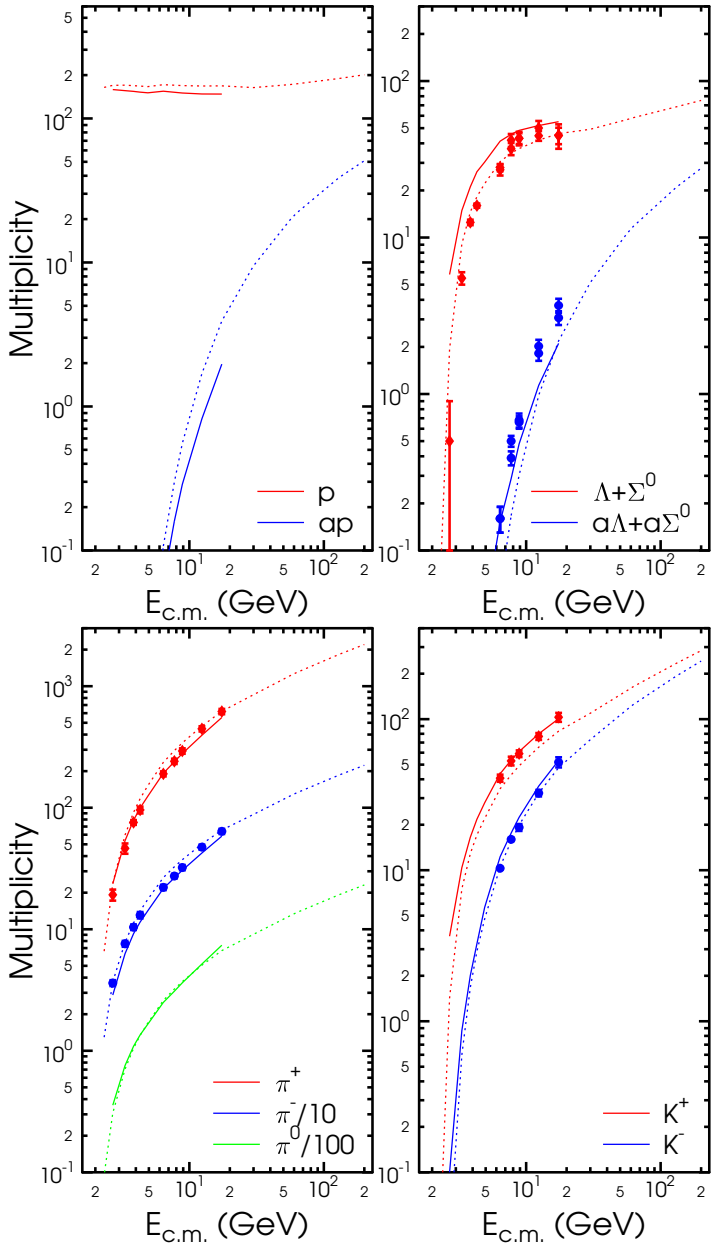

Figure 8.1: Excitation function of particle multiplicities (4π) in Au+Au/Pb+Pb collisions from $E_{\mathrm{lab}} = 2A$ GeV to $\sqrt{s_{NN}} = 200$ GeV. UrQMD+Hydro (HG) calculations are depicted with full lines, while UrQMD-2.3 calculations are depicted with dotted lines. The corresponding data from different experiments [Kla03, Pin02, Chu03, Alt08a, Afa02a, Anc04a, Ric05, Mit06, Alt08c, Blm05, Afa02b] are depicted with symbols.

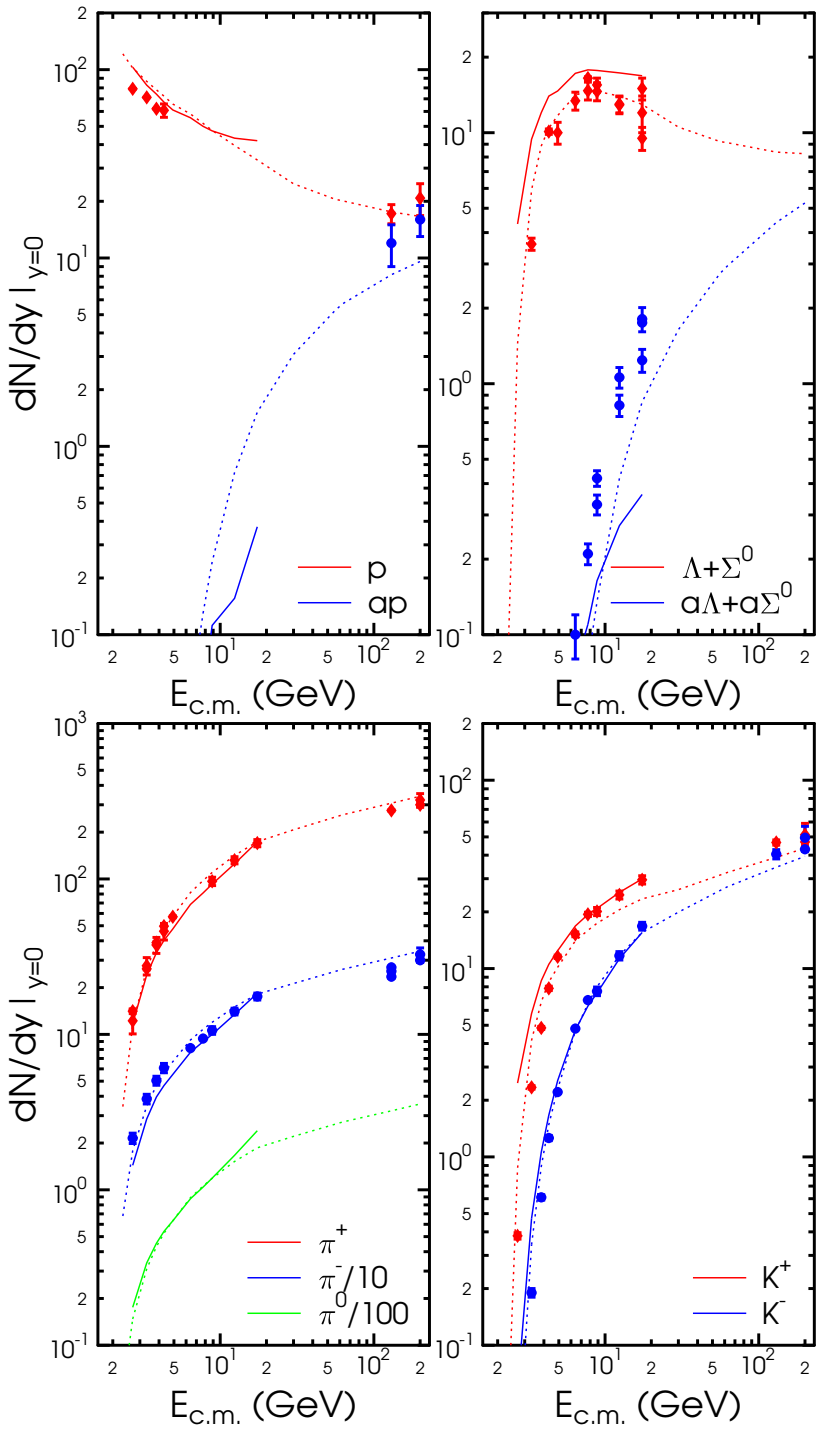

Figure 8.2: Excitation function of particle yields at midrapidity ($|y| < 0.5$) in Au+Au/Pb+Pb collisions from $E_{\mathrm{lab}} = 2A$ GeV to $\sqrt{s_{NN}} = 200$ GeV. UrQMD+Hydro (HG) calculations are depicted with full lines, while UrQMD-2.3 calculations are depicted with dotted lines. The corresponding data from different experiments [Ahl00a, Kla03, Afa02a, Alt08c, Adc04, Lee04, Ahl00b, Oue03, Ahm96, Mis02, Ads04] are depicted with symbols.

Fig. 8.2 shows the midrapidity yields of protons, pions, Λ's and kaons as a function of the beam energy for central Au+Au/Pb+Pb collisions at $E_{\rm lab} = 2 - 160A$ GeV. For pions, kaons and Λ's the same trend as for the 4π multiplicities is observed. There are less pions produced in the hybrid model calculation due to entropy conservation, but more strange particles because of the production according to the local thermal equilibrium distributions. The proton yield at midrapidity is very similar in both calculations while there are less antiprotons produced in the hybrid calculation. Also for the strange antiparticles a reduction of the midrapidity yield in the hybrid calculation at higher SPS energies can be seen.

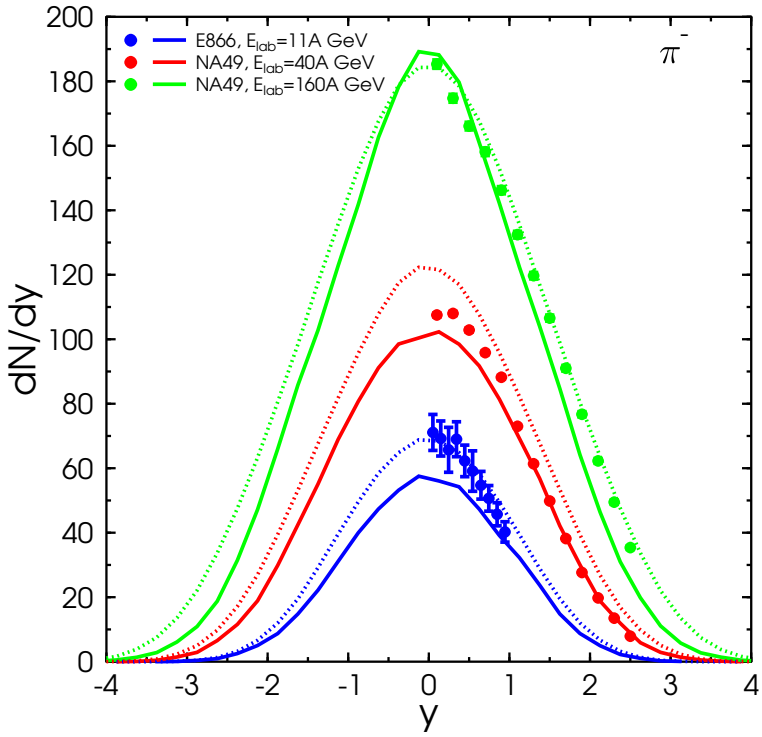

Figure 8.3: Rapidity spectra of π^- for central ($b < 3.4$ fm) Au+Au/Pb+Pb collisions for $E_{\rm lab} = 11, 40$ and $160A$ GeV. UrQMD+Hydro (HG) calculations are depicted with full lines, while UrQMD-2.3 calculations are depicted with dotted lines. The corresponding data from different experiments [Aki96, Afa02a] are depicted with symbols.

To explore the kinetics of the system in more detail, Fig. 8.3 shows the rapidity distribution for π^- at three different energies ($E_{\rm lab} = 11, 40$ and $160A$ GeV). The general shape of the distribution is very similar in both approaches and in line with the experimental data. At higher energies even the absolute yields become very close to each other in both approaches.

Fig. 8.4 shows the K^+ rapidity distributions. In this case, the yield is higher in the

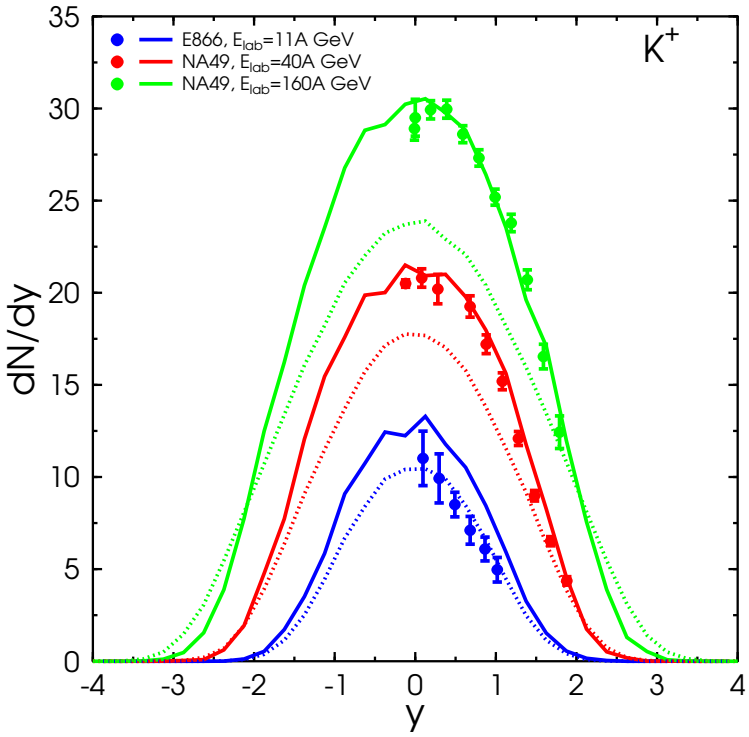

Figure 8.4: Rapidity spectra of K^+ for central ($b < 3.4$ fm) Au+Au/Pb+Pb collisions for $E_{\rm lab} = 11, 40$ and $160A$ GeV. UrQMD+Hydro (HG) calculations are depicted with full lines, while UrQMD-2.3 calculations are depicted with dotted lines. The corresponding data from different experiments [Aki96, Afa02a] are depicted with symbols.

hybrid calculation as already discussed above and also the shape of the distribution fits very nicely to the experimental data at SPS energies. Overall the rapidity distributions seem not to be too sensitive to the details of the dynamics for the hot and dense stage, but strangeness yields are influenced by the local equilibrium assumption. It seems that the local equilibrium assumption provides similar strangeness enhancement as previous calculations including additional strong color fields [Sof99a, Ble00e]. It is remarkable how well the hybrid calculation matches the rapidity spectra at lower energies ($E_{\rm lab} = 11A$ GeV), even though the transport calculation provides a slightly better description to the experimental data at this energy. One might still conclude from the rapidity spectra that the local equilibrium is not a good assumption for AGS energies.

8.2 Transverse Dynamics

After the longitudinal dynamics which reflects more the stopping power in the initial state we turn now to the transverse dynamics of the system. Transverse spectra are a promising candidate to be sensitive to the change in the underlying dynamics because they emerge from the transverse expansion which is mostly dominated by the evolution in the hot and dense stage of the reaction.

Figs. 8.5, 8.6 and 8.7 display the transverse mass spectra for pions, protons and kaons at midrapidity for central Au+Au/Pb+Pb reactions at three different beam energies. At $E_{\mathrm{lab}} = 11A$ GeV (Fig. 8.5) the differential transverse mass spectra are very similar for both calculations and are in line with the experimental data.

At $E_{\mathrm{lab}} = 40A$ GeV (Fig. 8.6) first differences become visible. Most notably is the strong flow of protons in the hybrid approach, that results in an overestimate of protons at high transverse momenta.

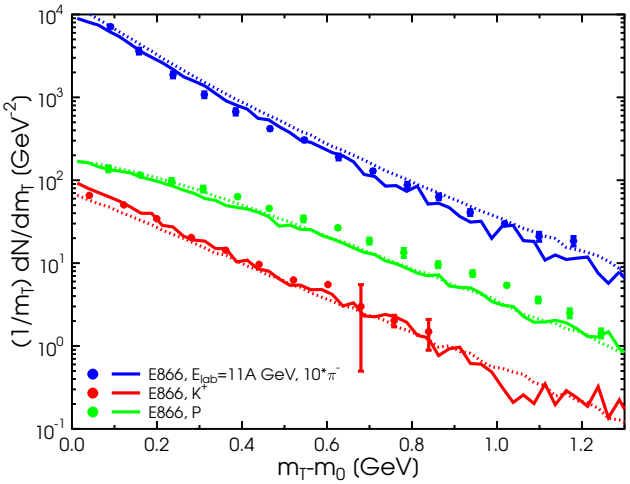

Figure 8.5: Transverse mass spectra of π^-, K^+ and protons at midrapidity ($|y| < 0.5$) for central ($b < 3.4$ fm) Au+Au collisions at $E_{\mathrm{lab}} = 11A$ GeV. UrQMD+Hydro (HG) calculations are depicted with full lines, while UrQMD-2.3 calculations are depicted with dotted lines. The corresponding data from the E866 experiment [Kla03, Ahl00b, Aki96] are depicted with symbols.

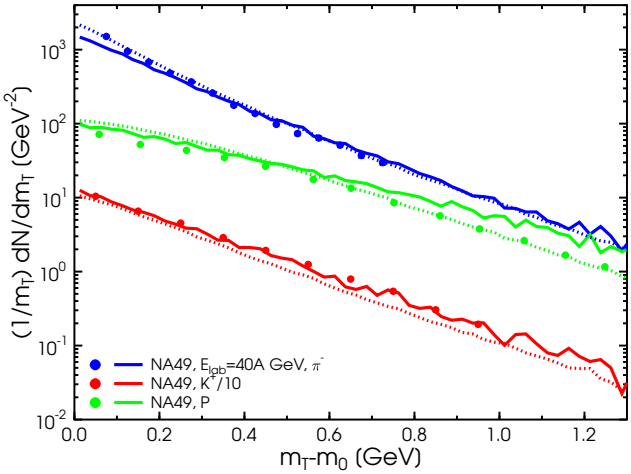

Figure 8.6: Transverse mass spectra of π^-, K^+ and protons at midrapidity ($|y| < 0.5$) for central ($b < 3.4$ fm) Pb+Pb collisions at $E_{\mathrm{lab}} = 40A$ GeV. UrQMD+Hydro (HG) calculations are depicted with full lines, while UrQMD-2.3 calculations are depicted with dotted lines. The corresponding data from the NA49 experiment [Afa02a, Alt06] are depicted with symbols.

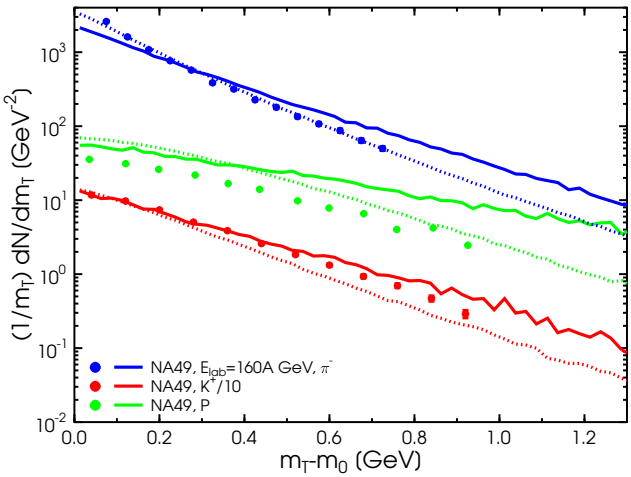

Figure 8.7: Transverse mass spectra of π^-,K^+ and protons at midrapidity ($|y| < 0.5$) for central ($b < 3.4$ fm) Pb+Pb collisions for $E_{\mathrm{lab}} = 160A$ GeV. UrQMD+Hydro (HG) calculations are depicted with full lines, while UrQMD-2.3 calculations are depicted with dotted lines. The corresponding data from the NA49 experiment [Afa02a, Alt06] are depicted with symbols.

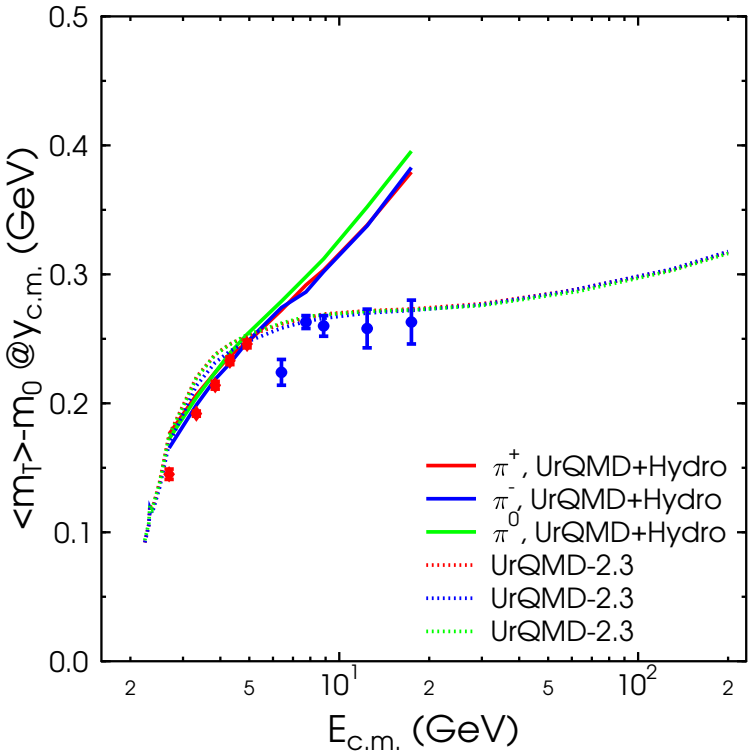

Figure 8.8: Mean transverse mass excitation function of pions at midrapidity ($|y| < 0.5$) for central ($b < 3.4$ fm) Au+Au/Pb+Pb collisions from $E_{\mathrm{lab}} = 2 - 160A$ GeV. UrQMD+Hydro (HG) calculations are depicted with full lines, while UrQMD-2.3 calculations are depicted with dotted lines. The corresponding data from different experiments [Ahl00a, Alt08a, Afa02a] are depicted with symbols.

At the highest SPS energy ($E_{\mathrm{lab}} = 160A$ GeV, Fig. 8.7) all the transverse mass spectra are flatter in the hybrid approach. The initial pressure gradients are higher in the hydrodynamic calculation due to the hadronic equation of state without phase transition. Therefore, the matter expands faster in the transverse plane and higher transverse masses are reached. At this energy either the introduction of a mixed phase (first order phase transition) or non-equilibrium effects are necessary to explain the experimental data.

Fig. 8.8 shows the mean transverse mass excitation function for pions. It confirms the observations from the differential spectra. Up to 10 GeV beam energy the hybrid model calculation leads to similar results as the default UrQMD calculation and is in line with the experimental data. The mean value of the transverse mass of pions is proportional to the temperature of the system and very different in the two calculations at higher energies. The UrQMD approach shows a softening of the equation of state in the region where the phase transition is expected because of non-equilibrium effects, while the hadron gas hydrodynamic calculation continuously rises as a function of the energy. This behaviour is well known, see, e.g., [Sor97] and is investigated in more detail

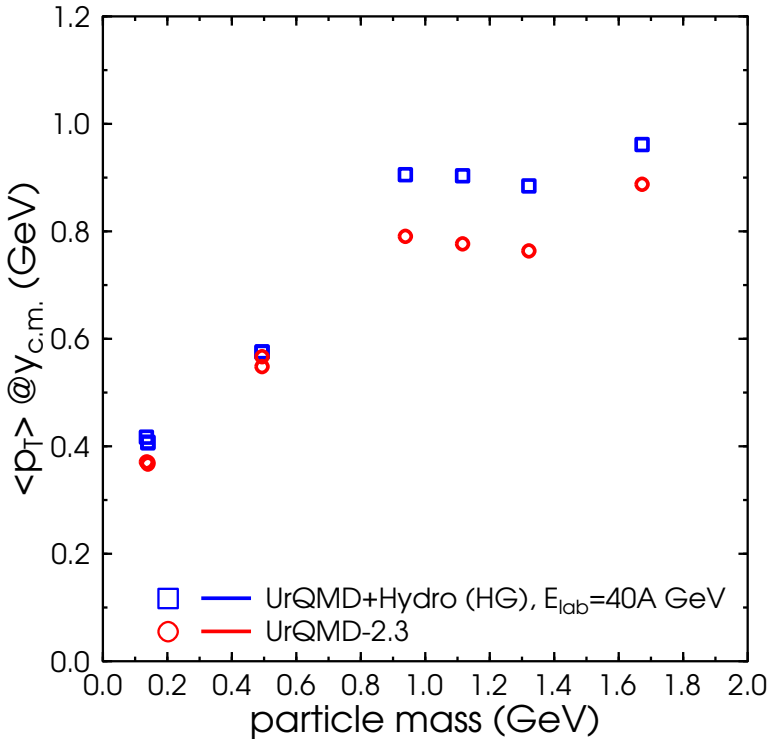

Figure 8.9: Mean transverse momentum at midrapidity ($|y| < 0.5$) as a function of the particle mass for pions, kaons, protons, Λ, Ξ and Ω in central ($b < 3.4$ fm) Pb+Pb collisions at $E_{\mathrm{lab}} = 40A$ GeV. UrQMD+Hydro (HG) calculations are depicted with blue squares, while UrQMD-2.3 calculations are depicted with red circles.

in Chapter 11.

Finally Fig. 8.9 shows the mean transverse momenta as a function of particle mass for π, K, p, Λ, Ξ, and Ω particles. Here we observe the behaviour known from previous hybrid studies, that with increased strangeness, baryons accumulate less flow than in a complete hydrodynamic approach. This effect can be traced back to the small cross sections of multi strange baryons in the hadronic cascade, thus showing, that the freeze-out/decoupling process proceeds gradually.

9 Strangeness Production

9.1 Rapidity Distributions

In this Chapter results on the centrality and system size dependence of (multi-strange) hyperons in Pb+Pb collisions at 40A and 158A GeV from the Ultra-relativistic Quantum Molecular Dynamics (UrQMD-v2.3) model and a coupled Boltzmann+hydrodynamics calculation are presented based on [Pet09c, Ste08c].

The strange (s) and anti-strange ($\bar{s}$) quarks are a well suited diagnostic tool to investigate the properties of the matter created in such collisions, because they are not contained in the colliding nuclei, but are newly produced. At the end of the reaction they show up in strange hadrons in the final state. In [Raf82, Koc86] the authors suggested almost 25 years ago that strange particle production is enhanced in the QGP with respect to a hadron gas. This enhancement can be quantified relative to a reaction where a transition to a QGP phase does not take place, such as p+p collisions where the system size is very small. The enhancement occurs because in the QGP different channels are responsible for strangeness production, leading to a strong reduction of the strangeness thermalization time as compared to the hadronic scenario. This is supported by the difference in threshold energies due to the fact that in a deconfined state, only the strange quarks have to be produced, rather than strange hadrons themselves. In a QGP the strange quarks are produced in gluon fusion ($gg \rightarrow s\bar{s}$) and light $q\bar{q}$ pair annihilation ($q\bar{q} \rightarrow s\bar{s}$) processes. The threshold energy required to create a pair of $s\bar{s}$ quarks in the QGP is just the bare mass of the two strange quarks ($E_{threshold} \approx 2m_s \approx 300$ MeV). Due to high temperatures involved in the QGP phase, the thermal production of $s\bar{s}$ pairs is possible. A further source of enhanced $s\bar{s}$ production comes from the process of Pauli blocking of light quarks. Therefore, as more and more light quarks are produced in the collision, they fill up the available energy levels and it becomes energetically favourable to create $s\bar{s}$ pairs.

It is expected that the extra mechanisms for $s\bar{s}$ production in a QGP should lead to a production rate which is 10 to 30 times higher than in a hadron gas, resulting in an equilibration of strangeness even in the short lifetime of the fireball. Therefore, it is assumed that the production of strange and anti-strange baryons at freeze-out will be enhanced, if the system passes through a deconfined phase, as compared to a system that remained in the hadron gas phase only.

Furthermore, strangeness is a good quantum number because it is conserved in strong interactions. Strange quarks (and therefore strange hadrons) decay via the weak inter-

Production reaction	$E_{Threshold}\ (MeV)$
$N + N \rightarrow \Lambda + K^+ + N$	700
$N + N \rightarrow N + N + \Lambda + \bar{\Lambda}$	2200
$N + N \rightarrow N + N + \Xi^- + \bar{\Xi}^+$	4500
$N + N \rightarrow N + N + \Omega^- + \bar{\Omega}^+$	5200

Table 9.1: The energy threshold to create strange hadrons in hadronic interactions.

action, where typical lifetimes are on the order of 10^{-10} s and so these decays are not important on the time scale of a hadronizing QGP and can be well reconstructed by experiments.

To create strange hadrons in a hadronic interaction a high threshold energy is needed, which is calculated from the differences in masses between the initial and the final state particles as shown in Table 9.1 for N+N → (anti-) hyperons.

Because of these large threshold energies (multi-)strange baryon production is suppressed even in initial collisions in the SPS energy regime ($\sqrt{s_{\rm NN}} \approx$ 5-20 GeV) [Dre02, Ble02b]. A further important source for (multi-strange)hyperon production are multi-step processes that lead to high mass resonance excitations and the rescatterings of initially produced anti-kaons. In regions of high net baryon density, also the production of strange baryons is more likely, especially Λ's are produced in association with a kaon and this reaction has the lowest threshold energy. In a hadron resonance gas it takes some time to equilibrate strangeness and the timescale of a heavy ion collision might be shorter than this equilibration time.

Different approaches to enhance strangeness production in semi-hadronic scenarios without a transition to a deconfined state have been proposed. In [Van99] a baryon junction exchange mechanism was proposed to explain valence baryon number transport in nuclear collisions and hence the production of (anti-)hyperons.

Another ansatz is the introduction of a strong color fields (color ropes) in string-hadronic models by a modification of the Schwinger mechanism [Scw51]. When moving from e^+e^- or $p + p$ interactions to heavy-ion collisions the string density can be so high that the color flux tubes are overlapping [Bir84, Kno88, Sor92, Ame93]. Practically, this results in the non-independent fragmentation of QCD-flux tubes with higher color charge representation, e.g. $\mathbf{8}-\bar{\mathbf{8}}$ strings instead of triplett charges. This implementation of the color electric field increases the production of hyperons.

Using multi-hadronic interactions can bring the system to local chemical equilibrium and enhance the production of anti-hyperons [Gre01]. A similar way to push the system into chemical equilibrium is the multiple interactions of pions [Cas02] or the oversaturation of pion number [Rap01]. Calculations in [BrM04] showed that reaching an equilibrium in a pure hadronic medium, considering collision rates and time scales of the hadronic

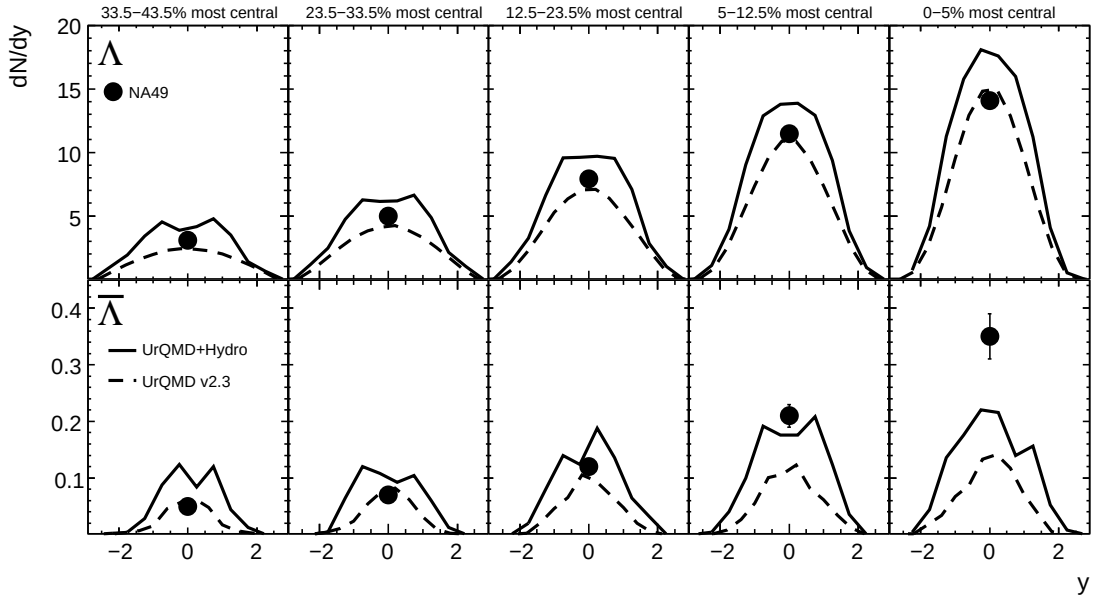

Figure 9.1: The points correspond to the measured yield at midrapidity ($|y| \leq 0.5$) for Λ (top) and $\bar{\Lambda}$ (bottom) from NA49 [Blm07, Mit06] measured for different centralities in Pb+Pb collisions at 40A GeV. The solid line represents calculations with UrQMD+Hydro and the dashed line with UrQMD.

fireball expansion, is only possible if hadronic multi-particle interaction are taken into account. Recently, counter arguments against this conclusion were suggested within a hadronic Hagedorn model [Nor08]. However, the main conclusion remains that close to the QGP phase boundary the densities are large and might drive the system quickly to a chemical equilibrium state.

The apparent enhancement of strangeness can be explained also in statistical models by the transition from a canonical ensemble, for small systems (e.g. like in p+p), which treats charge conservation exactly, to a grand canonical ensemble for heavier systems like Pb+Pb of Au+Au. With this constraint the phase space for particle production is reduced in small systems. To compare this crossover to experimental data the correlation volume V of the system is proportional to $\langle N_w \rangle$ for a constant center-of-mass energy ($V = \frac{V_0}{2} \langle N_w \rangle$ in [Red02], where V_0 is the volume of the nucleon). An alternative approach to determine the correlation volume is suggested in the percolation model [Hoh06]. However, none of the above discussed approaches allows for a consistent description of both spectra and multiplicities of (multi-)strange baryons up to now.

Here we attack this question by using a hadronic transport approach, namely the Ultra-relativistic Quantum Molecular Dynamics (UrQMD) in version 2.3 [Ble99c, Bas98b, Pet08a] (see Chapter 4) and compare the results to a hybrid approach where a hydrodynamic evolution is embedded into the model [Pet08b] (see Chapter 6). By doing this, we do not aim at the understanding of the dynamics of the strangeness equilibration process

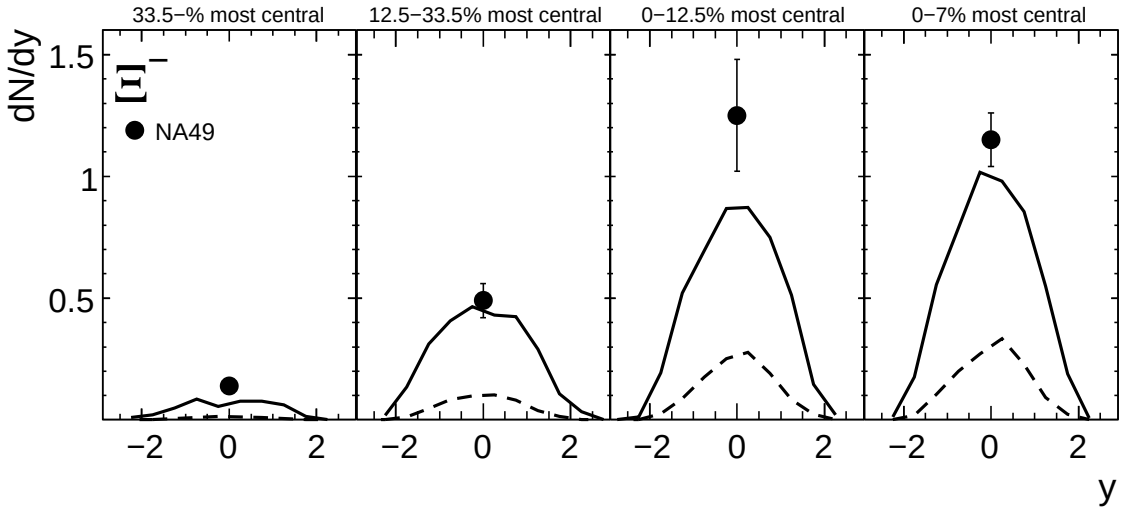

Figure 9.2: The points correspond to the measured yield at midrapidity ($|y| \leq 0.5$) for Ξ^- from NA49 [Alt08c, Blm07, Mit06] measured for different centralities in Pb+Pb collisions at 40A GeV. The solid line represents calculations with UrQMD+Hydro and the dashed line with UrQMD.

itself, but we are able to compare strangeness production in a full non-equilibrium approach with a dynamical approach involving local thermal and chemical (for strangeness) equilibrium. For the present comparison we restrict ourselves to a hadron gas equation of state which includes the same degrees of freedom as in UrQMD. The gradual freeze-out scenario with a transition criterion of $5\epsilon_0$ has been applied.

In the following results from UrQMD and the hybrid approach (UrQMD+Hydro) are shown. We compare these results to the measured total particle yields [1] and the abundancies at midrapidity from the NA49 and NA57 experiments on Pb+Pb collisions. Furthermore, we compare the model predictions to the measured Λ, $\bar{\Lambda}$ and Ξ^- rapidity spectra in central C+C and Si+Si collisions from the NA49 collaboration at 158A GeV. In addition, we present predictions from UrQMD and UrQMD+Hydro for the centrality dependence of Λ, $\bar{\Lambda}$ and Ξ^- rapidity spectra at $E_{\rm lab} = 40A$ GeV and $E_{\rm lab} = 158A$ GeV and compare these to the measured yields at midrapidity ($|y| \leq 0.5$).

Fig. 9.1 and Fig. 9.2 show the rapidity spectra for Λ, $\bar{\Lambda}$ and Ξ^- at $E_{\rm lab} = 40A$ GeV predicted from UrQMD (dashed line) and UrQMD+Hydro (solid line) for different centrality bins. Data are shown as full circles [Alt08c, Blm07, Mit06] [2]. UrQMD predicts a lower multiplicity compared to the hybrid approach. This can be understood, because at the transition from the hydrodynamic evolution to the hadronic cascade the particles are produced according to thermal distributions. In this manner, it is much easier to

[1] Note that only the NA49 has the acceptance to measure the total multiplicity.

[2] We extrapolate the midrapidity yields of the NA49 data for every centrality class of $\bar{\Lambda}$ by using an exponential fit.

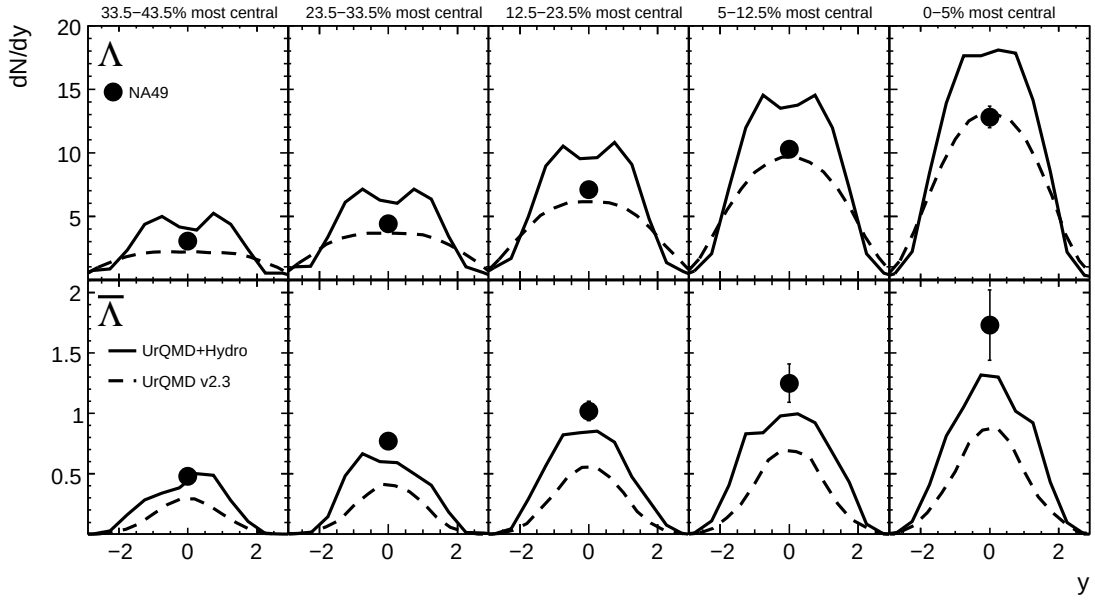

Figure 9.3: The points correspond to the measured yield at midrapidity ($|y| \leq 0.5$) for Λ (top) and $\bar{\Lambda}$ (bottom) from NA49 [Blm07, Mit06] measured for different centralities in Pb+Pb collisions at 158A GeV. The solid line represents calculations with UrQMD+Hydro and the dashed line with UrQMD.

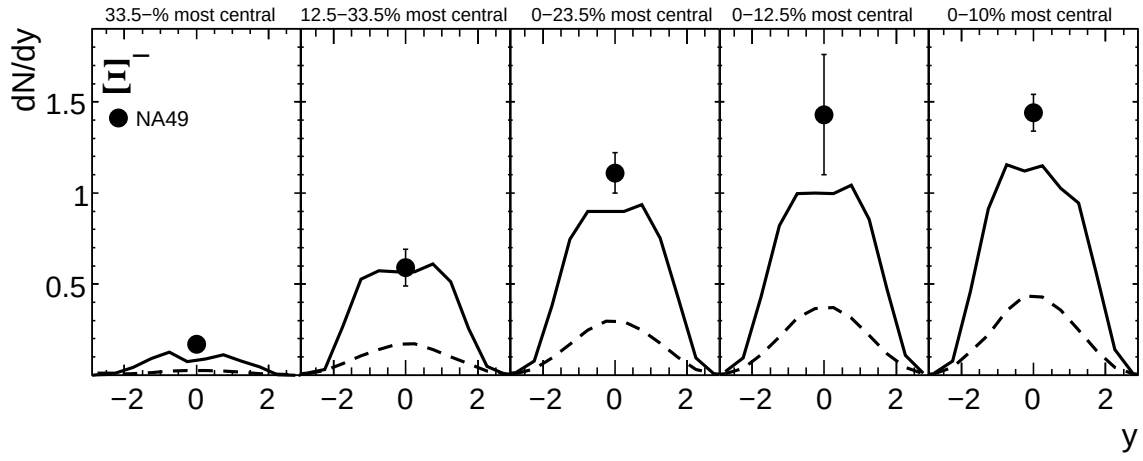

Figure 9.4: The points correspond to the measured yield at midrapidity ($|y| \leq 0.5$) for Ξ^- from NA49 [Alt08c, Blm07, Mit06] measured for different centralities in Pb+Pb collisions at 158A GeV. The solid line represents calculations with UrQMD+Hydro and the dashed line with UrQMD.

produce especially multistrange hyperons than via resonance and string excitation. The hadronic cross sections of strange baryons are small, so they do not get reequilibrated during the hadronic expansion phase once they are produced. The only exception are the $\bar{\Lambda}$'s which get absorbed even during the late stage of the evolution. The Λ production in the pure transport approach is in a reasonable agreement with the experimental data because their production threshold is not as high as for the other hyperons because they are likely to be produced in nucleon-nucleon collisions in association with a kaon (see Table 9.1). Therefore, the Λ's reflect the initial baryon stopping and the rapidity distribution of the net baryon number and should not be regarded as a part of the produced thermal system. The assumption of chemical euqilibrium leads to an enhanced $\bar{\Lambda}$ and Ξ production in good agreement to the experimental data. The same trend is also visible at $E_{\mathrm{lab}} = 158A$ GeV (see Fig. 9.3 and Fig. 9.4). However, here the difference between the $\bar{\Lambda}$ calculated in UrQMD (dashed line) and UrQMD+Hydro (solid line) is smaller than at $E_{\mathrm{lab}} = 40A$ GeV.

To explore the applicability limit of the hybrid model in terms of collision volume, Fig. 9.5 shows the rapidity spectra of Λ and $\bar{\Lambda}$ for central C+C and Si+Si collisions at $158A$ GeV measured by the NA49 collaboration [Alt05b, Kra04]. It is visible that for such small systems UrQMD (dashed line) describes the data better that UrQMD+Hydro (solid line). The reason for this observation is that the limited system size does not allow for a full thermalization in C+C and Si+Si interactions like in the case for Pb+Pb collisions. This indicates that up to Si+Si reactions, thermalization can not be achieved and the system is merely a (non-)trivial convolution of elementary baryon-baryon (and in smaller parts meson-baryon) interactions. From this, we also conclude that the possibility of a phase transition is reduced in such small systems.

9.2 Centrality Dependence

Let us next focus on a detailed study of the centrality dependence of strange baryons in Pb+Pb reactions. Fig. 9.6 depicts the predictions of the centrality dependence of the total yield of Λ, $\bar{\Lambda}$ and Ξ^- at $E_{\mathrm{lab}} = 40A$ GeV and $E_{\mathrm{lab}} = 158A$ GeV. One clearly observes that for central collisions the assumption of a thermalized system leads to a suitable description of the strangeness production within the hybrid model calculation.

The centrality and system size dependence of (anti-) hyperon production at $40A$ and $158A$ GeV at midrapidity ($|y| \leq 0.5$) is shown in Fig. 9.7 measured by the NA49 [Alt08c, Blm07, Mit06, Alt05a] and NA57 [Ant06, Ant04, NA57] collaboration. A discrepancy between both experiments is observed moving from peripheral to central collisions. However, for a qualitative interpretation, the present data are sufficient and we will therefore refrain from speculations on the origin of the experimental inconsistencies. The dashed line represents calculations with UrQMD and the solid line indicates predictions from UrQMD+Hydro simulations. The pure transport approach describes the data in very peripheral collisions quite well. The reason why UrQMD works for very peripheral Pb+Pb

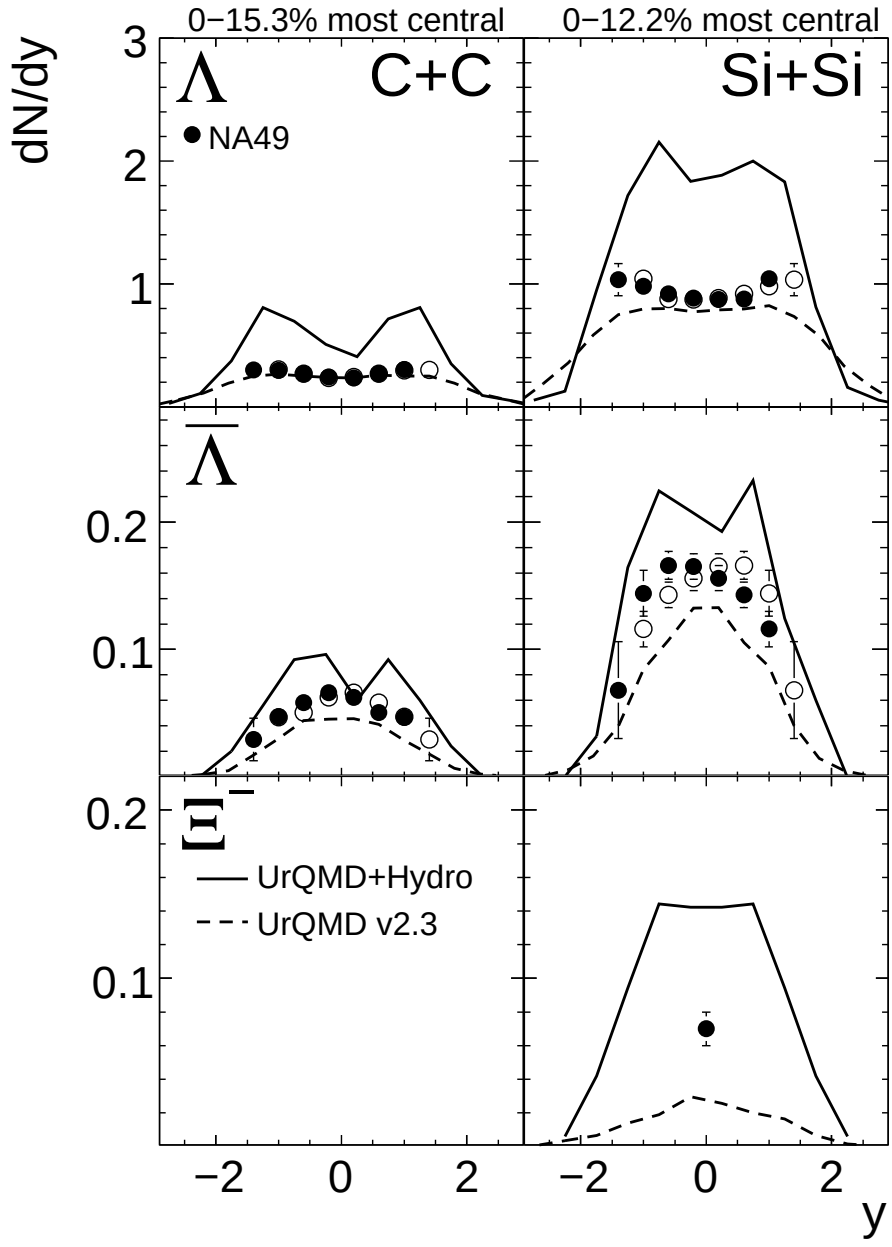

Figure 9.5: The rapidity spectra of Λ, $\bar{\Lambda}$ and Ξ^- produced in central C+C (left) and Si+Si (right) collisions at 158A GeV. The closed symbols indicate measured points, open points are reflected with respect to midrapidity. The solid line represents calculations with UrQMD+Hydro and the dashed line with UrQMD.

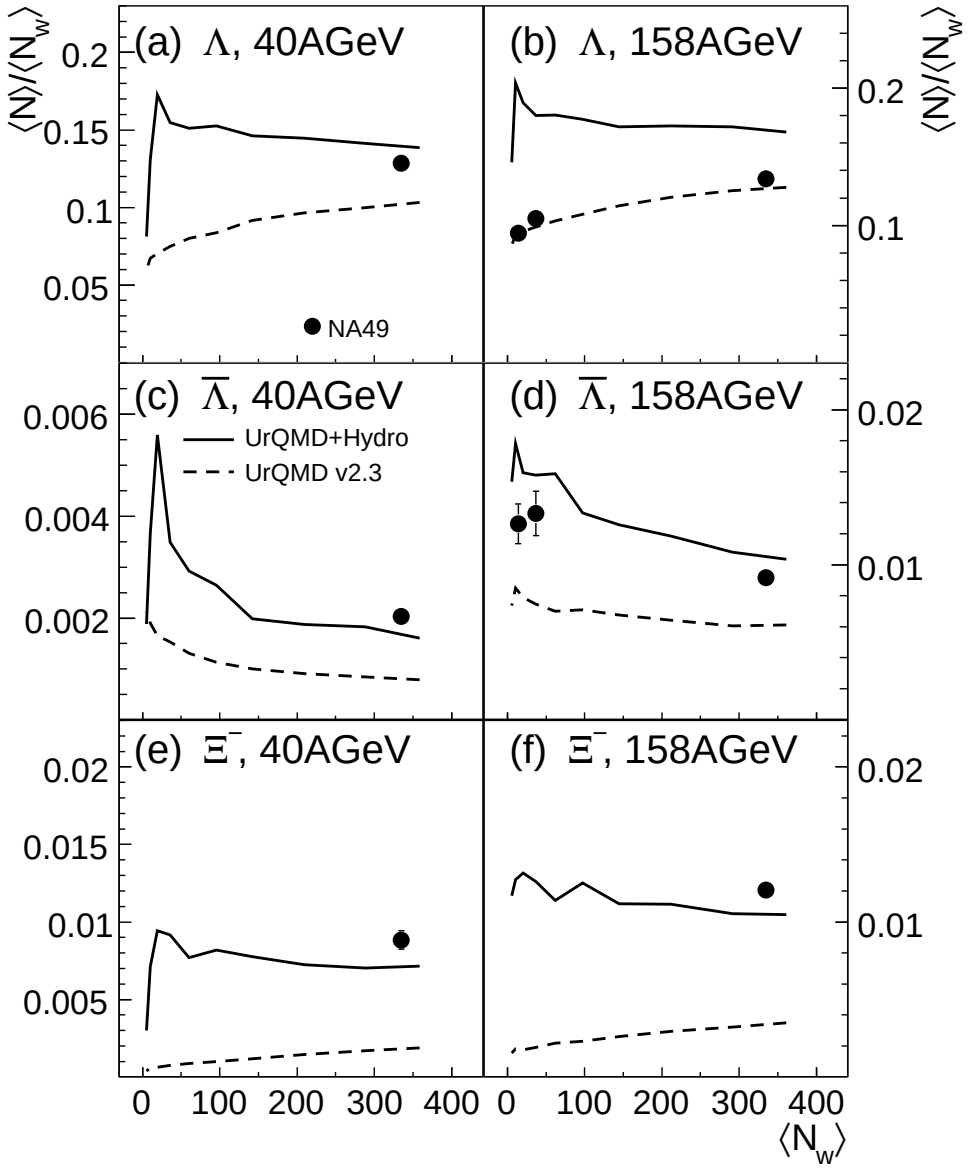

Figure 9.6: The points correspond to the measured total yield by NA49 at 40A (left) and 158A GeV (right) [Alt08c, Blm07, Mit06, Alt05b, Kra04, Alt05a]. The solid line represents calculations with UrQMD+Hydro and the dashed line with UrQMD.

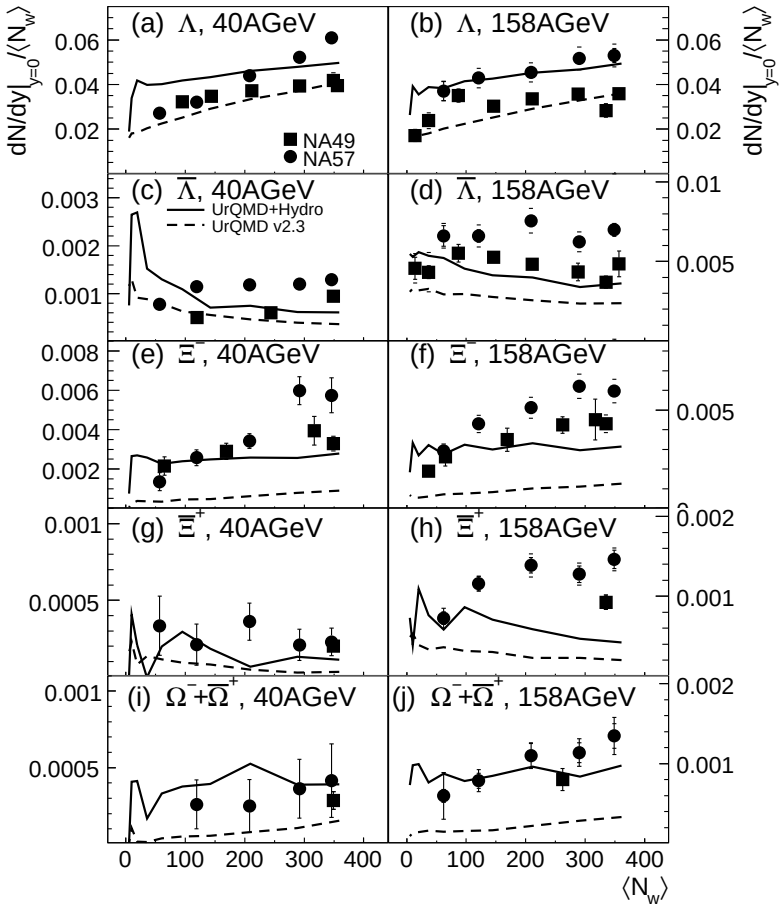

Figure 9.7: Centrality dependence of the (anti-)hyperon yields at midrapidity ($|y| \leq 0.5$) at 40A (left) and 158A GeV (right) measured by NA49 (squares) [Alt08c, Blm07, Mit06, Alt05b, Kra04, Alt05a] and NA57 (circles) [Ant06, Ant04, NA57]. The solid line represents calculations with UrQMD+Hydro and the dashed line with UrQMD.

or small systems like C+C/Si+Si is that the system is not in equilibrium as discussed above. Moving to more central Pb+Pb collisions it is visible that the thermal production of strange quarks is in much better agreement with the measured data than obtained the binary collision prescription. Especially for multistrange hyperons it is visible that the production via independent strings and resonance excitations is not sufficient to explain the experimentally measured yields. From this, we conclude that the assumption of thermalization alone allows to explain a major part of the strangeness enhancement in central collisions of massive nuclei. However, firm conclusion on the formation of a QGP can not be drawn from this. For peripheral reactions or small collision systems a description by subsequent hadronic interactions is favoured.

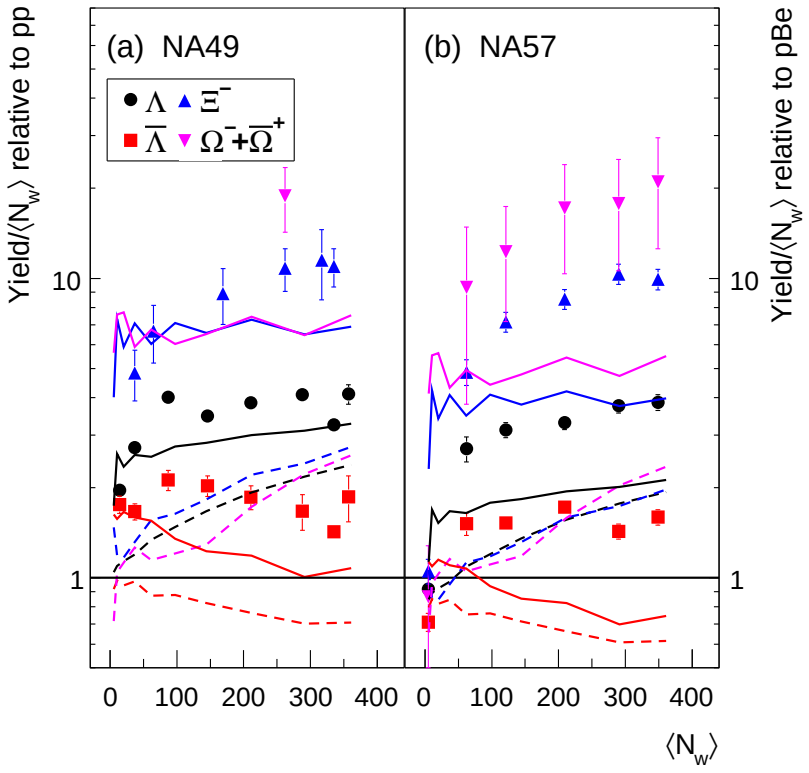

Figure 9.8: Hyperon enhancement as a function of N_w at 158A GeV measured from NA49 (right) and NA57 (left). Note NA57 uses p+Be instead of p+p as baseline.

Finally, the hyperon enhancement as a function of the number of wounded nucleons, $\langle N_w \rangle$, at 158A GeV measured by NA49 (a) [Alt05b, Kra04, Alt08c, Blm07, Mit06, Alt05a] and NA57 (b) [Ant06, Ant04, NA57] is shown in Fig. 9.8. The strangeness enhancement is defined as the yield per participant in Pb+Pb collisions normalized to the yield per participant in p+p or p+Be interactions as shown in Eq. 9.1.

$$E = \left(\frac{Yield}{N_w}\right)_{A+A} / \left(\frac{Yield}{N_w}\right)_{p+p/p+Be}, \tag{9.1}$$

The hybrid calculation leads to a mostly centrality independent result because the system at the freeze-out transition is described by grand-canonical distributions. For the $\bar{\Lambda}$ the absorption during the hadronic rescattering stage is reflected in the centrality dependence.

A clear hierarchy is visible depending on the strangeness content. The shape of the centrality dependence is changing from a decreasing distribution for $\bar{\Lambda}$ to an increasing shape for Λ, Ξ^- and $\Omega^- + \bar{\Omega}^+$ with an enhancement for $\Omega^- + \bar{\Omega}^+$ of approximately 10. UrQMD clearly underpredicts the effects, in all cases.

10 Elliptic Flow Excitation Function

This Chapter is based on [Pet09a]. Transverse collective flow is one of the earliest predicted observables to probe heated and compressed nuclear matter [Stö86, Vol08]. Elliptic flow, the anisotropy parameter that quantifies the momentum space anisotropy in the transverse plane of the outgoing particles of a heavy ion reaction, is a result of the pressure gradients that are present in the course of the evolution. Since it is a self-quenching effect, it is very sensitive to the early stage of the collision, i. e. the initial conditions and the mean free path during the high energy density stage of the evolution.

Previous calculations of elliptic flow in hadronic transport approaches have led to the conclusion that the pressure in the early stage of the collision is too low to reproduce the high elliptic flow values measured at RHIC [Bur05, Pet06a, Lin02]. To get a more consistent picture of the whole dynamics of heavy ion reactions various so called microscopic plus macroscopic hybrid approaches have been launched during the last decade [Non07, Dum99, Bas00, Tea01a, Tea01b, Gra05, Anr06a, Hir06, Hir08, Anr08a, Anr08b]). Here we use the same technique and employ a transport approach with an embedded three-dimensional ideal relativistic one fluid evolution for the hot and dense stage of the reaction based on the Ultra-relativistic Quantum Molecular Dynamics (UrQMD) model [Ste08a, Pet08b]. This approach allows to reduce the parameters for the initial conditions and provides a consistent freeze-out description and allows to compare the different underlying dynamics - ideal fluid dynamics vs. non-equilibrium transport - directly.

Serving as an input for the hydrodynamical calculation the equation of state (EoS) strongly influences the dynamics of an expanding system. In this work we employ a hadron gas (HG) equation of state, describing a non-interacting gas of free hadrons [Zsc02b]. Included here are all reliably known hadrons with masses up to ≈ 2 GeV, which is equivalent to the active degrees of freedom of the UrQMD model (note that this EoS does not contain any form of phase transition). The purely hadronic calculation serves as a baseline calculation to explore the effects of the change in the underlying dynamics - pure transport vs. hydrodynamic calculation.

10.1 Importance of the Initial Conditions

We begin our investigation with the initial conditions for the hydrodynamical evolution. Fig. 10.1 shows the initial local rest frame energy density distribution in the transverse plane for one single Pb+Pb collision. The spatial anisotropy that causes the development of elliptic flow is nicely observed. The distribution is not smooth and not symmetric in

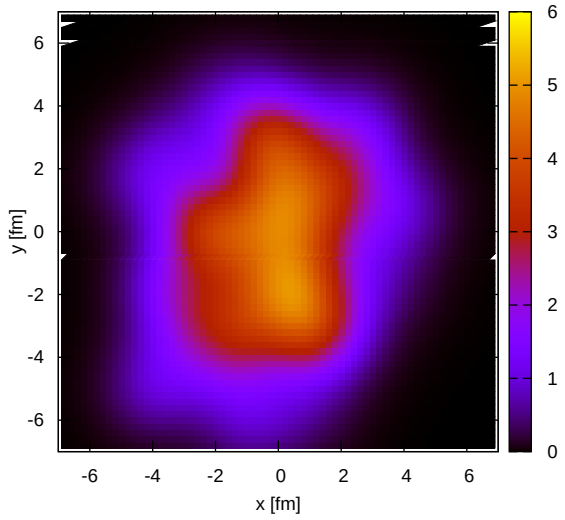

Figure 10.1: Energy density distribution in the $x-y$-plane for one midcentral ($b = 7$ fm) Pb+Pb collision at $E_{\mathrm{lab}} = 40A$ GeV.

any direction.

In Fig. 10.2 the initial velocity distribution is shown in the transverse plane. The value that is plotted here is the absolute value of the three-velocity of the hydrodynamic cells ($v = |\vec{v}|$) times the local rest frame energy density in the respective cell. In this way, one gets rid of the numerical noise in the almost empty cells. The velocity distribution is also not symmetric and fluctuates from event to event. As expected the velocities are higher at the edges of the almond shaped overlap region in x direction. In the middle of the system the matter is almost at rest. To see how these space-momentum correlations transform to observables we introduce the elliptic flow v_2.

10.2 Elliptic Flow Results

The second coefficient of the Fourier expansion of the azimuthal distribution of the emitted particles (v_2) is called elliptic flow [Sor99, Oll92, Ble02a]. v_2 is defined by

$$v_2 \equiv \langle \cos[2(\phi - \Phi_{\mathrm{RP}})] \rangle = \left\langle \frac{p_x^2 - p_y^2}{p_x^2 + p_y^2} \right\rangle \quad , \tag{10.1}$$

where ϕ is the azimuthal angle of the particle, Φ_{RP} is the azimuthal angle of the reaction plane and p_x and p_y are the momenta of the particle in x- and y-direction respectively.

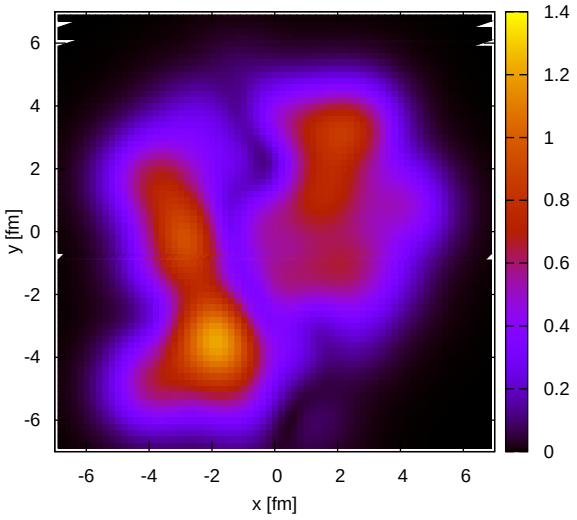

Figure 10.2: Velocity distribution in the transverse $x-y$-plane for one midcentral ($b = 7$ fm) Pb+Pb collision at $E_{\rm lab} = 40A$ GeV. The absolute value of the velocity has been multiplied by the energy density in the correspondig cell.

In Fig. 10.3 we show the excitation function of charged particle elliptic flow compared to data over a wide energy range, i.e from $E_{\rm lab} = 1A$ GeV to $\sqrt{s_{NN}} = 200$ GeV. In this figure, the data and the calculation are not divided by further model dependent quantities and therefore it allows for a direct comparison. The symbols indicate the data for charged particles from different experiments. In the SPS regime the pure transport model calculations are quite in line with the data, especially with the NA49 results. Above $E_{\rm lab} = 160A$ GeV the calculation underestimates the elliptic flow. This has been taken as a sign that partonic degrees of freedom become more important at these energies.

The smaller mean free path in the hybrid model calculation leads to higher elliptic flow values at higher SPS energies even without explicit phase transition. At lower energies the result is in line with the transport calculation since the hydrodynamic evolution is very short. The average duration of the hydrodynamic evolution increases from ~ 3 fm at low energies to around 8 fm at $E_{\rm lab} = 40A$ GeV and even ~ 12 fm at the highest SPS energy. Please note that the crucial observation is not only that there is higher elliptic flow than in the transport calculation, but that the hybrid approach shows that ideal hydrodynamics is less than 20 % away from the experimental data. This confirms that the initial conditions and the freeze-out treatment have important influence on the results of a hydrodynamic calculation.

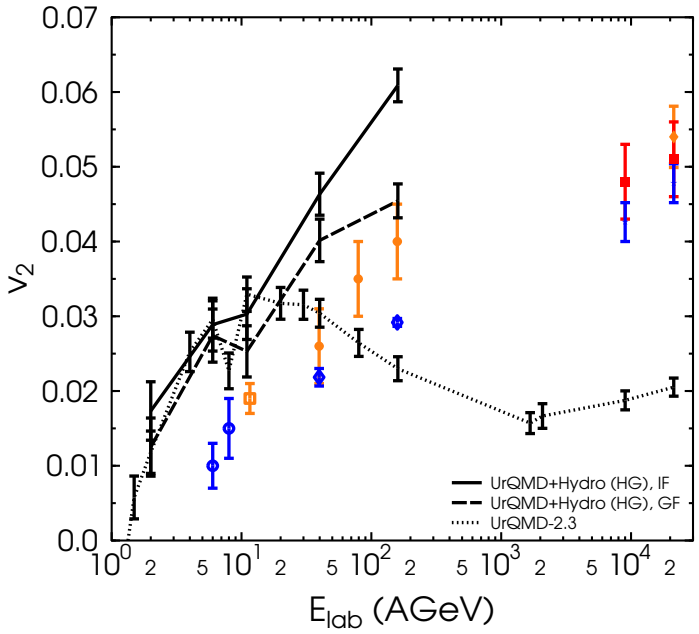

Figure 10.3: The energy excitation function of elliptic flow of charged particles in Au+Au/Pb+Pb collisions in mid-central collisions (b=5-9 fm) calculated at midrapidity ($|y| < 0.5$) within the hybrid model with isochronous freeze-out (black full line) and gradual freeze-out (black dashed line) is contrasted to the pure UrQMD transport calculation (black dotted line). These curves are compared to data (colored symbols) from different experiments (E895, E877, NA49, CERES, PHENIX, PHOBOS and STAR) [Alt03, Pin99, Chu02, Fil01, Sli03, Esu02, Esu03, Man03, Ray03].

The elliptic flow of pions as a function of transverse momentum is shown in Fig. 10.4. As it has been stated above the hydrodynamic evolution leads to higher elliptic flow values especially at higher p_t where the pure transport calculation underpredicts the data. For these differential results at midrapidity the difference between the two freeze-out prescriptions is less pronounced than for the integrated results. The hybrid model calculation leads also for the differential elliptic flow to a reasonable agreement with the experimental data.

Finally, we replot the $v_2(\sqrt{s}_{NN})$ values as a function of particle density and scaled by the eccentricity of the initial state. Fig. 10.5 shows v_2/ϵ as a function of $(1/S)dN_{\rm ch}/dy$ which is assumed to be a decreasing quantity in the investigated energy regime in ideal hydrodynamics calculations. $(1/S)dN_{\rm ch}/dy$ is the charged particle density at midrapidity divided by the initial state overlap area. This way of plotting the elliptic flow excitation function allows to compare results from different energies and centralities at the same time. The charged particle multiplicity in the overlap area is the same in a central low

energy collision as in a peripheral high energy collision.

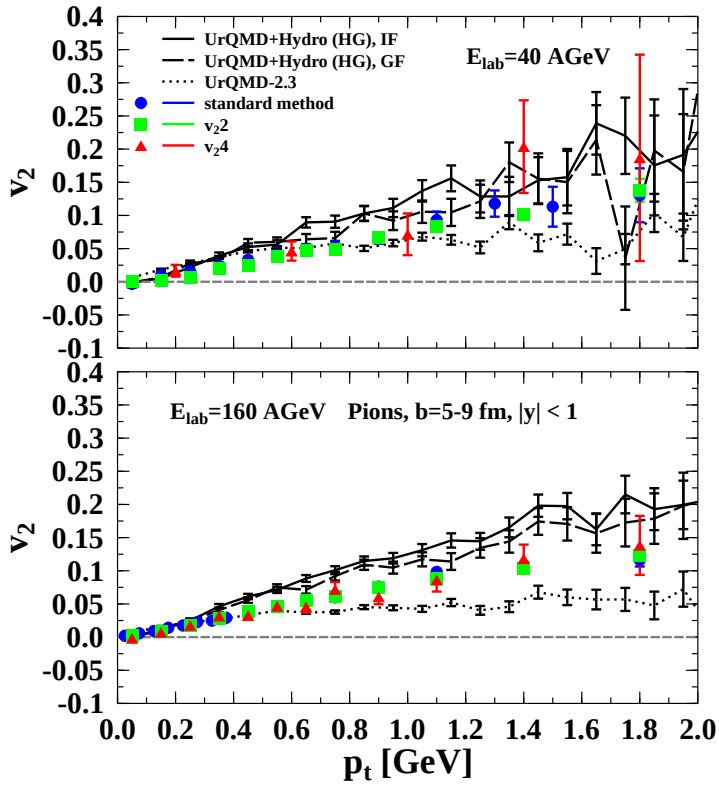

Figure 10.4: Elliptic flow of pions in mid-central (b=5-9) Pb+Pb collisions at $E_{\mathrm{lab}} = 40A$ GeV and $E_{\mathrm{lab}} = 160A$ GeV. The full black line depicts the hybrid model calculation with isochronous freeze-out, the black dashed line the hybrid calculation employing the gradual freeze-out while the pure transport calculation is shown as the black dotted line. The colored symbols display experimental data obtained with different measurement methods by NA49 [Alt03].

The calculations within the UrQMD + hydrodynamics approach have been performed for midcentral Pb+Pb/Au+Au collisions with $b = 5 - 9$ fm. The charged particle multiplicities and v_2 values have been calculated at midrapidity ($|y| < 0.5$).

For the evaluation of the relevant initial eccentricity and the overlap area we have stopped the calculation of 10.000 UrQMD events at the time of the overlap of the nuclei. The quantities of interest have been evaluated for the participating particles which are defined as the nucleons which have undergone at least one interaction plus the newly produced particles (the result is insensitive to the fact if only nucleons are considered or not) according to the following formula [Vol00, Sor99]:

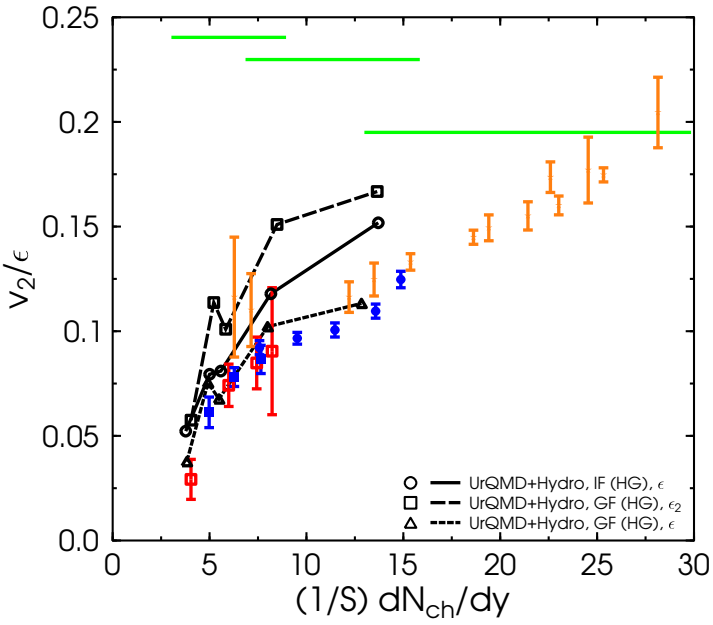

Figure 10.5: v_2/ϵ as a function of $(1/S)dN_{\rm ch}/dy$ for different energies and centralities for Pb+Pb/Au+Au collisions. The results from mid-central collisions (b=5-9 fm) calculated within the hybrid model with isochronous/gradual freeze-out (full line with circles and dashed line with triangles respectively) are shown. Furthermore, the hybrid model calculation with GF is divided by a different eccentricity (ϵ_2)(dashed line with squares). These curves are compared to data depicted by colored symbols from different experiments (E877, NA49 and STAR [Alt03]) for mid-central collisions. The green full lines correspond to the previously calculated hydrodynamic limits [Kol00].

$$\epsilon = \frac{\langle y^2\rangle - \langle x^2\rangle}{\langle y^2\rangle + \langle x^2\rangle} \quad \text{and } S = \pi\sqrt{\langle x^2\rangle\langle y^2\rangle} \quad , \tag{10.2}$$

where the averages are taken over particles and events at the same time. An alternative defintion is sometimes used [Vol08]

$$\epsilon_2 = \frac{\langle y^2 - x^2\rangle}{\langle y^2 + x^2\rangle} \tag{10.3}$$

where the averages are taken first over particles in one event and then the value for ϵ is averaged over events. In this way, the events with higher particle production have the same weight as those with lower multiplicities.

Since it is not obvious which way of calculating the initial eccentricity captures the

physical picture best (e.g. the Glauber values which are taken from experiment) we show both possibilities because they lead to different results.

It is remarkable that the shape of the curve is substantially changed in the hybrid model calculation compared to the previous calculated hydro limits [Kol00] (shown as horizontal lines). A similar shape has also been obtained in a two-dimensional hybrid calculation with a hadronic afterburner but simplified initial conditions and a EoS including a phase transition to the QGP (see [Tea01a]). The present calculation with ideal one fluid hydrodynamics with hadronic degrees of freedom as described above is however able to reproduce the shape of the experimental data points and even the magnitude at lower energies. Note that at very low energies the hydrodynamic stage is rather short and does not influence the evolution considerably. In this regime all different setups show the same results and are compatible with the data. Towards higher energies (where pure hadronic transport calculations have too much viscosity and underpredict the data), the hybrid calculation leads to higher pressure gradients in the early stage and therefore to suitable elliptic flow values. Most important here is the only moderate increase in v_2 because of the more realistic treatment via the inclusion of initial non-equilibrium effects and a complex shape (both in coordinate and momentum space) of the initial energy and baryon density distribution in addition to our sophisticated final state freeze-out. In fact, for the (more physical) gradual freeze-out, the v_2 values are reduced by more than a factor of 2 compared to ideal hydrodynamics with simplified initial conditions. The influence of the freeze-out prescription can be observed by comparing the isochronous to the gradual freeze-out scenario. The alternative calculation of the eccentricity (ϵ_2) leads to higher values because ϵ_2 is in general smaller than ϵ. Additional changes in magnitude may be caused by viscosity effects during the hot and dense stage and a possible phase transition which might weaken the pressure gradients in the early stage.

11 Mean Transverse Mass Excitation Function

This Chapter is based on [Pet09b]. To explore the deconfinement phase transition from a hadron gas to the so called Quark Gluon Plasma (QGP) is one of the main motivations to study heavy ion collisions at high energies [Stö86]. The mean transverse momentum excitation function has been proposed as a signal for the observation of this phase transition many years ago [VaH82] and has been further explored in the following years [Sce99, Gor03, Gaz04]. Experimentally, the energy dependences of various observables (including the mean transverse mass $\langle m_T \rangle$) show anomalies at low SPS energies which might be related to the onset of deconfinement [Gaz99, Gaz04, Alt08a].

The mean transverse mass of the particles is expected to be proportional to the temperature at kinetic freeze-out of the particles. If there is a phase transition the mean transverse mass excitation function should show a flattening because of the mixed phase region where the temperature of the system stays constant. However, recently, it has been suggested in a 3-fluid model with a hadron gas equation of state that the characteristic steplike-behaviour of the mean transverse mass in dependence of the incident beam energy might be a relic of the freeze-out treatment in a hydrodynamic calculation and may not be a unique sign of the transition to the QGP [Iva08].

We investigate here the effects of different freeze-out implementations and changes in the equation of state (EoS) in an integrated (3+1)d Boltzmann+hydrodynamics approach. The present implementation allows to disentangle different effects like e.g. change of the dynamics between hydrodynamics and transport or freeze-out prescriptions in a consistent manner and provides the opportunity to explore different equations of state within the same framework.

11.1 Freeze-out Dynamics

In this Section we address the 4π multiplicity (Figs. 11.1-11.2, upper plots) and the mean transverse mass (Figs. 11.1-11.2, lower plots) excitation functions for pions, protons and kaons calculated in the hybrid approach with a hadronic EoS to compare different freeze-out prescriptions. The dotted black line corresponds to the results directly after the isochronous hydrodynamic freeze-out without final state interactions (FSI). Immediate decay of the resonances is taken into account to provide comparable multiplicity results. All other calculations include the hadronic afterburner, however with different transi-

tion prescriptions applied: the isochronous freeze-out (red dashed line with circles), the gradual freeze-out (black full line with squares) and the gradual freeze-out with varied freeze-out energy density criterion $4\epsilon_0$ (blue dashed line with triangles).

In the following figures the beam energy dependence of the multiplicities (top) and the mean transverse mass (bottom) is shown. The results are calculated for central Au+Au/Pb+Pb collisions at midrapidity ($|y| < 0.5$) from $E_{\rm lab} = 2 - 160A$ GeV. In general, one observes that the mean transverse mass increases as a function of energy, because more energy becomes available that can be distributed in the transverse plane and the expansion phase lasts longer.

Let us start the detailed discussion with the pions as being the most abundant hadrons. The pion multiplicity (Fig. 11.1, left) is completely insensitive to the freeze-out procedure while the mean transverse mass at higher energies is decreased if the gradual freeze-out procedure is applied. The final state interactions and the variation of the freeze-out criterion do only weakly alter the results for pions. At AGS energies, the calculations are well in line with the data while at SPS energies where the hydrodynamic stage is a major part of the evolution the pion multiplicity stays below the data and the mean transverse mass exceeds the experimental data. We attribute these observations to the entropy conservation in the hydrodynamic evolution and the violent transverse expansion because of high pressure gradients.

Next, we explore the production and expansion of the baryon charge. In contrast to the previous case, the proton multiplicity (Fig. 11.1, right) is almost constant over the whole energy range. The final rescatterings lead in this case to a slightly higher multiplicity and an increased mean transverse mass. The protons acquire more transverse flow during the hadronic stage after the hydrodynamic evolution. As already observed for the pions the gradual freeze-out leads to a flattening of the transverse mass excitation function. Varying the energy density criterion (squares vs triangles) indicates only a weak dependence on this parameter.

Finally, we address strange particles. Fig. 11.2 show the results for positively and negatively charged kaons respectively. The kaon multiplicities are nicely reproduced, if the isochronous freeze-out procedure is applied with or without final state interactions. The mean transverse mass in the same calculation is too high at top SPS energies due to the violent transverse expansion because of the comparably stiff hadronic EoS. For K^- the final rescatterings lead to an increase in the mean transverse mass because the low p_T K^- are easily absorbed on the surrounding baryons. In the gradual freeze-out scenario the kaon production is enhanced by roughly 10% due to the higher average temperatures at the transition point from hydrodynamics to the tranport description at higher energies. For the kaon multiplicity the variation of the freeze-out criterion leads to a slight decrease of the yields when going from the gradual to the isochronous scenario. This reflects the sensitivity of the kaon yield to the temperature at the transition point between hydrodynamics and the final state hadron cascade. The mean transverse mass excitation functions are flatter with the gradual freeze-out scenario which leads to a better description of the experimental data.

Overall, the hybrid calculation with the gradual freeze-out procedure reproduces the multiplicities and the shape of the mean transverse mass excitation function best, in many cases there is even good quantitative agreement with the experimental data.

11.2 Equation of State Dependence

After these rather technical studies, we turn now to the investigation of different EoS. To exemplify the effects of the different underlying dynamics we contrast the hybrid model calculations with the pure hadronic transport calculation (UrQMD-2.3, dotted black line). By comparing this calculation with the hybrid calculation (employing the HG EoS, full black line with squares) one can estimate the effect of viscosities and the non-equilibrium dynamics. For the hybrid model calculations the gradual freeze-out with the criterion of $5\epsilon_0$ is applied as it provides the best fit to the data as shown before. The dashed blue line with triangles corresponds to the calculation with the chiral equation of state (CH) while the red dashed line with circles depicts the bag model EoS with a strong first order phase transition (BM).

Fig. 11.3 shows the multiplicity and the mean transverse mass excitation functions for pions and protons. The yields are reduced in the hybrid model compared to the pure transport calculation because of entropy conservation during the ideal hydrodynamic evolution. The changes in the EoS do not affect the multiplicities. The mean transverse mass that is more sensitive to the pressure in the transverse plane is changed. For pions the chiral EoS gives similar results as the hadron gas calculation while the bag model EoS decreases the mean transverse mass at high energies as it is expected for a first order phase transition. The pure transport calculation reproduces the flattening in the intermediate energy regime best.

For the protons 11.3 (right) the opposite behaviour can be observed. In this case, the BM EoS leads to a higher transverse mass than the chiral EoS which is still higher than the hadronic calculation. UrQMD-2.3 shows the strongest flattening again. The high baryon density regions, where most of the protons are produced at hydrodynamic freeze-out, are perhaps more sensitive to the early stage of the collision where the BM EoS exhibits a higher pressure (in the QGP phase) and the softening due to the mixed phase is only reflected in the mean transverse mass of mesons. The net baryon density is explicitly propagated in the hydrodynamic evolution. Therefore, the final distribution of the baryo-chemical potential at the transition from hydrodynamics to the hadronic cascade reflects the dynamics during the evolution and is sensitive to the initial stopping. The mesons are only influenced by the temperature distribution that mainly depends on the energy density distribution.

Fig. 11.4 shows the results for different EoS for positively and negatively charged kaons. Since the qualitative results are the same in both cases we will refer to kaons in the following without distinguishing the charges. The kaon multiplicities are higher in the hybrid model calculation as compared to the pure transport simulation, because strange

particles are produced according to thermal distributions during the Copper-Frye transition. The string and resonance dynamics in UrQMD-2.3 lead to an underestimation of strange particle yields while the mean transverse mass excitation function flattens at high AGS energies due to non-equilibrium effects. The multiplicities and the mean transverse mass are highest in the hadron gas hybrid calculation because the hadronic EoS is the stiffest EoS and can not be "softened" by non-equilibrium effects. Here also, the transverse expansion is more violent since the pressure and its gradients are large during the whole hydrodynamic evolution. The chiral EoS leads to a small decrease in the yields, but leaves the $\langle m_T \rangle$ excitation function essentially unchanged. Employing the chiral EoS the temperatures at the transition from hydrodynamics to transport are a bit lower than in the purely hadronic case, but the kaons acquire approximately the same transverse momentum during the evolution. The chiral phase transition exhibits only a small latent heat and therfore the pressure gradients are not affected that much. The BM calculation with a strong first order phase transition produces lower kaon multiplicites than the other hybrid model calculations, at low SPS energies even less than the pure transport calculation. The transition temperatures in this case are the lowest due to the long duration of the hydrodynamic stage. For the kaons the flattening of the mean transverse mass excitation function due to the softening of the EoS is best visible. The mean transverse mass values are even lower than in the nonequilibrium transport calculation.

The multiplicities are reasonable well reproduced in all the different scenarios, but the mean transverse mass excitation function reflects the different transverse pressure gradients due to the underlying EoS. The experimentally measured step-like behaviour can either be attributed to a first order phase transition with a large latent heat or a softening of the EoS due to hadronic non-equilibrium effects.

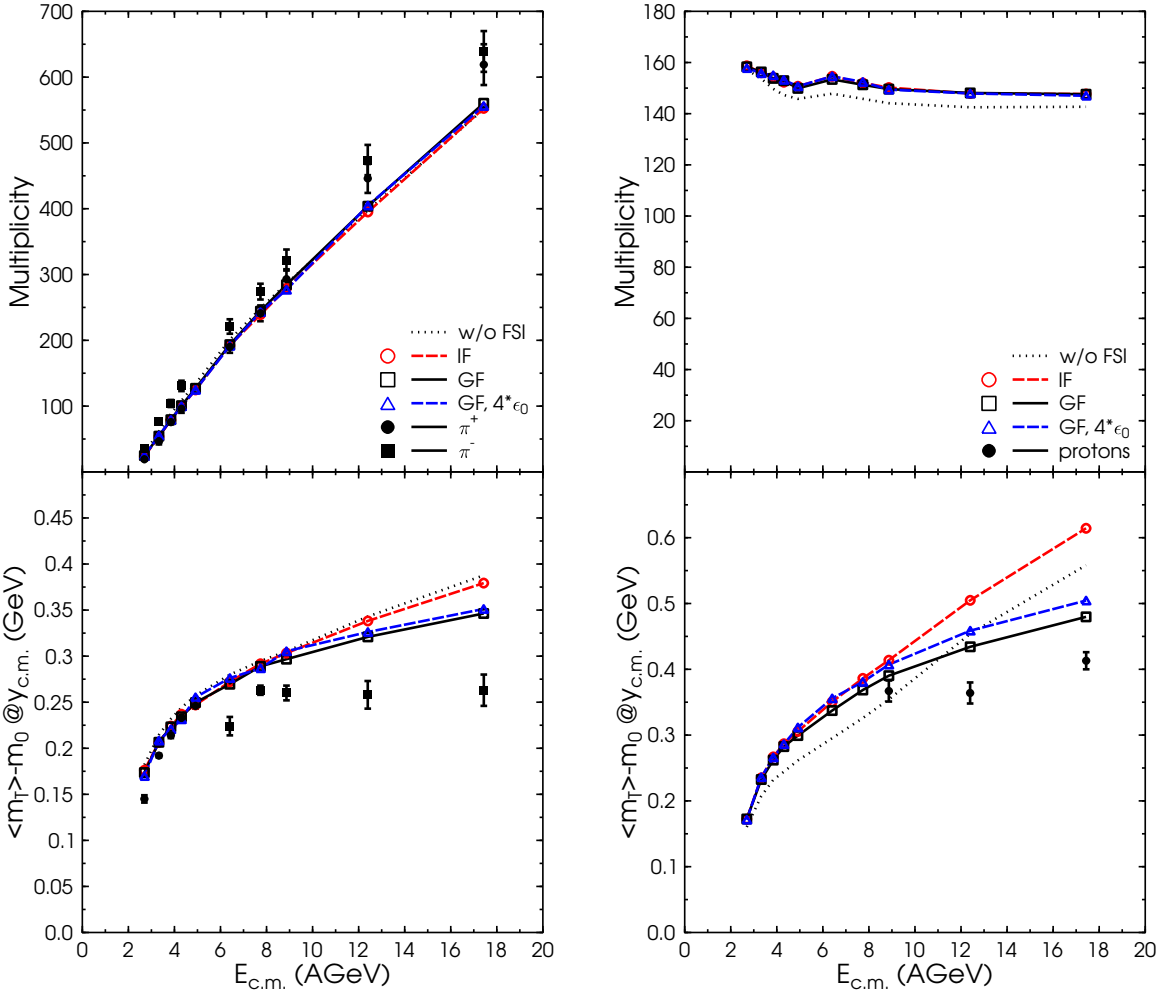

Figure 11.1: The multiplicity (4π, top) and the $\langle m_T \rangle$ (bottom) excitation function for pions (left) and protons (right) in central ($b < 3.4$ fm) Au+Au/Pb+Pb collisions at $E_{\rm lab} = 2 - 160$ AGeV is shown. The lines depict different freeze-out prescriptions for the hybrid model calculation with the hadron gas equation of state, while the symbols depict experimental data [Alt08a, Afa02a, Ahl00a, Anc04b].

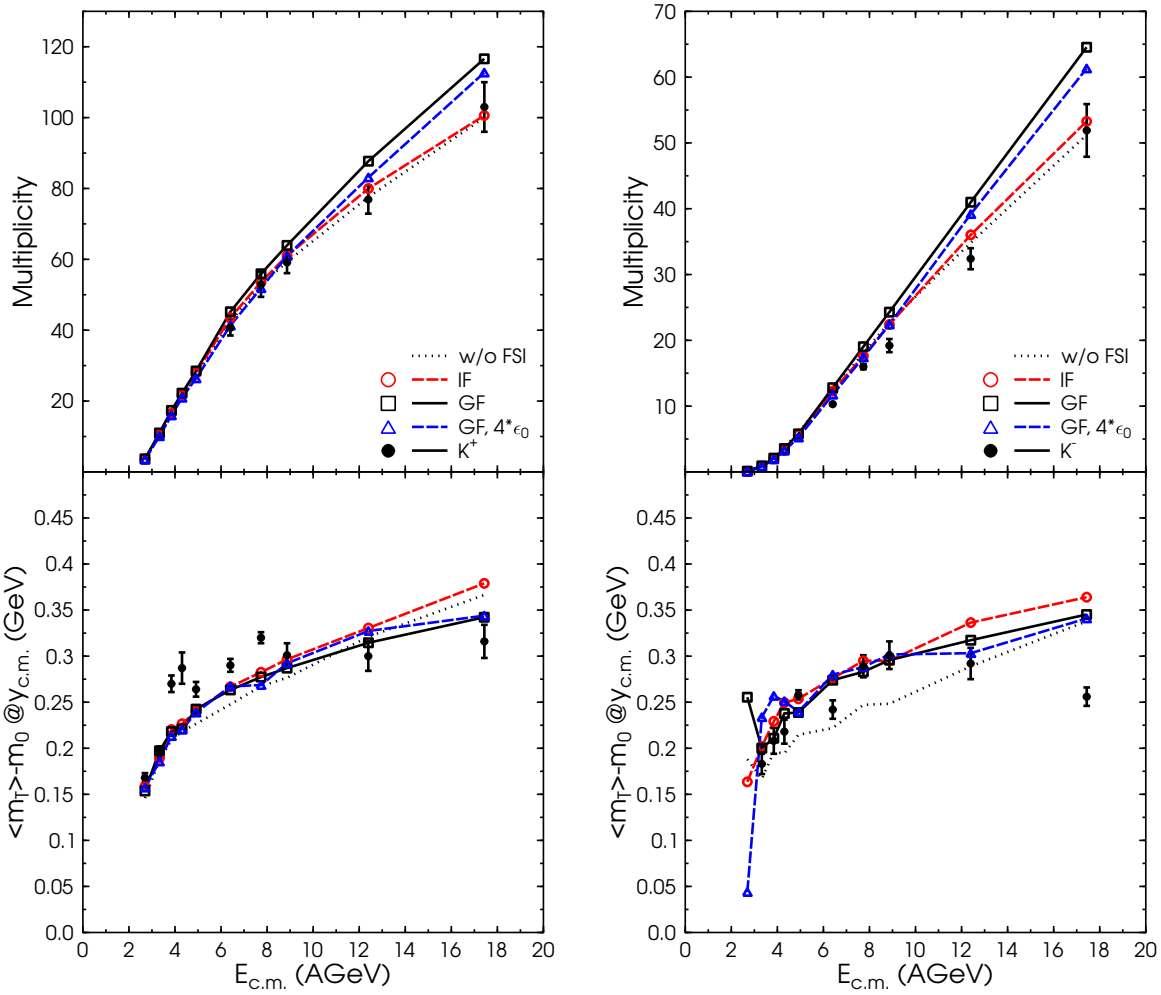

Figure 11.2: The multiplicity (4π, top) and the $\langle m_T \rangle$ (bottom) excitation function for positively/negatively (left/right) charged kaons in central ($b < 3.4$ fm) Au+Au/Pb+Pb collisions at $E_{\mathrm{lab}} = 2 - 160$ AGeV is shown. The lines depict different freeze-out prescriptions for the hybrid model calculation with the hadron gas equation of state, while the symbols depict experimental data [Alt08a, Afa02a, Ahl00a, Ahl00b].

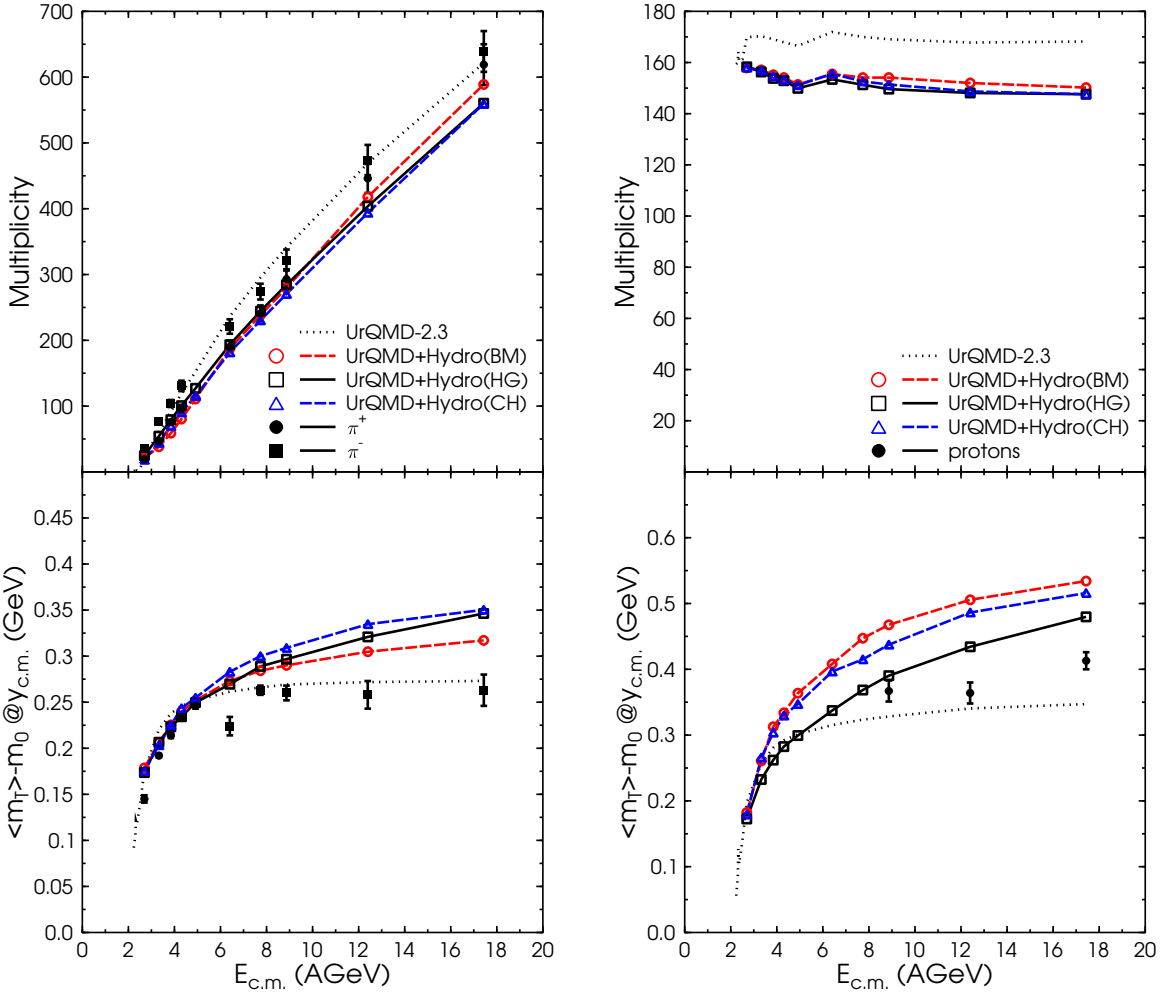

Figure 11.3: The multiplicity (4π, top) and the $\langle m_T \rangle$ (bottom) excitation function for pions (left) and protons (right) in central ($b < 3.4$ fm) Au+Au/Pb+Pb collisions at $E_{\rm lab} = 2-160$ AGeV is shown. The lines depict hybrid model calculations with different equations of state and the pure transport calculation in comparison to the experimental data (symbols)[Alt08a, Afa02a, Ahl00a, Anc04b].

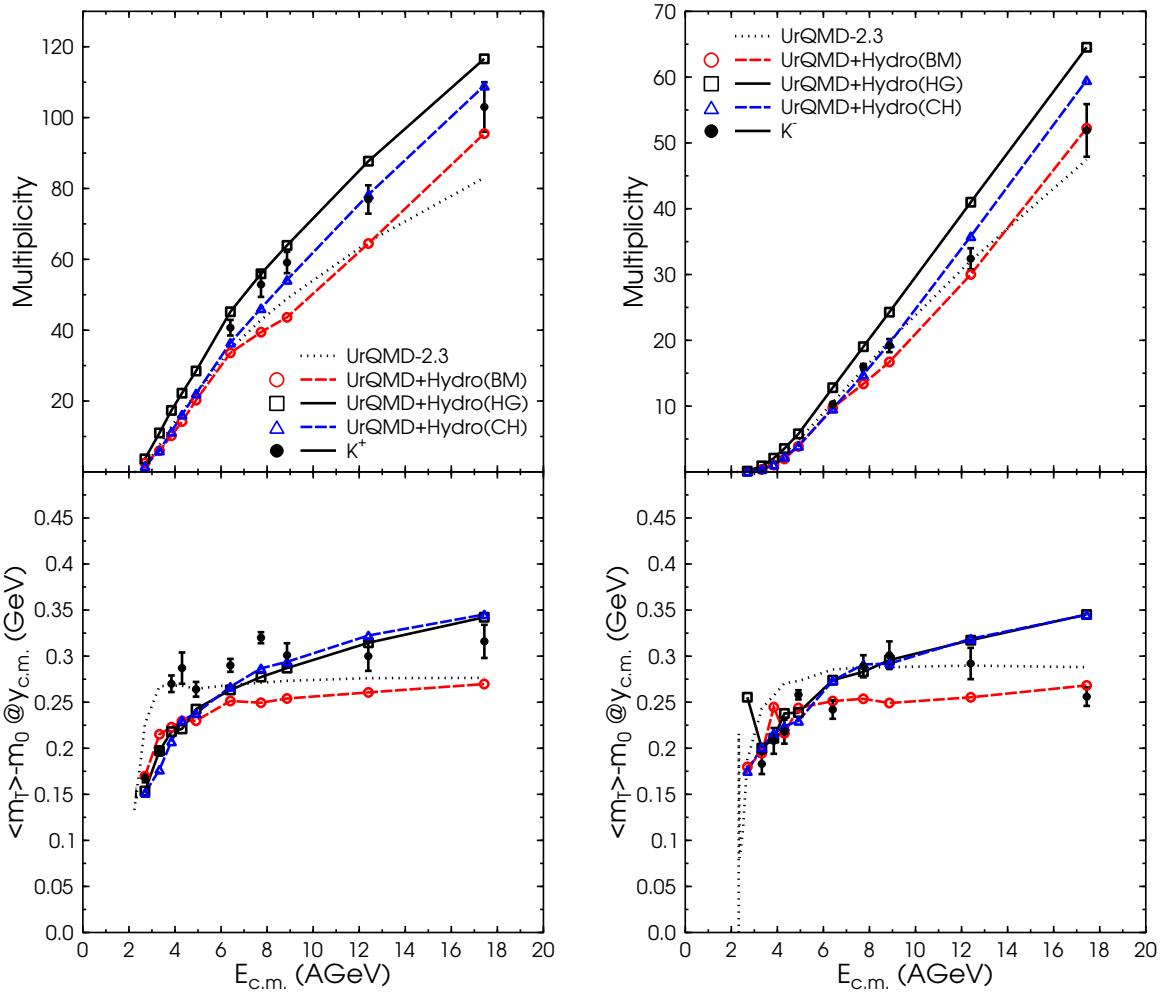

Figure 11.4: The multiplicity (4π, top) and the $\langle m_T \rangle$ (bottom) excitation function for positively/negatively (left/right) charged kaons in central ($b < 3.4$ fm) Au+Au/Pb+Pb collisions at $E_{\rm lab} = 2 - 160$ AGeV is shown. The lines depict hybrid model calculations with different equations of state and the pure transport calculation in comparison to the experimental data (symbols)[Alt08a, Afa02a, Ahl00a].

12 HBT Correlations

This Chapter is based on [Li08b]. To learn something about the hot and dense stage of the collision from the final state particle distributions, a dynamical modeling of the whole process is necessary. Some of the important ingredients which have to be considered in a consistent manner are

- the initial conditions and the initial nonequilibrium dynamics,
- the treatment of the phase transition and hadronization, as well as the right degrees of freedom,
- viscosity effects in the initial partonic as well as in the hadronic stage of the evolution,
- hadronic rescatterings and freeze-out dynamics.

We notice that part of these have been pointed out to be of importance especially for the understanding of the HBT results [Pra08, Lis08, Bro08].

It is well-known that by using HBT interferometry techniques one can get detailed information about the space-time configuration of the system at freeze-out. We concentrate here on the two (identical) pion interferometry and test the sensitivity of the HBT results on different stages of the evolution. In our previous investigations on the HBT correlation of various identical particle pairs from HICs at AGS, SPS, and RHIC energies [Li06c, Li07a, Li07b, Li08a, Li08c, Li09], we adopted the UrQMD model but further considered the mean field potentials for both confined and "pre-formed" particles in the model [Li08a, Li08c, Li09]. We found that the potentials afford a better description of interactions between particles at the early stage so that the HBT time-related puzzle disappears throughout the energies from AGS, SPS, up to RHIC.

In this Chapter we perform a systematic investigation of the sensitivity of HBT correlation of negatively charged pions to the EoS by applying the newly developed hybrid approach. Similar more focused studies were frequently discussed with microscopic transport or hydrodynamic models before [Ris96b, Sof01, Zsc02a, Lis05]. It is also interesting to study if the current set of EoS employed in the hydrodynamic phase support the conclusion about the origin of the HBT time-related puzzle. In addition, the effects of the hadronic rescattering and of resonance decays after the hydrodynamic freeze-out on the HBT radii and the R_O/R_S ratio deserve more investigation. We have also noticed that some recent progresses of this topic both from an improved hydrodynamic calculation [Bro08] and from the pion-optical-potential point of view [Luz08] have been published which provides additional new insights.

We use three different EoS to investigate their effect on the extracted HBT radii that are described in Section 6.3 in more detail.

12.1 CRAB analyzing program and the fitting process

To calculate the two-particle correlator, the CRAB program is adopted [Pra], which is based on the formula:

$$C(\mathbf{k},\mathbf{q}) = \frac{\int d^4x_i d^4x_j g(x_i,p_i) g(x_j,p_j) |\phi(\mathbf{r}',\mathbf{q}')|^2}{\int d^4x_i g(x_i,p_i) \int d^4x_j g(x_j,p_j)}. \tag{12.1}$$

Here $g(x_i,p_i)$ is an effective probability for emitting a particle i with 4-momentum $p_i = (E_i,\mathbf{p}_i)$ from the space-time point $x_i = (t_i,\mathbf{r}_i)$. $\phi(\mathbf{r}',\mathbf{q}')$ is the relative wave function with $\mathbf{r}'$ being the relative position in the pair's rest frame. $\mathbf{q} = \mathbf{p}_i - \mathbf{p}_j$ and $\mathbf{k} = (\mathbf{p}_i + \mathbf{p}_j)/2$ are the relative momentum and the average momentum of the two particles i and j.

In this work, we select central ($< 7.2\%$ of the total cross section σ_T) Pb+Pb collisions at SPS energies: $E_b = 20A$, $30A$, $40A$, $80A$ and $158A$ GeV, with a pair rapidity cut $|Y_{\pi\pi}| < 0.5$ ($Y_{\pi\pi} = \log((E_1+E_2+p_{\parallel 1}+p_{\parallel 2})/(E_1+E_2-p_{\parallel 1}-p_{\parallel 2}))/2$ is the pair rapidity with pion energies E_1 and E_2 and longitudinal momenta $p_{\parallel 1}$ and $p_{\parallel 2}$ in the center of mass system). For each EoS about 2500 events are calculated. All particles with their phase space coordinates at freeze-out are then given into the CRAB analyzing program. Only the negatively charged pions are considered during the analyzing process (for each analysis, one hundred million pion pairs are considered). For the cascade calculations, we take the results from our previous publications as reference [Li07a, Li08a]. We found that the residual Coulomb effect after the hadron freeze-out on the HBT radii of the pion source is small [Li08c], therefore we omit it in the present analysis. Please note that we will refer in the next sections to the hadronic rescattering stage as final state interactions (FSI), this should not be confused with the FSI in the context of the HBT calculation. Finally, we fit the correlator in the longitudinal comoving system (LCMS) (or called as the "Out-Side-Long" system) which is frequently adopted in recent years. The corresponding 3D Gaussian correlation function can be expressed as

$$\begin{aligned} C(q_O,q_S,q_L) &= K[1+\lambda \\ &\times \exp(-R_L^2 q_L^2 - R_O^2 q_O^2 - R_S^2 q_S^2 - 2R_{OL}^2 q_O q_L)]. \end{aligned} \tag{12.2}$$

Here K is the overall normalization factor, the q_x and R_x are the components of the pair relative momentum and homogeneity length (HBT radius) in the x direction, respectively. The λ parameter is commonly called the incoherence factor and lies between 0 (complete coherence) and 1 (complete incoherence) for bosons in realistic HICs. Because the parameter λ might be influenced by many additional factors, such as contamination, long-lived resonances, or the details of the residual Coulomb modification, we regard it as a free parameter. The R_{OL}^2 represents the cross-term and plays a role at large rapidity.

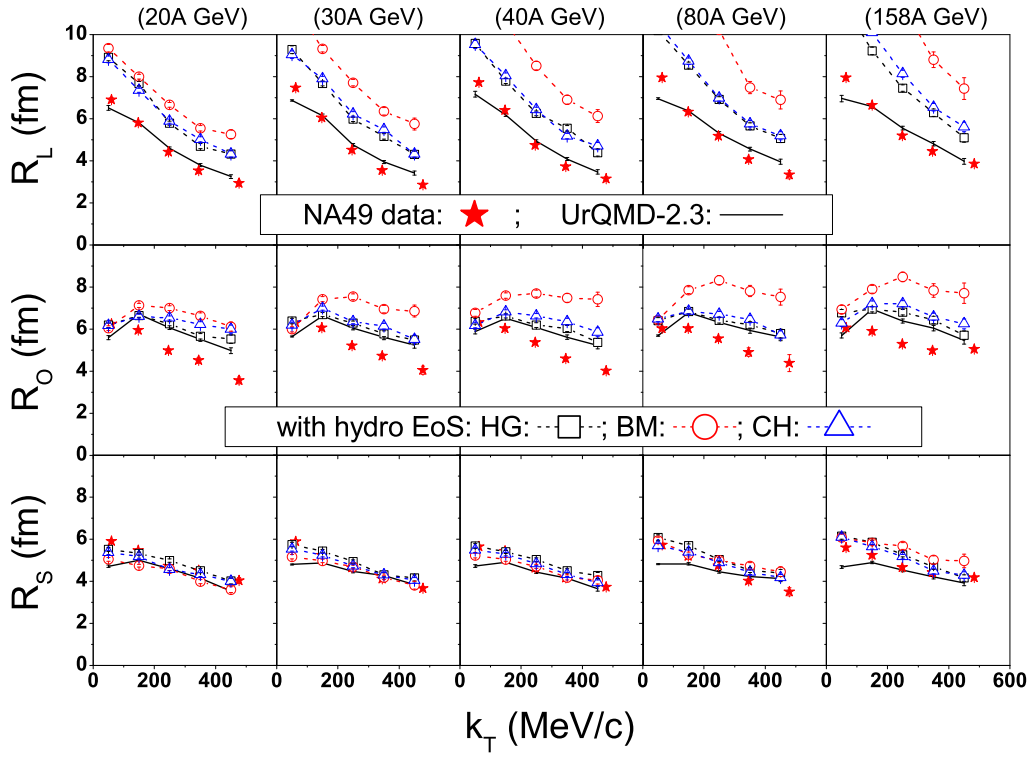

Figure 12.1: Transverse momentum k_T dependence of the HBT radii R_L, R_O, and R_S (at midrapidity) of π^- source from central HICs at SPS energies ($E_{\rm lab}$ = 20A, 30A, 40A, 80A, and 158A GeV). The NA49 data are indicated by solid stars [Alt08b]. The pure cascade calculation is depicted by lines while the hybrid model calculations with different EoS (HG, BM and CH) are depicted by dashed lines with open symbols.

To fit the correlator with Eq. (12.2), we use ROOT [ROOT] software and the χ-squared method.

12.2 HBT results

Fig. 12.1 shows the transverse momentum k_T ($\mathbf{k}_T = (\mathbf{p}_{1T} + \mathbf{p}_{2T})/2$) dependence of the HBT radii R_L, R_O, and R_S (at midrapidity) of π^- source from central Pb+Pb collisions at SPS energies. The data (solid stars) are from the NA49 Collaboration [Alt08b]. The pure cascade calculation is depicted by lines while the hybrid model calculations with different EoS (HG, BM and CH) are depicted by dashed lines with open symbols. As was shown before, the cascade calculation gives a fairly good result of the k_T dependence of R_L and R_S values except at quite small k_T, while for R_O, it is slightly larger than data at large k_T. In contrast, the hybrid model calculations show large HBT (for all employed

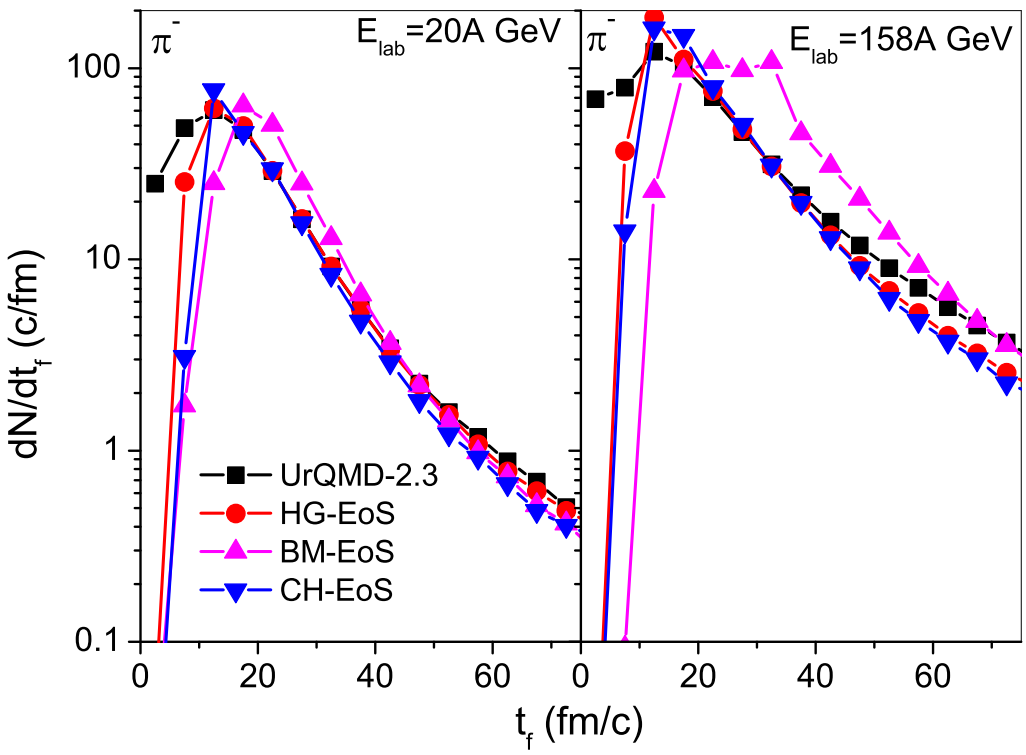

Figure 12.2: Freeze-out time dependence of the π^- emission in central Pb+Pb at $E_{\rm lab} = 20A$ GeV (left plot) and $158A$ GeV (right). Calculations with the UrQMD cascade are compared with the hybrid model calculations with the EoS of HG, BM, and CH.

EoS, but to a varying degree) in all directions, especially in the longitudinal direction. The HG and CH are moderately increased and lead to very similar results for all three directions. The large latent heat in the bag model leads to a further strong increase in the longitudinal direction and in the transverse direction at large k_T. This increase in the BM mode becomes more pronounced at higher beam energies. At first glance, this result might be surprising because at least in the transverse direction one would expect a faster expansion including a hydrodynamic evolution. On the other hand, one knows that the system spends a longer time without emitting any particles in the hybrid model calculation.

Fig. 12.2 exhibits the freeze-out time dependence of the π^- emission in central Pb+Pb at $E_{\rm lab} = 20A$ GeV (left plot) and $E_{\rm lab} = 158A$ GeV (right plot). It is clearly seen that there are almost no pions emitted before $\sim 10{\rm fm}/c$ in the hybrid model calculations. This is easy to understand because even in the gradual hydro-freeze-out which is applied here, it takes a while until the first slices have cooled down and are frozen out from the hydrodynamic evolution. There is no particle emission from earlier times in contrast to the pure cascade calculation. For the BM-EoS, this effect is present even for a longer

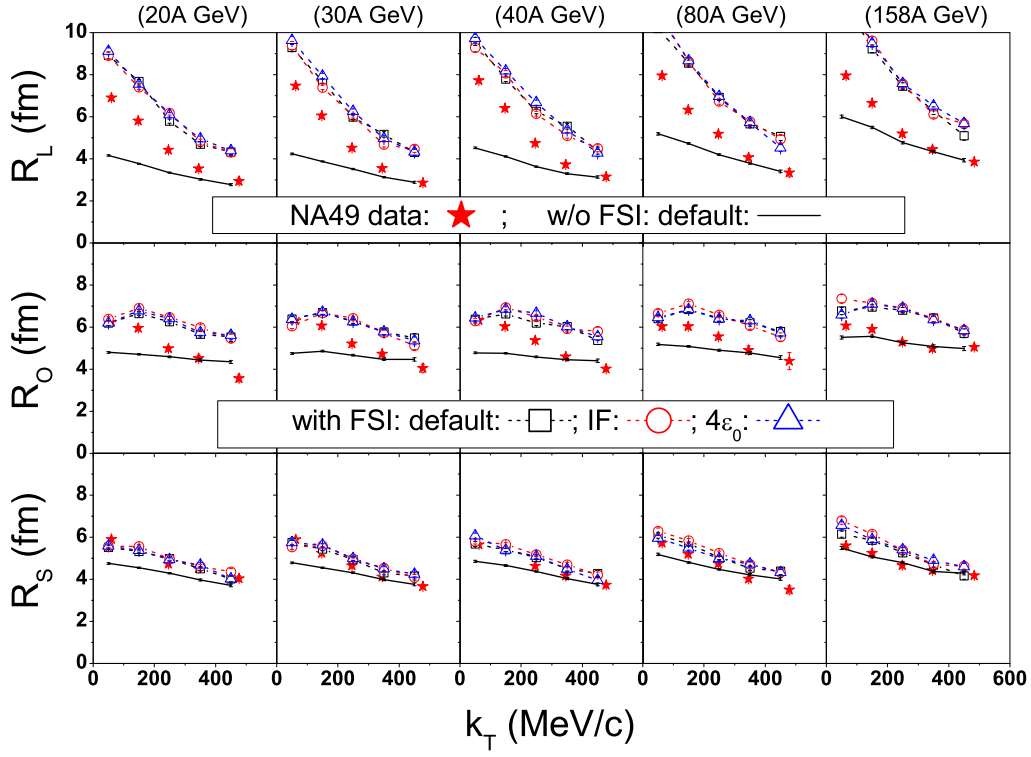

Figure 12.3: k_T dependence of the HBT radii R_L, R_O, and R_S (at midrapidity) for central HICs at SPS energies ($E_{\rm lab} = 20A$, $30A$, $40A$, $80A$, and $158A$ GeV). The NA49 data are indicated by solid stars [Alt08b]. The HG-EoS is employed in all calculations but under different freeze-out conditions: 1) without FSI, calculations with default hydro-freeze-out criteria (GF, $5 \cdot \varepsilon_0$) are depicted by lines. 2) full hybrid model calculations with two different cuts of the energy density (default and $4 \cdot \varepsilon_0$) for the GF and with the default cut of the energy density for the IF are depicted by dashed lines with symbols.

time since the expansion lasts longer [1]. The on-the-average longer freeze-out time leads to an apparently larger size of the pion source. Furthermore, it is clear (and expected) that the EoS with larger latent heat (such as in the BM mode) leads to a longer emission duration of the particles (as seen in Fig. 12.2 when $t_f \gtrsim 15\text{fm}/c$) so that it produces larger HBT radii. This behaviour is clearly seen in the more time-dependent directions R_L and R_O. This behaviour might be improved by allowing particles also to freeze out and fly into the detector at all times of the collision. Especially, if there are fast pions produced during the first hard collisions in UrQMD at the edge of the system they should be able to fly into the detector without being forced into the hydrodynamic evolution.

Fig. 12.3 illustrates the k_T dependence of the HBT radii under various freeze-out con-

[1] This might change, if a continuous emission approach is used for the hydrodynamic model e.g. suggested in [Gra95, Kno08].

ditions, which may be divided into two parts: 1) without FSI and 2) with FSI after the hydrodynamic phase. Here, without FSI (lines) means that the evolution is stopped immediately after the Cooper-Frye freeze-out from the hydrodynamic phase (GF and $5 \cdot \varepsilon_0$ are adopted as default hydro-freeze-out criteria), with instantaneous resonance decays. The observed size of the pion source is small at this hydrodynamic freeze-out. In previous investigations [Pet08b] it has been found that binary baryon-meson and meson-meson collisions still frequently happen after the hydrodynamic freeze-out. In baryon-meson reactions, the most abundant interactions are the excitation and the decay of the Δ resonance (i.e. $\Delta \rightleftharpoons \pi N$), while in meson-meson collisions, the $\rho \rightleftharpoons \pi\pi$ process is dominant. A large number of these final hadron interactions in which pions are involved contribute significantly to the final HBT radii of pions.

Let us therefore explore if the finally observed HBT radii do depend on the transition criterion from hydrodynamics to the transport model. The full hybrid model calculations (dashed lines with open symbols) are shown with two different cuts of the energy density ($5 \cdot \varepsilon_0$ as default and $4 \cdot \varepsilon_0$) for the GF and with the energy density cut $5 \cdot \varepsilon_0$ for the IF. It is found that the final state interactions are sufficient that the effects of different treatments of the hydrodynamic freeze-out on the final HBT radii are almost totally washed out in all directions and at all investigated energies.

Let us finally explore the dependence of the R_O/R_S ratio on the different EoS and freeze-out prescriptions. This ratio was expected to be sensitive to the duration time of the homogeneity region. In Fig. 12.4 the excitation function of the R_O/R_S ratio with the different EoS (lines with solid symbols) and freeze-out prescriptions (dashed lines with open symbols) are shown. The k_T bin $200 - 300\text{MeV}/c$ is chosen. The result for the pure cascade calculation is also shown as a baseline (dotted line). It is seen clearly that the R_O/R_S ratio is sensitive to the EoS, but not to the various hydrodynamic freeze-out prescriptions when including FSI (shown as open triangles and open inverted triangles) as it has already been implied from the results of the HBT radii shown in Figs. 12.1 and 12.3. With increasing latent heat which corresponds to the softness of EoS implied from Fig. 6.4, the R_O/R_S ratio is increased. The "excessively" large latent heat in BM-EoS results in a long duration time of the pion source and hence a large R_O/R_S ratio. Although the overall height is largely overpredicted by the BM-EoS, the qualitative behaviour of the data (with a maximal lifetime at beam energies around $40 - 100A$ GeV) is well reproduced. In addition, the "peak structure" is less pronounced than in previous predictions [Ris96b], due to the different initial state and seems to provide a more reasonable estimate of the magnitude of the lifetime enhancement.

The chiral EoS CH exhibits a lower R_O/R_S ratio because the first-order phase transition is less pronounced. The calculation with HG mode (line with solid squares) leads to the smallest R_O/R_S ratio due to the most stiffest EoS among the three ones. The result of the cascade calculation lies in between the CH and the BM modes, which implies a relatively soft EoS. It can be understood since in the pure UrQMD model the new particle production is treated either as a resonance decay or a fragmentation of the string, which introduces a finite lifetime and hence leads to a softer EoS. After considering the

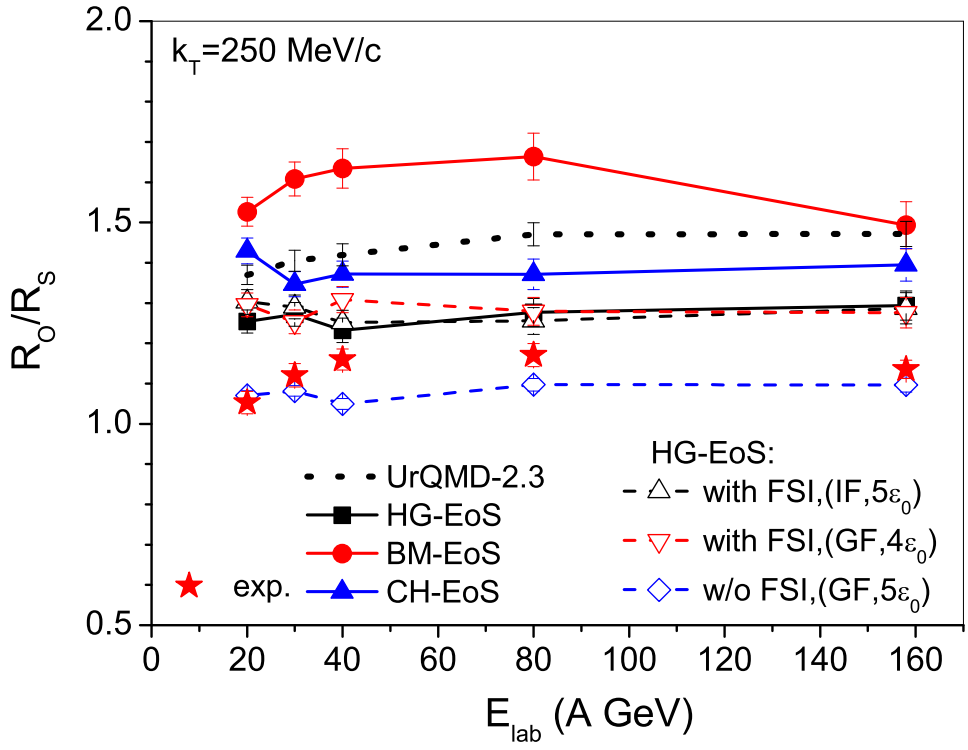

Figure 12.4: Excitation function of the R_O/R_S ratio at $k_T = 250\text{MeV}/c$. The NA49 data are indicated by solid stars [Alt08b]. UrQMD cascade calculation is shown by dotted line. Hybrid model calculations with EoS of HG, BM, and CH and with FSI are shown by lines with solid symbols (the default hydro-freeze-out criteria (GF, $5 \cdot \varepsilon_0$) are used). In the HG-EoS mode, various criteria of freeze-out, (IF, $5 \cdot \varepsilon_0$) and (GF, $4 \cdot \varepsilon_0$) with FSI, and the default (GF, $5 \cdot \varepsilon_0$) without FSI are shown by dashed lines with open symbols.

mean field potentials for both confined and "pre-formed" particles [Li08a, Li08c], which gives a strong repulsion at the early stage, the R_O/R_S ratio was seen to decrease in line with results obtained here.

For the full hybrid model calculation the different freeze-out prescriptions do not affect the final results (when comparing the results by dashed lines with open triangles with that by the line with solid squares). The calculation with HG-EoS but without FSI (dashed line with open diamonds) seems to provide the best description of the data, but, seems clearly unphysical to the authors as a solution to the duration time problem.

13 Summary

In this thesis the first fully integrated Boltzmann+hydrodynamics approach to relativistic heavy ion reactions has been developed. After a short introduction that motivates the study of heavy ion reactions as the tool to get insights about the QCD phase diagram, the most important theoretical approaches to describe the system have been reviewed. Lattice QCD is very useful to compute thermodynamic properties directly from the QCD Lagrangian, but it is restricted by approximations due to the finite size lattices and cannot be applied to dynamical simulations. To extract chemical freeze-out temperatures and baryo-chemical potentials statistical models that fit final state particle abundancies according to grand-canonical distributions are widely used. To model the dynamical evolution of the collective system assuming local thermal equilibrium ideal hydrodynamics seems to be a good tool. Nowadays, the development of either viscous hydrodynamic codes or hybrid approaches is favoured. For the microscopic description of the hadronic as well as the partonic stage of the evolution transport approaches have beeen successfully applied, since they generate the full phse-space dynamics of all the particles.

The hadron-string transport approach that this work is based on is the Ultra-relativistic Quantum Molecular Dynamics (UrQMD) approach. It constitutes an effective solution of the relativistic Boltzmann equation and is restricted to binary collisions of the propagated hadrons. Therefore, the Boltzmann equation and the basic assumptions of this model have been introduced. Recent developments like the inclusion of PYTHIA for hard scatterings and a new treatment of high mass resonances have been described and the current status of the results obtained within this approach have been discussed in the context of the available data. Overall, UrQMD-2.3 calculations agree well to the experimental data for the multiplicities and mean transverse momenta in the whole energy range from $E_{\mathrm{lab}} = 2A$ GeV to $\sqrt{s}_{\mathrm{NN}} = 200$ GeV in p+p as well as in A+A collisions. Apart from the success of transport simulations to describe spectra and yields certain problems remain, like e.g. underprediction of the strange particle abundancies, too small elliptic flow values above SPS energies and HBT radii hint to a very small R_o/R_s ratio. These observables that are sensitive to the early stage of the collision (pressure) or to the approach of thermal and chemical equilibrium during the collision history hint to the fact that a purely hadronic transport model may not be sufficient to describe the dynamics of the hot and dense stage of heavy ion reactions at higher energies. Therefore, these observations exemplify the need to embed a full three-dimensional relativistic fluid dynamics description for these stages of the reaction.

Furthermore, predictions for the charged particle multiplicities at LHC energies have

been made. UrQMD describes the charged particle pseudorapidity spectra in p+$\bar{\text{p}}$ as well as for Pb+Pb/Au+Au collisions up to Tevatron energies. Furthermore, it also describes the energy dependence of charged particles in mid-pseudorapidity in p+$\bar{\text{p}}$ and Pb+Pb/Au+Au collisions. The observed similar RMS-width of the charged particle pseudorapidity distribution in p+$\bar{\text{p}}$ and Pb+Pb/Au+Au collisions can also be described within the present transport appraoch. At LHC $dN_{ch}/d\eta\,|_{14\text{A TeV p+p}} \approx 6.3$ and $dN_{ch}/d\eta\,|_{5.5\text{ TeV Pb+Pb}} \approx 2000$ have been predicted.

The next step has been the development of a new framework to calculate the baryon number density in a transport approach. The density is the zero component of the net baryon number current in the local rest frame. The corresponding four-vector has been calculated by a sum of Gaussian distributions that represent the particles and is boosted with the velocity of the local rest frame. Time evolutions of the net baryon number and the quark density have been calculated at AGS, SPS and RHIC energies and the new approach leads to reasonable results over the whole energy range.

Studies of phase diagram trajectories using hydrodynamics have been performed as a first move into the direction of the development of the hybrid approach. Calculating the initial conditions of an heavy ion collision with the UrQMD model, yields very similar S/A values for a given beam energy as the simple overlap model. An isentropic expansion scenario has been compared to a full (3+1)dimensional ideal hydrodynamic evolution with a chiral EoS including a CEP with constant S/A lines. For the hydro evolution, the systems mean values of energy- and baryon-density follow isentropic paths in the $\epsilon - n$ phase-diagram, while in the $T - \mu$ plane, a single cell follows the isentropic path, while the averaged quantities deviate from the isentropic expectation. Most importantly it was shown, that concerning the search for the critical end point, it might not be sufficient to apply a free hadron gas EoS to estimate the energy needed to generate a system that, during its expansion, goes through the critical region. Applying different EoS (as we have done) can very much change predictions at what beam energy that CEP is reached.

The hybrid approach that has been developed as the main part of this thesis is based on the UrQMD transport approach with an intermediate hydrodynamical evolution for the hot and dense stage of the collision. The specific coupling procedure including the initial conditions and the freeze-out prescription have been explained. The initial energy and baryon number density distributions are not smooth and not symmetric in any direction and the initial velocity profiles are non-trivial since they are generated by the non-equilibrium transport approach. The fulll (3+1) dimensional ideal relativistic one fluid dynamics evolution is solved using the SHASTA algorithm. For the present work, three different equations of state have been used, namely a hadron gas equation of state without a QGP phase transition, a chiral EoS and a bag model EoS including a strong first order phase transition. For the freeze-out transition from hydrodynamics to the cascade calculation two different set-ups are employed. Either an in the computational frame isochronous freeze-out or an gradual freeze-out that mimics an iso-eigentime criterion. The particle vectors are generated by Monte Carlo methods according to the Cooper-Frye formula and UrQMD takes care of the final decoupling procedure of the

particles. The event-by-event character of the hybrid approach has been emphasized.

The present implementation allows to compare pure microscopic transport calculations with hydrodynamic calculations using exactly the same initial conditions and freeze-out procedure. The parameter dependences of the model have been investigated and the time evolution of different quantities have been explored. These tests have led to the conclusion that the choice of the starting time and the freeze-out criterium does generally alter the multiplicities and transverse mass spectra only on a 20% level. The time evolution has shown that there are no discontinuities at the switching times in the hybrid model calculation. The importance of the final state interactions has been emphasized by demonstrating that there is still resonance regeneration after the hydrodynamic evolution.

The effects of the change in the underlying dynamics - ideal fluid dynamics vs. non-equilibrium transport theory - have been explored. The final pion and proton multiplicities are lower in the hybrid model calculation due to the isentropic hydrodynamic expansion while the yields for strange particles are enhanced due to the local equilibrium in the hydrodynamic evolution. The results of the different calculations for the mean transverse mass excitation function, rapidity and transverse mass spectra for different particle species at three different beam energies have been discussed in the context of the available data. The transverse expansion of the system is much faster in the hybrid model calculation, especially at higher energies which leads to differences in the observables that are sensitive to the transverse dynamics. This finding indicates qualitatively that "new" physical effects like, e.g., non-equilibrium effects or a phase transition have to be taken into account.

The system and centrality dependence of strange (anti-)hyperons at $40A$ and $158A$ GeV from the UrQMD and the hybrid model have been investigated. The predicted centrality dependence of the rapidity spectra for Λ, $\bar{\Lambda}$ and Ξ^- in Pb+Pb collisions at $E_{\mathrm{lab}} = 40A$ GeV and $E_{\mathrm{lab}} = 158A$ GeV have been shown where it is visible that due to the thermal production of strangeness in the UrQMD+Hydro model a higher hyperon yield is generated. Compared to Pb+Pb collisions the system is not fully thermalized in C+C and Si+Si collisions and therefore using only UrQMD gives a better description of the measured rapidity spectra. The conclusion is that full thermalization is only reached for central Pb+Pb collision. The production of strange (anti-)hyperons in smaller systems like C+C and Si+Si can be described with a transport approach like UrQMD.

The elliptic flow values at SPS energies have been shown to be in line with an ideal hydrodynamic evolution if a proper initial state is used and the final freeze-out proceeds gradually. The hybrid model calculation is able to reproduce the experimentally measured integrated as well as transverse momentum dependent v_2 values for charged particles. This points to the fact that the treatment of initial conditions and freeze-out is crucial for any hydrodynamic calculation.

The multiplicity and mean transverse mass excitation function has been calculated for pions, protons and kaons in the energy range from $E_{\mathrm{lab}} = 2-160A$ GeV. The dependence of the results on a change of the freeze-out prescription has been investigated. It has

been observed that the different freeze-out procedures have almost as much influence on the mean transverse mass excitation function as the EoS. A comparison to the available data suggests that a gradual transition from hydrodynamics to the transport simulation at an energy density of $5\epsilon_0$ provides the best description of the data. The experimentally observed step-like behaviour of the mean transverse mass excitation function is only reproduced, if a first order phase transition with a large latent heat is applied or the EoS is effectively softened due to non-equilibrium effects in the hadronic transport calculation.

The HBT correlation of the negatively charged pion source created in central Pb+Pb collisions at SPS energies have been investigated with the hybrid model. Different settings have been explored, one where the EoS has been varied without changing the initial conditions and the freeze-out prescription and another where the EoS was fixed and the treatment of the freeze-out has been changed. A systematic investigation of these effects on the HBT radii has been presented. It has been found that the latent heat influences the emission of particles visibly and hence the HBT radii of the pion source. The final hadronic interactions after the hydrodynamic freeze-out are very important for the HBT correlation since a large amount of collisions and decays still takes place during this period. The details of the hydro-freeze-out prescription do not affect the HBT radii as well as the R_O/R_S ratio as long as the final state interactions in the subsequent hadronic transport model were taken into account. Overall, the HBT data seem to favor a stiff EoS, but one should also keep in mind that viscosity effects are neglected during the hydrodynamic stage and that the particle emission from the early stages should be handled more carefully.

Overall, the careful treatment of initial conditions and the freeze-out procedure has been proven to be very important in hydrodynamic calculations. To resolve the remaining problems a dynamical coupling of a transport and a hydrodynamic description including source terms on both sides is a promising idea. Furthermore, the inclusion of viscosity during the hydrodynamic evolution might give more insights about the transport properties of the hot and dense QCD matter. To extend the scope of the hybrid approach to higher beam energies would be useful to cross check the results with different approaches which are mostly applied at RHIC and LHC energies.

Appendices

A Lorentz-Contraction of the Gaussian

In heavy ion collisions at higher energies the nuclei are highly contracted and resemble rather thin disks than spherical balls. Therefore, one has to account for this contraction also in the density calculation. In the PhD thesis of Henning Weber [Web02] this issue has already been adressed. It has been stated there that the right thing to do is a fully three-dimensional contraction in the following way. Since one deals with an effective one-dimensional Gaussian with a somehow defined three-distance as the argument one only has to know the Lorentz-contraction in this direction. In the quoted thesis one copes with this problem by applying the scalar product between the velocity and the relative distance. Then the gaussians look like this:

$$P = N \exp\left(-\frac{(\vec{r}-\vec{r_0})^2\gamma^2\left[\frac{(\vec{r}-\vec{r_0})\cdot\vec{\beta}}{|\vec{r}-\vec{r_0}|}\right]}{2\sigma^2}\right), \quad \text{with } \gamma[v] = \frac{1}{\sqrt{1-v^2}} \tag{A.1}$$

This definition reduces to the right limits in the special cases where the particle flies parallel/orthogonal to the direction which should be contracted. In the first case the scalar product reduces to the product of the absolute values, so we get the usual definition for $\gamma(\beta)$. In the second case the scalar product is zero and $\gamma = 1$.

The problem with this ansatz is the normalization. The only reasonable idea is numerical calculation of the normalization factor for different velocities with the aim to get a parametrization for the normalization factor. The results of these integrations show the problem that with the definition in Eqn. A.1 one cannot easily normalize because the gamma factor for the normalization has to be another one than in the exponential and things become extremely complicated and messy.

The only possibility is to rotate into the coordinate system where the normalization is clear because the contracted direction defines one axis of the system and to transform then back into the old system. But this does not resolve the problem that always all dimensions are contracted.

Another idea is to contract the different directions with their individual γ-factors:

$$P = \left(\frac{1}{\sqrt{2\pi}\sigma}\right)^3 \gamma_x\,\gamma_y\,\gamma_z \exp\left(-\frac{x^2\gamma_x^2 + y^2\gamma_y^2 + z^2\gamma_z^2}{2\sigma^2}\right) \tag{A.2}$$

But this would result in a smaller sphere if the particle moves with $\beta_x = \beta_y = \beta_z$ which is also not the right thing to do.

The final solution is to take into account only the Lorentz-contraction in z-direction. This has been checked to be reasonable because $\gamma_x, \gamma_y \ll \gamma_z$ in our case. The full three-dimensional, in z-direction contracted and correctly normalized gaussian looks like:

$$P = \left(\frac{1}{\sqrt{2\pi}\sigma}\right)^3 \gamma_z \exp\left(-\frac{x^2 + y^2 + z^2\gamma_z^2}{2\sigma^2}\right) \tag{A.3}$$

with $\gamma_z = \frac{1}{\sqrt{1-\beta_z^2}}$. One has to take care of the fact that now also the normalization is not the same for all particles but differs due to the different γ factors.

B Rest Frame Method

The idea is to calculate the density in the rest frame of particle i. We know the velocity $\vec{\beta}_i = \frac{\vec{p}_i}{E_i}$ of this particle, so we can perform a general lorentz boost (see Eqn. 5.2) into the rest frame of this particle using its velocity. Now, we have the information for all particles in the rest frame of particle i. To evaluate a distance which is necessary for the density calculation they have to be at the same time. Since we have performed a lorentz boost from the computational frame, where they are at equal times but different positions, the particles are most likely at different times after the transformation. Therefore, they are propagated to the same time of particle i according to:

$$\vec{r}_j = \vec{r}_j + \vec{\beta}_j \cdot \Delta t \,, \tag{B.1}$$

where $\Delta t = t_j - t_i$. After that, it is possible to calculate the density with the usual three-distance $|\vec{r_i} - \vec{r_j}|$ in the local rest frame of particle i as the argument for the gaussians. One still has to take care of the lorentz contraction of the gaussians due to the relative velocity of particle j to particle i. This can be done according to the method which discussed in Appendix A (see Eqn. A.1).

The problem with this method is that we assume some kind of equilibrium if we propagate the particles j on straight lines to a new timestep because we do not care about the real collision history of each individual particle but assume that it does not matter where particle A or B is. Otherwise, it is not clear, if this is really the density one is interested in, because the particle i does not contribute to this density and one cannot have the situation that a particle is moving through this density. Furthermore, the gaussians are not properly normalized.

To avoid the problems with the lorentz contraction of the gaussians one can furthermore perform a rotation (after boost into the rest frame of particle i and the additional propagation of particles j) into the coordinate system where one axis is parallel to the relative vector between two particles. So one axis is defined by:

$$\hat{r_\parallel} = \frac{\vec{r}_j - \vec{r}_i}{|\vec{r}_j - \vec{r}_i|} \,, \tag{B.2}$$

where all quantities $\vec{r}$ are given in the rest frame of particle i. One has to construct two more unit vectors which form an orthogonal system with the vector $\hat{r_\parallel}$. The first can be found easily by using the requirement that the scalar product has to vanish. The third vector can be calculated via the cross product of the first two. In this new coordinate system one can now calculate the real three-dimensional gaussian with only

one direction lorentz-contracted. The result is that the gaussians in the two orthogonal directions are 1 because the argument is by construction zero, so this falls back to the case that is discussed above.

$$(\vec{r}_j \cdot \vec{r}_{\perp 1}) - (\vec{r}_i \cdot \vec{r}_{\perp 1}) = (\vec{r}_j - \vec{r}_i) \cdot \vec{r}_{\perp 1} = 0 \tag{B.3}$$

So this reduces to the gaussian with the usual three-distance as the argument and lorentz-contraction only in this direction.

$$\begin{aligned}
(\vec{r}_j \cdot \hat{r}_{\parallel}) - (\vec{r}_i \cdot \hat{r}_{\parallel}) &= (\vec{r}_j - \vec{r}_i) \cdot \hat{r}_{\parallel} && \text{(B.4)} \\
&= (\vec{r}_j - \vec{r}_i) \frac{\vec{r}_j - \vec{r}_i}{|\vec{r}_j - \vec{r}_i|} && \text{(B.5)} \\
&= |\vec{r}_j - \vec{r}_i| = \sqrt{(x_j - x_i)^2 + (y_j - y_i)^2 + (z_j - z_i)^2} && \text{(B.6)} \\
& && \text{(B.7)}
\end{aligned}$$

This does not help out of the normalization problem because it is not clear at all which γ factor should be used.

C Explicit Calculation of t_{start}

Here is the explicit calculation for the starting time. The starting point is the geometric overlap criterium

$$t_{start} = \frac{\text{length}}{\text{velocity}} = \frac{D}{\gamma v} = \frac{2R}{\gamma v}\,. \tag{C.1}$$

One can express the velocity through the gamma factor

$$\begin{aligned}
\gamma &= \frac{1}{\sqrt{1-v^2}} && \text{(C.2)}\\
\gamma^2 &= \frac{1}{1-v^2} && \text{(C.3)}\\
1-v^2 &= \frac{1}{\gamma^2} && \text{(C.4)}\\
v^2 &= -\left(\frac{1}{\gamma^2}-1\right) = 1-\frac{1}{\gamma^2} && \text{(C.5)}\\
v &= \sqrt{1-\frac{1}{\gamma^2}} = \frac{1}{\gamma}\sqrt{\gamma^2-1} && \text{(C.6)}\\
\Rightarrow t_{start} &= \frac{2R}{\gamma v} = \frac{2R}{\sqrt{\gamma^2-1}}\,. && \text{(C.7)}\\
& && \text{(C.8)}
\end{aligned}$$

From now on, we have to decide between the two cases. First, we will consider the case where E_{lab} is the total energy in the laboratory frame.

$$
\begin{aligned}
E_{\text{lab}} &= \sqrt{m_1^2 + p_{lab}^2} && \text{(C.9)}\\
E_{\text{CM}} &= 2\gamma m_N \Rightarrow \gamma = \frac{E_{\text{CM}}}{2m_N} && \text{(C.10)}\\
E_{\text{CM}} &= (m_1^2 + m_2^2 + 2E_{\text{lab}} m_2)^{\frac{1}{2}} && \text{(C.11)}\\
&= (2m_N^2 + 2E_{\text{lab}} m_N)^{\frac{1}{2}} && \text{(C.12)}\\
\Rightarrow \gamma &= \frac{\sqrt{2m_N^2 + 2E_{\text{lab}} m_N}}{2m_N} = \frac{\sqrt{2m_N(m_N + E_{\text{lab}})}}{2m_N} && \text{(C.13)}\\
&= \sqrt{\frac{m_N + E_{\text{lab}}}{2m_N}} = \sqrt{\frac{E_{\text{lab}}}{2m_N} + \frac{1}{2}} && \text{(C.14)}\\
\rightarrow t_{start} &= \frac{2R}{\sqrt{\gamma^2 - 1}} = \frac{2R}{\sqrt{\frac{E_{\text{lab}}}{2m_N} + \frac{1}{2} - 1}} = \frac{2R}{\sqrt{\frac{E_{\text{lab}}}{2m_N} - \frac{1}{2}}} && \text{(C.15)}\\
& && \text{(C.16)}
\end{aligned}
$$

The second case which is actually used in the final program is the one where E_{lab} corresponds only to the kinetic energy.

$$
\begin{aligned}
E_{\text{CM}} &= 2\gamma m_N \Rightarrow \gamma = \frac{E_{\text{CM}}}{2m_N} && \text{(C.17)}\\
E_{\text{CM}} &= \sqrt{s} = \sqrt{p^2 + m^2} && \text{(C.18)}\\
&= \sqrt{E_{\text{lab}} \cdot 2m_N + 4m_N^2} && \text{(C.19)}\\
\gamma &= \frac{\sqrt{E_{\text{lab}} \cdot 2m_N + 4m_N^2}}{2m_N} && \text{(C.20)}\\
&= \frac{\sqrt{2m_N(E_{\text{lab}} + 2m_N)}}{2m_N} = \sqrt{\frac{(E_{\text{lab}} + 2m_N)}{2m_N}} && \text{(C.21)}\\
&= \sqrt{\frac{E_{\text{lab}}}{2m_N} + 1} && \text{(C.22)}\\
\rightarrow t_{start} &= \frac{2R}{\sqrt{\gamma^2 - 1}} = \frac{2R}{\sqrt{\frac{E_{\text{lab}}}{2m_N} + 1 - 1}} = \frac{2R}{\sqrt{\frac{E_{\text{lab}}}{2m_N}}} && \text{(C.23)}\\
&= \frac{2R\sqrt{2m_N}}{\sqrt{E_{\text{lab}}}} && \text{(C.24)}
\end{aligned}
$$

D Chiral Lagrangian

In mean-field approximation, the expectation values of the scalar fields relevant for symmetric nuclear matter correspond to the non-strange and strange chiral quark condensates, namely the σ and its $s\bar{s}$ counterpart ζ, respectively, and further the ω and ϕ vector meson fields. Another scalar iso-scalar field, the dilaton χ, is introduced to model the QCD scale anomaly. However, if χ does not couple strongly to baryonic degrees of freedom it remains essentially "frozen" below the chiral transition [Pap99]. Consequently, we focus here on the role of the quark condensates.

Interactions between baryons and scalar (BM) or vector (BV) mesons, respectively, are introduced as

$$\mathcal{L}_{\rm BM} = -\sum_i \overline{\psi}_i \left(g_{i\sigma}\sigma + g_{i\zeta}\zeta\right)\psi_i \ , \tag{D.1}$$

$$\mathcal{L}_{\rm BV} = -\sum_i \overline{\psi}_i \left(g_{i\omega}\gamma_0\omega^0 + g_{i\phi}\gamma_0\phi^0\right)\psi_i \ , \tag{D.2}$$

Here, i sums over the baryon octet (N, Λ, Σ, Ξ). A term $\mathcal{L}_{\rm vec}$ with mass terms and quartic self-interaction of the vector mesons is also added:

$$\mathcal{L}_{\rm vec} = \frac{1}{2}a_\omega\chi^2\omega^2 + \frac{1}{2}a_\phi\chi^2\phi^2 + g_4^4(\omega^4 + 2\phi^4) \ .$$

The scalar self-interactions are

$$\begin{aligned}\mathcal{L}_0 = & -\frac{1}{2}k_0\chi^2(\sigma^2+\zeta^2) + k_1(\sigma^2+\zeta^2)^2 + k_2(\frac{\sigma^4}{2}+\zeta^4) \\ & + k_3\chi\sigma^2\zeta - k_4\chi^4 - \frac{1}{4}\chi^4\ln\frac{\chi^4}{\chi_0^4} + \frac{\delta}{3}\chi^4\ln\frac{\sigma^2\zeta}{\sigma_0^2\zeta_0} \ .\end{aligned} \tag{D.3}$$

Interactions between the scalar mesons induce the spontaneous breaking of chiral symmetry (first line) and the scale breaking via the dilaton field χ (last two terms).

Non-zero current quark masses break chiral symmetry explicitly in QCD. In the effective Lagrangian this corresponds to terms such as

$$\mathcal{L}_{\rm SB} = -\frac{\chi^2}{\chi_0^2}\left[m_\pi^2 f_\pi\sigma + (\sqrt{2}m_K^2 f_K - \frac{1}{\sqrt{2}}m_\pi^2 f_\pi)\zeta\right] \ . \tag{D.4}$$

According to $\mathcal{L}_{\rm BM}$ (D.1), the effective masses of the baryons, $m_i^*(\sigma,\zeta) = g_{i\sigma}\,\sigma + g_{i\zeta}\,\zeta$, are generated through their coupling to the chiral condensates, which attain non-zero vacuum expectation values due to their self-interactions [Pap99] in $\mathcal{L}_0$ (D.3). The effective

masses of the mesons are obtained as the second derivatives of the mesonic potential $\mathcal{V}_{\rm Meson} \equiv -\mathcal{L}_0 - \mathcal{L}_{\rm vec} - \mathcal{L}_{\rm SB}$ about its minimum.

The baryon-vector couplings $g_{i\omega}$ and $g_{i\phi}$ result from pure f-type coupling as discussed in [Pap99], $g_{i\omega} = (n_q^i - n_{\bar{q}}^i) g_8^V$, $g_{i\phi} = -(n_s^i - n_{\bar{s}}^i)\sqrt{2} g_8^V$, where g_8^V denotes the vector coupling of the baryon octet and n^i the number of constituent quarks of species i in a given hadron. The resulting relative couplings agree with additive quark model constraints.

All parameters of the model discussed so far are fixed by either symmetry relations, hadronic vacuum observables or nuclear matter saturation properties (for details see [Pap99]). In addition, the model also provides a satisfactory description of realistic (finite-size and isospin asymmetric) nuclei and of neutron stars [Pap99, Scr03, Scr02].

If the baryonic degrees of freedom are restricted to the members of the lowest lying octet, the model exhibits a smooth decrease of the chiral condensates (crossover) for both high T and high μ [Pap99, Zsc02a]. However, additional baryonic degrees of freedom may change this into a first-order phase transition in certain regimes of the T-μ_q plane, depending on the couplings [The83, Zsc02a, Zsc05]. To model the influence of such heavy baryonic states, we add a single resonance with mass $m_R = m_0 + g_R \sigma$ and vector coupling $g_{R\omega} = r_V g_{N\omega}$.

In what follows, the meson fields are replaced by their (classical) expectation values, which corresponds to neglecting quantum and thermal fluctuations. Fermions have to be integrated out to one-loop. The grand canonical potential can then be written as

$$\begin{aligned} \Omega/V &= -\mathcal{L}_{\rm vec} - \mathcal{L}_0 - \mathcal{L}_{\rm SB} - \mathcal{V}_{\rm vac} \\ &\quad - T \sum_{i \in B} \frac{\gamma_i}{(2\pi)^3} \int d^3k \left[\ln\left(1 + e^{-\frac{1}{T}[E_i^*(k) - \mu_i^*]}\right)\right] \\ &\quad + T \sum_{l \in M} \frac{\gamma_l}{(2\pi)^3} \int d^3k \left[\ln\left(1 - e^{-\frac{1}{T}[E_l^*(k) - \mu_l^*]}\right)\right], \end{aligned} \tag{D.5}$$

where γ_B, γ_M denote the baryonic and mesonic spin-isospin degeneracy factors and $E^*_{B,M}(k) = \sqrt{k^2 + {m^*_{B,M}}^2}$ are the corresponding single particle energies. In the second line we sum over the baryon octet states plus the additional heavy resonance with degeneracy γ_R (assumed to be 16). The effective baryo-chemical potentials are $\mu_i^* = \mu_i - g_{i\omega}\omega - g_{i\phi}\phi$, with $\mu_i = (n_q^i - n_{\bar{q}}^i)\mu_q + (n_s^i - n_{\bar{s}}^i)\mu_s$. The chemical potentials of the mesons are given by the sum of the corresponding quark and anti-quark chemical potentials. The vacuum energy $\mathcal{V}_{\rm vac}$ (the potential at $\rho_B = T = 0$) has been subtracted.

By extremizing Ω/V one obtains self-consistent gap equations for the meson fields. Here, globally non-strange matter is considered and μ_s for any given T and μ_q is adjusted to obtain a vanishing net strangeness. The dominant "condensates" are then the σ and the ω fields. There have also been first attempts to model the dynamical evolution of the condensates themselves instead of 'locking' them at their equilibrium values (see e.g. [Pae03, Pae05]).

E Particle Density Integration

The relativistic Boltzmann distribution is also called the Jüttner distribution and looks like

$$f(x,p) = \frac{g}{(2\pi)^3} e^{-\left(\frac{p_\mu u^\mu}{T}\right)} \tag{E.1}$$

The particle density in one cell is

$$\frac{N_{\text{cell}}}{V_{\text{cell}}} = n = u_\mu N^\mu = u_\mu \int \frac{d^3p}{E} p^\mu f(x,p) \tag{E.2}$$

$$= \frac{g}{(2\pi)^3} \int \frac{d^3p}{E} p_\mu u^\mu e^{-\left(\frac{p_\mu u^\mu}{T}\right)} \tag{E.3}$$

In the local rest frame the velocity vector simplifies to $u^\mu = (1,0,0,0)$. Since $p^\mu = (E, p_x, p_y, p_z)$ the scalar product is

$$p_\mu u^\mu = E \tag{E.4}$$

The remaining integral is

$$n = \frac{g}{(2\pi)^3} \int \frac{d^3p}{E} E e^{-E/T} \tag{E.5}$$

$$= \frac{g4\pi}{(2\pi)^3} \int_0^\infty dp p^2 e^{-\sqrt{p^2+m^2}/T} \tag{E.6}$$

With the substitution $x = \sqrt{p^2+m^2} \rightarrow p = \sqrt{x^2-m^2}$ and $dp = (x^2-m^2)^{-(1/2)} x dx$ the integral has the form

$$\int_m^\infty dx x \sqrt{x^2-m^2} e^{-x/T} \tag{E.7}$$

which has the modified Bessel functions as a result. The final result depends only on the temperature and the mass. The fugacity factor That is influenced by the chemical potential can be factorized and taken as a constant factor. In the local rest frame (=LRF) the particle number density is

$$N^\mu u_\mu = n = \rho = \rho u_\mu u^\mu \tag{E.8}$$

where ρ is really the particle density. In all other frames n is just some number, but does not necessarily have the physical meaning of a particle number density. This is the number we have calculated by solving the integral over the momentum ditribution. For

the implementation we need the particle number density in the computational frame because we know the volume only in this frame. So

$$N^{\mu}_{\mathrm{CF}} = (\gamma\rho_{\mathrm{LRF}}, \gamma\vec{\beta}\rho_{\mathrm{LRF}}) \tag{E.9}$$

and the zero-component of this vector is the wanted quantity. The particle number has to be the same in both frames. This assumption leads to

$$\begin{aligned} \mathrm{LRF}: \rho_{\mathrm{LRF}} \cdot V_{\mathrm{LRF}} &= N & \text{(E.10)} \\ \mathrm{CF}: \underbrace{\rho_{\mathrm{CF}}}_{=\gamma\rho_{\mathrm{LRF}}} \cdot V_{\mathrm{CF}} &= N & \text{(E.11)} \\ \Rightarrow N &= \rho_{\mathrm{LRF}} \underbrace{\gamma V_{\mathrm{CF}}}_{V_{\mathrm{LRF}}} \text{ with } \gamma = u^0_{\mathrm{CF}} & \text{(E.12)} \end{aligned}$$

F Maximum of the Momentum Distribution

During the freeze-out process the particles get randomly chosen momenta according to the respective boosted Fermi or Bose distribution. To use the rejection method in an effective way that is not too time-consuming one has too find the maximum of the distribution. The distribution to be considered is

$$
\begin{aligned}
f(\vec{p}) &= \frac{1}{exp\left(\frac{p_\mu u^\mu - \mu}{T}\right) + \alpha} \quad p_\mu u^\mu = \gamma(p^0 - \vec{p}\cdot\vec{v}) && \text{(F.1)}\\
&= \frac{1}{exp\left(\frac{\gamma(p^0 - \vec{p}\cdot\vec{v}) - \mu}{T}\right) + \alpha} && \text{(F.2)}\\
&= \frac{1}{exp(\underbrace{\frac{\gamma}{T}}_{\beta}(p^0 - \vec{p}\cdot\vec{v}))\cdot\underbrace{exp\left(-\frac{\mu}{T}\right)}_{\delta} + \alpha} \quad \text{with } E = \sqrt{p^2 + m^2} && \text{(F.3)}\\
&= (\delta \cdot exp[\beta(\sqrt{\vec{p}^2 + m^2} - \vec{p}\cdot\vec{v})] + \alpha)^{-1} && \text{(F.4)}\\
& && \text{(F.5)}
\end{aligned}
$$

We have to calculate now the derivative in three dimensions, the gradient. As an example, the p_x derivative is shown here.

$$
\begin{aligned}
\frac{\partial f}{\partial p_x} &= -1\left[\delta exp[\beta(\sqrt{p^2 + m^2} - \vec{p}\cdot\vec{v})] + \alpha\right]^{-2} \cdot \delta exp[\beta(\sqrt{p^2 + m^2} - \vec{p}\cdot\vec{v})]\\
&\quad \cdot\beta\left(\frac{p_x}{\sqrt{p_x^2 + m^2}} - v_x\right) && \text{(F.6)}\\
&= -f^2 \cdot exp\left(-\frac{\mu}{T}\right) exp\left[\frac{\gamma}{T}(p^0 - \vec{p}\cdot\vec{v})\right] \cdot \beta\left(\frac{p_x}{p_0} - v_x\right) && \text{(F.7)}\\
& && \text{(F.8)}
\end{aligned}
$$

To find the roots of this term the easiest way is to take the last factor. Setting those terms for all three dimensions to zero leads to the following system of equations:

$$p_x = v_x\sqrt{p_x^2+p_y^2+p_z^2+m^2} \Rightarrow p_x^2 = v_x^2(p_x^2+p_y^2+p_z^2+m^2) \tag{F.9}$$

$$p_y = v_y\sqrt{p_x^2+p_y^2+p_z^2+m^2} \tag{F.10}$$

$$p_z = v_z\sqrt{p_x^2+p_y^2+p_z^2+m^2} \tag{F.11}$$

$$\tag{F.12}$$

Solving this system of equations via Maple leads to the following solution

$$p_x^2 = -\frac{v_x^2m^2}{v_x^2+v_y^2+v_z^2-1} \quad , p_y^2 = -\frac{v_y^2m^2}{v_x^2+v_y^2+v_z^2-1} \quad , p_z^2 = -\frac{v_z^2m^2}{v_x^2+v_y^2+v_z^2-1} \tag{F.13}$$

We have to choose always the right sign for

$$p_x = \pm\sqrt{-\frac{v_x^2m^2}{v^2-1}}\,. \tag{F.14}$$

The sign has to be chosen to be the same as the one of the correspondig velocity. Now, we plug the solution in and calculate the maximum of the momentum distribution.

Bibliography

[Abe90] F. Abe *et al.* [CDF Collaboration], Phys. Rev. D **41**, 2330 (1990).

[Abr02] M. C. Abreu *et al.* [NA50 Collaboration], Phys. Lett. B **530**, 43 (2002).

[Ada03] D. Adamova *et al.* [CERES/NA45 Collaboration], Phys. Rev. Lett. **91**, 042301 (2003) [arXiv:nucl-ex/0209024].

[Ada03] D. Adamova *et al.* [CERES Collaboration], Phys. Rev. Lett. **90**, 022301 (2003) [arXiv:nucl-ex/0207008].

[Adc04] K. Adcox *et al.* [PHENIX Collaboration], Phys. Rev. C **69**, 024904 (2004) [arXiv:nucl-ex/0307010].

[Adc05] K. Adcox *et al.* [PHENIX Collaboration], Nucl. Phys. A **757**, 184 (2005) [arXiv:nucl-ex/0410003].

[Ads04] J. Adams *et al.* [STAR Collaboration], Phys. Rev. Lett. **92**, 112301 (2004) [arXiv:nucl-ex/0310004].

[Ads05] J. Adams *et al.* [STAR Collaboration], Nucl. Phys. A **757**, 102 (2005) [arXiv:nucl-ex/0501009].

[Afa02a] S. V. Afanasiev *et al.* [The NA49 Collaboration], Phys. Rev. C **66**, 054902 (2002) [arXiv:nucl-ex/0205002].

[Afa02b] S. V. Afanasiev *et al.* [NA49 Collaboration], Phys. Lett. B **538**, 275 (2002) [arXiv:hep-ex/0202037].

[Afa03] S. V. Afanasiev *et al.*, Nucl. Phys. A **715**, 161 (2003) [arXiv:nucl-ex/0208014].

[Aga07] G. Agakichiev *et al.* [HADES Collaboration], Phys. Rev. Lett. **98**, 052302 (2007) [arXiv:nucl-ex/0608031].

[Agu01] C. E. Aguiar, T. Kodama, T. Osada and Y. Hama, J. Phys. G **27**, 75 (2001) [arXiv:hep-ph/0006239].

[Agu02] C. E. Aguiar, Y. Hama, T. Kodama and T. Osada, Nucl. Phys. A **698**, 639 (2002) [arXiv:hep-ph/0106266].

[Agu07] C. E. Aguiar, T. Kodama, T. Koide and Y. Hama, Braz. J. Phys. **37**, 95 (2007).

[Ahl00a] L. Ahle *et al.* [E866 Collaboration and E917 Collaboration], Phys. Lett. B **476**, 1 (2000) [arXiv:nucl-ex/9910008].

[Ahl00b] L. Ahle *et al.* [E866 Collaboration and E917 Collaborations], Phys. Lett. B **490**, 53 (2000) [arXiv:nucl-ex/0008010].

[Ahm96] S. Ahmad *et al.*, Phys. Lett. B **382**, 35 (1996).

[Aic86] J. Aichelin and H. Stoecker, Phys. Lett. B **176**, 14 (1986).

[Aic91] J. Aichelin, Phys. Rept. **202**, 233 (1991).

[Aic07] J. Aichelin, H. Petersen, S. Vogel and M. Bleicher, PoS **CPOD07**, 004 (2007) [arXiv:0711.2995 [nucl-th]].

[Aki96] Y. Akiba *et al.* [E802 Collaboration], Nucl. Phys. A **610**, 139C (1996).

[Ale06] B. Alessandro *et al.* [ALICE Collaboration], J. Phys. G **32**, 1295 (2006).

[Aln87] G. J. Alner *et al.* [UA5 Collaboration], Phys. Rept. **154**, 247 (1987).

[Alt03] C. Alt *et al.* [NA49 Collaboration], Phys. Rev. C **68**, 034903 (2003) [arXiv:nucl-ex/0303001].

[Alt05a] C. Alt *et al.* [NA49 Collaboration], Phys. Rev. Lett. **94**, 192301 (2005) [arXiv:nucl-ex/0409004].

[Alt05b] C. Alt *et al.* [NA49 Collaboration], Phys. Rev. Lett. **94**, 052301 (2005) [arXiv:nucl-ex/0406031].

[Alt05c] C. Alt *et al.* [NA49 Collaboration],

[Alt06] C. Alt *et al.* [NA49 Collaboration], Phys. Rev. C **73**, 044910 (2006).

[Alt08a] C. Alt *et al.* [NA49 Collaboration], Phys. Rev. C **77**, 024903 (2008) [arXiv:0710.0118 [nucl-ex]].

[Alt08b] C. Alt *et al.* [NA49 Collaboration], Phys. Rev. C **77**, 064908 (2008) [arXiv:0709.4507 [nucl-ex]].

[Alt08c] C. Alt *et al.* [NA49 Collaboration], Phys. Rev. C **78**, 034918 (2008) [arXiv:0804.3770 [nucl-ex]].

[Alv07a] B. Alver *et al.* [PHOBOS Collaboration], arXiv:nucl-ex/0702036.

[Alv07b] B. Alver *et al.*, arXiv:0709.4008 [nucl-ex].

[Ame90] N. S. Amelin, K. K. Gudima, S. Y. Sivoklokov and V. D. Toneev, Sov. J. Nucl. Phys. **52**, 172 (1990) [Yad. Fiz. **52**, 272 (1990)].

[Ame93] N. S. Amelin, M. A. Braun and C. Pajares, Phys. Lett. B **306**, 312 (1993).

[Anc04a] T. Anticic *et al.* [NA49 Collaboration], Phys. Rev. Lett. **93**, 022302 (2004) [arXiv:nucl-ex/0311024].

[Anc04b] T. Anticic *et al.* [NA49 Collaboration], Phys. Rev. C **69**, 024902 (2004).

[And99] C. Anderlik *et al.*, Phys. Rev. C **59**, 3309 (1999) [arXiv:nucl-th/9806004].

[Ani05] A. Andronic *et al.* [FOPI Collaboration], Phys. Lett. B **612**, 173 (2005) [arXiv:nucl-ex/0411024].

[Ani06] A. Andronic, P. Braun-Munzinger and J. Stachel, Nucl. Phys. A **772**, 167 (2006) [arXiv:nucl-th/0511071].

[Ano77] B. Andersson, G. Gustafson and C. Peterson, Nucl. Phys. B **135**, 273 (1978).

[Ano83] B. Anderson, G. Gustafson, G. Ingelman, T. Sjöstrand, Phys. Rep. **97**,(1983),31 .

[Ano86] B. Andersson, G. Gustafson and B. Nilsson-Almqvist, Nucl. Phys. B **281**, 289 (1987).

[Anr06a] R. Andrade, F. Grassi, Y. Hama, T. Kodama, O. . J. Socolowski and B. Tavares, Eur. Phys. J. A **29**, 23 (2006) [arXiv:nucl-th/0511021].

[Anr06b] R. Andrade, F. Grassi, Y. Hama, T. Kodama and O. . J. Socolowski, Phys. Rev. Lett. **97**, 202302 (2006) [arXiv:nucl-th/0608067].

[Anr08a] R. P. G. Andrade, F. Grassi, Y. Hama, T. Kodama and W. L. Qian, Phys. Rev. Lett. **101**, 112301 (2008) [arXiv:0805.0018 [hep-ph]].

[Anr08b] R. P. G. Andrade, A. L. V. Reis, F. Grassi, Y. Hama, W. L. Qian, T. Kodama and J. Y. Ollitrault, arXiv:0812.4143 [nucl-th].

[Ant99] F. Antinori *et al.* [WA97 Collaboration], Nucl. Phys. A **661**, 130 (1999).

[Ant04] F. Antinori *et al.* [NA57 Collaboration], Phys. Lett. B **595**, 68 (2004) [arXiv:nucl-ex/0403022].

[Ant06] F. Antinori *et al.* [NA57 Collaboration], J. Phys. G **32**, 427 (2006) [arXiv:nucl-ex/0601021].

[Anu73] M. Antinucci *et al.*, Lett. Nuovo Cim. **6**, 121 (1973).

[App99] H. Appelshauser *et al.* [NA49 Collaboration], Phys. Rev. Lett. **82**, 2471 (1999) [arXiv:nucl-ex/9810014].

[Aok06a] Y. Aoki, G. Endrodi, Z. Fodor, S. D. Katz and K. K. Szabo, Nature **443**, 675 (2006) [arXiv:hep-lat/0611014].

[Aok06b] Y. Aoki, Z. Fodor, S. D. Katz and K. K. Szabo, Phys. Lett. B **643**, 46 (2006) [arXiv:hep-lat/0609068].

[Arm00] N. Armesto and C. Pajares, Int. J. Mod. Phys. A **15**, 2019 (2000) [arXiv:hep-ph/0002163].

[Arm08] N. Armesto *et al.*, J. Phys. G **35**, 054001 (2008) [arXiv:0711.0974 [hep-ph]].

[Arn06] R. Arnaldi *et al.* [NA60 Collaboration], Phys. Rev. Lett. **96**, 162302 (2006) [arXiv:nucl-ex/0605007].

[Aro83] G. Arnison *et al.* [UA1 Collaboration], Phys. Lett. B **123**, 108 (1983).

[Ars05] I. Arsene *et al.* [BRAHMS Collaboration], Nucl. Phys. A **757**, 1 (2005) [arXiv:nucl-ex/0410020].

[Ars07] I. C. Arsene *et al.*, Phys. Rev. C **75**, 034902 (2007) [arXiv:nucl-th/0609042].

[Asa06] M. Asakawa and C. Nonaka, Nucl. Phys. A **774**, 753 (2006) [arXiv:nucl-th/0509091].

[Bac01] B. B. Back *et al.* [E917 Collaboration], Phys. Rev. Lett. **86**, 1970 (2001) [arXiv:nucl-ex/0003007].

[Bac03] B. B. Back *et al.* [PHOBOS Collaboration], arXiv:nucl-ex/0301017.

[Bac05] B. B. Back *et al.*, Nucl. Phys. A **757**, 28 (2005) [arXiv:nucl-ex/0410022].

[Bac06] B. B. Back *et al.* [PHOBOS Collaboration], Phys. Rev. C **74**, 021902 (2006).

[Bai07] R. Baier and P. Romatschke, Eur. Phys. J. C **51**, 677 (2007) [arXiv:nucl-th/0610108].

[Bar01] H. W. Barz and B. Kampfer, Nucl. Phys. A **683**, 594 (2001) [arXiv:nucl-th/0005063].

[Bas98a] S. A. Bass *et al.*, Phys. Rev. Lett. **81**, 4092 (1998) [arXiv:nucl-th/9711032].

[Bas98b] S. A. Bass *et al.*, Prog. Part. Nucl. Phys. **41**, 255 (1998) [Prog. Part. Nucl. Phys. **41**, 225 (1998)] [arXiv:nucl-th/9803035].

[Bas99a] S. A. Bass, M. Gyulassy, H. Stoecker and W. Greiner, J. Phys. G **25**, R1 (1999) [arXiv:hep-ph/9810281].

[Bas99b] S. A. Bass, M. Hofmann, M. Bleicher, L. Bravina, E. Zabrodin, H. Stoecker and W. Greiner, Phys. Rev. C **60**, 021901 (1999) [arXiv:nucl-th/9902055].

[Bas99c] S. A. Bass, A. Dumitru, M. Bleicher, L. Bravina, E. Zabrodin, H. Stoecker and W. Greiner, Phys. Rev. C **60**, 021902 (1999) [arXiv:nucl-th/9902062].

[Bas99d] S. A. Bass *et al.*, Nucl. Phys. A **661**, 205 (1999) [arXiv:nucl-th/9907090].

[Bas00] S. A. Bass and A. Dumitru, Phys. Rev. C **61**, 064909 (2000) [arXiv:nucl-th/0001033].

[Bay61] G. Baym and L. P. Kadanoff, Phys. Rev. **124**, 287 (1961).

[Bea01] I. G. Bearden *et al.* [BRAHMS Collaboration], Phys. Rev. Lett. **88**, 202301 (2002) [arXiv:nucl-ex/0112001].

[Bea04] I. G. Bearden *et al.* [BRAHMS Collaboration], Phys. Rev. Lett. **93**, 102301 (2004) [arXiv:nucl-ex/0312023].

[Bec02] F. Becattini and G. Passaleva, Eur. Phys. J. C **23**, 551 (2002) [arXiv:hep-ph/0110312].

[Bec04a] F. Becattini and L. Ferroni, Eur. Phys. J. C **35**, 243 (2004) [arXiv:hep-ph/0307061].

[Bec04b] F. Becattini and L. Ferroni, Eur. Phys. J. C **38**, 225 (2004) [arXiv:hep-ph/0407117].

[Bec08] F. Becattini, P. Castorina, J. Manninen and H. Satz, Eur. Phys. J. C **56**, 493 (2008) [arXiv:0805.0964 [hep-ph]].

[Bel98] M. Belkacem *et al.*, Phys. Rev. C **58**, 1727 (1998) [arXiv:nucl-th/9804058].

[Ber05] C. Bernard *et al.* [MILC Collaboration], Phys. Rev. D **71**, 034504 (2005) [arXiv:hep-lat/0405029].

[Bet08] B. Betz, P. Rau and H. Stocker, Int. J. Mod. Phys. E **16**, 3082 (2008) [arXiv:0707.3942 [hep-th]].

[Bir84] T. S. Biro, H. B. Nielsen and J. Knoll, Nucl. Phys. B **245**, 449 (1984).

[Bir99] T. S. Biro, P. Levai and J. Zimanyi, Phys. Rev. C **59**, 1574 (1999) [arXiv:hep-ph/9807303].

[Bir06] T. S. Biro, P. Levai, P. Van and J. Zimanyi, J. Phys. G **32**, S205 (2006) [arXiv:hep-ph/0605274].

[Blb07] J. Bleibel, G. Burau, A. Faessler and C. Fuchs, Phys. Rev. C **76**, 024912 (2007) [arXiv:nucl-th/0610021].

[Blb08] J. Bleibel, G. Burau and C. Fuchs, Phys. Lett. B **659**, 520 (2008) [arXiv:0711.3366 [nucl-th]].

[Ble98a] M. Bleicher *et al.*, Nucl. Phys. A **638**, 391 (1998).

[Ble98b] M. Bleicher *et al.*, Phys. Lett. B **435**, 9 (1998) [arXiv:hep-ph/9803345].

[Ble99a] M. Bleicher *et al.*, Phys. Rev. C **59**, 1844 (1999) [arXiv:hep-ph/9811459].

[Ble99b] M. Bleicher *et al.*, Phys. Lett. B **447**, 227 (1999) [arXiv:hep-ph/9803346].

[Ble99c] M. Bleicher *et al.*, J. Phys. G **25**, 1859 (1999) [arXiv:hep-ph/9909407].

[Ble00a] M. J. Bleicher *et al.*, Phys. Rev. C **62**, 024904 (2000) [arXiv:hep-ph/9911420].

[Ble00b] M. Bleicher, S. Jeon and V. Koch, Phys. Rev. C **62**, 061902 (2000) [arXiv:hep-ph/0006201].

[Ble00c] M. Bleicher, J. Randrup, R. Snellings and X. N. Wang, Phys. Rev. C **62**, 041901 (2000) [arXiv:nucl-th/0006047].

[Ble00d] M. Bleicher, M. Belkacem, S. A. Bass, S. Soff and H. Stoecker, Phys. Lett. B **485**, 133 (2000) [arXiv:hep-ph/0004045].

[Ble00e] M. Bleicher, W. Greiner, H. Stoecker and N. Xu, Phys. Rev. C **62**, 061901 (2000) [arXiv:hep-ph/0007215].

[Ble02a] M. Bleicher and H. Stoecker, Phys. Lett. B **526**, 309 (2002) [arXiv:hep-ph/0006147].

[Ble02b] M. Bleicher *et al.*, Phys. Rev. Lett. **88**, 202501 (2002) [arXiv:hep-ph/0111187].

[Ble02c] M. Bleicher and J. Aichelin, Phys. Lett. B **530**, 81 (2002) [arXiv:hep-ph/0201123].

[Ble03] M. Bleicher, Nucl. Phys. A **715**, 85 (2003) [arXiv:hep-ph/0212378].

[Ble04] M. Bleicher and H. Stoecker, J. Phys. G **30**, S111 (2004) [arXiv:hep-ph/0312278].

[Ble05] M. Bleicher and J. Aichelin, Phys. Lett. B **612**, 201 (2005) [arXiv:nucl-th/0205069].

[Blm05] C. Blume [NA49 Collaboration], J. Phys. G **31**, S685 (2005) [arXiv:nucl-ex/0411039].

[Blm07] C. Blume [Na49 Collaboration], J. Phys. G **34**, S951 (2007) [arXiv:nucl-ex/0701042].

[Blu05] M. Bluhm, B. Kampfer and G. Soff, Phys. Lett. B **620**, 131 (2005) [arXiv:hep-ph/0411106].

[Blu07] M. Bluhm, B. Kampfer, R. Schulze, D. Seipt and U. Heinz, Phys. Rev. C **76**, 034901 (2007) [arXiv:0705.0397 [hep-ph]].

[Bjo83] J. D. Bjorken, Phys. Rev. D **27**, 140 (1983).

[Bor06] V. G. Bornyakov *et al.*, PoS **LAT2005**, 157 (2006) [arXiv:hep-lat/0509122].

[Bor07] V. G. Bornyakov, E. V. Luschevskaya, S. M. Morozov, M. I. Polikarpov, E. M. Ilgenfritz and M. Muller-Preussker, PoS **LAT2007**, 315 (2007) [arXiv:0710.2799 [hep-lat]].

[Bra97] J. Brachmann, A. Dumitru, J. A. Maruhn, H. Stoecker, W. Greiner and D. H. Rischke, Nucl. Phys. A **619**, 391 (1997) [arXiv:nucl-th/9703032].

[Bra00a] J. Brachmann, A. Dumitru, H. Stoecker and W. Greiner, Eur. Phys. J. A **8**, 549 (2000) [arXiv:nucl-th/9912014].

[Bra00b] J. Brachmann *et al.*, Phys. Rev. C **61**, 024909 (2000) [arXiv:nucl-th/9908010].

[BrM95] P. Braun-Munzinger, J. Stachel, J. P. Wessels and N. Xu, Phys. Lett. B **344**, 43 (1995) [arXiv:nucl-th/9410026].

[BrM96] P. Braun-Munzinger, J. Stachel, J. P. Wessels and N. Xu, Phys. Lett. B **365**, 1 (1996) [arXiv:nucl-th/9508020].

[BrM04] P. Braun-Munzinger, J. Stachel and C. Wetterich, Phys. Lett. B **596**, 61 (2004) [arXiv:nucl-th/0311005].

[Bro08] W. Broniowski, M. Chojnacki, W. Florkowski and A. Kisiel, Phys. Rev. Lett. **101**, 022301 (2008) [arXiv:0801.4361 [nucl-th]].

[Brt04] E. L. Bratkovskaya *et al.*, Phys. Rev. C **69**, 054907 (2004) [arXiv:nucl-th/0402026].

[Brv98] L. V. Bravina *et al.*, Phys. Lett. B **434**, 379 (1998) [arXiv:nucl-th/9804008].

[Brv99] L. V. Bravina *et al.*, Phys. Rev. C **60**, 024904 (1999) [arXiv:hep-ph/9906548].

[Brv99] L. V. Bravina *et al.*, Phys. Lett. B **459**, 660 (1999).

[Brv00] L. V. Bravina *et al.*, Phys. Rev. C **62**, 064906 (2000) [arXiv:nucl-th/0011011].

[Brv01] L. V. Bravina *et al.*, Phys. Rev. C **63**, 064902 (2001) [arXiv:hep-ph/0010172].

[Brv08] L. V. Bravina *et al.*, Phys. Rev. C **78**, 014907 (2008) [arXiv:0804.1484 [hep-ph]].

[Bug99] K. A. Bugaev and M. I. Gorenstein, arXiv:nucl-th/9903072.

[Bug03] K. A. Bugaev, Phys. Rev. Lett. **90**, 252301 (2003) [arXiv:nucl-th/0210087].

[Bug04] K. A. Bugaev, Phys. Rev. C **70**, 034903 (2004) [arXiv:nucl-th/0401060].

[Bur05] G. Burau, J. Bleibel, C. Fuchs, A. Faessler, L. V. Bravina and E. E. Zabrodin, Phys. Rev. C **71**, 054905 (2005) [arXiv:nucl-th/0411117].

[Cas90] W. Cassing, V. Metag, U. Mosel and K. Niita, Phys. Rept. **188**, 363 (1990).

[Cas00] W. Cassing, E. L. Bratkovskaya and S. Juchem, Nucl. Phys. A **674**, 249 (2000) [arXiv:nucl-th/0001024].

[Cas02] W. Cassing, Nucl. Phys. A **700**, 618 (2002) [arXiv:nucl-th/0105069].

[Cas08] W. Cassing and E. L. Bratkovskaya, Phys. Rev. C **78**, 034919 (2008) [arXiv:0808.0022 [hep-ph]].

[Car04] F. Carminati *et al.* [ALICE Collaboration], J. Phys. G **30**, 1517 (2004).

[Che06] M. Cheng *et al.*, Phys. Rev. D **74**, 054507 (2006) [arXiv:hep-lat/0608013].

[Chn07] J. W. Chen and E. Nakano, Phys. Lett. B **647**, 371 (2007) [arXiv:hep-ph/0604138].

[Chu02] P. Chung *et al.* [E895 Collaboration], Phys. Rev. C **66**, 021901 (2002) [arXiv:nucl-ex/0112002].

[Chu03] P. Chung *et al.* [E895 collaboration], Phys. Rev. Lett. **91**, 202301 (2003) [arXiv:nucl-ex/0302021].

[Cla86] R. B. Clare and D. Strottman, Phys. Rept. **141**, 177 (1986).

[Cle98] J. Cleymans and K. Redlich, Phys. Rev. Lett. **81**, 5284 (1998) [arXiv:nucl-th/9808030].

[Cle99] J. Cleymans and K. Redlich, Phys. Rev. C **60**, 054908 (1999) [arXiv:nucl-th/9903063].

[Cle06] J. Cleymans, H. Oeschler, K. Redlich and S. Wheaton, J. Phys. G **32**, S165 (2006) [arXiv:hep-ph/0607164].

[Coo74] F. Cooper and G. Frye, Phys. Rev. D **10**, 186 (1974).

[Den08] G. S. Denicol, T. Kodama, T. Koide and Ph. Mota, Phys. Rev. C **78**, 034901 (2008) [arXiv:0805.1719 [hep-ph]].

[Dre02] H. J. Drescher, J. Aichelin and K. Werner, Phys. Rev. D **65**, 057501 (2002) [arXiv:hep-ph/0105020].

[Dre03] H. J. Drescher, G. R. Farrar, M. Bleicher, M. Reiter, S. Soff and H. Stoecker, arXiv:astro-ph/0305429.

[Dre04] H. J. Drescher, M. Bleicher, S. Soff and H. Stoecker, Astropart. Phys. **21**, 87 (2004) [arXiv:astro-ph/0307453].

[Dre07] H. J. Drescher and Y. Nara, Phys. Rev. C **75**, 034905 (2007) [arXiv:nucl-th/0611017].

[Dum98] A. Dumitru, M. Bleicher, S. A. Bass, C. Spieles, L. Neise, H. Stoecker and W. Greiner, Phys. Rev. C **57**, 3271 (1998) [arXiv:hep-ph/9709487].

[Dum99] A. Dumitru, S. A. Bass, M. Bleicher, H. Stoecker and W. Greiner, Phys. Lett. B **460**, 411 (1999) [arXiv:nucl-th/9901046].

[Dum01] A. Dumitru *et al.*, Heavy Ion Phys. **14**, 121 (2001) [arXiv:nucl-th/0010107].

[Dum056] A. Dumitru, L. Portugal and D. Zschiesche, Phys. Rev. C **73**, 024902 (2006) [arXiv:nucl-th/0511084].

[Dum07] A. Dumitru, E. Molnar and Y. Nara, Phys. Rev. C **76**, 024910 (2007) [arXiv:0706.2203 [nucl-th]].

[Eid04] S. Eidelman *et al.* [Particle Data Group], Phys. Lett. B **592**, 1 (2004).

[El08] A. El, A. Muronga, Z. Xu and C. Greiner, arXiv:0812.2762 [hep-ph].

[Ell03] J. B. Elliott *et al.* [EOS Collaboration], Phys. Rev. C **67**, 024609 (2003) [arXiv:nucl-ex/0205004].

[Els95] J. R. Ellis and K. Geiger, Phys. Rev. D **52**, 1500 (1995) [arXiv:hep-ph/9503349].

[Ern98] C. Ernst, S. A. Bass, M. Belkacem, H. Stoecker and W. Greiner, Phys. Rev. C **58**, 447 (1998) [arXiv:nucl-th/9712069].

[Esu02] S.I.Esumi, J. Slivova, J. Milosevic for CERES Collaboration SFIN, year XV, Series A: Conferences, No. A2(2002)

[Esu03] S. Esumi [PHENIX Collaboration], Nucl. Phys. A **715**, 599 (2003) [arXiv:nucl-ex/0210012].

[FAIR] An International Accelerator Facility for Beams of Ions and Antiprotons, Conceptual Design Report, http://www.gsi.de/GSI-Future/cdr/

[Fil01] K. Filimonov *et al.* [CERES/NA45 Collaboration], arXiv:nucl-ex/0109017.

[Foc06] O. Fochler, S. Vogel, M. Bleicher, C. Greiner, P. Koch-Steinheimer and Z. Xu, Phys. Rev. C **74**, 034902 (2006) [arXiv:nucl-th/0601062].

[Fod04] Z. Fodor and S. D. Katz, JHEP **0404**, 050 (2004) [arXiv:hep-lat/0402006].

[For07] P. de Forcrand and O. Philipsen, JHEP **0701**, 077 (2007) [arXiv:hep-lat/0607017].

[Gaz99] M. Gazdzicki and M. I. Gorenstein, Acta Phys. Polon. B **30**, 2705 (1999) [arXiv:hep-ph/9803462].

[Gaz04] M. Gazdzicki, M. I. Gorenstein, F. Grassi, Y. Hama, T. Kodama and O. . J. Socolowski, Braz. J. Phys. **34**, 322 (2004) [arXiv:hep-ph/0309192].

[Gaz04] M. Gazdzicki *et al.* [NA49 Collaboration], J. Phys. G **30**, S701 (2004) [arXiv:nucl-ex/0403023].

[Gei92] K. Geiger and B. Muller, Nucl. Phys. B **369**, 600 (1992).

[Gor03] M. I. Gorenstein, M. Gazdzicki and K. A. Bugaev, Phys. Lett. B **567**, 175 (2003) [arXiv:hep-ph/0303041].

[Gra95] F. Grassi, Y. Hama and T. Kodama, Phys. Lett. B **355**, 9 (1995).

[Gra05] F. Grassi, Y. Hama, O. Socolowski and T. Kodama, J. Phys. G **31**, S1041 (2005).

[Gra05] A. Gray, I. Allison, C. T. H. Davies, E. Dalgic, G. P. Lepage, J. Shigemitsu and M. Wingate, Phys. Rev. D **72**, 094507 (2005) [arXiv:hep-lat/0507013].

[Gre01] C. Greiner and S. Leupold, J. Phys. G **27**, L95 (2001) [arXiv:nucl-th/0009036].

[DeG80] S. R. De Groot, W. A. Van Leeuwen and C. G. Van Weert, *Amsterdam, Netherlands: North-holland (1980) 417p*

[Gyu97] M. Gyulassy, D. H. Rischke and B. Zhang, Nucl. Phys. A **613**, 397 (1997) [arXiv:nucl-th/9609030].

[Hai96] J. W. Harris and B. Muller, Ann. Rev. Nucl. Part. Sci. **46**, 71 (1996) [arXiv:hep-ph/9602235].

[Ham00] S. Hamieh, K. Redlich and A. Tounsi, Phys. Lett. B **486**, 61 (2000) [arXiv:hep-ph/0006024].

[Ham05] Y. Hama, T. Kodama and O. . J. Socolowski, Braz. J. Phys. **35**, 24 (2005) [arXiv:hep-ph/0407264].

[Har97] R. Harr *et al.*, Phys. Lett. B **401**, 176 (1997) [arXiv:hep-ex/9703002].

[Has06] S. Haussler, H. Stoecker and M. Bleicher, Phys. Rev. C **73**, 021901 (2006) [arXiv:hep-ph/0507189].

[Has07] S. Haussler, M. Abdel-Aziz and M. Bleicher, Nucl. Phys. A **785**, 253 (2007) [arXiv:nucl-th/0608021].

[Hat89] C. Hartnack *et al.*, Nucl. Phys. A **495**, 303C (1989).

[Hau08] M. Hauer, V. V. Begun and M. I. Gorenstein, Eur. Phys. J. C **58**, 83 (2008) [arXiv:0706.3290 [nucl-th]].

[Hei02] U. W. Heinz and P. F. Kolb, arXiv:hep-ph/0204061.

[Hei06] U. W. Heinz, H. Song and A. K. Chaudhuri, Phys. Rev. C **73**, 034904 (2006) [arXiv:nucl-th/0510014].

[Hir02] T. Hirano, Phys. Rev. C **65**, 011901 (2002) [arXiv:nucl-th/0108004].

[Hir06] T. Hirano, U. W. Heinz, D. Kharzeev, R. Lacey and Y. Nara, Phys. Lett. B **636**, 299 (2006) [arXiv:nucl-th/0511046].

[Hir08] T. Hirano, U. W. Heinz, D. Kharzeev, R. Lacey and Y. Nara, Phys. Rev. C **77**, 044909 (2008) [arXiv:0710.5795 [nucl-th]].

[Hof00] M. Hofmann, M. Bleicher, S. Scherer, L. Neise, H. Stoecker and W. Greiner, Phys. Lett. B **478**, 161 (2000) [arXiv:nucl-th/9908030].

[Hoh06] C. Hohne, F. Puhlhofer and R. Stock, Phys. Lett. B **640**, 96 (2006) [arXiv:hep-ph/0507276].

[Huo07] S. C. Huot, S. Jeon and G. D. Moore, Phys. Rev. Lett. **98**, 172303 (2007) [arXiv:hep-ph/0608062].

[Huv01] P. Huovinen, P. F. Kolb, U. W. Heinz, P. V. Ruuskanen and S. A. Voloshin, Phys. Lett. B **503**, 58 (2001) [arXiv:hep-ph/0101136].

[ICE06] ICE 2006 Institut de Ciències de l'Espai, www.ice.csic.es/en/graphics/phase.jpg

[Iva06] Yu. B. Ivanov, V. N. Russkikh and V. D. Toneev, Phys. Rev. C **73**, 044904 (2006) [arXiv:nucl-th/0503088].

[Iva08] Yu. B. Ivanov and V. N. Russkikh, Eur. Phys. J. A **37**, 139 (2008) [arXiv:nucl-th/0607070].

[Jeo06] S. Jeon, L. Shi and M. Bleicher, Phys. Rev. C **73**, 014905 (2006) [arXiv:nucl-th/0506025].

[Kar07a] F. Karsch, PoS **CPOD07**, 026 (2007) [arXiv:0711.0656 [hep-lat]].

[Kar07b] F. Karsch, PoS **LAT2007**, 015 (2007) [arXiv:0711.0661 [hep-lat]].

[Kat93] U. Katscher, D. H. Rischke, J. A. Maruhn, W. Greiner, I. N. Mishustin and L. M. Satarov, Z. Phys. A **346**, 209 (1993).

[Kho92] Dao T. Khoa *et al.*, Nucl. Phys. A **548**,(1992),102.

[Kis06] A. Kisiel, T. Taluc, W. Broniowski and W. Florkowski, Comput. Phys. Commun. **174**, 669 (2006) [arXiv:nucl-th/0504047].

[Kla03] J. L. Klay *et al.* [E-0895 Collaboration], Phys. Rev. C **68**, 054905 (2003) [arXiv:nucl-ex/0306033].

[Kni06] S. Kniege *et al.* [NA49 Collaboration], AIP Conf. Proc. **828**, 473 (2006) [arXiv:nucl-ex/0601024].

[Kno88] J. Knoll, Z. Phys. C **38**, 187 (1988).

[Kno08] J. Knoll, arXiv:0803.2343 [nucl-th].

[Koc86] P. Koch, B. Muller and J. Rafelski, Phys. Rept. **142**, 167 (1986).

[Koh02] V. Koch, M. Bleicher and S. Jeon, Nucl. Phys. A **698**, 261 (2002) [Nucl. Phys. A **702**, 291 (2002)] [arXiv:nucl-th/0103084].

[Koi07] T. Koide, G. S. Denicol, Ph. Mota and T. Kodama, Phys. Rev. C **75**, 034909 (2007) [arXiv:hep-ph/0609117].

[Kol00] P. F. Kolb, J. Sollfrank and U. W. Heinz, Phys. Rev. C **62**, 054909 (2000) [arXiv:hep-ph/0006129].

[Kol01a] P. F. Kolb, P. Huovinen, U. W. Heinz and H. Heiselberg, Phys. Lett. B **500**, 232 (2001) [arXiv:hep-ph/0012137].

[Kol01b] P. F. Kolb, U. W. Heinz, P. Huovinen, K. J. Eskola and K. Tuominen, Nucl. Phys. A **696**, 197 (2001) [arXiv:hep-ph/0103234].

[Kol03] P. F. Kolb and U. W. Heinz, arXiv:nucl-th/0305084.

[Kon06] V. P. Konchakovski, S. Haussler, M. I. Gorenstein, E. L. Bratkovskaya, M. Bleicher and H. Stoecker, Phys. Rev. C **73**, 034902 (2006) [arXiv:nucl-th/0511083].

[Kra04] I. Kraus, PhD thesis, Johann Wolfgang Goethe-Universität Frankfurt (2004).

[Kra07] I. Kraus, J. Cleymans, H. Oeschler, K. Redlich and S. Wheaton, Phys. Rev. C **76**, 064903 (2007) [arXiv:0707.3879 [hep-ph]].

[Lan53] L. D. Landau, Izv. Akad. Nauk Ser. Fiz. **17**, 51 (1953).

[Lar07] A. B. Larionov, O. Buss, K. Gallmeister and U. Mosel, Phys. Rev. C **76**, 044909 (2007) [arXiv:0704.1785 [nucl-th]].

[Lee04] J. H. Lee *et al.* [BRAHMS Collaboration], J. Phys. G **30**, S85 (2004).

[Lev98] P. Levai and U. W. Heinz, Phys. Rev. C **57**, 1879 (1998) [arXiv:hep-ph/9710463].

[Li05a] Q. Li, Z. Li, S. Soff, M. Bleicher and H. Stoecker, Phys. Rev. C **72**, 034613 (2005) [arXiv:nucl-th/0506030].

[Li05b] Q. f. Li, Z. x. Li, S. Soff, R. K. Gupta, M. Bleicher and H. Stoecker, J. Phys. G **31**, 1359 (2005) [arXiv:nucl-th/0507068].

[Li06a] Q. f. Li, Z. x. Li, S. Soff, M. Bleicher and H. Stoecker, J. Phys. G **32**, 151 (2006) [arXiv:nucl-th/0509070].

[Li06b] Q. f. Li, Z. x. Li, S. Soff, M. Bleicher and H. Stoecker, J. Phys. G **32**, 407 (2006) [arXiv:nucl-th/0601047].

[Li06c] Q. Li, M. Bleicher and H. Stoecker, Phys. Rev. C **73**, 064908 (2006) [arXiv:nucl-th/0602032].

[Li07a] Q. Li, M. Bleicher, X. Zhu and H. Stoecker, J. Phys. G **33**, 537 (2007) [arXiv:nucl-th/0612030].

[Li07b] Q. Li, M. Bleicher and H. Stocker, J. Phys. G **34**, 2037 (2007) [arXiv:0706.2091 [nucl-th]].

[Li08a] Q. Li, M. Bleicher and H. Stocker, Phys. Lett. B **659**, 525 (2008) [arXiv:0709.1409 [nucl-th]].

[Li08b] Q. f. Li, J. Steinheimer, H. Petersen, M. Bleicher and H. Stocker, Phys. Lett. B **674**, 111 (2009) arXiv:0812.0375 [nucl-th].

[Li08c] Q. Li, M. Bleicher and H. Stocker, Phys. Lett. B **663**, 395 (2008) [arXiv:0802.3618 [nucl-th]].

[Li09] Q. Li and M. Bleicher, J. Phys. G **36**, 015111 (2009) [arXiv:0808.3457 [nucl-th]].

[Lin02] Z. w. Lin and C. M. Ko, Phys. Rev. C **65**, 034904 (2002) [arXiv:nucl-th/0108039].

[Lin05] Z. W. Lin, C. M. Ko, B. A. Li, B. Zhang and S. Pal, Phys. Rev. C **72**, 064901 (2005) [arXiv:nucl-th/0411110].

[Lis05] M. A. Lisa, S. Pratt, R. Soltz and U. Wiedemann, Ann. Rev. Nucl. Part. Sci. **55**, 357 (2005) [arXiv:nucl-ex/0505014].

[Lis08] M. A. Lisa and S. Pratt, arXiv:0811.1352 [nucl-ex].

[Liu04] F. M. Liu, J. Aichelin, K. Werner and M. Bleicher, Phys. Rev. C **69**, 054002 (2004) [arXiv:hep-ph/0307008].

[Lu06] Y. Lu *et al.*, J. Phys. G **32**, 1121 (2006) [arXiv:nucl-th/0602009].

[Lun07] B. Lungwitz and M. Bleicher, Phys. Rev. C **76**, 044904 (2007) [arXiv:0707.1788 [nucl-th]].

[Luz08] M. Luzum and P. Romatschke, Phys. Rev. C **78**, 034915 (2008) [arXiv:0804.4015 [nucl-th]].

[Luz08] M. Luzum, J. G. Cramer and G. A. Miller, arXiv:0809.0520 [nucl-th].

[Mae07] Y. Maezawa, S. Aoki, S. Ejiri, T. Hatsuda, N. Ishii, K. Kanaya and N. Ukita, J. Phys. G **34**, S651 (2007) [arXiv:hep-lat/0702005].

[Mag99] V. K. Magas *et al.*, Heavy Ion Phys. **9**, 193 (1999) [arXiv:nucl-th/9903045].

[Man03] S. Manly *et al.* [PHOBOS Collaboration], Nucl. Phys. A **715**, 611 (2003) [arXiv:nucl-ex/0210036].

[Meh08] Y. Mehtar-Tani and G. Wolschin, arXiv:0811.1721 [hep-ph].

[Mih88] I. N. Mishustin, V. N. Russkikh and L. M. Satarov, Sov. J. Nucl. Phys. **48**, 454 (1988) [Yad. Fiz. **48**, 711 (1988)].

[Mih89] I. N. Mishustin, V. N. Russkikh and L. M. Satarov, Nucl. Phys. A **494**, 595 (1989).

[Mis02] A. Mischke *et al.* [NA49 Collaboration], J. Phys. G **28**, 1761 (2002) [arXiv:nucl-ex/0201012].

[Mit06] M. K. Mitrovski *et al.* [NA49 Collaboration], J. Phys. G **32**, S43 (2006) [arXiv:nucl-ex/0606004].

[Mit08] M. Mitrovski, T. Schuster, G. Graf, H. Petersen and M. Bleicher, Phys. Rev. C **79**, 044901 (2009) arXiv:0812.2041 [hep-ph].

[Mol04] D. Molnar and M. Gyulassy, Phys. Rev. Lett. **92**, 052301 (2004) [arXiv:nucl-th/0211017].

[Mol05] D. Molnar and P. Huovinen, Phys. Rev. Lett. **94**, 012302 (2005) [arXiv:nucl-th/0404065].

[Mon99] B. Monreal *et al.*, Phys. Rev. C **60**, 031901 (1999) [arXiv:nucl-th/9904080].

[NA57] http://wa97.web.cern.ch/WA97/yields.html

[Nil87] B. Nilsson-Almqvist and E. Stenlund, Comput. Phys. Commun. **43**, 387 (1987).

[Non05] C. Nonaka and M. Asakawa, Phys. Rev. C **71**, 044904 (2005) [arXiv:nucl-th/0410078].

[Non06] C. Nonaka and S. A. Bass, Nucl. Phys. A **774**, 873 (2006) [arXiv:nucl-th/0510038].

[Non07] C. Nonaka and S. A. Bass, Phys. Rev. C **75**, 014902 (2007) [arXiv:nucl-th/0607018].

[Nor08] J. Noronha-Hostler, C. Greiner and I. A. Shovkovy, Phys. Rev. Lett. **100**, 252301 (2008) [arXiv:0711.0930 [nucl-th]].

[Oll92] J. Y. Ollitrault, Phys. Rev. D **46**, 229 (1992).

[Oue03] D. Ouerdane [BRAHMS Collaboration], Nucl. Phys. A **715**, 478 (2003) [arXiv:nucl-ex/0212001].

[Pae03] K. Paech, H. Stoecker and A. Dumitru, Phys. Rev. C **68**, 044907 (2003) [arXiv:nucl-th/0302013].

[Pae05] K. Paech and A. Dumitru, Phys. Lett. B **623**, 200 (2005) [arXiv:nucl-th/0504003].

[Pae06] K. Paech and S. Pratt, Phys. Rev. C **74**, 014901 (2006) [arXiv:nucl-th/0604008].

[Pai97] S. Paiva, Y. Hama and T. Kodama, Phys. Rev. C **55**, 1455 (1997).

[Pap99] P. Papazoglou, D. Zschiesche, S. Schramm, J. Schaffner-Bielich, H. Stoecker and W. Greiner, Phys. Rev. C **59**, 411 (1999) [arXiv:nucl-th/9806087].

[Pet06a] H. Petersen, Q. Li, X. Zhu and M. Bleicher, Phys. Rev. C **74**, 064908 (2006) [arXiv:hep-ph/0608189].

[Pet06b] H. Petersen and M. Bleicher, PoS **CPOD2006**, 025 (2006) [arXiv:nucl-th/0611001].

[Pet06c] H. Petersen, S. Vogel, X. Zhu, M. Bleicher, Proceedings for WWND 2006, La Jolla, EP Systema, Budapest, Hungary, Edited by E.Bauer, R. Bellwied, p. 149

[Pet07] H. Petersen and M. Bleicher, Eur. Phys. J. C **49**, 91 (2007).

[Pet08a] H. Petersen, M. Bleicher, S. A. Bass and H. Stocker, arXiv:0805.0567 [hep-ph].

[Pet08b] H. Petersen, J. Steinheimer, G. Burau, M. Bleicher and H. Stocker, Phys. Rev. C **78**, 044901 (2008) [arXiv:0806.1695 [nucl-th]].

[Pet08c] H. Petersen, J. Steinheimer, G. Burau, M. Bleicher, accepted in Eur. Phys. J. C

[Pet08d] H. Petersen, J. Steinheimer, Q. Li, G. Burau and M. Bleicher, Proceedings for WWND 2008, South Padre Island, arXiv:0806.1805

[Pet09a] H. Petersen and M. Bleicher, Phys. Rev. C **79**, 054904 (2009) arXiv:0901.3821 [nucl-th].

[Pet09b] H. Petersen, J. Steinheimer, M. Bleicher and H. Stoecker, J. Phys. G **36**, 055104 (2009) arXiv:0902.4866 [nucl-th].

[Pet09c] H. Petersen, M. Mitrovski, T. Schuster and M. Bleicher, arXiv:0903.0396 [hep-ph], submitted to PRC.

[Pin99] C. Pinkenburg *et al.* [E895 Collaboration], Phys. Rev. Lett. **83**, 1295 (1999) [arXiv:nucl-ex/9903010].

[Pin99] C. Pinkenburg *et al.* [E895 Collaboration], *Prepared for Centennial Celebration and Meeting of the American Physical Society (Combining Annual APS General Meeting and the Joint Meeting of the APS and the AAPT), Atlanta, Georgia, 20-26 Mar 1999*

[Pin02] C. Pinkenburg *et al.* [E895 Collaboration], Nucl. Phys. A **698**, 495 (2002) [arXiv:nucl-ex/0104025].

[Pol01] G. Policastro, D. T. Son and A. O. Starinets, Phys. Rev. Lett. **87**, 081601 (2001) [arXiv:hep-th/0104066].

[Pra08] S. Pratt and J. Vredevoogd, Phys. Rev. C **78**, 054906 (2008) [arXiv:0809.0516 [nucl-th]].

[Pra] S. Pratt, CRAB version 3, http://www.nscl.msu.edu/∼pratt/freecodes/crab/home.html.

[QM08] Proceedings of Quark Matter 2008, J. Phys. G **35** (2008)

[Raf82] J. Rafelski and B. Muller, Phys. Rev. Lett. **48**, 1066 (1982) [Erratum-ibid. **56**, 2334 (1986)].

[Rap01] R. Rapp and E. V. Shuryak, Phys. Rev. Lett. **86**, 2980 (2001) [arXiv:hep-ph/0008326].

[Ray03] R. L. Ray [STAR Collaboration], Nucl. Phys. A **715**, 45 (2003) [arXiv:nucl-ex/0211030].

[Red02] K. Redlich and A. Tounsi, Eur. Phys. J. C **24**, 589 (2002) [arXiv:hep-ph/0111261].

[Red08] K. Redlich, B. Friman and C. Sasaki, J. Phys. G **35**, 044013 (2008) [arXiv:0712.2926 [hep-ph]].

[Rei98] M. Reiter, A. Dumitru, J. Brachmann, J. A. Maruhn, H. Stoecker and W. Greiner, Nucl. Phys. A **643**, 99 (1998) [arXiv:nucl-th/9806010].

[Rei03] M. Reiter, E. L. Bratkovskaya, M. Bleicher, W. Bauer, W. Cassing, H. Weber and H. Stoecker, Nucl. Phys. A **722**, 142 (2003) [arXiv:nucl-th/0301067].

[Ric05] A. Richard [NA49 Collaboration], J. Phys. G **31**, S155 (2005).

[Ris95a] D. H. Rischke, Y. Pursun and J. A. Maruhn, Nucl. Phys. A **595**, 383 (1995) [Erratum-ibid. A **596**, 717 (1996)] [arXiv:nucl-th/9504021].

[Ris95b] D. H. Rischke, S. Bernard and J. A. Maruhn, Nucl. Phys. A **595**, 346 (1995) [arXiv:nucl-th/9504018].

[Ris96a] D. H. Rischke and M. Gyulassy, Nucl. Phys. A **597**, 701 (1996) [arXiv:nucl-th/9509040].

[Ris96b] D. H. Rischke and M. Gyulassy, Nucl. Phys. A **608**, 479 (1996) [arXiv:nucl-th/9606039].

[Rom07] P. Romatschke and U. Romatschke, Phys. Rev. Lett. **99**, 172301 (2007) [arXiv:0706.1522 [nucl-th]].

[ROOT] http://root.cern.ch/

[Ros75] A. M. Rossi, G. Vannini, A. Bussiere, E. Albini, D. D'Alessandro and G. Giacomelli, Nucl. Phys. B **84**, 269 (1975).

[Rus04] V. N. Russkikh, Yu. B. Ivanov, E. G. Nikonov, W. Norenberg and V. D. Toneev, Phys. Atom. Nucl. **67**, 199 (2004) [Yad. Fiz. **67**, 195 (2004)] [arXiv:nucl-th/0302029].

[Sar06] E. K. G. Sarkisyan and A. S. Sakharov, AIP Conf. Proc. **828**, 35 (2006) [arXiv:hep-ph/0510191].

[Sca01] O. Scavenius, A. Mocsy, I. N. Mishustin and D. H. Rischke, Phys. Rev. C **64**, 045202 (2001) [arXiv:nucl-th/0007030].

[Sce99] S. Scherer *et al.*, Prog. Part. Nucl. Phys. **42**, 279 (1999).

[Sch74] W. Scheid, H. Muller and W. Greiner, Phys. Rev. Lett. **32**, 741 (1974).

[Scn93] V. Schneider, U. Katscher, D. H. Rischke, B. Waldhauser, J. A. Maruhn and C. D. Munz, J. Comput. Phys. **105**, 92 (1993).

[Scr02] S. Schramm, Phys. Rev. C **66**, 064310 (2002) [arXiv:nucl-th/0207060].

[Scr03] S. Schramm, Phys. Lett. B **560**, 164 (2003) [arXiv:nucl-th/0210053].

[Scu06] D. Schumacher, S. Vogel and M. Bleicher, Acta Phys. Hung. A **27**, 451 (2006) [arXiv:nucl-th/0608041].

[Scw51] J. S. Schwinger, Phys. Rev. **82**, 664 (1951).

[Sen93] P. Senger *et al.* [KaoS Collaboration], Nucl. Instrum. Meth. A **327**, 393 (1993).

[Sjo94] T. Sjostrand, Comput. Phys. Commun. **82**, 74 (1994).

[Sjo06] T. Sjostrand, S. Mrenna and P. Skands, JHEP **0605**, 026 (2006) [arXiv:hep-ph/0603175].

[Sko06] V. V. Skokov and V. D. Toneev, Phys. Rev. C **73**, 021902 (2006) [arXiv:nucl-th/0509085].

[Sli03] J. Slivova [CERES/NA45 Collaboration], Nucl. Phys. A **715**, 615 (2003) [arXiv:nucl-ex/0212013].

[Soc04] O. . J. Socolowski, F. Grassi, Y. Hama and T. Kodama, Phys. Rev. Lett. **93**, 182301 (2004) [arXiv:hep-ph/0405181].

[Sof99a] S. Soff *et al.*, Phys. Lett. B **471**, 89 (1999) [arXiv:nucl-th/9907026].

[Sof99b] S. Soff, S. A. Bass, M. Bleicher, H. Stoecker and W. Greiner, arXiv:nucl-th/9903061.

[Sof01] S. Soff, S. A. Bass and A. Dumitru, Phys. Rev. Lett. **86**, 3981 (2001) [arXiv:nucl-th/0012085].

[Sof02] S. Soff, S. A. Bass, D. H. Hardtke and S. Y. Panitkin, Phys. Rev. Lett. **88**, 072301 (2002) [arXiv:nucl-th/0109055].

[Son08] H. Song and U. W. Heinz, Phys. Lett. B **658**, 279 (2008) [arXiv:0709.0742 [nucl-th]].

[Sor89] H. Sorge, H. Stoecker and W. Greiner, Nucl. Phys. A **498**, 567C (1989).

[Sor92] H. Sorge, M. Berenguer, H. Stoecker and W. Greiner, Phys. Lett. B **289**, 6 (1992).

[Sor97] H. Sorge, Phys. Lett. B **402**, 251 (1997) [arXiv:nucl-th/9701012].

[Sor99] H. Sorge, Phys. Rev. Lett. **82**, 2048 (1999) [arXiv:nucl-th/9812057].

[Spi98a] C. Spieles, H. Stoecker and C. Greiner, Phys. Rev. C **57**, 908 (1998) [arXiv:hep-ph/9708280].

[Spi98b] C. Spieles *et al.*, Eur. Phys. J. C **5**, 349 (1998) [arXiv:hep-ph/9706525].

[Spi98c] C. Spieles *et al.*, Nucl. Phys. A **638**, 507 (1998).

[Spi98d] C. Spieles *et al.*, arXiv:hep-ph/9810486.

[Spi99a] C. Spieles, R. Vogt, L. Gerland, S. A. Bass, M. Bleicher, H. Stoecker and W. Greiner, J. Phys. G **25**, 2351 (1999) [arXiv:hep-ph/9809441].

[Spi99b] C. Spieles *et al.*, Phys. Lett. B **458**, 137 (1999).

[Spi99c] C. Spieles, R. Vogt, L. Gerland, S. A. Bass, M. Bleicher, H. Stoecker and W. Greiner, Phys. Rev. C **60**, 054901 (1999) [arXiv:hep-ph/9902337].

[Ste08a] J. Steinheimer, M. Bleicher, H. Petersen, S. Schramm, H. Stocker and D. Zschiesche, Phys. Rev. C **77**, 034901 (2008) [arXiv:0710.0332 [nucl-th]].

[Ste08b] J. Steinheimer, M. Mitrovski, T. Schuster, H. Petersen, M. Bleicher and H. Stoecker, arXiv:0811.4077 [hep-ph], accepted in PLB.

[Ste08c] J. Steinheimer, H. Petersen, G. Burau, M. Bleicher and H. Stoecker, Proceedings for WPCF 2008, Krakau, Poland

[Ste08d] J. Steinheimer, H. Petersen, G. Burau, M. Bleicher, S. Schramm, H. Stöcker, D. Zschiesche, Proceedings for WWND 2008, South Padre,

[Sth04] M. A. Stephanov, Prog. Theor. Phys. Suppl. **153**, 139 (2004) [Int. J. Mod. Phys. A **20**, 4387 (2005)] [arXiv:hep-ph/0402115].

[Stö80] H. Stoecker, J. A. Maruhn and W. Greiner, Phys. Rev. Lett. **44**, 725 (1980).

[Stö86] H. Stoecker and W. Greiner, Phys. Rept. **137**, 277 (1986).

[Stö92] H. Stoecker *et al.*, Nucl. Phys. A **538**, 53C (1992).

[Stö06] H. Stoecker, B. Betz and P. Rau, PoS **CPOD2006**, 029 (2006) [arXiv:nucl-th/0703054].

[Tea01a] D. Teaney, J. Lauret and E. V. Shuryak, Phys. Rev. Lett. **86**, 4783 (2001) [arXiv:nucl-th/0011058].

[Tea01b] D. Teaney, J. Lauret and E. V. Shuryak, arXiv:nucl-th/0110037.

[The83] J. Theis, G. Graebner, G. Buchwald, J. A. Maruhn, W. Greiner, H. Stoecker and J. Polonyi, Phys. Rev. D **28**, 2286 (1983).

[Ton05] V. D. Toneev, Yu. B. Ivanov, E. G. Nikonov, W. Norenberg and V. N. Russkikh, Phys. Part. Nucl. Lett. **2**, 288 (2005) [Pisma Fiz. Elem. Chast. Atom. Yadra **2N5**, 43 (2005)].

[Tor05] G. Torrieri, S. Steinke, W. Broniowski, W. Florkowski, J. Letessier and J. Rafelski, Comput. Phys. Commun. **167**, 229 (2005) [arXiv:nucl-th/0404083].

[Tor08a] G. Torrieri, B. Tomasik and I. Mishustin, Phys. Rev. C **77**, 034903 (2008) [arXiv:0707.4405 [nucl-th]].

[Tor08b] G. Torrieri and I. Mishustin, Phys. Rev. C **78**, 021901 (2008) [arXiv:0805.0442 [hep-ph]].

[Tra99] C. T. Traxler, U. Mosel and T. S. Biro, Phys. Rev. C **59**, 1620 (1999) [arXiv:hep-ph/9808298].

[VaH82] L. Van Hove, Phys. Lett. B **118**, 138 (1982).

[Van99] S. E. Vance and M. Gyulassy, Phys. Rev. Lett. **83**, 1735 (1999) [arXiv:nucl-th/9901009].

[Ver99] G. I. Veres [NA49 Collaboration], Nucl. Phys. A **661**, 383 (1999).

[Vid95] F. Videbaek and O. Hansen, Phys. Rev. C **52**, 2684 (1995).

[Vog06a] S. Vogel and M. Bleicher, Phys. Rev. C **74**, 014902 (2006) [arXiv:nucl-th/0509105].

[Vog06b] S. Vogel and M. Bleicher, Acta Phys. Hung. A **27**, 421 (2006).

[Vog07] S. Vogel, G. Torrieri and M. Bleicher, arXiv:nucl-th/0703031.

[Vog08a] S. Vogel and M. Bleicher, Phys. Rev. C **78**, 064910 (2008) [arXiv:0710.1158 [hep-ph]].

[Vog08b] S. Vogel, H. Petersen, K. Schmidt, E. Santini, C. Sturm, J. Aichelin and M. Bleicher, Phys. Rev. C **78**, 044909 (2008) [arXiv:0710.4463 [hep-ph]].

[Vol00] S. A. Voloshin and A. M. Poskanzer, Phys. Lett. B **474**, 27 (2000) [arXiv:nucl-th/9906075].

[Vol08] S. A. Voloshin, A. M. Poskanzer and R. Snellings, arXiv:0809.2949 [nucl-ex].

[Wal92] R. Waldhauser, D. H. Rischke, U. Katscher, J. A. Maruhn, H. Stoecker and W. Greiner, Z. Phys. C **54**, 459 (1992).

[Web98] H. Weber *et al.*, Phys. Lett. B **442**, 443 (1998) [arXiv:nucl-th/9808021].

[Web02] H. Weber, PhD thesis, Johann Wolfgang Goethe-Universität Frankfurt (2002)

[Wer93] K. Werner, Phys. Rept. **232**, 87 (1993).

[Won01] S. M. H. Wong, M. Belkacem, J. I. Kapusta, S. A. Bass, M. Bleicher and H. Stoecker, Phys. Rev. C **63**, 014903 (2001) [arXiv:hep-ph/0008119].

[Xu05] Z. Xu and C. Greiner, Phys. Rev. C **71**, 064901 (2005) [arXiv:hep-ph/0406278].

[Xu08a] Z. Xu and C. Greiner, Phys. Rev. Lett. **100**, 172301 (2008) [arXiv:0710.5719 [nucl-th]].

[Xu08b] Z. Xu, C. Greiner and H. Stocker, Phys. Rev. Lett. **101**, 082302 (2008) [arXiv:0711.0961 [nucl-th]].

[Zee04] G. Zeeb, M. Reiter and M. Bleicher, Phys. Lett. B **586**, 297 (2004) [arXiv:nucl-th/0312015].

[Zhu05] X. l. Zhu, M. Bleicher and H. Stoecker, Phys. Rev. C **72**, 064911 (2005) [arXiv:nucl-th/0509081].

[Zhu06a] X. Zhu, H. Petersen and M. Bleicher, J. Phys. G **32**, S365 (2006).

[Zhu06b] X. l. Zhu, M. Bleicher and H. Stoecker, J. Phys. G **32**, 2181 (2006) [arXiv:nucl-th/0601049].

[Zhu:2006c] X. Zhu, H. Petersen and M. Bleicher, AIP Conf. Proc. **828**, 17 (2006).

[Zhu07] X. Zhu, M. Bleicher, S. L. Huang, K. Schweda, H. Stoecker, N. Xu and P. Zhuang, Phys. Lett. B **647**, 366 (2007) [arXiv:hep-ph/0604178].

[Zsc02a] D. Zschiesche, S. Schramm, H. Stoecker and W. Greiner, Phys. Rev. C **65**, 064902 (2002) [arXiv:nucl-th/0107037].

[Zsc02b] D. Zschiesche, S. Schramm, J. Schaffner-Bielich, H. Stoecker and W. Greiner, Phys. Lett. B **547**, 7 (2002) [arXiv:nucl-th/0209022].

[Zsc05] D. Zschiesche, G. Zeeb, S. Schramm and H. Stoecker, J. Phys. G **31**, 935 (2005) [arXiv:nucl-th/0407117].

[Zsc07] D. Zschiesche, G. Zeeb and S. Schramm, J. Phys. G **34**, 1665 (2007) [arXiv:nucl-th/0602073].

Acknowledgements

First of all, I would like to thank my supervisor Marcus Bleicher for all the support and confidence he had in me and my work. Without his "late-night" emails this thesis would not have been written. The good working atmosphere and the inspiring discussions - ("Kommste mal mit runter?") - are an unforgetable experience.

Next, I would like to thank the man behind everything Horst Stöcker for all the opportunities that he offered me and for his believe in me. Despite his very limited time at the institute he always dropped in our office for a few words and it was good to know that he is there in case one needs him.

I would like to thank Jörg Aichelin for his hospitality during my two-month stay in Nantes. It was a very good experience to work together with Mickael on the NJL model.

I would like to thank Dirk Rischke for providing the one fluid ideal hydrodynamics code.

I would like to thank the Deutsche Telekom Stiftung for the financial support in form of a scholarship and for the opportunities to participate in many international conferences due to the generous travel money. The support from Frau Frense-Heck concerning all technical issues and the very interesting meetings of all the scholarship holders is acknowledged. I would like to thank my mentor, Markus Lennartz, who has given me the opportunity to visit him for two days in his office. To talk with him is always a great pleasure.

All the nice supporting features like, e.g. lectures, lecture weeks, softskill courses or travel money, that completed the education during my PhD time that were offered by the Helmholtz Research School on Quark Matter Studies are gratefully acknowledged. In this respect, I would like to thank Henner Büsching who made this all possible with his calm and optimistic character. He often helped me to reduce the hectic that I usually produce and has taken care of the other parts in life like singing NGL songs, dancing valse or a visit of the merry-go-round on the christmas market.

Most of the calculations in this work have been performed using the ressources of the Center fo Scientific Computing (CSC) cluster. Therefore, the crew of the CSC administration, namely Manuel Reiter, Guido Laubender and Christian Jankowiak, was always a great help.

As a neccessary basis for the every-day work, the ITP and FIAS computer administration is acknowledged for doing a very good job. I would like to mention here especially Alexander Achenbach and Thomas Weber, but also Oliver Fochler and Thilo Kalkbrenner, that always had time to give advice, if problems or questions occured.

I would like to thank the UrQMD group, Elvira Santini, Sascha Vogel, Qingfeng Li, Stephane Haussler, Katharina Schmidt, Daniel Krieg, Timo Spielmann, Michael Mitrovski, Tim Schuster, for good collaborations and a nice working environment. Furthermore, it has always been fun to work with Gunnar Gräf, my first diploma student. For the development of the hybrid approach Gerhard Burau and Jan Steinheimer have contributed a lot and I would like to thank you for all the discussions and the staying power. Special thanks go to Björn Bäuchle for all the things that I have learned from/with him concerning physics or the rest of life.

I appreciated the good working atmosphere in the office together with Benjamin Koch and later on Marlene Nahrgang and all the international guests that changed weekly or monthwise. I was always happy about the calm working periods that contrasted the chaotic surroundings at ITP in general.

I would like to thank Gabriela Meyer and Etele Molnar for interesting conversations during lunch time that helped to relax a bit and take a break.

As members of my PhD committee Christoph Blume and Harald Appelshäuser accompanied this work always with a critical eye and good questions about the feasibility of the ideas. The meetings every half year had a great value to sit back and sort out all the new projects.

I would like to thank Thorsten Renk for hundreds of motivating emails, many discussions about physics, philosophy or politics and the great times we spent together in Montreal, Jyväskylä and Prag. After two month together in the student housing in Nantes and some bottles of red wine Marcus Bluhm became a good friend of mine and it was always a pleasure to talk and make fun with him. I would like to thank my friends, especially Sabrina, Sarah, Jeannette, Isa, Gudrun and Alexander, for the times that we have spent together in museums, bars or on other relaxing activities.

Last but not least I would like to thank my parents Christel and Karsten Petersen who always supported me and tried to understand what I am doing. They gave me the self-confidence and optimism that is necessary to write a PhD thesis.

Lebenslauf

Name:	Hannah Petersen
Addresse:	Würzburger Strasse 20 60385 Frankfurt am Main
Geburtsdatum:	12.10.1982
Geburtsort:	Frankfurt am Main
Nationalität:	deutsch
Familienstand:	ledig

Ausbildung:

- 1989-1993: Schwarzburgschule, Grundschule, Frankfurt am Main
- 1993-2002: Musterschule
  Gymnasium, Frankfurt am Main (Abitur-Durchschnittsnote:1,0)
- Oktober 2002: Beginn des Physikstudiums an der J.W.-Goethe Universität Frankfurt
- April 2004: Physik-Vordiplom,
  J.W. Goethe-Universität Frankfurt, "sehr gut"
- Juni 2006: Physik-Diplom
  Diplomarbeit mit dem Titel "Elliptic and directed flow in heavy ion collisions",
  J.W. Goethe-Universität Frankfurt, "Ausgezeichnet"
- seit August 2006: Doktorandin in Physik an der J.W. Goethe-Universität Frankfurt
- seit Januar 2007: Promotions-Stipendium der Deutsche Telekom Stiftung
- Juni 2007: Michael-Loulakis-Preis für die Diplomarbeit
- seit Oktober 2006: Studentin in der Helmholtz Research School on Quark Matter Studies
- seit November 2007: Studentin in der Otto Stern School
- seit Januar 2009: Studentin in der Helmholtz Graduate School for Heavy Ion Research

Meine akademischen Lehrer waren:

JProf. Dr. Bleicher
JProf. Dr. Blume
Prof. Dr. Constantinescu
Prof. Dr. Detel
Prof. Dr. Dörner
JProf. Dr. Dumitru
Prof. Dr. Greiner
Prof. Dr. Kolbesen
Prof. Dr. Lang
Prof. Dr. Maruhn
PD Dr. Pflaum
Prof. Dr. Rischke
Prof. Dr. Schempp
Prof. Dr. Stöcker
Prof. Dr. Stroth
Prof. Dr. Ströbele